Drift-diffusion models for innovative semiconductor devices and their numerical solution

Dr. Patricio Farrell
Habilitationsschrift
Fachbereich Mathematik und Informatik

März 2022

Contents

1 Introduction **1**

2 Semiconductor charge transport models **2**
2.1 Model hierarchy 2
2.2 Drift-diffusion equations for charge transport 3
2.2.1 Maxwell-Stefan diffusion and electrostatic drift 3
2.2.2 Statistics function 6
2.3 The van Roosbroeck system 8
2.3.1 Thermodynamic equilibrium 11
2.3.2 Free energy and dissipation rate 12
2.3.3 Existence and uniqueness results 13
2.4 Inverse problems 15
2.4.1 The lateral photovoltage scanning method 16

3 Numerical solution and simulation of charge transport **18**
3.1 The finite volume method on Voronoi meshes 18
3.1.1 Finite volume method in higher dimensions 18
3.2 Flux discretization 21
3.2.1 The electric displacement flux 21
3.2.2 The classical Scharfetter-Gummel scheme 21
3.2.3 Generalized Scharfetter-Gummel schemes 22
3.2.4 Modified Scharfetter-Gummel schemes 23
3.2.5 Quadrature-based Scharfetter-Gummel schemes 24
3.3 Consistency with the thermodynamic equilibrium 28
3.4 Free energy and dissipation rate 28
3.5 Existence, uniqueness and convergence 29
3.6 Mesh generation 29
3.7 Solvers 31
3.7.1 Gummel iterations 31
3.7.2 Newton's method and path continuation 32

References **33**

4 Publication list 41

5 Overview of published work relevant for the *Habilitation* 45

6 Assessing the quality of the excess chemical potential flux scheme for degenerate semiconductor device simulation 46

7 Modelling charge transport in perovskite solar cells: Potential-based and limiting ion vacancy depletion 58

8 Modeling and simulation of the lateral photovoltage scanning method 60

9 Assessing doping inhomogeneities in GaAs crystal via simulations of lateral photovoltage scanning method 61

10 From atomistic tight binding theory to macroscale drift diffusion: multiscale modeling and numerical simulation of uni-polar charge transport in (In,Ga)N devices with random fluctuations 62

11 Nonlinear diffusion, boundary layers and nonsmoothness: Analysis of challenges in drift-diffusion semiconductor simulations 77

12 Highly Accurate Quadrature-based Scharfetter-Gummel Schemes for Charge Transport in Degenerate Semiconductors 95

13 A Novel Surface Remeshing Scheme via Radial Basis Functions and Higher-Dimensional Embedding 97

14 Tetrahedral Mesh Improvement Using Moving Mesh Smoothing, Lazy Searching Flips, and RBF Surface Reconstruction 124

15 Computational and Analytical Comparison of Flux Discretizations for the Semiconductor Device Equations beyond Boltzmann Statistics 137

16 Uniform Second Order Convergence of a Complete Flux Scheme on Unstructured 1D Grids for a Singularly Perturbed Advection–Diffusion Equation and Some Multidimensional Extensions 139

17 On Thermodynamic Consistency of a Scharfetter-Gummel Scheme Based on a Modified Thermal Voltage for Drift-Diffusion Equations with Diffusion Enhancement 141

1

Introduction

This document presents an extended overview/summary of published papers submitted for the habilitation qualification at *Freie Universität Berlin*. In Chapter 2, we present (mostly) macroscale drift-diffusion models which describe charge transport in a self-consistent electric field with a particular focus on nonlinear diffusion, correctly describing the physical statistics as well as relevant generalizations to ions and relevant applications such as inverse problems. In Chapter 3, we discuss the numerical solution of these models via the Voronoi finite volume method with careful focus on the different flux discretization. Then in Chapter 5, we give a summary of each relevant paper, link in to the previous two chapters, and explain to which extent the author was involved in the implementation, conceptualization and writing.

2

Semiconductor charge transport models

2.1 Model hierarchy

In this section, we introduce macroscopic semi-classical drift-diffusion models which describe how electric charge carriers move in a semiconductor. The main premise of these models is that electrons and holes do not act like discrete quantities but can be thought of as oceans of charge with a fluid-type nature. This assumption is valid if particles collide easily, that is the collision-free *mean free path* along which the particles do not change their direction or energies is relatively short. In this case, one may introduce averaged densities for currents or charge carriers. Such computed current densities can then be directly compared to the current which experimentalists measure with an ammeter.

For completeness we point out some other types of charge transport models. If it is no longer possible to introduce averaged densities, one has to resort to more general kinetic equations of which the Boltzmann equation is arguably the most prominent one. In this case, statistical distribution functions describe the charge carriers. While kinetic equations may yield a more complete physical understanding, the arising systems are significantly more complex and harder to solve. The Boltzmann equation, for example, is a nonlinear integro-differential equation with seven different independent variables. While quantum mechanical information enters macroscale drift-diffusion as well as kinetic models indirectly, for example via the corresponding right-hand sides, at times even more accurate quantum models may be required which involve Schrödinger type of equations.

Besides drift and diffusion, there are also additional types of transport mechanisms. These include hopping, scattering or tunneling effects. While hopping we will at best focus on indirectly via appropriate state equations [20], we neglect the other final two completely.

More information concerning different types of model can be found in [36].[1] The current chapter is based in large parts on [PF2] and [PF25].

[1] My own publications are prefixed with my initials, e.g. [PF26], whereas general references are not, e.g. [36].

2.2 Drift-diffusion equations for charge transport

In this section, we describe an isothermal drift-diffusion-reaction model for an ensemble of charge carriers as developed in [PF2]. The drift is due to an electric field (the negative gradient of the electrostatic potential) which is self-consistently coupled to the moving charge carriers via Poisson's equation. The diffusion may take nonlinear effects into account, increasing even more in areas of large changes in concentration. We denote the charged species in the mixture with α and their particle densities with n_α. The electrostatic potential ψ is linked to the electrical field via $\mathbf{E} = -\nabla\psi$. The general system reads

$$-\nabla \cdot (\varepsilon_s \nabla \psi) = q \sum_{\alpha \in \mathbb{M}} z_\alpha n_\alpha, \tag{2.1a}$$

$$\partial_t n_\alpha + \nabla \cdot \mathbf{J}_\alpha = r_\alpha, \quad \alpha \in \mathbb{M}, \tag{2.1b}$$

where q is the positive elementary charge and $z_\alpha \in \mathbb{Z}$ denotes the charge number of species α. The species are labeled by a finite index set $\mathbb{M}$. With $\varepsilon_s = \varepsilon_0 \varepsilon_r$ we refer to the dielectric permittivity, where ε_0 is the vacuum dielectric constant and ε_r the relative permittivity of the material. The particle fluxes are given by $\mathbf{J}_\alpha$ and the density production/reduction rates of species α are denoted by r_α. We point out that system (2.1) is formulated in terms of densities. Eventually we will rewrite the system in terms of quasi Fermi potentials φ_α since they allow a more compact formulation of the flux.

In the next sections, we introduce the fluxes $\mathbf{J}_\alpha$ in the context of charge transport.

2.2.1 Maxwell-Stefan diffusion and electrostatic drift

As discussed in Section 2.1, under the assumption that the mean free path is relatively short, the isothermal friction between the species in the mixture can be modelled via Maxwell-Stefan diffusion [57, 99] and electrostatic drift

$$n_\alpha \left(\nabla \Phi_\alpha + z_\alpha q \nabla \psi\right) = \sum_{\beta \in \mathbb{M}, \beta \neq \alpha} \zeta_{\alpha\beta} \left(\frac{\mathbf{J}_\beta}{n_\beta} - \frac{\mathbf{J}_\alpha}{n_\alpha} \right), \quad \alpha \in \mathbb{M}, \tag{2.2}$$

where Φ_α denotes the chemical potential (per particle) of species α (see [51, (18.2.4)]) and $\zeta_{\alpha\beta} = \zeta_{\beta\alpha}$ the symmetric binary friction coefficient between species α and β. The quantities $\mathbf{J}_\alpha / n_\alpha$ correspond to the velocities of species α.

Let us assume that one of the species within the mixture, $\beta = L$, represents the lattice. Moreover, assume that the friction constitutes solely an interaction between the lattice and the remaining species,

$$\zeta_{\alpha\beta} = 0 \quad \text{and} \quad \zeta_{\alpha L} \geq 0 \,, \quad \alpha, \beta \in \mathbb{M} \setminus \{L\}.$$

In order to avoid that the lattice density n_L appears in the mass balances (2.1b), we describe the transport of the species $\alpha \in \mathbb{M} \setminus \{L\}$ from the viewpoint of the crystalline lattice. In other words, we assume that a vanishing flux, $\mathbf{J}_L = \mathbf{0}$, and that there is no

production/reaction of lattice species, $r_L = 0$. This implies by (2.1b) that $\partial_t n_L = 0$. Furthermore, we assume that the friction does not cause a deformation of the lattice. Moreover, the lattice shall not have a charge, i.e. $z_L = 0$. This also implies that the lattice species does not contribute to Poisson's equation (2.1a).

Finally, we distinguish between mobile and stationary (immobile) species and refer to the latter with the index set $\mathbb{S} \subset \mathbb{M}$. Hence, we model the different particle fluxes by

$$\mathbf{J}_\alpha = -\frac{n_\alpha}{\zeta_{\alpha L}} n_\alpha \left(\nabla \Phi_\alpha + z_\alpha q \nabla \psi\right), \qquad \alpha \in \mathbb{M} \setminus (\mathbb{S} \cup \{L\}), \tag{2.3}$$

$$\mathbf{J}_\alpha = 0, \qquad \alpha \in \mathbb{S} \cup \{L\}. \tag{2.4}$$

Also, there should be no production of immobile species, i.e.

$$r_\alpha = 0, \quad \text{for } \alpha \in \mathbb{S} \cup \{L\}.$$

The quasi Fermi vs. electrochemical potential

In analogy to semiconductor theory, we use the following relation between the chemical Φ_α, the electrostatic ψ and the quasi Fermi potential φ_α,

$$\varphi_\alpha = \frac{1}{z_\alpha q} \Phi_\alpha + \psi, \tag{2.5}$$

see also [51]. Using this definition, we can highlight the fact that the gradient of the quasi Fermi potentials are the driving forces of the current particle densities (2.3), namely

$$\mathbf{J}_\alpha = -z_\alpha q \frac{n_\alpha}{\zeta_{\alpha L}} n_\alpha \nabla \varphi_\alpha, \quad \alpha \in \mathbb{M} \setminus (\mathbb{S} \cup \{L\}).$$

Particle vs. electric currents

The charge density carried by species α is given by $z_\alpha q n_\alpha$. The electric current $\mathbf{j}_\alpha$ observed due to the transport of species α is related to the particle flux $\mathbf{J}_\alpha$ via

$$\mathbf{j}_\alpha = z_\alpha q \mathbf{J}_\alpha \quad \alpha \in \mathbb{M} \setminus (\mathbb{S} \cup \{L\}). \tag{2.6}$$

Relating the friction coefficient of species α inversely to the mobility μ_α via

$$\zeta_{\alpha L} = q \frac{n_\alpha}{\mu_\alpha}, \tag{2.7}$$

with phenomenological units $\mathrm{kg}/(\mathrm{m}^3\mathrm{s})$, leads to an electric current of the form

$$\mathbf{j}_\alpha = -(z_\alpha q)^2 \frac{n_\alpha}{\zeta_{\alpha L}} n_\alpha \nabla \varphi_\alpha = -(z_\alpha)^2 q \mu_\alpha n_\alpha \nabla \varphi_\alpha, \quad \alpha \in \mathbb{M} \setminus (\mathbb{S} \cup \{L\}). \tag{2.8}$$

For such an electric flux the general drift-diffusion equation (2.1b) now finally reads

$$z_\alpha q \partial_t n_\alpha + \nabla \cdot \mathbf{j}_\alpha = z_\alpha q r_\alpha \;, \quad \alpha \in \mathbb{M} \setminus (\mathbb{S} \cup \{L\}). \tag{2.9}$$

We emphasize that the carrier densities n_α depend on the quasi Fermi potentials φ_α and the electrostatic potential ψ, i.e. $n_\alpha = n_\alpha(\psi, \varphi_\alpha)$ which we discuss next. With this dependence Equation (2.9) can be written exclusively in terms of potentials.

State equation and generalized Einstein relation

It is possible to link the densities n_α to their quasi Fermi potentials φ_α via a state equation [43], given by

$$n_\alpha = N_\alpha \mathcal{F}_\alpha\Big(\eta_\alpha(\psi, \varphi_\alpha)\Big), \quad \eta_\alpha = z_\alpha \frac{q(\varphi_\alpha - \psi) + E_\alpha}{k_B T}, \tag{2.10}$$

where $\mathcal{F}_\alpha \colon \mathbb{R} \to \mathbb{R}$ describes the carrier statistics, N_α denotes an effective density and E_α an energy. We assume that $\mathcal{F}_\alpha$ is continuously differentiable and monotonously increasing. Several different physically relevant choices for $\mathcal{F}_\alpha$ will be discussed in Section 2.2.2. To see the connection with the literature, we express the electric fluxes (2.8) mathematically equivalently in terms of densities. To this end, we introduce the *generalized Einstein relation*

$$D_\alpha = \mu_\alpha U_T g_\alpha(\eta_\alpha), \tag{2.11}$$

where $U_T = k_B T/q$ is the thermal voltage, k_B denotes the Boltzmann constant, T the constant absolute temperature, and g the *nonlinear diffusion enhancement* [38] given by

$$g_\alpha(\eta_\alpha) = \frac{\mathcal{F}_\alpha(\eta_\alpha)}{\mathcal{F}_\alpha{}'(\eta_\alpha)}. \tag{2.12}$$

Mathematically, the diffusion enhancement can be seen as some a nonlinear, potential-dependent diffusion. With the help of the state equation (2.10) as well as the generalized Einstein relation (2.11) it is now possible to derive the electric currents in drift-diffusion form

$$\mathbf{j}_\alpha = -z_\alpha q \mu_\alpha \Big(U_T g_\alpha(\eta_\alpha) \nabla n_\alpha + z_\alpha n_\alpha \nabla \psi\Big) = -z_\alpha q \Big(D_\alpha(n_\alpha) \nabla n_\alpha + z_\alpha \mu_\alpha n_\alpha \nabla \psi\Big). \tag{2.13}$$

We stress that the diffusion enhancement g_α in (2.12) can be equivalently reformulated in terms of densities

$$g_\alpha\left(\frac{n_\alpha}{N_\alpha}\right) = \frac{n_\alpha}{N_\alpha} \left(\mathcal{F}_\alpha^{-1}\right)' \left(\frac{n_\alpha}{N_\alpha}\right). \tag{2.14}$$

2.2.2 Statistics function

In the following, we present some physically meaningful choices for $\mathcal{F}_\alpha$ given in the state equation (2.10). Four common choices are conceivable:

$$\mathcal{F}_\alpha(\eta) = \exp(\eta), \qquad \text{(Boltzmann)} \tag{2.15}$$

$$\mathcal{F}_\alpha(\eta) = F_{B,\gamma}(\eta) := \frac{1}{\exp(-\eta) + \gamma}, \qquad \text{(Blakemore)} \tag{2.16}$$

$$\mathcal{F}_\alpha(\eta) = F_j(\eta) := \frac{1}{\Gamma(j+1)} \int_0^\infty \frac{\xi^j}{\exp(\xi - \eta) + 1} \, \mathrm{d}\xi, \; j > -1. \qquad \text{(Fermi-Dirac)} \tag{2.17}$$

$$\mathcal{F}_\alpha(\eta) = G(\eta; \sigma) := \frac{1}{\sigma} \frac{1}{\sqrt{2\pi}} \int_{-\infty}^\infty \exp\left(-\frac{\xi^2}{2\sigma^2}\right) \frac{1}{\exp(\xi - \eta) + 1} \, \mathrm{d}\xi. \qquad \text{(Gauß-Fermi)} \tag{2.18}$$

The Fermi-Dirac integral of order one-half [43], denoted by $F_{1/2}$, with $\Gamma(1/2+1) = \sqrt{\pi}/2$, is fundamental in the simulation of inorganic, classical three-dimensional (3D) semiconductors [PF25, 78]. Especially for high doping concentrations or low temperatures Fermi-Dirac statistics is indispensable. The Gauss-Fermi integral [29] is the statistics of choice in the context of organic semiconductors, such as OLEDs. These integrals can be approximated by Blakemore ($\gamma = 0.27$) [97] and by Boltzmann statistics in the low density limit. The relationships between the different statistic are shown in Figure 2.1.

Statistics functions deviating from the Boltzmann approximation lead to nonlinear diffusion which grows for larger densities/potentials as can be seen from (2.11) and (2.12) or visually in Figure 2.2. Non-Boltzmann statistics are indispensable for high doping concentrations, organic semiconductors or very low temperatures. Since they lead to nonlinear diffusion, solving the drift diffusion system in a thermodynamically consistent way requires additional care [PF10].

Remark 2.1 *Via the relation $F_j'(\eta) = F_{j-1}(\eta)$, the Fermi-Dirac statistics (2.17) can be defined for negative integers j as well [81]. In particular, for order -1, we have*

$$F_{-1}(\eta) = \frac{1}{\exp(-\eta) + 1}.$$

We observe that $F_{-1} = F_{B,1}$. This type of statistics corresponds physically to a mean-field ideal lattice gas, see [80, Eqn. 3.5.1].

We finish this section by motivating very briefly the state equation (2.10) for the case of electrons. Assuming that the electrons in the conduction band are in quasi equilibrium, i. e. they are described by the quasi Fermi level $E_{F_n} = q\varphi_n$, the electron density $n = n_n$

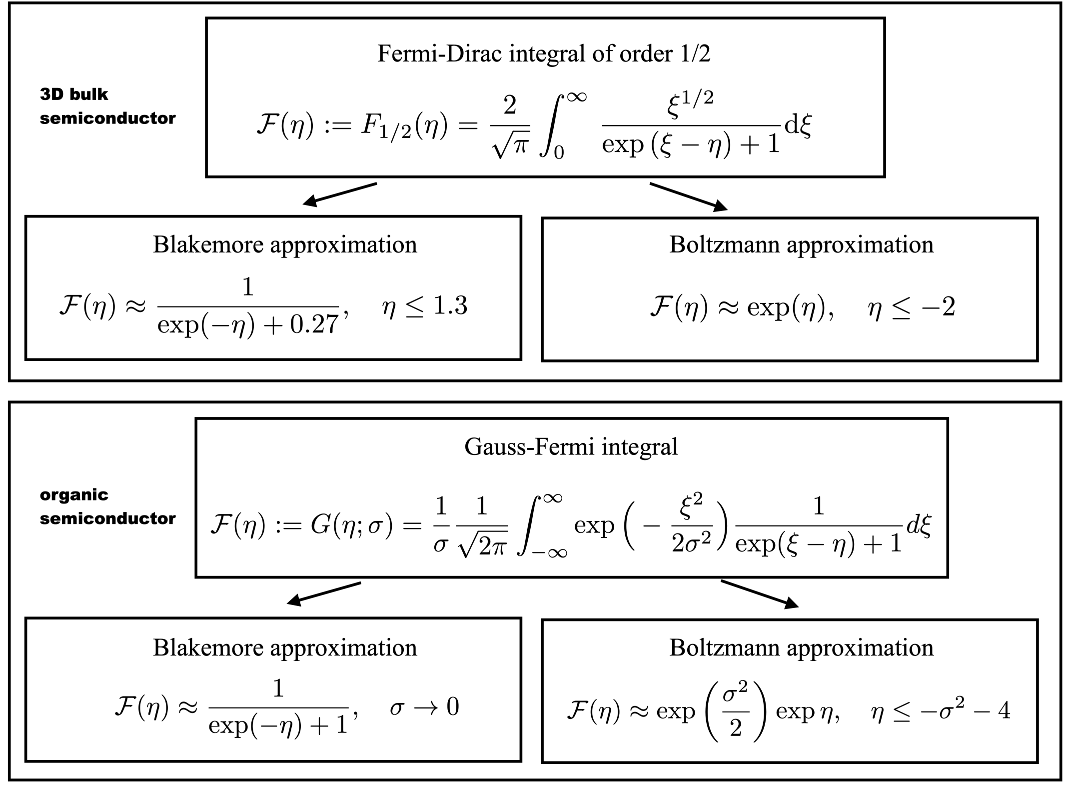

Figure 2.1: This figure, similar to a figure in [PF25], shows two important classes of the statistical distribution function: for inorganic 3D semiconductors and for organic semiconductors [29]. Both can be approximated using the Blakemore or Boltzmann distribution function.

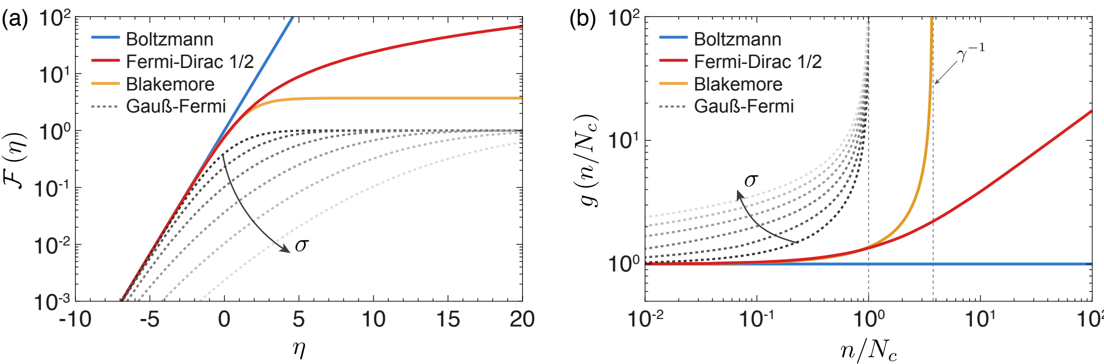

Figure 2.2: Some common statistics $\mathcal{F}$ (left) and their corresponding diffusion enhancements g (right). For the Blakemore and the Gauß-Fermi functions the carrier density saturates for high values of η which implies that the corresponding diffusion enhancement factors blow up. The figure is a color version of a figure found in [PF25].

is given by a convolution integral of the density of states DOS(E)

$$n = \int_{-\infty}^{\infty} \mathrm{DOS}\,(E)\, f_{\mathrm{FD}}\,(E - E_{F_n})\,\mathrm{d}E, \tag{2.19}$$

with the Fermi-Dirac distribution function f_{FD} which is defined to be

$$f_{\mathrm{FD}}\,(E - E_{F_n}) = \frac{1}{\exp\left(\frac{E - E_{F_n}}{k_B T}\right) + 1} \tag{2.20}$$

Within the effective mass approximation [43], it is possible to express this convolution as a product of the *effective* density of states N_α and one of the nondimensionalized statistical distribution function $\mathcal{F}$ from the beginning of this subsection, leading to the state equation (2.10).

2.3 The van Roosbroeck system

Even though we have introduced a rather general setup in the previous section, we explicitly formulate the drift-diffusion model now for a (doped) bipolar semiconductor device. The literature refers to this special case of (2.1) as *basic semiconductor equations* or *van Roosbroeck system* [98]. In this special case, we can give a bit more meaning to some of the constants, state boundary and initial conditions, discuss generation and recombination as well as introduce the thermodynamic equilibrium. Because the van Roosbroeck system is bipolar, we consider apart from the Poisson equation two continuity equations for the density of free (negatively charged) electrons $n = n(\mathbf{x}, t)$ occupying the conduction band as well as the density of (positively charged) holes $p = p(\mathbf{x}, t)$ occupying the valence band. Here we have simplified the earlier notation in the sense that $n = n_n$ and $p = n_p$. Furthermore, we consider fixed charges namely density of ionized built-in *dopants* $C(\mathbf{x}) = N_D^+(\mathbf{x}) - N_A^-(\mathbf{x})$, where N_D^+ denotes the density of singly ionized donor atoms and N_A^- is the density of singly ionized acceptor atoms.

Let $\Omega \subset \mathbb{R}^d$ be a bounded domain for $d \in \{1, 2, 3\}$, the van Roosbroeck system consists of three coupled nonlinear partial differential equations of the form

$$-\nabla \cdot (\varepsilon_s \nabla \psi) = q\,(p - n + C)\,, \tag{2.21a}$$

$$-q\partial_t n + \nabla \cdot \mathbf{j}_n = -q(G - R), \tag{2.21b}$$

$$q\partial_t p + \nabla \cdot \mathbf{j}_p = q(G - R), \tag{2.21c}$$

for $\mathbf{x} \in \Omega$ and $t \in [0, T]$. The current densities in (2.21b) and (2.21c) are given by the usual expressions

$$\mathbf{j}_n = -q\mu_n n \nabla \varphi_n \qquad \text{and} \qquad \mathbf{j}_p = -q\mu_p p \nabla \varphi_p. \tag{2.21d}$$

That is, the negative gradients of the quasi Fermi potentials are the driving forces of the currents [44]. From the numerical point of view, this formulation is advantageous, as the

quasi-Fermi potentials and the electrostatic potential have the same physical units and similar ranges. The state equation (2.10) now reads

$$n = N_c \mathcal{F}\left(\frac{q(\psi - \varphi_n) - E_c}{k_B T}\right) \qquad \text{and} \qquad p = N_v \mathcal{F}\left(\frac{E_v - q(\psi - \varphi_p)}{k_B T}\right). \tag{2.22}$$

The state equations (2.22) indicate that the electric potential effectively leads to a bending of the energy band edge levels and thus a nonlinear, self-consistent coupling to the carrier densities is achieved. We assume a constant temperature for both carrier species and the crystal lattice. The generation and recombination rates G and R will be discussed in Section 2.3.

Initial and boundary conditions

The van Roosbroeck system (2.21) must be supplemented with initial and boundary conditions. The initial conditions for time $t = 0$ are given by the initial distributions ψ^I, φ_n^I and φ_p^I, i. e.

$$\psi(\mathbf{x}, 0) = \psi^I(\mathbf{x}), \qquad \varphi_n(\mathbf{x}, 0) = \varphi_n^I(\mathbf{x}), \qquad \varphi_p(\mathbf{x}, 0) = \varphi_p^I(\mathbf{x}) \quad \text{for} \;\; \mathbf{x} \in \Omega.$$

As for the boundary conditions, we will discuss the three most important conditions. Let us assume the boundary of the domain Ω can be decomposed into ohmic contacts, a gate contact and *artificial* interfaces, i. e.

$$\partial\Omega = \left(\bigcup_{\alpha=1}^{N_O} \Gamma_{O,\alpha}\right) \cup \Gamma_G \cup \Gamma_A.$$

Semiconductor-metal interfaces, such as ohmic contacts, are modeled usually by Dirichlet boundary conditions. For any ohmic contact $\Gamma_{O,\alpha}$ with $\alpha = 1, \ldots, N_O$, we set

$$\psi(\mathbf{x}, t) = \psi_0(\mathbf{x}) + U_\alpha(t), \tag{2.23a}$$

$$\varphi_n(\mathbf{x}, t) = U_\alpha(t), \qquad \text{for all } \mathbf{x} \in \Gamma_{O,\alpha} \text{ and } t \in [0, T] \tag{2.23b}$$

$$\varphi_p(\mathbf{x}, t) = U_\alpha(t), \tag{2.23c}$$

where U_α denotes the corresponding externally applied contact voltage. The value ψ_0 at the boundary is defined by local charge neutrality:

$$0 = N_v \mathcal{F}\left(\frac{E_v - q\psi_0(\mathbf{x})}{k_B T}\right) - N_c \mathcal{F}\left(\frac{q\psi_0(\mathbf{x}) - E_c}{k_B T}\right) + C(\mathbf{x}). \tag{2.24}$$

We just remark, that in general, this equation yields no analytical solution, and therefore its solution needs to be obtained by a nonlinear solver. The boundary conditions for the more advanced nonlinear semiconductor-metal interfaces (Schottky contacts) can be found in [78].

Gate contacts are modeled by Robin boundary conditions for the electrostatic potential and homogeneous Neumann boundary conditions for the quasi Fermi potentials

$$\begin{aligned} \varepsilon_s \nabla\psi(\mathbf{x},t)\cdot\boldsymbol{\nu} + \tfrac{\varepsilon_{\text{ox}}}{d_{\text{ox}}}(\psi(\mathbf{x},t) - U_G(t)) &= 0, \\ \mathbf{j}_n(\mathbf{x},t)\cdot\boldsymbol{\nu} = \mathbf{j}_p(\mathbf{x},t)\cdot\boldsymbol{\nu} &= 0, \end{aligned} \qquad \text{for all } \mathbf{x}\in\Gamma_G \text{ and } t\in[0,T], \tag{2.25}$$

where ε_{ox} and d_{ox} are the absolute dielectric permittivity and the thickness of the oxide, respectively. The outer normal vector to the boundary $\partial\Omega$ is denoted with $\boldsymbol{\nu}$. The function $U_G(t)$ is the gate voltage applied at the outside of the insulating gate oxide at Γ_G.

On the remaining (artificial) interfaces one typically imposes homogeneous Neumann boundary conditions (natural boundary conditions), namely

$$\nabla\psi(\mathbf{x},t)\cdot\boldsymbol{\nu} = \mathbf{j}_n(\mathbf{x},t)\cdot\boldsymbol{\nu} = \mathbf{j}_p(\mathbf{x},t)\cdot\boldsymbol{\nu} = 0 \qquad \text{for all } \mathbf{x}\in\Gamma_A \text{ and } t\in[0,T]. \tag{2.26}$$

Generation and recombination rates

The recombination rate R on the right-hand side of equations (2.21b) and (2.21c) describes the radiative and non-radiative generation or recombination of carriers due to thermal excitation and various scattering effects. We assume that the recombination rate $R(n,p)$ is given by the sum of the most common processes, namely the Shockley-Read-Hall recombination R_{SRH}, the spontaneous radiative recombination R_{rad} and the Auger recombination R_{Auger}. All of these rates are of the form

$$R(n,p) = r(n,p)np\left(1 - \exp\left(\frac{q\varphi_n - q\varphi_p}{k_B T}\right)\right), \tag{2.27}$$

where $r(n,p)$ corresponds to one of three recombination mechanism [43, 78, 40]. In Figure 2.3, one finds the definitions of these rates together with a schematic illustration of the corresponding processes. For Boltzmann statistics, (2.27) is equivalent to the widely used $R(n,p) = r(n,p)(np - N_{\text{intr}}^2)$, where N_{intr} is the intrinsic carrier density given by

$$N_{\text{intr}}^2 = N_c N_v \exp\left(-\frac{E_c - E_v}{k_B T}\right) \qquad \text{and} \qquad U_T = \frac{k_B T}{q}. \tag{2.28}$$

Electron-hole pairs may be generated optically for example via sunlight or lasers. In this case, some photons are reflected with a constant reflectivity $\mathcal{R}$. The other *impinged* photons create electron-hole pairs, resulting in a generation rate

$$G(\mathbf{x}) = N_{ph}(1-\mathcal{R})S(\mathbf{x}), \tag{2.29}$$

where depending on the spatial dimension d, we may set the shape function S (normalized

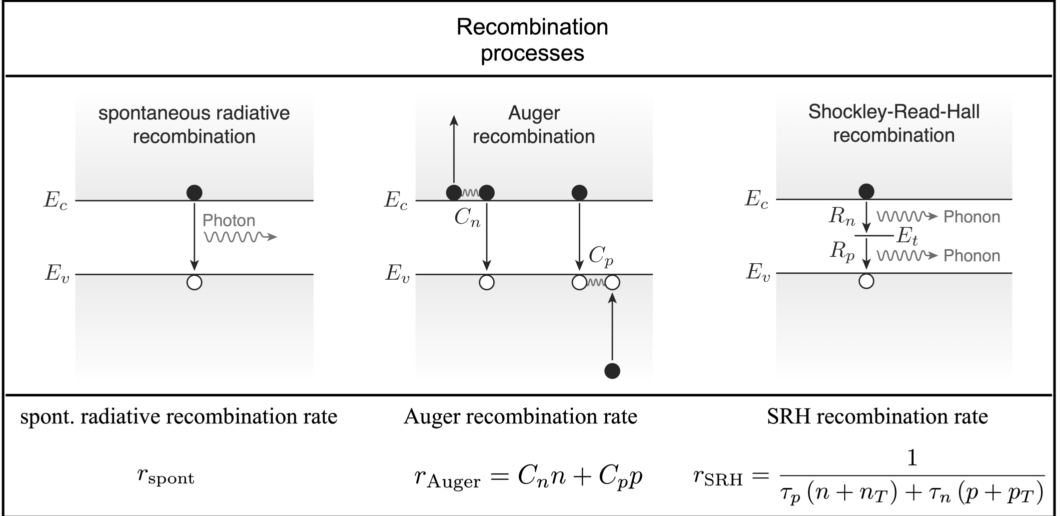

Figure 2.3: This figure, a modified version from an image found in [PF25], illustrates three different recombination processes. The carrier life times τ_n, τ_p, the reference carrier densities n_T, p_T and the coefficients r_{spont}, C_n, C_p are material dependent parameters.

by $\int_{\mathbb{R}^d} S(\mathbf{x})d\mathbf{x} = 1$) for example to be

$$S(x) = \frac{1}{\sqrt{2\pi}\sigma} \exp\left(-\frac{1}{2}\left(\frac{x - x_0}{\sigma}\right)^2\right), \tag{2.30}$$

$$S(x, z) = \frac{1}{2d_A} \exp\left(-\frac{|z|}{d_A}\right), \tag{2.31}$$

$$S(x, y, z) = \frac{1}{2\pi\sigma^2} \frac{1}{2d_A} \exp\left(-\frac{1}{2}\left(\frac{x - x_0}{\sigma}\right)^2\right) \exp\left(-\frac{1}{2}\left(\frac{y - y_0}{\sigma}\right)^2\right) \exp\left(-\frac{|z|}{d_A}\right). \tag{2.32}$$

Here the σ denotes the beam width and d_A the penetration depth. N_{ph} is the impinging photon rate on the whole surface of the sample given by

$$N_{ph} = \frac{P\lambda}{hc}, \tag{2.33}$$

where P denotes the power of the light source, λ the wave length of the laser and $hc = 6.6 \times 10^{-34}\,\text{m}^2\text{kg/s} = 6.6 \times 10^{-34}\,\text{Js}$ the Planck constant.

2.3.1 Thermodynamic equilibrium

The thermodynamic equilibrium is characterized by vanishing current fluxes $\mathbf{j}_n(\mathbf{x}, t) = \mathbf{j}_p(\mathbf{x}, t) = \mathbf{0}$. As a consequence, there is neither recombination nor generation $R(n, p) = G(\mathbf{x}) = 0$, the applied/gate voltages vanish $U_\alpha = U_G = 0$ and the quasi Fermi potentials

assume constant values which due to (2.27) are equal and due to the boundary conditions are zero:

$$\varphi_n = \varphi_p = 0.$$

Therefore, the van Roosbroeck system (2.21) reduces to the nonlinear Poisson equation

$$-\nabla \cdot \varepsilon_s \nabla \psi = q \left(N_v \mathcal{F}\left(\frac{E_v - q\psi}{k_B T}\right) - N_c \mathcal{F}\left(\frac{q\psi - E_c}{k_B T}\right) + C \right). \tag{2.34}$$

The solution of (2.34) with corresponding boundary conditions defines the *built-in potential* denoted with ψ_{eq}.

2.3.2 Free energy and dissipation rate

We consider consistency with fundamental principles of thermodynamics to be a quality measure for models describing natural processes. So it is of significant interest to study this consistency for continuous as well as discrete models. Due to our simplifying assumption of constant temperature, we cannot expect energy conservation in the classical sense. The second law of thermodynamics for nonequilibrium processes [92, 86] requires non-negativity of the local entropy production which, multiplied by the temperature T, gives the *dissipation rate*.

For the sake of readability, we discuss these concepts for Boltzmann statistics [59] here, see [68] and [49] for more general statistics. For the triple (ψ, n, p) and a thermodynamic equilibrium solution $(\psi_{\text{eq}}, n_{\text{eq}}, p_{\text{eq}}) := (\psi_{\text{eq}}, n(\psi_{\text{eq}}), p(\psi_{\text{eq}}))$ of the full van Roosbroeck system the *free energy* is defined as

$$\begin{aligned} \mathbb{F}(\psi, n, p) = &\int_\Omega \left(n \log \frac{n}{n_{\text{eq}}} - n + p \log \frac{p}{p_{\text{eq}}} - p + n_{\text{eq}} + p_{\text{eq}} \right) d\mathbf{x} \\ &+ \int_\Omega \frac{\varepsilon_s}{2} \left\| \nabla \left(\psi - \psi_{\text{eq}}\right) \right\|^2 d\mathbf{x} + \frac{1}{2} \int_{\Gamma_G} \frac{\varepsilon_{\text{ox}}}{d_{\text{ox}}} \left(\psi - \psi_{\text{eq}}\right)^2 ds. \end{aligned} \tag{2.35}$$

For a transient solution $(\psi(t), n(t), p(t))$ of (2.21), the function $\mathbb{L}(t) = \mathbb{F}(\psi(t), n(t), p(t))$ decays exponentially as t tends to infinity and one has

$$\mathbb{L}(t) = \mathbb{L}(0) - \int_0^t \mathbb{D}(\tau) d\tau,$$

where $\mathbb{D}(t)$ is the nonnegative dissipation rate [59]

$$\mathbb{D}(t) = \int_\Omega \Big(n\mu_n \|\nabla \varphi_n\|^2 + p\mu_p \|\nabla \varphi_p\|^2 + r(n,p)(np-1)\log(np) \Big) d\mathbf{x} \geq 0 \tag{2.36}$$

depending on t because the densities n, p vary with time. This result confirms the consistency with the second law of thermodynamics. Incidentally, the function $\mathbb{L}$ is a Lyapunov function, allowing in certain situations to prove the global stability of the thermodynamical equilibrium. Furthermore, it can be used as a tool to prove uniqueness of solutions to the van Roosbroeck system (2.21). This leads us naturally to the following subsection.

2.3.3 Existence and uniqueness results

When modeling complex physical phenomena, it is often necessary to simplify the underlying physical model. Therefore, a sound mathematical investigation is necessary to assess the implications of such simplifications. Take, for example, the electrostatic potential of a device. Physically, we know that such a potential exists. Hence, a sound model should guarantee its existence – also from a mathematical point of view. If the existence cannot be shown, then the model does not represent the physical world accurately. Apart from existence, uniqueness of the solution is often desirable as well as continuous dependence on the initial data.

The mathematical technique used to prove existence and uniqueness depends on the device geometry and the model. The first existence result of the van Roosbroeck system was shown by Mock [83]. Since then several results have been obtained by Gajewski and Gröger, we refer the interested reader to [73, 76]. In [76], the key tool to show the existence and uniqueness of the time dependent system is based on finding a Lyapunov function. Moreover, Gajewski and Gröger presented the first result which considered Fermi-Dirac statistics instead of Boltzmann statistics. There are other important existence results. We would like to mention explicitly the results studied by Markowich see for example [77], Jüngel [62], and Jerome [60].

We would like to point out that these results are not of purely analytical interest but can also be used to design numerical methods. Gummel's method [91], for example, (see Section 3.7) is based on the same fixed point iteration technique used to obtain the existence result which we discuss next. The connection to numerics can be found in [60]. We would like to give the reader an idea regarding the proof of a standard result without going into the tricky details. We follow ideas from Markowich's textbook [74].

We consider the stationary van Roosbroeck system with Boltzmann statistics. Using a scaling that can be found in [74, Section 2.4] and making a change of variables, we can rewrite the steady-state van Roosbroeck system in the following way

$$-\lambda^2 \Delta\psi = \delta^2 e^{-\psi} v - \delta^2 e^{\psi} u + C, \tag{2.37a}$$

$$\nabla \cdot (\mu_n e^{\psi} \nabla u) = \tilde{R}, \tag{2.37b}$$

$$\nabla \cdot (\mu_p e^{-\psi} \nabla v) = \tilde{R}. \tag{2.37c}$$

The densities n and p are related to the so-called *Slotboom variables* u and v via $n = \delta^2 e^{\psi} u$ and $p = \delta^2 e^{-\psi} v$. In (2.37), the parameter λ denotes the normed characteristic Debye length of the device, δ^2 indicates the scaled intrinsic carrier density and $\tilde{R}$ is the scaled recombination term. It is of the form $\tilde{R} = c(\psi, u, v)(uv - 1)$ with $c(\psi, u, v) > 0$. The chosen scaling and change of variables make it possible to rewrite the boundary conditions. We consider only ohmic contacts and homogeneous Neumann boundaries.

In order to prove the existence of solutions for the system (2.37) equipped with suitable boundary conditions, we need to make several technical assumptions. We refer the interested reader to [74] where these assumptions are well explained as well as physically and mathematically justified. Here, we would rather like to focus on the key idea of the proof which is exploited numerically, omitting mathematical detail. The existence proof

is based on an iteration scheme which considers the Poisson equation (2.37a) decoupled from the continuity equations (2.37b) and (2.37c). The proof consists of the following steps:

1. We fix some $u_0, v_0 > 0$, and consider the semilinear elliptic problem

$$-\lambda^2 \Delta\psi = \delta^2 e^{-\psi} v_0 - \delta^2 e^{\psi} u_0 + C, \text{ in } \Omega, \qquad \text{(plus BC for } \psi \text{ on } \partial\Omega). \tag{2.38}$$

   Using standard analytical results for semilinear elliptic equations (namely the Leray-Schauder's fixed point theorem and the maximum principle [52]) we prove that there exists a unique solution of the problem (2.38) that we denote with ψ_1.

2. We insert the solution ψ_1 of (2.38) into the decoupled linear elliptic equations

$$\nabla \cdot (\mu_n e^{\psi_1} \nabla u) = c(\psi_1, u_0, v_0)(u v_0 - 1), \text{ in } \Omega, \qquad \text{(plus BC for } u \text{ on } \partial\Omega), \tag{2.39}$$

$$\nabla \cdot (\mu_p e^{-\psi_1} \nabla v) = c(\psi_1, u_0, v_0)(u_0 v - 1), \text{ in } \Omega, \qquad \text{(plus BC for } v \text{ on } \partial\Omega). \tag{2.40}$$

   We point out that in the right-hand side of (2.39) the rate c depends only on ψ_1 determined from the previous step and on the fixed u_0, v_0. The other term, $uv_0 - 1$, depends linearly on the unknown u. Analogous considerations are valid for (2.40). Physically, this means that in the factor describing relaxation to equilibrium, $uv - 1$, we freeze the hole density, more precisely the Slotboom variable v_0, in the continuity equation for the electrons and vice versa. Thanks to the non-negativity of $c(\psi_1, u, v)$ there exist unique solutions u_1 and v_1 to (2.39) and (2.40). This is ensured by standard results on linear elliptic equations (see for example [52]).

3. Based on the first two steps, we can now define a map H which maps (u_0, v_0) onto (u_1, v_1). This map is known as *Gummel map*. It is possible to prove that this map has a fixed point (u^*, v^*) which determines a (weak) solution (ψ^*, u^*, v^*) of the coupled system (2.37). The electrostatic potential ψ^* which solves Poisson's equation (2.37a) can be determined using the first step by substituting (u_0, v_0) with (u^*, v^*).

Finally, we discuss the uniqueness of solutions to the van Roosbroeck system. It is well known that for the steady-state system the uniqueness of the solution cannot be shown without additional assumptions, for example, on the applied voltage. This is no surprise, as in fact, some semiconductor devices (e.g. thyristors [67]) are designed to have multiple steady states. However, for a device in thermal equilibrium (see Section 2.3.1), we have $u = v = 1$. In this case, there is a unique function which satisfies the Poisson equation (2.37a). Hence, the solution $(\psi_e, 1, 1)$ is the unique equilibrium solution of the system (2.37), see [83]. For sufficiently small bias voltages the uniqueness of the solution is shown in [74] under some specific assumptions on the recombination rates. All recombination mechanisms appearing in Figure 2.3 fulfill these assumptions. However, impact ionization rates for example are excluded.

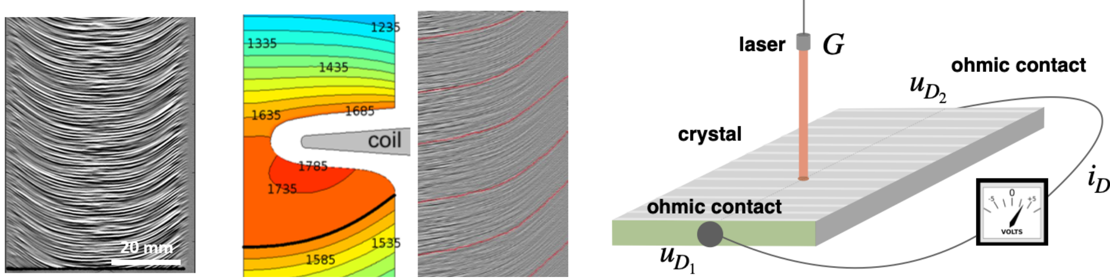

Figure 2.4: Striations from LPS measurement (left); temperature field simulation created by a coil (the black line represents the solid-liquid interface at $1687K$) as well the corresponding striations (middle); LPS measurement setup (right). This image is a modified version of a figure found in [PF3].

2.4 Inverse problems

Semiconductor crystals are the very basis for any optoelectronic component such as transistors, LEDs or solar cells. Crystals are solid substances with an inherent structure/symmetry. The higher the crystal quality (the symmetry), the more technologically challenging and expensive it is to grow these crystals.

Thus, it is important to improve the furnaces used for crystal growth. If one knows the temperature field of these furnaces, better crystals can be grown. Unfortunately, it is impossible to measure the temperature distribution during crystal growth without damaging the crystal structure and introducing impurities. Moreover, silicon, for example, melts at extremely high temperatures, around $1687K$. While it is virtually impossible to predict the temperature distribution in the furnace and the growing crystal experimentally, one may reconstruct it after the crystal has cooled down. During growth along the solid-liquid interface microscopic variations in the crystal appear, see Figure 2.4 (left and middle). These so-called *striations* can be measured even in the cooled-down crystal and correspond to isothermal contour lines of the temperature field. Thus, the striations can be used to predict the temperature field. So the question of finding the temperature field becomes a question of finding the striations which are proportional to the doping gradient – ideally without damaging the crystal.

Traditionally, the local doping concentration is measured by studying the electrical resistivity by a four-point-probe resistivity setup after the crystal has been sawed into individual wafers or into a set of longitudinal cuts [95]. The main drawback of this technique is the relatively poor spatial resolution (few millimeters [8]) and the rather long acquisition time. Even though lateral resolution can be improved to approach the micrometer scale by using spreading resistance imaging, this gain in resolution comes at the expense of even longer acquisition times [89, 88]. Moreover since the tip touches the wafer surface, the measurement itself may alter the surface properties. Another technique is *secondary ion mass spectroscopy* (SIMS). Unfortunately, it is intrinsically destructive and detects only high doping concentrations $N_A > 1 \times 10^{15}\,\mathrm{cm}^{-3}$ for light elements such

as boron [75]. There are also noninvasive microwave-based techniques such as scanning microwave impedance microscopy [9]. Since microwaves have a larger penetration depth than lasers, simulation times would take significantly longer.

To overcome all these limitations, the *lateral photovoltage scanning* method (LPS) has been proposed [55]. This opto-electrical measurement procedure detects doping inhomogeneities at wafer-scale and room temperature in a non-destructive fashion, see Figure 2.4 (right). Interestingly, besides being very cost-effective and fast, this tabletop setup is especially suitable for low doping concentrations ($10^{12}\,\mathrm{cm}^{-3}$ to $10^{16}\,\mathrm{cm}^{-3}$) and thus applies to a larger range of doping concentrations than SIMS. The LPS method excites the semiconductor crystal with a laser, creating a voltage difference at the sample edges which is proportional to the gradient in doping density at the illumination site. This voltage difference can be measured, from which one can infer the doping profile from the voltage difference. However, from a mathematical point of view one has to solve an inverse problem. An efficient solution of this inverse problem – an ambitious future task – requires a fast and reliable solution of the *forward* problem (where the voltage difference is determined from a implicit boundary condition).

2.4.1 The lateral photovoltage scanning method

The laser generates a potential difference at both ohmic contacts Γ_{D_1} and Γ_{D_2}, see Figure 2.4 (right). Let $i_D := j_{D_1} = -j_{D_2}$ be the current through the ohmic contact Γ_{D_1} and the voltmeter be modeled as a simple circuit with resistance ∇.

We denote both electric potentials in the network at ohmic contacts Γ_{D_1} and Γ_{D_2} with u_{D_1} and u_{D_2}, respectively. Without loss of generality, we set $u_{D_1} = 0$, which implies that the LPS signal is measured at the second contact $u_{LPS} := u_{D_2}$. Modified nodal analysis (MNA) yields

$$u_{LPS} + \psi_0|_{\Gamma_{D_2}} - \psi_0|_{\Gamma_{D_1}} = \nabla i_D(u_{LPS}), \tag{2.41}$$

where ψ_0 refers to the charge neutral potential defined in (2.24). Notice that (2.41) is an implicit equation for u_{LPS} since i_D depends on u_{LPS} via the van Roosbroeck system (2.21). Modeling ohmic contacts is achieved by Dirichlet boundary conditions for both quasi Fermi potentials

$$\varphi_n|_{\Gamma_{D_1}} = \varphi_p|_{\Gamma_{D_1}} = u_{D_1} = 0 \qquad \text{and} \qquad \varphi_n|_{\Gamma_{D_2}} = \varphi_p|_{\Gamma_{D_2}} = u_{D_2} = u_{LPS}. \tag{2.42}$$

How to solve (2.21) thermodynamically consistently for nonlinear diffusion via Voronoi finite volume methods has recently been addressed in [PF25, PF10, PF7] and will be discussed in Chapter 3.1.

In the LPS application, the doping profile C is not known and the LPS voltage u_{LPS} is determined such that the implicit boundary condition (2.41) is automatically satisfied by the voltmeter. Since the doping profile enters the van Roosbroeck system (2.21) as an unknown parameter, we have indeed an inverse PDE problem. The forward problem, on the other hand, assumes that the doping profile C is known but the LPS voltage u_{LPS} is not given explicitly. In this case, we have to guarantee that the nonlinear and implicit boundary condition (2.41) is satisfied. We summarize both problems here:

Definition 2.2 (Forward LPS problem) *For a given doping profile C and an unknown LPS signal u_{LPS}, we consider the van Roosbroeck system* (2.21) *with ohmic contacts* (2.42) *and ensure that the implicit and nonlinear boundary equation* (2.41) *is satisfied.*

Definition 2.3 (Inverse LPS problem) *For a given LPS signal u_{LPS} and an unknown doping profile C, we consider the van Roosbroeck system* (2.21) *with ohmic contacts* (2.42) *and use for the electrostatic potential the Dirichlet boundary conditions $\psi|_{\Gamma_{D_2}} = u_{LPS}$ and $\psi|_{\Gamma_{D_1}} = 0$.*

3

Numerical solution and simulation of charge transport

Several different numerical techniques were proposed to solve the previously introduced models numerically such as finite difference (FD) [78, 27], finite element (FE) [22, 10, 12, 45] and mixed or discontinuous Galerkin (DG) methods [65, 6]. In the following, we focus on the finite volume (FV) method on Voronoi meshes which is similarly flexible as the finite element or the discontinuous Galerkin method. It can handle relatively well boundary layers, nonlinear diffusion and complex domains. Furthermore, one can often provably preserve physical properties such as exponential decay of the free energy or the positivity of densities.

3.1 The finite volume method on Voronoi meshes

The finite volume method is close to the physicist's approach to derive partial differential equations by subdividing the computational domain into *representative elementary volumes* or *control volumes*. The *two-point flux* finite volume method described here can be interpreted as a straightforward generalization of the one-dimensional Scharfetter-Gummel scheme [85] to higher dimensions. The 2D variant of this approach was introduced as *box method* in [79]. Historically, it goes back to [96]. The 3D variant of this method was probably first investigated in [56, 59].

We first describe how we divide our computational domain into control volumes, then dedicate several sections to consistent flux discretizations and finally discuss some properties of these fluxes.

3.1.1 Finite volume method in higher dimensions

Suppose, we partition our domain Ω into N non-intersecting, convex, polyhedral control volumes ω_k. That is $\Omega = \bigcup_{k=1}^{N} \omega_k$. We associate with each control volume a node $\mathbf{x}_k \in \omega_k$. For interior control volumes the node shall lie in the volume. However, if the control volume intersects with the boundary of our domain, we demand that the node

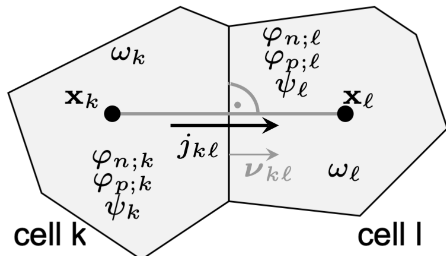

Figure 3.1: Two adjacent control volumes ω_k and ω_ℓ with corresponding data.

lies on the boundary of the control volume $\mathbf{x}_k \in \partial\Omega \cap \omega_k$. We assume that the partition is *admissible* in the sense of [53], that is the *edge* $\overline{\mathbf{x}_k\mathbf{x}_\ell}$ with length $h_{k\ell} = \|\mathbf{x}_\ell - \mathbf{x}_k\|$ is orthogonal to $\partial\omega_k \cap \partial\omega_\ell$. Thus, the normal vectors to $\partial\omega_k$ can be calculated by

$$\boldsymbol{\nu}_{k\ell} = \frac{\mathbf{x}_\ell - \mathbf{x}_k}{\|\mathbf{x}_\ell - \mathbf{x}_k\|},$$

see Figure 3.1 for details. We will refer to such to the set of nodes and control volumes in 1D, 2D or 3D as *Voronoi mesh* since by construction cell k contains all points which are closest in the Euclidean sense to the node $\mathbf{x}_k$. Even though Voronoi cells look rather complicated, it has to be pointed out that they never have to be calculated explicitly since the Voronoi mesh is the dual mesh of a Delaunay triangulation. Some more details concerning the mesh generation will be given in Section 3.6.

In order to keep the following discrete version of the van Roosbroeck system (2.21) simple, we introduce two abbreviations similar to (2.10), namely

$$\eta_n(\psi, \varphi_n) = \frac{q(\psi - \varphi_n) - E_c}{k_B T} \quad \text{and} \quad \eta_p(\psi, \varphi_p) = \frac{E_v - q(\psi - \varphi_n)}{k_B T}, \tag{3.1}$$

and assume that we have one gate contact with gate voltage U_G. Next, we integrate the van Roosbroeck system (2.21) over ω_k and apply Gauss's divergence theorem, resulting in the integral equations

$$\begin{aligned}
-\int_{\partial\omega_k} \varepsilon_s \nabla\psi \cdot \boldsymbol{\nu} ds + \int_{\partial\omega_k \cap \Gamma_G} \frac{\varepsilon_{\text{ox}}}{d_{\text{ox}}}(\psi - U_G) ds &= q \int_{\omega_k} \left(C - N_c \mathcal{F}(\eta_n(\psi, \varphi_n)) + N_v \mathcal{F}(\eta_p(\psi, \varphi_p))\right) d\mathbf{x} \\
-q \frac{\partial}{\partial t} \int_{\omega_k} N_c \mathcal{F}(\eta_n(\psi, \varphi_n)) d\mathbf{x} + \int_{\partial\omega_k} \mathbf{j}_n \cdot \boldsymbol{\nu} ds &= q \int_{\omega_k} R d\mathbf{x}, \\
q \frac{\partial}{\partial t} \int_{\omega_k} N_v \mathcal{F}(\eta_p(\psi, \varphi_p)) d\mathbf{x} + \int_{\partial\omega_k} \mathbf{j}_p \cdot \boldsymbol{\nu} ds &= -q \int_{\omega_k} R d\mathbf{x},
\end{aligned}$$

for $k = 1, \ldots, N$. Here, $\boldsymbol{\nu}$ is the outward-pointing unit normal, see Figure 3.1. These equations represent a local integral version of the van Roosbroeck system for every control volume. In particular, the first equation is Gauss' law of electrodynamics. The other two

equations are balance laws or continuity equations for the carrier densities. The densities in each control volume change only due to either in and outflow through the boundary or recombination/generation of charge carriers.

We split the surface integrals into the sum of integrals over the interfaces between the control volume ω_k and its neighbors. Employing one point quadrature rules for the surface and volume integrals, we deduce the finite volume scheme

$$\sum_{\omega_\ell \in \mathcal{N}(\omega_k)} |\partial\omega_k \cap \partial\omega_\ell| D_{k,\ell} = q|\omega_k| \left(C_k - N_c \mathcal{F}\left(\eta_n\left(\psi_k, \varphi_{n;k}\right)\right) + N_v \mathcal{F}\left(\eta_p\left(\psi_k, \varphi_{p;k}\right)\right)\right) + |\partial\omega_k \cap \Gamma_G| \frac{\varepsilon_{\mathrm{ox}}}{d_{\mathrm{ox}}}(U_G - \psi_k) \tag{3.2a}$$

$$-q|\omega_k| N_c \frac{d}{dt} \mathcal{F}\left(\eta_n\left(\psi_k, \varphi_{n;k}\right)\right) + \sum_{\omega_\ell \in \mathcal{N}(\omega_k)} |\partial\omega_k \cap \partial\omega_\ell| j_{n;k,\ell} = q|\omega_k| R_k, \tag{3.2b}$$

$$q|\omega_k| N_v \frac{d}{dt} \mathcal{F}\left(\eta_p\left(\psi_k, \varphi_{p;k}\right)\right) + \sum_{\omega_\ell \in \mathcal{N}(\omega_k)} |\partial\omega_k \cap \partial\omega_\ell| j_{p;k,\ell} = -q|\omega_k| R_k. \tag{3.2c}$$

In the above formulas, $\mathcal{N}(\omega_k)$ denotes the set of all control volumes neighboring ω_k. In 2D, the measure $|\partial\omega_k \cap \partial\omega_\ell|$ corresponds to the length of the boundary line segment and in 3D to the area of the intersection of the boundary surfaces. The measure $|\omega_k|$ is in 2D given by the area and in 3D by the volume of the control volume ω_k. The unknowns ψ_k, $\varphi_{n;k}$ and $\varphi_{p;k}$ are approximations of the electric potential as well as the quasi Fermi potentials for electrons and holes evaluated at node $\mathbf{x}_k$ which will have to be determined by solving the nonlinear discrete system (3.2).

Accordingly, R_k is defined as

$$R_k = R\big(N_c \mathcal{F}\left(\eta_n\left(\psi_k, \varphi_{n;k}\right)\right), N_v \mathcal{F}\left(\eta_p\left(\psi_k, \varphi_{p;k}\right)\right)\big).$$

The doping is defined by the integral average

$$C_k = \frac{1}{|\omega_k|} \int_{\omega_k} C(\mathbf{x}) d\mathbf{x}$$

which can be estimated by its nodal value $C(\mathbf{x}_k)$. The numerical fluxes $D_{k,\ell}$, $j_{n;k,\ell}$ and $j_{p;k,\ell}$ approximate $-\varepsilon \nabla\psi \cdot \boldsymbol{\nu}_{k\ell}$, $\mathbf{j}_n \cdot \boldsymbol{\nu}_{k\ell}$ and $\mathbf{j}_p \cdot \boldsymbol{\nu}_{k\ell}$, respectively, on the interfaces between two adjacent control volumes ω_k and ω_ℓ, see Figure 3.1. We assume that these fluxes can be expressed as nonlinear functions depending on the values $\psi_k, \varphi_{n;k}, \varphi_{p;k}$ and $\psi_\ell, \varphi_{n;\ell}, \varphi_{p;\ell}$.

In theory, any classical technique such as central differences or upwinding could be used to discretize the numerical fluxes. However, the former suffers from instability issues [PF25] and neither scheme is consistent with the thermodynamic equilibrium which we explain in Section 3.3.

Starting from the local perspective (3.2), we can assemble a global system by taking into account every cell ω_k. Supposing there are N cells, the finite volume scheme (3.2)

yields a nonlinear system of $3N$ equations depending on $3N$ variables. We can directly substitute Dirichlet boundary values in the equations. In practice, however, this way of handling Dirichlet values is very technical to implement. Exploiting floating point arithmetic, the Dirichlet penalty method [71] provides a reasonable alternative. Physically, it replaces the Dirichlet boundary conditions by gate boundary conditions with very high oxide permittivity, see (3.2a).

3.2 Flux discretization

In this section we introduce and discuss different flux approximations.

3.2.1 The electric displacement flux

The easiest flux to approximate is the electric displacement flux. We can simply employ a central difference flux approximation of the form:

$$D_{k,\ell} = -\varepsilon_s \frac{\psi_\ell - \psi_k}{\|\mathbf{x}_\ell - \mathbf{x}_k\|}.$$

Such an approach will not work for the drift-diffusion fluxes as unphysical oscillations can be introduced in the system [PF25].

3.2.2 The classical Scharfetter-Gummel scheme

In 1D, Scharfetter and Gummel proposed for Boltzmann statistics [85] a highly efficient flux approximation which is also sometimes referred to as exponential fitting. They derive the numerical flux

$$j_{\alpha;k,\ell} = -z_\alpha q \mu_\alpha N_\alpha \frac{U_T}{h_{k\ell}} \left\{ B\left(-z_\alpha \frac{\psi_\ell - \psi_k}{U_T}\right) e^{\eta_{\alpha;\ell}} - B\left(z_\alpha \frac{\psi_\ell - \psi_k}{U_T}\right) e^{\eta_{\alpha;k}} \right\} \tag{3.3}$$

by locally solving a linear two-point boundary value problem. The one-dimensional idea immediately carries over to higher dimensions if we insert the Scharfetter-Gummel flux (3.3) into the discrete system (3.2). However, if the Boltzmann approximation is not valid anymore, we can no longer derive the flux like Scharfetter and Gummel suggested.

For the sake of readability, we continue providing the formulas for electrons only. The formulas for holes follow similarly.

This motivated the work in [41] where the Scharfetter-Gummel idea was generalized to a large class of nonlinear convection-diffusion problems, allowing to define consistent numerical fluxes from nonlinear two-point boundary value problems. Unfortunately, these *generalized Scharfetter-Gummel schemes* cannot be expressed by closed formulas. Sometimes, however, the local fluxes can be obtained iteratively [24]. It is also possible to approximate the two-point boundary value problems by simpler ones (for example by freezing some coefficients). This leads to *modified Scharfetter-Gummel schemes*. We will address some of these schemes now.

3.2.3 Generalized Scharfetter-Gummel schemes

By the construction of the Voronoi mesh, the flux between two neighboring cell (nodes) is perpendicular to the interface between both cells. Hence even in 2D or 3D, it suffices to study the one-dimensional flux j_n along the edge $\overline{\mathbf{x}_k\mathbf{x}_\ell}$ between node $\mathbf{x}_k$ and $\mathbf{x}_l$. Generalizing the original idea by Scharfetter and Gummel to general statistics $\mathcal{F}$, see [41], we solve the ordinary differential equation

$$\frac{d}{dx}j_\alpha = \frac{d}{dx}\Big(- z_\alpha^2 q\mu_\alpha N_\alpha \mathcal{F}\left(\eta_\alpha\left(\psi, \varphi_\alpha\right)\right) \frac{d}{dx}\varphi_\alpha \Big) = 0$$

on the interval $[0, h_{k\ell}]$ with boundary conditions

$$\varphi_\alpha\left(0\right) = \varphi_{\alpha;k} \quad \text{and} \quad \varphi_\alpha\left(h_{k\ell}\right) = \varphi_{\alpha;\ell},$$

where $\varphi_{\alpha;k}$ and $\varphi_{\alpha,\ell}$ are the approximations of the quasi Fermi potential at the nodes $\mathbf{x}_k$ and $\mathbf{x}_\ell$, respectively. Assuming as before that the flux between both nodes $j_{\alpha;k,\ell}$ is constant, we can integrate twice, leading to an integral equation for the unknown current, namely

$$\int\limits_{\eta_{\alpha;k}}^{\eta_{\alpha;\ell}} \left[\left(\frac{j_{\alpha;k,l}/j_0}{\mathcal{F}(\eta)} - z_\alpha \frac{\psi_\ell - \psi_k}{U_T}\right)\right]^{-1} d\eta = 1, \tag{3.4}$$

where for simplicity we introduced the factor $j_0 = -z_\alpha q\mu_\alpha N_\alpha \dfrac{U_T}{h_{k\ell}}$. The limits are given by $\eta_{\alpha;k} = \eta_\alpha\left(\psi_k, \varphi_{\alpha;k}\right)$ and $\eta_{\alpha;\ell} = \eta_\alpha\left(\psi_\ell, \varphi_{\alpha;\ell}\right)$. For strictly monotonously increasing $\mathcal{F}(\eta)$ this equation has always a unique solution [18].

For the Boltzmann approximation $\mathcal{F}(\eta) = \exp(\eta)$ this integral equation can be solved analytically and yields the classical Scharfetter-Gummel flux expression (3.3). In [24] it was shown that for the Blakemore distribution function $\mathcal{F}\left(\eta\right) = \frac{1}{\exp(-\eta)+\gamma}$, the integral equation leads to a fixed point equation

$$\widehat{j}_{\alpha;k,\ell} = B\left(\gamma\widehat{j}_{\alpha;k,\ell} - z_\alpha\frac{\psi_\ell - \psi_k}{U_T}\right)e^{\eta_{\alpha;\ell}} - B\left(-\left[\gamma\widehat{j}_{\alpha;k,\ell} - z_\alpha\frac{\psi_\ell - \psi_k}{U_T}\right]\right)e^{\eta_{\alpha;k}} \tag{3.5}$$

for the non-dimensionalized edge current $\widehat{j}_{\alpha;k,\ell} = j_{\alpha;k,l}/j_0$. The right-hand side is a Scharfetter-Gummel expression where the argument of the Bernoulli function is shifted by $\gamma\widehat{j}_{\alpha;k,\ell}$. Hence, for $\gamma = 0$ (3.5) reduces to the classical Scharfetter-Gummel scheme.

Again, since the Bernoulli function is strictly decreasing, this fixed point equation possesses a unique solution $\widehat{j}_{\alpha;k,\ell}$. If we want to use the flux given by (3.5) in the discrete system (3.2), we need to solve for the flux $\widehat{j}_{\alpha;k,\ell}$ twice (once for electrons and once for holes) on each discretization edge $\overline{\mathbf{x}_k\mathbf{x}_\ell}$. A few Newton steps are sufficient to solve this equation iteratively.

Even though (3.5) is restricted to the Blakemore approximation, it provides a useful scheme in the context of organic semiconductors. There it arises naturally as a model for materials with δ-shaped density of states [30, 23], describing a single transport level, see Figures 2.1 and 2.2. Furthermore, it is useful for benchmarking purposes [PF10].

Unfortunately, for a general statistical distribution function, no corresponding equation has been derived so far. Therefore, in [18] it was proposed to use piecewise approximations of $\mathcal{F}$ by Blakemore type or rational approximations of Padé type in order to obtain piecewise integrable expression from the local boundary value problem.

3.2.4 Modified Scharfetter-Gummel schemes

Whereas in the previous section, we focussed on fluxes which were exact solutions to linear and nonlinear boundary value problems, we focus in this section on approximate but reasonable solutions to nonlinear boundary value problems. Physically, these schemes are inspired by either modifying the thermal voltage, the effective density of state or the electric potential difference.

From (2.13) we see that for a nonlinear diffusion term g, we have to somehow freeze g along the discretization edge. Bessemoulin-Chatard [25] derived a finite volume scheme for convection-diffusion problems which is consistent with the vanishing analytic flux in thermodynamic equilibrium. This idea was translated to a physical context in terms of potentials and statistics in [PF12], introducing a logarithmic average of the nonlinear diffusion enhancement

$$g_{\alpha;k,\ell} = \frac{\eta_{\alpha;k} - \eta_{\alpha;\ell}}{\log \mathcal{F}\left(\eta_{\alpha;k}\right) - \log \mathcal{F}\left(\eta_{\alpha;\ell}\right)}$$

along the discretization edge $\overline{\mathbf{x}_k \mathbf{x}_\ell}$. Equation (2.13) implies that the diffusion enhancement g can be interpreted as a modification factor of the thermal voltage U_T. Replacing U_T in the Scharfetter-Gummel expression (3.3) by $U_T^* = U_T g_{\alpha;k,\ell}$, thus we obtain the following modified Scharfetter-Gummel scheme [25, PF12]

$$j_{\alpha;k,\ell} = -z_\alpha \frac{q\mu_n N_\alpha U_T g_{\alpha;k,\ell}}{h_{k\ell}} \left(B\left(-z_\alpha \frac{\psi_\ell - \psi_k}{U_T g_{\alpha;k,\ell}} \right) \mathcal{F}\left(\eta_{\alpha;\ell}\right) - B\left(z_\alpha \frac{\psi_\ell - \psi_k}{U_T g_{\alpha;k,\ell}} \right) \mathcal{F}\left(\eta_{\alpha;k}\right) \right). \tag{3.6}$$

Instead of adjusting the thermal voltage by a suitable average along the edge, we may start from the original Scharfetter-Gummel flux (3.3) and modify the density of states N_α accordingly, for example choose

$$N_\alpha \mathcal{F}(\eta) \approx N^*_{\alpha;k,\ell} \exp(\eta).$$

This choice makes it possible to use the original Scharfetter-Gummel flux (3.3) and replace N_α with $N^*_{\alpha;k,\ell}$. One choice for the modified density of states is

$$N^*_{\alpha;k,\ell}(\eta^*) = N_\alpha \frac{\mathcal{F}(\eta^*)}{e^{\eta^*}},$$

where $\eta^* \in [\eta_k, \eta_\ell]$, assuming $\eta_k \leq \eta_\ell$. In practice, we might consider taking the geometric average between $N_\alpha(\eta_k)$ and $N_\alpha(\eta_\ell)$, which leads to another modified Scharfetter-Gummel scheme:

$$j_{\alpha;k,\ell} = -\, z_\alpha \frac{q\mu_\alpha U_T}{h_{k\ell}} N_\alpha \sqrt{\frac{\mathcal{F}\left(\eta_{\alpha;k}\right)\mathcal{F}\left(\eta_{\alpha;\ell}\right)}{e^{\eta_{\alpha;k}} e^{\eta_{\alpha;\ell}}}} \left(B\left(-z_\alpha \frac{\psi_\ell - \psi_k}{U_T} \right) e^{\eta_{\alpha;\ell}} - B\left(z_\alpha \frac{\psi_\ell - \psi_k}{U_T} \right) e^{\eta_{\alpha;k}} \right). \tag{3.7}$$

The idea behind this scheme was introduced in [16] for the numerical solution of the generalized Nernst-Planck system which is similar to the van Roosbroeck system (2.21). A variant of this scheme for Fermi-Dirac statistics is described in [44, 64] and numerically implemented in the semiconductor device simulation package WIAS-TeSCA [13].

Finally, it is also possible to modify the drift term instead of the diffusion term. Starting from (2.13), we may rewrite the flux as follows For a node x_k it reads as follows

$$\mathbf{j}_\alpha = -z_\alpha q \mu_\alpha U_T \left(\nabla n_\alpha + z_\alpha n_\alpha \nabla \left(\frac{\psi}{U_T} \right) + n_\alpha \nabla \nu(n_\alpha) \right). \tag{3.8}$$

where

$$\nu(n_\alpha) = \mathcal{F}^{-1}(n_\alpha) - \log(n_\alpha).$$

Then the corresponding scheme takes the form

$$j_\alpha = -z_\alpha \frac{q\mu_\alpha N_\alpha U_T}{h_{kl}} \Big(B(-Q_{\alpha;k,\ell}) \mathcal{F}\left(\eta_{\alpha;\ell}\right) - B\left(Q_{\alpha;k,\ell}\right) \mathcal{F}\left(\eta_{\alpha;k}\right) \Big), \tag{3.9}$$

where

$$Q_{\alpha;k,\ell} = z_\alpha \frac{\psi_\ell - \psi_k}{U_T} + (\eta_{\alpha;\ell} - \eta_{\alpha,k}) - \log\left(\frac{\mathcal{F}(\eta_{\alpha;\ell})}{\mathcal{F}(\eta_{\alpha;k})} \right).$$

The earliest reference, we could find for this thermodynamically consistent flux discretization scheme is in [69]. This scheme was compared in [PF2, 7] and numerically analyzed in [4]. We refer to it either as *SEDAN* or *excess chemical potential* scheme. The latter is due to its interpretation in electrochemistry.

3.2.5 Quadrature-based Scharfetter-Gummel schemes

In [PF18] it was shown that it is feasible to numerically approximate the integral (3.4) via quadrature. This is particularly useful if highly accurate flux approximations are required. We introduce now a whole family of such approximation schemes by choosing different quadrature rules and explain in detail the algorithms used to obtain them. Solving (3.4) numerically yields effectively new modified schemes, which become practically exact schemes when the number of quadrature points is large enough. We refer to them as *quadrature-based Scharfetter-Gummel schemes*. The implementation is challenging due to two reasons: first one needs to approximate the integral accurately and then solve a nonlinear equation. We will discuss both steps separately.

Discretization of the integral equation

Denoting the integrand in (3.4) with $G(\eta; \delta\psi_{k\ell}, j_{gsg})$ for $j_{gsg} = j_\alpha / j_0$ and $\delta\psi_{k\ell} = (\psi_\ell - \psi_k)/U_T$, we can approximate (3.4) by

$$H(j_{gsg}) := \sum_{i=1}^{N} w_i G(\eta_i; \delta\psi_{k\ell}, j_{gsg}) - 1 = 0, \tag{3.10}$$

where w_i are some integration weights, η_i the quadrature nodes and N the number of quadrature nodes. We make explicit choices for the numerical integration in Section 7.

When implementing this method one needs to treat two limiting cases separately. For pure diffusive currents, i. e. $\delta\psi_{k\ell} = 0$ and arbitrary $\delta\eta_{k\ell}$, the integral equation (3.4) implies that one obtains the current simply by integrating $\mathcal{F}(\eta)$ from η_k to η_ℓ. On the other hand, for small $\delta\eta_{k\ell}$ and arbitrary $\delta\psi_{k\ell}$, the mean value theorem for definite integrals yields

$$1 = \int_{\eta_k}^{\eta_\ell} \frac{\mathcal{F}(\eta)}{j_{gsg} - z_\alpha \delta\psi_{k\ell}\mathcal{F}(\eta)} d\eta = \frac{\delta\eta_{k\ell}\mathcal{F}\left(\bar{\eta}_{k\ell} + \frac{1}{2}\delta\eta_{k\ell}\xi\right)}{j_{gsg} - z_\alpha \delta\psi_{k\ell}\mathcal{F}\left(\bar{\eta}_{k\ell} + \frac{1}{2}\delta\eta_{k\ell}\xi\right)},$$
$$\text{where} \quad \bar{\eta}_{k\ell} := \frac{\eta_\ell + \eta_k}{2},$$

for some $\xi \in (-1, 1)$. Hence, in the pure drift limit when $\delta\eta_{k\ell} = 0$, we obtain $j_{gsg} = z_\alpha \mathcal{F}(\bar{\eta}_{k\ell})\delta\psi_{k\ell}$ for any $\delta\psi_{k\ell} \in \mathbb{R}$. We point out that this case is incorporated in the low-order series expansion of (3.4) for electrons $z_\alpha = -1$ as well as small $\delta\eta_{k\ell}$ and $\delta\psi_{k\ell}$, derived in [PF25], namely

$$\begin{aligned} j_{gsg} = &- \mathcal{F}(\bar{\eta}_{k\ell})\delta\psi_{k\ell} + \mathcal{F}(\bar{\eta}_{k\ell})\delta\eta_{k\ell} + \frac{1}{12}\frac{\mathcal{F}'(\bar{\eta}_{k\ell})^2}{\mathcal{F}(\bar{\eta}_{k\ell})}\delta\psi_{k\ell}^2\delta\eta_{k\ell} \\ &- \left(\frac{\mathcal{F}'(\bar{\eta}_{k\ell})^2}{12\mathcal{F}(\bar{\eta}_{k\ell})} + \frac{\mathcal{F}''(\bar{\eta}_{k\ell})}{24}\right)\delta\psi_{k\ell}\delta\eta_{k\ell}^2 + \frac{1}{24}\mathcal{F}''(\bar{\eta}_{k\ell})\delta\eta_{k\ell}^3 \\ &+ \mathcal{O}(\delta\eta_{k\ell}^5) + \mathcal{O}(\delta\psi_{k\ell}\delta\eta_{k\ell}^4) + \mathcal{O}(\delta\psi_{k\ell}^2\delta\eta_{k\ell}^3) + \mathcal{O}(\delta\psi_{k\ell}^3). \end{aligned} \tag{3.11}$$

Due to these considerations, we propose the following implementation for some suitable tolerances ε_η and ε_ψ:

1 **if** $|\delta\eta_{k\ell}| < \varepsilon_\eta$ **then**
2 | use series expansion (3.11);
3 **else if** $|\delta\eta_{k\ell}| \geq \varepsilon_\eta$ *and* $|\delta\psi_{k\ell}| < \varepsilon_\psi$ **then**
4 | $j_{gsg} = \int_{\eta_k}^{\eta_\ell} \mathcal{F}(\eta)d\eta$;
5 **else if** $|\delta\eta_{k\ell}| \geq \varepsilon_\eta$ *and* $|\delta\psi_{k\ell}| \geq \varepsilon_\psi$ **then**
6 | use Newton's method for (3.10) with the diffusion-enhanced scheme (3.6) as starting guess;
7 **end**

Numerical integration

Numerical integration, also known as quadrature, approximates definite integrals of a given function f. Without loss of generality, we confine the following considerations to the interval $[-1, 1]$. For some weight function ω, let us introduce a general approximation

	Gauss-Legendre	**Clenshaw-Curtis**	**Gauss-Lobatto**	**Gauss-Kronrod**
polynomials	Legendre	Chebyshev	Jacobi	Stieltjies
degree	$2N-1$	N	$2N-1$	$2N+1$
convergence	exponential	exponential	exponential	exponential
adaptivity	no	no	no	yes
integral limits	not included	are included	are included	not included
weights	positive	positive	positive	positive

Table 3.1: Comparison of the several quadrature rules. The quantity N refers to the number of quadrature points.

of an integral

$$\int_{-1}^{1} f(x)\omega(x)dx \approx \sum_{i=1}^{N} w_i f(x_i), \tag{3.12}$$

where x_i are the quadrature nodes, w_i the quadrature weights and N is the number of quadrature points.

A huge variety of quadrature rules are based on interpolation polynomials which are simple to integrate. To evaluate the integral (3.4) we use four different quadrature rules based on optimal points: Clenshaw-Curtis, Gauss-Legendre, Gauss-Lobatto and adaptive Gauss-Kronrod quadrature [72, 37]. The nodes and the weights are chosen to minimize the approximation error. We use the code [47] for Gauss-Legendre quadrature and [14] for the other ones. There are several advantages to the quadrature rules studied here: the quadrature weights for these quadrature rules are positive, minimizing numerical (cancellation) errors. Moreover, these quadrature rules converge exponentially for sufficiently smooth integrands and there exist well-tested and well-documented implementations [46, 37]. For a quick comparison between the several quadrature rules used in our calculations, we report the main features for each ones in Table 3.1.

Gauss-Legendre quadrature Gauss-Legendre quadrature exactly integrates polynomials of degree $2N-1$ by choosing suitable nodes x_i and weights w_i for $i = 1, \dots, N$, where N is the number of quadrature points. The nodes x_i are precisely the ith roots of Legendre polynomials $P_N(x)$ on $[-1, 1]$ and the weights w_i are given by

$$w_i = \frac{2}{(1-x_i^2)[P_N'(x_i)]^2}, \tag{3.13}$$

see [90] for details. The zeros of the N Legendre polynomial are computed by means of the Newton method. Gauss-Legendre quadrature is highly efficient for smooth integrands and also excludes the integration limits.

In [18] it is shown that no pole can appear within the integration limits of (3.4). However, poles can come close to the integration limits.

Clenshaw-Curtis quadrature Clenshaw-Curtis quadrature is another numerical integration technique. It expands the integrand f by means of Chebyshev polynomials. Using the change of variable $x = \cos(t)$ and the discrete cosine transform (DCT) we can approximate our integrand with

$$f(t) = \frac{a_1}{2} + \frac{a_N}{2}T_N + \sum_{i=2}^{N-1} a_i T_i(t), \tag{3.14}$$

where a_i and $T_i(t)$ denote the Chebyshev coefficients and polynomials, respectively [93]. The jth node corresponds to a maximum or minimum of the Chebyshev polynomial $T_i(t)$ in the range $[-1, 1]$ given by

$$t_j = \cos\left(\frac{\pi j}{N}\right). \tag{3.15}$$

The Clenshaw-Curtis quadrature also evaluates the integrand at N points but integrates exactly only polynomials up to degree N rather than to degree $2N - 1$ like Gaussian quadrature. However, the Clenshaw-Curtis rule appears to be more than just half as effective as Gaussian quadrature. In [87] the authors show that the method is fast and as accurate as Gaussian quadrature.

Gauss-Lobatto quadrature Gauss-Lobatto quadrature is another numerical integration technique which exactly integrates polynomials up to order $2N - 1$. In the early seventies, Golub [82] proposed a method to compute the zeros of orthogonal polynomials by using the eigenvalues of a tridiagonal Jacobi matrix. The idea is to generate the nodes and weights needed for the quadrature rule by computing eigenvalues and the first component of the respective eigenvectors of a modified tridiagonal matrix. The use of the Gauss-Lobatto rule is efficient for extrapolating the nodes but the calculation of the weights is quite complicated. A more simple and elegant approach is reported in [32], where the authors derive the nodes via a special Jacobi matrix based on the derivatives of Jacobi polynomial rather and also present an explicit formula to obtain the weights.

Adaptive Gauss-Kronrod quadrature An adaptive quadrature rule is a technique where the integration interval is recursively split into two halves and the quadrature is applied to each subinterval if the integral is not evaluated with the desired accuracy. The Gauss-Kronrod quadrature, proposed by Alexander Kronrod in the 1960s, belongs to the set of adaptive quadrature rules and was formulated as an extension of the Gaussian quadrature formula. The integral approximation and resulting estimated error are calculated by adding $N+1$ roots of Stieltjes polynomials to N nodes obtaining a formula of order $2N + 1$. These extra points allow to calculate a higher-order approximation of the integral and the difference between this value with the lower-order one is used as an estimate for the integration error to be compared with the required tolerance [1].

3.3 Consistency with the thermodynamic equilibrium

As discussed in Section 2.3.1, the thermodynamic equilibrium is characterized by vanishing hole and electron fluxes. That is, there is neither recombination nor generation ($R = G = 0$) as well as zero applied bias and gate voltage ($U_\alpha = U_G = 0$). A vanishing applied bias results into zero Dirichlet boundary conditions. Due to Equation (2.21d), zero fluxes are equivalent to constant quasi Fermi potentials.

If a numerical scheme with the same zero boundary conditions and vanishing right-hand sides, results into zero numerical fluxes, we call it *globally consistent with the thermodynamical equilibrium* or slightly shorter *thermodynamically consistent*. In practice, one can check this consistency by checking whether locally constant quasi Fermi potentials $\varphi_{n;k} = \varphi_{n;\ell}$ and $\varphi_{p;k} = \varphi_{p;\ell}$ are equivalent to vanishing numerical fluxes $j_{n;k,\ell} = j_{p;k,\ell} = 0$. Under the stated conditions the *local* consistency will translate into to the *global* one. Violating this thermodynamic consistency causes unphysical dissipation (spurious Joule heating) in the steady state attained despite zero bias boundary conditions [25].

Theorem 3.1 *All generalized and modified schemes introduced in Sections 3.2.3 and 3.2.4 are consistent with the thermodynamical equilibrium.*

Proof. Indeed, let us assume that locally the quasi Fermi potentials φ_n and φ_p between two adjacent control volumes ω_k and ω_ℓ are equal. The consistency of the classical Scharfetter-Gummel (3.3), the scheme using a modified density of states (3.7) and the Sedan scheme (3.9) are obvious since the Bernoulli function satisfies $B(-x) = e^x B(x)$ and the definition of η, see (3.1).

Due to the definition from the solution of the two-point boundary value problem, the generalized Scharfetter-Gummel scheme defined in (3.4) and its specialization for the Blakemore approximation (3.5) are consistent with the thermodynamic equilibrium. Furthermore, the logarithmic average of the diffusion enhancement is the only possible average wich guarantees consistency with thermodynamic equilibrium in the scheme (3.6). □

For details see [24, 18, PF12]. Finally, we point out that the quadrature-based Scharfetter-Gummel scheme are not thermodynamically consistent but on a practical or numerical level they are [PF7].

3.4 Free energy and dissipation rate

For Boltzmann statistics it is rather straightforward to define discrete versions of the free energy (2.35) and the dissipation rate (2.36). The positivity of the discrete dissipation rate was shown in [59], and the exponential decay of the free energy to its equilibrium value was proven in [35]. An overview of the entropy method for finite volume schemes has been given in [21]. First results on more general statistics functions in this respect have been obtained in [11, 4].

These pioneering works indicate that the chosen discretization approach results in discrete models which are consistent with the structural assumptions of nonequilibrium

thermodynamics. A full account of these issues in the context of general statistics functions remains an open topic of research and depends on the underlying model.

3.5 Existence, uniqueness and convergence

There are very few existence proofs for the solutions of the discretized system (3.2). For the Boltzmann approximation, Gärtner [34] proved that the discretized steady state system has a solution which becomes unique if a small bias is applied. A similar result for Fermi statistics has been obtained in [17].

A convergence theory for the finite volume scheme for the full discrete system (3.2) and general flux functions is still missing. However, practical experience and a number of results make its convergence plausible.

For example, in one space dimension, second order convergence in the discrete maximum norm for the Scharfetter-Gummel scheme has been shown in [84]. Under the assumption that second derivatives of the continuous solution exist, in [61] for moderately sized drift terms and two-dimensional, square grids, first order convergence for the simple upwind scheme (see e.g. [39]), and second order convergence for the exponential fitting scheme in the L_2-norm has been shown. Re-interpretations of the finite volume Scharfetter-Gummel scheme as a nonstandard finite element method allowed to obtain convergence estimates for Scharfetter-Gummel schemes on Delaunay grids [63, 54], see Section 3.6. For a general approach to the convergence theory of finite volume schemes, see [53]. In [41], weak convergence (no order estimate) for a generalization of the Scharfetter-Gummel scheme to nonlinear convection-diffusion problems has been shown. A convergence proof for a variant of the van Roosbroeck system discretized with the simple upwind scheme was given in [48].

3.6 Mesh generation

In this section, we would like to give some practical information about generating the Voronoi mesh. Even though the Voronoi mesh has a relatively complex structure, see Section 3.1, we never need to compute the Voronoi cells directly. The reason is that the Voronoi mesh is dual to a Delaunay mesh for which different mesh generators exist.

So let us begin with a partition of our polyhedral domain $\Omega = \bigcup_{k=1}^{N_\sigma} \sigma_k$ into into disjoint simplices σ_k as commonly used for finite element methods [50]. We denote the set of all vertices with S. In 2D such a partition shall correspond to a triangulation and in 3D to a tetrahedralization. We demand two additional properties of our mesh:

- Every simplex σ (triangle in 2D or tetrahedra in 3D) shall be Delaunay. That is, no other simplex vertex in S shall lie in σ's circumscribed sphere.
- The circumcenter of any boundary simplex shall lie inside our domain Ω.

The first condition guarantees that the dual mesh is a Voronoi partition. For a given vertex $\mathbf{x}_i \in S$, the corresponding *Voronoi cell* around S is given by the set

$$V_i = \left\{ \mathbf{x} \in \mathbb{R}^d : \|\mathbf{x} - \mathbf{x}_i\| < \|\mathbf{x} - \mathbf{x}_j\| \text{ for all } \mathbf{x}_j \in S \text{ with } \mathbf{x}_j \neq \mathbf{x}_i \right\}.$$

The *Voronoi diagram* – the set of Voronoi cells for all vertices in S – is dual to the *Delaunay triangulation* of the point set S in the sense that for each edge $\overline{\mathbf{x}_i\mathbf{x}_j}$ in the Delaunay triangulation, $\partial V_i \cap \partial V_j \neq \emptyset$. Geometrically, the infinite Voronoi diagram can also be obtained by connecting all circumcenters of each simplex and allowing boundary edges to tend to infinity.

The second condition ensures that we can properly constrain the otherwise infinite boundary Voronoi cells. To be more explicit, let us denote the restricted Voronoi cells with $\omega_i = \Omega \cap V_i$. Interior cells are not affected by this restriction. However, if circumcenters near the boundary are outside of the domain Ω, Voronoi edges between two neighboring boundary cells may be skewed. The second condition now ensures that Voronoi edges between two neighboring boundary cells are perpendicular to the boundary of the polygonal domain $\partial\Omega$. It is sometimes reformulated in terms of a Gabriel property [33, 31].

Such restricted Voronoi cells provide an admissible partition as required by the finite volume method introduced in Section 3.1. A partition/mesh satisfying both conditions is called *boundary conforming Delaunay mesh* [31].

For a 2D triangulation we may slightly rephrase these two conditions:

(i) For any two triangles with a common edge, the sum of their respective angles opposite to that edge is less or equal to 180°.

(ii) For any triangle sharing an edge with $\partial\Omega$, its angle opposite to that edge is less or equal to 90°. That is, the circumcenter of the circle passing through the triangle vertices lies within the domain.

Figure 3.2 shows 2D (boundary conforming) Delaunay triangulations.

We point out that in order to implement the finite volume method as described in Section 3.1, there is no need for an explicit construction of the control volumes ω_i. Given the simplicial partition, it is sufficient to base the calculations on the simplicial contributions $s_{ij}^k = |\partial\omega_i \cap \partial\omega_j \cap \sigma_k|$ and $|\omega_i \cap \sigma_K|$, and to use a simplex based assembly loop like often done for finite elements [59].

There are several efficient algorithms to construct Delaunay triangulations for a given point set S [70, 26]. However, satisfying the boundary conforming Delaunay property is more difficult as it requires the carefully inserting additional points on the boundary. In 3D slivers (very flat tetrahedra) must be avoided. And lastly, it may be very complicated to fulfill additional requirements to improve the overall mesh size like constraints on the minimum angle or the local element size. Even though there are still unsolved problems, the `triangle` ([2], 2D, free for non-commercial use) and `TetGen` ([3], 3D, open source) mesh generators help to create boundary conforming Delaunay meshes based on

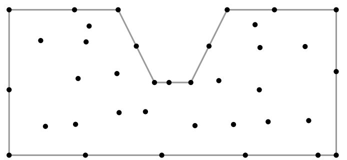 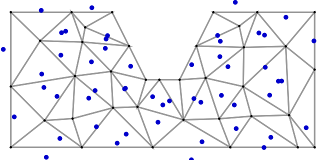 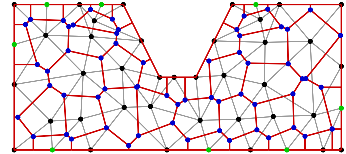

Figure 3.2: First row: Piecewise linear description of computational domain with given point cloud (black dots). Middle row: Delaunay triangulation of domain (gray edges) and triangle circumcenters (blue dots). As some boundary triangles have angles larger than 90° opposite to the boundary, their circumcenters lie outside of the domain. Last row: Boundary conforming Delaunay triangulation with automatically inserted additional points at the boundary (green dots) by projecting the circumcenters outside onto the boundary of the computational domain. The boundary conforming Delaunay triangulation is created from the original point cloud (black dots) plus the projected circumcenters (green dots). Now all circumcenters (blue dots) lie within the computational domain. The boundaries of the (restricted) Voronoi cells are shown as well (red edges). Since the Voronoi cells are constructed from a boundary conforming Delaunay triangulation, the edge between any two neighboring boundary cells is perpendicular to both boundary nodes. This is by construction also true for interior nodes and the edge separating them. The images were created with `triangle` [2].

algorithms which provably deliver meshes with the desired properties reasonably fast for a broad class of piecewise linear geometries.

Other mesh generation approaches, in particular the advancing front [58] and the octree method [66], are similarly widespread. However, while popular in finite element community, their design makes it much harder to use them as a starting point for generating boundary conforming Delaunay meshes.

For simpler geometries rectangular and cuboid (tensor product) meshes are can be used to generate admissible finite volume partitions [79]. Extending a 2D boundary conforming Delaunay base mesh to a 3D prism mesh (and optionally further subdividing these prisms into tetrahedra) provides another method to create an admissible finite volume mesh [42].

3.7 Solvers

We briefly discuss two main techniques to solve the arising discrete nonlinear systems introduced here.

3.7.1 Gummel iterations

Gummel [91, 78] suggested decoupling the three equations in the van Roosbroeck system. He devised an iterative method at the continuous level, which for Boltzmann statistics and drift-diffusion form leads to alternating between solving linear differential equations

for the electric potential as well as the charge carrier densities. The connection between Gummel's map and Gummel's iteration can be found in [60]. Gummel's method is known to have a larger convergence region and a slower asymptotic convergence rate compared to Newtons's method.

3.7.2 Newton's method and path continuation

An important advantage of finite element and finite volume discretizations is the fact that they create only next-neighbor couplings in the discretized systems. The resulting linearized systems are therefore sparse, i. e. the maximum number of nonzero elements in a matrix row is bounded by a constant independent of the number of discretization cells, making it possible to use highly economic storage schemes.

Assuming that a good starting guess has been provided for example by following the ideas in Section 2.3, Newton's method constructs a new iterate by solving a linearized system. The advantage of Newton's method is that it converges quadratically if the starting guess is sufficiently close to the solution [28], allowing to obtain highly accurate discrete solutions at low additional cost. The major drawback is that the method might converge very slowly or even fail to converge if the starting guess is too far from the actual solution. Damping – multiplying the update with a factor less than 1 – is known to increase the convergence region. Another remedy is parameter embedding where one slowly changes a parameter, always using the old solution as a new starting guess.

References

[1] A. Kronrod. *Nodes and Weights for Quadrature Formulae. Sixteen-place Tables.* Nauka, Moscow, 1964 [English Translation: Consultants Bureau, New York, 1965].

[2] J. Shewchuk. *Triangle: A Two-Dimensional Quality Mesh Generator and Delaunay Triangulator.* http://www.cs.cmu.edu/~quake/triangle.html.

[3] H. Si. *TetGen version 1.5.* URL: http://tetgen.org/.

[4] C. Cancès, C. Chainais-Hillairet, J. Fuhrmann, and B. Gaudeul. A numerical-analysis-focused comparison of several finite volume schemes for a unipolar degenerate drift-diffusion model. *IMA Journal of Numerical Analysis* 41.1 (2021), pp. 271–314.

[5] S. Kayser. *The lateral photovoltage scanning method to probe spatial inhomogeneities in semiconductors: a joined numerical and experimental investigation.* PhD thesis. Brandenburg University of Technology, 2021.

[6] L. Chen and H. Bagci. Steady-State Simulation of Semiconductor Devices Using Discontinuous Galerkin Methods. *IEEE Access* 8 (2020), pp. 16203–16215. DOI: 10.1109/ACCESS.2020.2967125.

[7] M. Kantner. Generalized Scharfetter–Gummel schemes for electro-thermal transport in degenerate semiconductors using the Kelvin formula for the Seebeck coefficient. *Journal of Computational Physics* 402 (2020), p. 109091. DOI: 10.1016/j.jcp.2019.109091.

[8] Ossila. *Four-Point Probe User Manual 3.0c.* Tech. rep. Ossila, 2019, p. 11.

[9] K. A. Rubin, Y. Yang, O. Amster, D. A. Scrymgeour, and S. Misra. Scanning Microwave Impedance Microscopy (sMIM) in Electronic and Quantum Materials. In: *Electrical Atomic Force Microscopy for Nanoelectronics.* Springer International Publishing, 2019, pp. 385–408. DOI: 10.1007/978-3-030-15612-1_12.

[10] N. Courtier, G. Richardson, and J. Foster. A fast and robust numerical scheme for solving models of charge carrier transport and ion vacancy motion in perovskite solar cells. *Applied Mathematical Modelling* 63 (2018), pp. 329–348. DOI: 10.1016/j.apm.2018.06.051.

[11] M. Bessemoulin-Chatard and C. Chainais-Hillairet. Exponential decay of a finite volume scheme to the thermal equilibrium for drift–diffusion systems. *arXiv preprint arXiv:1601.00813* (2016).

[12] P. Calado, A. M. Telford, D. Bryant, X. Li, J. Nelson, B. C. O'Regan, and P. R. F. Barnes. Evidence for ion migration in hybrid perovskite solar cells with minimal hysteresis. *Nature Communications* 7 (Dec. 2016), p. 13831.

[13] H. Gajewski, M. Liero, R. Nürnberg, and H. Stephan. WIAS-Tesca User manual 1.2. *WIAS Technical Report* 0.14 (2016).

[14] G. Papazafeiropoulos. Vectorized Numerical Integration Matlab. *MathWorks* (2016).

[15] P. Farrell and J. Pestana. Block Preconditioners for Linear Systems arising from Multiscale Collocation with Compactly Supported RBFs. *Numerical Linear Algebra with Applications* 22 (2015), pp. 731–747. DOI: 10.1002/nla.1984.

[16] J. Fuhrmann. Comparison and numerical treatment of generalised Nernst-Planck models. *Computer Physics Communications* 196 (2015), pp. 166–178. DOI: http://dx.doi.org/10.1016/j.cpc.2015.06.004.

[17] K. Gärtner. Existence of bounded discrete steady state solutions of the van Roosbroeck system with monotone Fermi-Dirac statistic functions. *J. Comput. Electron.* 14.3 (2015), pp. 773–787.

[18] K. Gärtner. Existence of bounded discrete steady state solutions of the van Roosbroeck system with monotone Fermi–Dirac statistic functions. *Journal of Computational Electronics* 14.3 (2015), pp. 773–787. DOI: 10.1007/s10825-015-0712-2.

[19] T. Koprucki, N. Rotundo, P. Farrell, D. H. Doan, and J. Fuhrmann. On Thermodynamic Consistency of a Scharfetter-Gummel Scheme Based on a Modified Thermal Voltage for Drift-Diffusion Equations with Diffusion Enhancement. *Optical and Quantum Electronics* 47.6 (2015), pp. 1327–1332. DOI: 10.1007/s11082-014-0050-9.

[20] A. V. Nenashev, J. O. Oelerich, and S. D. Baranovskii. Theoretical tools for the description of charge transport in disordered organic semiconductors. *Journal of Physics: Condensed Matter* 27.9 (Feb. 2015), p. 093201. DOI: 10.1088/0953-8984/27/9/093201.

[21] C. Chainais-Hillairet. Entropy method and asymptotic behaviours of finite volume schemes. In: *Finite Volumes for Complex Applications VII – Methods and Theoretical Aspects*. Ed. by J. Fuhrmann, M. Ohlberger, and C. Rohde. Springer, 2014, pp. 17–35.

[22] M. Auf der Maur, A. Pecchia, G. Penazzi, F. Sacconi, and A. Carlo. Coupling atomistic and continuous media models for electronic device simulation. *J. Comput. Electron.* 12.4 (2013), pp. 553–562. DOI: 10.1007/s10825-013-0517-0.

[23] M. Gruber, E. Zojer, F. Schürrer, and K. Zojer. Impact of Materials versus Geometric Parameters on the Contact Resistance in Organic Thin-Film Transistors. *Advanced Functional Materials* 23.23 (2013), pp. 2941–2952. DOI: 10.1002/adfm.201203250.

[24] T. Koprucki and K. Gärtner. Discretization scheme for drift-diffusion equations with strong diffusion enhancement. English. *Optical and Quantum Electronics* 45.7 (2013), pp. 791–796. DOI: 10.1007/s11082-013-9673-5.

[25] M. Bessemoulin-Chatard. A finite volume scheme for convection–diffusion equations with nonlinear diffusion derived from the Scharfetter–Gummel scheme. *Numerische Mathematik* 121.4 (2012), pp. 637–670. DOI: 10.1007/s00211-012-0448-x.

[26] S.-W. Cheng, T. K. Dey, and J. R. Shewchuk. *Delaunay Mesh Generation*. 1st. Boca Raton, FL: Chapman & Hall/CRC, 2012.

[27] A. Deinega and S. John. Finite difference discretization of semiconductor drift-diffusion equations for nanowire solar cells. *Computer Physics Communications* 183.10 (2012), pp. 2128–2135.

[28] P. Deuflhard. *Newton methods for nonlinear problems: affine invariance and adaptive algorithms*. Vol. 35. Springer, 2011.

[29] G. Paasch and S. Scheinert. Charge carrier density of organics with Gaussian density of states: Analytical approximation for the Gauss-Fermi integral. *J. Appl. Phys.* 107.10 (2010), p. 104501. DOI: DOI:10.1063/1.3374475.

[30] G. Paasch and S. Scheinert. Charge carrier density of organics with Gaussian density of states: Analytical approximation for the Gauss-Fermi integral. *J. Appl. Phys.* 107.10 (2010), p. 104501. DOI: DOI:10.1063/1.3374475.

[31] H. Si, K. Gärtner, and J. Fuhrmann. Boundary conforming Delaunay mesh generation. *Computational Mathematics and Mathematical Physics* 50.1 (2010), pp. 38–53. DOI: 10.1134/S0965542510010069.

[32] Z. Zheng and G. Huang. Computation for Jacobi–Gauss–Lobatto quadrature based on derivative relation. *Proceedings of Modeling in Geosciences* (2010).

[33] R. Dyer, H. Zhang, and T. Möller. "Gabriel meshes and Delaunay edge flips". In: *2009 SIAM/ACM Joint Conference on Geometric and Physical Modeling*. 2009, pp. 295–300.

[34] K. Gärtner. Existence of Bounded Discrete Steady-State Solutions of the Van Roosbroeck System on Boundary Conforming Delaunay Grids. *SIAM Journal on Scientific Computing* 31.2 (Jan. 2009), pp. 1347–1362. DOI: 10.1137/070710950.

[35] A. Glitzky and K. Gärtner. Energy estimates for continuous and discretized electro-reaction–diffusion systems. *Nonlinear Analysis* 70.2 (2009), pp. 788–805.

[36] A. Jüngel. *Transport Equations for Semiconductors*. Springer, 2009.

[37] G. Dahlquist and Å. Björck. *Numerical Methods in Scientific Computing, Volume I.* Society for Industrial and Applied Mathematics, 2008. DOI: 10.1137/1.9780898717785.

[38] S. L. M. van Mensfoort and R. Coehoorn. Effect of Gaussian disorder on the voltage dependence of the current density in sandwich-type devices based on organic semiconductors. *Physical Review B* 78.8 (Aug. 2008). DOI: 10.1103/physrevb.78.085207.

[39] H.-G. Roos, M. Stynes, and L. Tobiska. *Robust numerical methods for singularly perturbed differential equations.* Vol. 24. Springe, 2008.

[40] S. Y. Karpov. "Visible Light-Emitting Diodes". In: *Nitride Semiconductor Devices: Principles and Simulation.* Weinheim, Germany: Wiley-VCH Verlag GmbH & Co. KGaA, 2007. Chap. 14, pp. 303–325. DOI: 10.1002/9783527610723.ch14.

[41] R. Eymard, J. Fuhrmann, and K. Gärtner. A finite volume scheme for nonlinear parabolic equations derived from one-dimensional local Dirichlet problems. *Numerische Mathematik* 102.3 (2006), pp. 463–495.

[42] K. Gärtner and R. Richter. DEPFET sensor design using an experimental 3d device simulator. *Nuclear Instruments and Methods in Physics Research Section A: Accelerators, Spectrometers, Detectors and Associated Equipment* 568.1 (2006), pp. 12–17.

[43] S. M. Sze and K. K. Ng. *Physics of Semiconductor Devices.* 3rd. Wiley, Nov. 2006.

[44] U. Bandelow, H. Gajewski, and R. Hünlich. Fabry–Perot Lasers: Thermodynamics-Based Modeling. In: *Optoelectronic Devices.* Ed. by J. Piprek. Springer, 2005.

[45] C. de Falco, E. Gatti, A. L. Lacaita, and R. Sacco. Quantum-corrected drift-diffusion models for transport in semiconductor devices. *Journal of Computational Physics* 204.2 (2005), pp. 533–561. DOI: 10.1016/j.jcp.2004.10.029.

[46] P. K. Kythe and M. R. Schäferkotter. *Handbook of computational methods for integration.* CRC Press, 2004.

[47] G. von Winckel. Legendre–Gauss Quadrature Weights and Nodes. *MathWorks* (2004).

[48] C. Chainais-Hillairet, J.-G. Liu, and Y.-J. Peng. Finite volume scheme for multi-dimensional drift-diffusion equations and convergence analysis. *ESAIM: Mathematical Modelling and Numerical Analysis-Modélisation Mathématique et Analyse Numérique* 37.2 (2003), pp. 319–338.

[49] G. Albinus, H. Gajewski, and R. Hünlich. Thermodynamic design of energy models of semiconductor devices. *Nonlinearity* 15.2 (2002), p. 367.

[50] P. Ciarlet. *The Finite Element Method for Elliptic Problems.* Society for Industrial and Applied Mathematics, 2002. DOI: 10.1137/1.9780898719208.

[51] A. J. Bard and L. R. Faulkner. *Electrochemical Methods: Fundamentals and applications*. Vol. 2. 482. Wiley New York, 2001.

[52] D. Gilbarg and N. S. Trudinger. *Elliptic Partial Differential Equations of Second Order*. Classics in Mathematics. Berlin: Springer, 2001, pp. xiv+517.

[53] R. Eymard, T. Gallouët, and R. Herbin. Finite volume methods. *Handbook of numerical analysis* 7 (2000), pp. 713–1018.

[54] J. Xu and L. Zikatanov. A monotone finite element scheme for convection-diffusion equations. *Mathematics of Computation of the American Mathematical Society* 68.228 (1999), pp. 1429–1446.

[55] A. Lüdge and H. Riemann. Doping Inhomogeneities in Silicon Crystals Detected by the Lateral Photovoltage Scanning (LPS) Method. *Inst. Phys. Conf. Ser.* 160 (1997), pp. 145–148.

[56] P. Fleischmann and S. Selberherr. "Three-dimensional Delaunay mesh generation using a modified advancing front approach". In: *Proceedings of IMR97*. 1997, pp. 267–278.

[57] R. Krishna and J. Wesselingh. The Maxwell-Stefan approach to mass transfer. *Chemical Engineering Science* 52.6 (Mar. 1997), pp. 861–911. DOI: 10.1016/s0009-2509(96)00458-7.

[58] J. Schöberl. NETGEN An advancing front 2D/3D-mesh generator based on abstract rules. *Computing and visualization in science* 1.1 (1997), pp. 41–52.

[59] H. Gajewski and K. Gärtner. On the discretization of van Roosbroeck's equations with magnetic field. *Z. Angew. Math. Mech.* 76.5 (1996), pp. 247–264.

[60] J. W. Jerome. *Analysis of Charge Transport. A Mathematical Study of Semiconductor Devices.* Springer, Berlin Heidelberg, 1996.

[61] R. D. Lazarov, I. Mishev, and P. S. Vassilevski. Finite volume methods for convection-diffusion problems. *SIAM J. Numer. Anal.* 33.1 (1996), pp. 31–55. DOI: http://dx.doi.org/10.1137/0733003.

[62] A. Jüngel. On the existence and uniqueness of transient solutions of a degenerate nonlinear drift-diffusion model for semiconductors. *Math. Models Methods Appl. Sci.* 04 (1994), p. 677.

[63] J. J. H. Miller and S. Wang. An analysis of the Scharfetter-Gummel box method for the stationary semiconductor device equations. *RAIRO-Modélisation mathématique et analyse numérique* 28.2 (1994), pp. 123–140.

[64] H. Gajewski. Analysis und Numerik von Ladungstransport in Halbleitern. *WIAS Report* 0.6 (1993).

[65] B. Cockburn and I. Triandaf. Convergence of a Finite Element Method for the Drift-Diffusion Semiconductor Device Equations: The Zero Diffusion Case. *Mathematics of Computation* 59.200 (1992), pp. 383–401.

[66] M. S. Shephard and M. K. Georges. Automatic three-dimensional mesh generation by the finite octree technique. *International Journal for Numerical methods in engineering* 32.4 (1991), pp. 709–749.

[67] I. Rubinstein. *Electro-diffusion of ions.* Vol. 11. SIAM, 1990.

[68] H. Gajewski and K. Gröger. Semiconductor Equations for variable Mobilities Based on Boltzmann Statistics or Fermi-Dirac Statistics. *Math. Nachr.* 140.1 (1989), pp. 7–36.

[69] Z. Yu and R. Dutton. *SEDAN III – A one-dimensional device simulator.* www-tcad.stanford.edu/tcad/programs/sedan3.html. 1988.

[70] H. Edelsbrunner. *Algorithms in combinatorial geometry.* Heidelberg: Springer-Verlag, 1987.

[71] J. W. Barrett and C. M. Elliott. Finite element approximation of the Dirichlet problem using the boundary penalty method. *Numerische Mathematik* 49.4 (1986), pp. 343–366.

[72] L. M. Delves and J. L. Mohamed, eds. *Computational Methods for Integral Equations.* New York, NY, USA: Cambridge University Press, 1986.

[73] H. Gajewski and K. Gröger. On the Basic Equations for Carrier Transport in Semiconductors. *Journal of Mathematical Analysis and Applications* 113 (1986), pp. 12–35.

[74] P. A. Markowich. *The Stationary Semiconductor Device Equations.* Springer-Verlag Wien New York, 1986. DOI: 10.1007/978-3-7091-3678-2.

[75] K. Cho, M. Numan, T. G. Finstad, W. K. Chu, J. Liu, and J. J. Wortman. Transient enhanced diffusion during rapid thermal annealing of boron implanted silicon. *Applied Physics Letters* 47.12 (1985), pp. 1321–1323. DOI: 10.1063/1.96267.

[76] H. Gajewski. On existence, uniqueness and asymptotic behavior of solutions of the basic equations for carrier transport in semiconductors. *Z. Angew. Math. Mech. 65* 2 (1985), pp. 101–108.

[77] P. A. Markowich. A Nonlinear Eigenvalue Problem Modelling the Avalanche Effect in Semiconductor Diodes. *SIAM J. Math. Anal.* 6 (16 1985), pp. 1268–1283.

[78] S. Selberherr. *Analysis and simulation of semiconductor devices.* Wien, New York: Springer, 1984.

[79] W. Fichtner, D. J. Rose, and R. E. Bank. Semiconductor device simulation. *SIAM Journal on Scientific and Statistical Computing* 4.3 (1983), pp. 391–415.

[80] R. J. Baxter. *Exactly solved models in statistical mechanics.* London, United Kingdom: Academic Press, 1982.

[81] J. Blakemore. Approximations for Fermi-Dirac integrals, especially the function $F_{1/2}(\eta)$ used to describe electron density in a semiconductor. *Solid-State Electronics* 25.11 (1982), pp. 1067–1076.

[82] G. Golub. Some Modified Matrix Eigenvalue Problems. *SIAM Review* 15.2 (1973), pp. 318–334.

[83] M. S. Mock. On equations describing steady-state carrier distributions in a semiconductor device. *Comm. Pure Appl. Math.* 25.25 (1972), pp. 781–792.

[84] A. M. Il'in. A difference scheme for a differential equation with a small parameter multiplying the second derivative. *Mat. zametki* 6 (1969), pp. 237–248.

[85] D. Scharfetter and H. Gummel. Large-signal analysis of a silicon Read diode oscillator. *IEEE Transactions on Electron Devices* 16.1 (1969), pp. 64–77. DOI: 10.1109/T-ED.1969.16566.

[86] R. Haase. *Thermodynamics of irreversible processes.* Addison-Wesley, 1968.

[87] H. O'Hara and F. J. Smith. Error Estimation in the Clenshaw–Curtis Quadrature Formula. *The Computer Journal* 11.2 (1968), pp. 213–219. DOI: 10.1093/comjnl/11.2.213.

[88] D. H. Dickey. A Spreading Resistance Technique for Resistivity Measurements on Silicon. *Journal of the Electrochemical Society* 113.3 (1966), pp. 255–259.

[89] R. G. Mazur and D. H. Dickey. A Spreading Resistance Technique for Resistivity Measurements on Silicon. *Journal of The Electrochemical Society* 113.3 (1966), pp. 255–259.

[90] M. Abramowitz and I. Stegun. Integration. In: *Handbook of Mathematical Functions with Formulas, Graphs and Mathematical Tables.* Ed. by A. M. Series. 55. Dover Publications, 1964. Chap. 25.4.

[91] H. Gummel. A self-consistent iterative scheme for one-dimensional steady state transistor calculations. *Electron Devices, IEEE Transactions on* 11.10 (Oct. 1964), pp. 455–465. DOI: 10.1109/T-ED.1964.15364.

[92] S. R. de Groot and P. Mazur. *Non-equilibrium thermodynamics.* North Holland: Dover, 1962.

[93] C. Clenshaw and A. Curtis. A method for numerical integration on an automatic computer. *Numerische Mathematik* 2 (1960), pp. 197–205.

[94] J. Tauc. The Theory of a Bulk Photo-Voltaic Phenomenon in Semiconductors. *Czech J Phys* 5 (1955), pp. 178–191.

[95] L. Valdes. Resistivity Measurements on Germanium for Transistor. *Proceeding of the I.R.E* 42.2 (1954), pp. 420–427. DOI: 10.1109/JRPROC.1954.274680.

[96] R. H. Macneal. An asymmetrical finite difference network. *Quart. Math. Appl.* 11 (1953), pp. 295–310.

[97] J. Blakemore. The Parameters of Partially Degenerate Semiconductors. *Proc. Phys. Soc. London A* 65 (1952), pp. 460–461.

[98] W. Van Roosbroeck. Theory of the Flow of Electrons and Holes in Germanium and Other Semiconductors. *Bell System Technical Journal* 29.4 (Oct. 1950), pp. 560–607. DOI: 10.1002/j.1538-7305.1950.tb03653.x.

[99] J. Stefan. Über das Gleichgewicht und die Bewegung, insbesondere die Diffusion von Gasgemengen. *Sitzungsberichte der Mathematisch-Naturwissenschaftlichen Classe der Kaiserlichen Akademie der Wissenschaften Wien, 2te Abteilung* 63 (1871), pp. 63–124.

4

Publication list

The following presents a complete list of my publications, organized into different categories.

Habilitation related publications

[PF1] D. Abdel, P. Farrell, and J. Fuhrmann. Assessing the quality of the excess chemical potential flux scheme for degenerate semiconductor device simulation. *Optical and Quantum Electronics* 53.163 (2021). DOI: 10.1007/s11082-021-02803-4.

[PF2] D. Abdel, P. Vagner, J. Fuhrmann, and P. Farrell. Modelling charge transport in perovskite solar cells: Potential-based and limiting ion vacancy depletion. *Electrochimica Acta* 390 (2021), p. 138696. DOI: 10.1016/j.electacta.2021.138696.

[PF3] P. Farrell, S. Kayser, and N. Rotundo. Modeling and simulation of the lateral photovoltage scanning method. *Computer and Mathematics with Applications* 102 (2021), pp. 248–260. DOI: 10.1016/j.camwa.2021.10.017.

[PF4] S. Kayser, N. Rotundo, N. Dropka, and P. Farrell. Assessing doping inhomogeneities in GaAs crystal via simulations of lateral photovoltage scanning method. *Journal of Crystal Growth* 571 (2021), p. 126248. DOI: 10.1016/j.jcrysgro.2021.126248.

[PF5] M. O'Donovan, D. Chaudhuri, T. Streckenbach, P. Farrell, S. Schulz, and T. Koprucki. From atomistic tight binding theory to macroscale drift diffusion: multiscale modeling and numerical simulation of uni-polar charge transport in (In,Ga)N devices with random fluctuations. *Journal of Applied Physics* 130.6 (2021), p. 065702. DOI: 10.1063/5.0059014.

[PF6] P. Farrell and D. Peschka. Nonlinear diffusion, boundary layers and nonsmoothness: Analysis of challenges in drift-diffusion semiconductor simulations. *Computers and Mathematics with Applications* (2019), pp. 3731–3747. DOI: d2zg.

[PF7] M. Patriarca, P. Farrell, J. Fuhrmann, and T. Koprucki. Highly Accurate Quadrature-based Scharfetter-Gummel Schemes for Charge Transport in Degenerate Semiconductors. *Computer Physics Communications* 235 (2018), pp. 40–49. DOI: 10.1016/j.cpc.2018.10.004.

[PF8] F. Dassi, P. Farrell, and H. Si. A Novel Surface Remeshing Scheme via Radial Basis Functions and Higher-Dimensional Embedding. *SIAM Journal on Scientific Computing* 39.3 (2017), B522–B547. DOI: 10.1137/16m1077015.

[PF9] F. Dassi, L. Kamenski, P. Farrell, and H. Si. Tetrahedral Mesh Improvement Using Moving Mesh Smoothing, Lazy Searching Flips, and RBF Surface Reconstruction. *Computer-Aided Design* (2017). DOI: 10.1016/j.cad.2017.11.010.

[PF10] P. Farrell, T. Koprucki, and J. Fuhrmann. Computational and Analytical Comparison of Flux Discretizations for the Semiconductor Device Equations beyond Boltzmann Statistics. *Journal of Computational Physics* 346 (2017), pp. 497–513. DOI: 10.1016/j.jcp.2017.06.023.

[PF11] P. Farrell and A. Linke. Uniform Second Order Convergence of a Complete Flux Scheme on Unstructured 1D Grids for a Singularly Perturbed Advection–Diffusion Equation and Some Multidimensional Extensions. *Journal of Scientific Computing* 72.1 (2017), pp. 373–395. DOI: 10.1007/s10915-017-0361-7.

[PF12] T. Koprucki, N. Rotundo, P. Farrell, D. H. Doan, and J. Fuhrmann. On Thermodynamic Consistency of a Scharfetter-Gummel Scheme Based on a Modified Thermal Voltage for Drift-Diffusion Equations with Diffusion Enhancement. *Optical and Quantum Electronics* 47.6 (2015), pp. 1327–1332. DOI: 10.1007/s11082-014-0050-9.

Submitted publications

Other peer-reviewed journal publications

[PF13] D. Chaudhuri, M. O'Donovan, T. Streckenbach, O. Marquardt, P. Farrell, S. K. Patra, T. Koprucki, and S. Schulz. Multiscale simulations of the electronic structure of III-nitride quantum wells with varied Indium content: Connecting atomistic and continuum-based models. *Journal of Applied Physics* 129 (2021), p. 073104. DOI: 10.1063/5.0031514.

[PF14] S. Kayser, P. Farrell, and N. Rotundo. Detecting striations via the lateral photovoltage scanning method without screening effect. *Optical and Quantum Electronics* 53 (2021), p. 288. DOI: 10.1007/s11082-021-02911-1.

[PF15] S. Schulz, D. Chaudhuri, M. O'Donovana, S. K. Patra, T. Streckenbach, P. Farrell, O. Marquardt, and T. Koprucki. Multi-scale modeling of electronic, optical, and transport properties of III-N alloys and heterostructures. *SPIE Photonics West* 11274 (2020), pp. 157–166. DOI: 10.1117/12.2551055.

[PF16] I. Selmer, P. Farrell, I. Smirnova, and P. Gurikov. Comparison of Finite Difference and Finite Volume Simulations for a Sc-Drying Mass Transport Mode. *Gels* 6.45 (2020).

[PF17] M. Lübbering, J. Kunkel, and P. Farrell. "What Company Does My News Article Refer to? Tackling Multi Class Problems With Topic Modeling". In: *Proceedings of the Conference on "Lernen, Wissen, Daten, Analysen", Berlin, Germany, September 30 - October 2, 2019.* 2019, pp. 353–364. DOI: 10.20347/WIAS.PREPRINT.2621.

[PF18] P. Farrell, M. Patriarca, J. Fuhrmann, and T. Koprucki. Comparison of Thermodynamically Consistent Charge Carrier Flux Discretizations for Fermi-Dirac and Gauss-Fermi Statistics. *Optical and Quantum Electronics* 50.101 (2018). DOI: 10.1007/s11082-018-1349-8.

[PF19] I. Selmer, A.-S. Behnecke, P. Farrell, A. B. Morales, P. Gurikov, and I. Smirnova. Model development for sc-drying kinetics of aerogels: Part 2. Packed bed of spherical particles. *Journal of Supercritical Fluids* 147 (2018), pp. 149–161. DOI: 10.1016/j.supflu.2018.07.006.

[PF20] P. Farrell, K. Gillow, and H. Wendland. Multilevel Interpolation of Divergence-Free Vector Fields. *IMA Journal of Numerical Analysis* 37.1 (2017), pp. 332–353. DOI: 10.1093/imanum/drw006.

[PF21] F. Dassi, P. Farrell, and H. Si. An Anisoptropic Surface Remeshing Strategy Combining Higher Dimensional Embedding with Radial Basis Functions. *Procedia Engineering* 164 (2016), pp. 72–83. DOI: 10.1016/j.proeng.2016.11.022.

[PF22] P. Farrell and J. Pestana. Block Preconditioners for Linear Systems arising from Multiscale Collocation with Compactly Supported RBFs. *Numerical Linear Algebra with Applications* 22 (2015), pp. 731–747. DOI: 10.1002/nla.1984.

[PF23] P. Farrell and H. Wendland. RBF Multiscale Collocation for Second Order Elliptic Boundary Value Problems. *SIAM Journal on Numerical Analysis* 51.4 (2013), pp. 2403–2425. DOI: 10.1137/120898383.

Book chapters and theses

[PF24] P. Farrell. Silicon - An Electronic Hybrid. In: *Material Effects – Product Designs, Photographs, Experiments.* Ed. by L. Pense. Jovis, 2018, pp. 138–143.

[PF25] P. Farrell, N. Rotundo, D. H. Doan, M. Kantner, J. Fuhrmann, and T. Koprucki. Mathematical Methods: Drift-Diffusion Models. In: *Handbook of Optoelectronic Device Modeling and Simulation.* Ed. by J. Piprek. Vol. 2. CRC Press, 2017. Chap. 50, pp. 733–771.

[PF26] P. Farrell. *Multilevel Collocation with Radial Basis Functions.* PhD thesis. University of Oxford, 2014.

[PF27] P. Farrell. *Algebraic Image Reconstruction in Computed Tomography with Radial Basis Functions*. Diplom thesis, University of Hamburg. 2010.

Peer-reviewed proceedings

[PF28] S. Kayser, N. Rotundo, J. Fuhrmann, N. Dropka, and P. Farrell. "The lateral photovoltage scanning method (LPS): Understanding doping variations in silicon crystals". In: *2020 International Conference on Numerical Simulation of Optoelectronic Devices (NUSOD)*. 2020, pp. 49–50. DOI: 10.1109/NUSOD49422.2020.9217779.

[PF29] T. Koprucki, T. Streckenbach, P. Farrell, O. Marquardt, D. Chaudhuri, M. O'Donovan, S. Patra, and S. Schulz. "Towards multiscale modeling of III-N-based LEDs". In: *19th International Conference on Numerical Simulation of Optoelectronic Devices*. July 2019.

[PF30] M. Patriarca, P. Farrell, T. Koprucki, and M. Auf der Maur. "Highly Accurate Discretizations for non-Boltzmann Charge Transport in Semiconductors". In: Nov. 2018, pp. 53–54. DOI: 10.1109/NUSOD.2018.8570265.

[PF31] P. Farrell, T. Koprucki, and J. Fuhrmann. Comparison of Consistent Flux Discretizations for Drift Diffusion beyond Boltzmann Statistics. *Proceedings of the 17th International Conference on Numerical Simulation of Optoelectronic Devices (IEEE), J. Piprek and M. Willatzen (eds.)* (2017). Ed. by J. Piprek and M. Willatzen, pp. 219–220. DOI: 10.1109/NUSOD.2017.8010070.

[PF32] P. Farrell, T. Koprucki, and J. Fuhrmann. "Comparison of Scharfetter-Gummel Flux Discretizations Under Blakemore Statistics". In: *Progress in Industrial Mathematics at ECMI 2016*. Ed. by P. Quintela, P. Barral, D. Gómez, F. J. Pena, J. Rodríguez, P. Salgado, and M. E. Vázquez-Méndez. Berlin: Springer, 2017, pp. 91–97. DOI: 10.1007/978-3-319-63082-3_13.

[PF33] P. Farrell and A. Linke. Uniform Second Order Convergence of a Complete Flux Scheme on Nonuniform 1D Grids. *Finite Volumes for Complex Applications VIII - Methods and Theoretical Aspects, Clément Cancès and Pascal Omnes (eds.)* (2017). Ed. by C. Cancès and P. Omnes, pp. 303–311.

Software

[PF34] D. Abdel, P. Farrell, and J. Fuhrmann. *ChargeTransport.jl*. Version: 0.1.0. https://github.com/PatricioFarrell/ChargeTransport.jl, 2022.

[PF35] D. H. Doan, P. Farrell, J. Fuhrmann, M. Kantner, T. Koprucki, and N. Rotundo. *ddfermi – a drift-diffusion simulation tool*. Version: 0.1.0. doi: http://doi.org/10.20347/WIAS.SOFTWARE.14: Weierstrass Institute (WIAS), 2018.

5

Overview of published work relevant for the *Habilitation*

In the following chapters, I will present the relevant publications submitted as part of the *Habilitation* with an abstract, linking it to the previous summary in Chapters 2 and 3. Furthermore, since the publications are coauthored with other researchers, I detail how I contributed to conception (*Konzeption*), execution (*Durchführung*), reporting (*Berichtsabfassung*). I have informed every coauthor about the present endeavor and consent to having them contacted by Freie Universität Berlin.

6

Assessing the quality of the excess chemical potential flux scheme for degenerate semiconductor device simulation

D. Abdel, P. Farrell, and J. Fuhrmann. Assessing the quality of the excess chemical potential flux scheme for degenerate semiconductor device simulation. *Optical and Quantum Electronics* 53.163 (2021). DOI: 10.1007/s11082-021-02803-4

Abstract The van Roosbroeck system models current flows in (non-)degenerate semiconductor devices. Focusing on the stationary model, we compare the excess chemical potential discretization scheme, the flux approximation which is based on the modification of the drift term in the current densities (3.9), with another state-of-the-art Scharfetter-Gummel scheme, namely the diffusion-enhanced scheme (3.6). Physically, the diffusion-enhanced scheme can be interpreted as a flux approximation which modifies the thermal voltage. As a reference solution we consider an implicitly defined integral flux, using Blakemore statistics. The integral flux refers to the exact solution of a local two point boundary value problem for the continuous current density and can be interpreted as a generalized Scharfetter-Gummel scheme. All numerical discretization schemes can be used within a Voronoi finite volume method to simulate charge transport in (non-)degenerate semiconductor devices. The investigation includes the analysis of Taylor expansions, a derivation of error estimates and a visualization of errors in local flux approximations to extend previous discussions. Additionally, drift-diffusion simulations of a p-i-n device are performed.

Conception: This publication is the product of Dilara Abdel's master's thesis, which Jürgen Fuhrmann and myself supervised. The initial idea for such a comparison was by Jürgen Fuhrmann, whereas I guided the day to day supervision, comparing the schemes by following a methodology I had developed

in [PF10].

Execution: Most of the implementation has been carried out by Dilara Abdel, guided by Jürgen Fuhrmann and myself. The figures in Fig. 3, were created by code that I developed for [PF10].

Reporting: The first drafts of the paper were written by Dilara Abdel, which I then improved.

This article has been published under a Creative Common license.

Optical and Quantum Electronics (2021) 53:163
https://doi.org/10.1007/s11082-021-02803-4

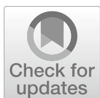

Assessing the quality of the excess chemical potential flux scheme for degenerate semiconductor device simulation

Dilara Abdel[1] · **Patricio Farrell**[1] · **Jürgen Fuhrmann**[1]

Received: 30 October 2020 / Accepted: 21 February 2021 / Published online: 15 March 2021
© The Author(s) 2021

Abstract

The van Roosbroeck system models current flows in (non-)degenerate semiconductor devices. Focusing on the stationary model, we compare the excess chemical potential discretization scheme, a flux approximation which is based on a modification of the drift term in the current densities, with another state-of-the-art Scharfetter–Gummel scheme, namely the diffusion-enhanced scheme. Physically, the diffusion-enhanced scheme can be interpreted as a flux approximation which modifies the thermal voltage. As a reference solution we consider an implicitly defined integral flux, using Blakemore statistics. The integral flux refers to the exact solution of a local two point boundary value problem for the continuous current density and can be interpreted as a generalized Scharfetter–Gummel scheme. All numerical discretization schemes can be used within a Voronoi finite volume method to simulate charge transport in (non-)degenerate semiconductor devices. The investigation includes the analysis of Taylor expansions, a derivation of error estimates and a visualization of errors in local flux approximations to extend previous discussions. Additionally, drift-diffusion simulations of a p–i–n device are performed.

Keywords Degenerate semiconductors · Drift-diffusion equations · Finite volume method · Flux discretization · Scharfetter–Gummel scheme

Mathematics Subject Classification 35Q81 · 35K57 · 65N08

This article is part of the Topical Collection on Numerical Simulation of Optoelectronic Devices.

Guest edited by Stefan Schulz, Silvano Donati, Karin Hinzer, Weida Hu, Slawek Sujecki, Alex Walker and Yuhrenn Wu.

✉ Dilara Abdel
abdel@wias-berlin.de

Patricio Farrell
farrell@wias-berlin.de

Jürgen Fuhrmann
fuhrmann@wias-berlin.de

[1] Weierstrass Institute for Applied Analysis and Stochastics (WIAS), Mohrenstr. 39, 10117 Berlin, Germany

1 Introduction

The standard drift-diffusion model for semi-classical charge transport of free electrons and holes due to a self-consistent electric field in a semiconductor device is the van Roosbroeck system. We consider Voronoi finite volume schemes for the discretization of the semiconductor device equations. We are interested in the numerically more challenging degenerate case and pay particular attention to the choice of flux approximations. One of the most classical numerical flux scheme is arguably the Scharfetter–Gummel scheme (Scharfetter and Gummel 1969), which yields a numerical stable and thermodynamically consistent numerical flux, but cannot be used for general charge carrier statistics. A generalization of the Scharfetter–Gummel scheme is available (Eymard et al. 2006), but computationally expensive. Hence, several thermodynamically consistent numerical flux schemes, which modify this generalization to lower the computational costs, are proposed in the literature (Farrell et al. 2017b, a, 2018; Patriarca et al. 2018). We focus on the excess chemical potential scheme (Yu and Dutton 1988) which appears to be used in parts of the device simulation community (Silvaco International 2016; Synopsys, Inc 2010). However, unfortunately, there seem to be no direct comparisons of this scheme with other recent modified Scharfetter–Gummel schemes. This paper aims to fill this gap by comparing it to the diffusion enhanced scheme (Bessemoulin-Chatard 2012), which was already compared to other modified Scharfetter–Gummel schemes and seems to be the most promising modified Scharfetter–Gummel flux (Farrell et al. 2017b). The integral flux by Eymard et al. is used as a reference flux. It supplements previously made temperature-dependent observations (Kantner 2020).

2 Van Roosbroeck model

The stationary variant of the van Roosbroeck system is given by

$$-\nabla \cdot \left(\varepsilon_s \nabla \psi\right) = q\Big((p - N_A) - (n - N_D)\Big), \tag{1a}$$

$$\nabla \cdot \mathbf{j}_n = qR(n,p), \tag{1b}$$

$$\nabla \cdot \mathbf{j}_p = -qR(n,p), \tag{1c}$$

where q denotes the elementary charge, ε_s the dielectric permittivity, N_A and N_D describe the density of singly ionized acceptor and donor atoms, and R the recombination. The set of unknowns is expressed by the electrostatic potential ψ and the quasi Fermi potentials for electrons φ_n and holes φ_p. The current densities in the continuity Eqs. (1b) and (1c) are given by

$$\mathbf{j}_n = -q\mu_n n \nabla \varphi_n, \qquad \mathbf{j}_p = -q\mu_p p \nabla \varphi_p, \tag{2}$$

where the electron and hole densities n and p are defined by (Sze and Ng 2006)

$$n = N_c \mathcal{F}(\eta_n), \quad \eta_n = \frac{q(\psi - \varphi_n) - E_c}{k_B T}, \tag{3a}$$

$$p = N_v \mathcal{F}(\eta_p), \quad \eta_p = \frac{q(\varphi_p - \psi) + E_v}{k_B T}. \tag{3b}$$

The strictly monotonously increasing statistics function $\mathcal{F}$ will be discussed later. The conduction and valence band density of states are given by N_c and N_v, the mobilities by μ_n and μ_p and the Boltzmann constant by k_B. The conduction and valence band-edge energies are denoted by E_c and E_v and T refers to the temperature. With help of the generalized Einstein relation it is possible to model the diffusion coefficients D_n and D_p via the the nonlinear diffusion enhancement

$$g(\xi) = \xi(\mathcal{F}^{-1})'(\xi) \tag{4}$$

by (introducing the thermal voltage $U_T = k_B T/q$)

$$D_n = \mu_n U_T g\left(\frac{n}{N_c}\right), \quad D_p = \mu_p U_T g\left(\frac{p}{N_v}\right).$$

With this relation, we can rewrite the electric fluxes (2) into a drift-diffusion form

$$\mathbf{j}_n = -q\mu_n n \nabla\psi + qD_n \nabla n, \quad \mathbf{j}_p = -q\mu_p p \nabla\psi - qD_p \nabla p. \tag{5}$$

In general, inorganic semiconductor devices can be modeled by choosing the Fermi-Dirac integral of order one-half (Sze and Ng 2006) for the statistics function $\mathcal{F}$. Non-degenerate semiconductors are modeled with the Boltzmann approximation $\mathcal{F}(\eta) = \exp(\eta)$. In this case, the diffusion enhancement (4) is equal to one. In this work, we focus on degenerate semiconductors, i.e. nonlinear diffusive problems. To compare our flux approximations, we choose the Blakemore statistics function $\mathcal{F}(\eta) = (\exp(-\eta) + \gamma)^{-1}$ with $\gamma = 0.27$ which is a valid approximation of the Fermi-Dirac integral of order one-half in the low density limit $\eta < 1.3$ with a relative error of ≤ 0.03 (Blakemore 1952, 1982). Additionally, an expensive but accurate numerical flux is known for the Blakemore case (Koprucki and Gärtner 2013). The different statistics with the corresponding diffusion enhancements are depicted in Fig. 1. For brevity, we consider only the current density for electrons from now on and will partially omit the index n.

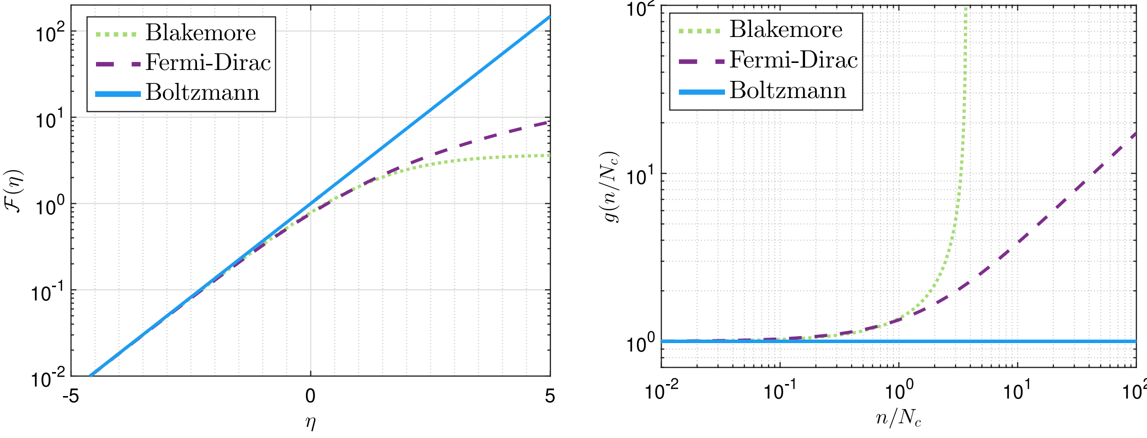

Fig. 1 Left: Semi-logarithmic plot of different statistics functions $\mathcal{F}$ for $-5 \leq \eta \leq 5$. Right: Corresponding logarithmic plot of the diffusion enhancement g in (4). This function can be seen as a measure of how far away we are from the Boltzmann regime

3 Scharfetter–Gummel type fluxes

The open, bounded domain $\mathbf{\Omega}$, on which the model (1) is defined, is partitioned into N control volumes $\boldsymbol{\omega}_K$ such that $\mathbf{\Omega} = \bigcup_{K=1}^{N} \boldsymbol{\omega}_K$, where each $\boldsymbol{\omega}_K$ is associated with a collocation point $\mathbf{x}_K \in \boldsymbol{\omega}_K$. We are interested in a numerical flux j along the edge connecting the collocation points of two neighboring control volumes $\boldsymbol{\omega}_K$ and $\boldsymbol{\omega}_L$ which is assumed to be aligned with the normal direction with respect to the interface $\boldsymbol{\omega}_K \cap \boldsymbol{\omega}_L$. In the following, a subindex K corresponds to an evaluation of a physical quantity at node $\mathbf{x}_K$ and a subindex L to an evaluation at node $\mathbf{x}_L$, respectively. Integrating (1b) over $\boldsymbol{\omega}_K$, using the Gauss divergence theorem and one point quadrature rules yields the discrete counterpart

$$\sum_{\boldsymbol{\omega}_L \in \mathcal{N}(\boldsymbol{\omega}_K)} |\partial\boldsymbol{\omega}_K \cap \partial\boldsymbol{\omega}_L| j_{n;KL} = q|\boldsymbol{\omega}_K| R(n_K, p_K),$$

where $\mathcal{N}(\boldsymbol{\omega}_K)$ denotes the set of all control volumes neighboring $\boldsymbol{\omega}_K$. The nonlinear flux function $j_{n;KL} = j_{n;KL}(\eta_K, \eta_L, \psi_K, \psi_L)$ approximates the projected flux $\mathbf{j} \cdot \boldsymbol{\nu}_{KL}$ locally along the edge $\partial\boldsymbol{\omega}_K \cap \partial\boldsymbol{\omega}_L$, where $\boldsymbol{\nu}_{KL}$ is the corresponding normal vector along $\partial\boldsymbol{\omega}_K \cap \partial\boldsymbol{\omega}_L$. For details concerning the finite volume method see Farrell et al. (2017a).

Furthermore, one property which holds on a continuous level to avoid unphysical state dissipation is the *preservation of thermodynamic equilibrium* (Farrell et al. 2017a). Mathematically, this means that vanishing fluxes shall imply constant quasi Fermi potentials. A numerical flux $j = j_{KL}$ is now said to be thermodynamically consistent, if it satisfies an analogous discrete relation, i.e.

$$j = 0 \quad \text{implies} \quad \delta\eta_{KL} = \delta\psi_{KL},$$

where $\delta\eta_{KL} = \eta_L - \eta_K$ and $\delta\psi_{KL} = (\psi_L - \psi_K)/U_T$. Thermodynamic consistency is also important, when coupling the van Roosbroeck system to heat transport models (Farrell et al. 2017b). We discuss now different thermodynamically consistent numerical fluxes that may be used within a Voronoi finite volume framework.

3.1 Generalized Scharfetter–Gummel scheme

Under the assumption that the flux $\mathbf{j}_n$ and the electric field $-\nabla\psi$ are constant along each face of a Voronoi cell, the flux can be projected onto the shared edge between two neighboring control volumes. Then, an integral equation can be derived (Eymard et al. 2006), which shall be satisfied by the unknown local numerical flux j

$$\int_{\eta_K}^{\eta_L} \left(\frac{j/j_0}{\mathcal{F}(\eta)} + \delta\psi_{KL} \right)^{-1} d\eta = 1, \quad j_0 = q\mu_n N_c \frac{U_T}{h_{KL}}, \tag{6}$$

where η is defined in (3). The integration limits are given by $\eta_K = \eta_n(\psi_K, \varphi_K)$ and $\eta_L = \eta_n(\psi_L, \varphi_L)$ and h_{KL} denotes the Euclidean distance between two neighboring nodes $\mathbf{x}_K$ and $\mathbf{x}_L$. The existence of a solution to (6) was proven by Gärtner (2015), even though the integral equation is in general not explicitly solvable. We refer to the solution of (6) as *generalized* Scharfetter–Gummel flux. Note that for non-degenerate semiconductor devices the generalized scheme reduces to the classical Scharfetter–Gummel scheme (Scharfetter and Gummel 1969)

$$j_{sg} = B(\delta\psi_{KL})e^{\eta_L} - B(-\delta\psi_{KL})e^{\eta_K}, \tag{7}$$

for a non-dimensionalized edge current $j_{sg} = j/j_0$ with B as the Bernoulli function which is defined by $B(x) := x/(e^x - 1)$, $B(0) = 1$. Additionally, it was shown by Koprucki and Gärtner (2013) that for degenerate semiconductors based on Blakemore statistics the integral Eq. (6) can be reduced to a fixed point equation, namely

$$j_g = B(\delta\psi_{KL} + \gamma j_g)\mathrm{e}^{\eta_L} - B(-[\delta\psi_{KL} + \gamma j_g])\mathrm{e}^{\eta_K}. \tag{8}$$

The implicit Eq. (8) can be solved within a few Newton steps, but the efficiency of this flux is highly dependent on the choice of initial value. Hence, computationally less expensive flux discretization schemes are needed as an alternative. Still, we will use this scheme as a reference flux for the case of degenerated semiconductors, modeled by Blakemore statistics.

3.2 Diffusion enhanced scheme

Recently, another *modified* Scharfetter–Gummel discretization scheme was introduced (Bessemoulin-Chatard 2012). There, a logarithmic average for the nonlinear diffusion enhancement g in (4) is considered,

$$g_{KL} = \frac{\eta_L - \eta_K}{\log \mathcal{F}(\eta_L) - \log \mathcal{F}(\eta_K)}, \tag{9}$$

resulting in the local flux approximation

$$j_d = g_{KL}\left[B\left(\frac{\delta\psi_{KL}}{g_{KL}}\right)\mathcal{F}(\eta_L) - B\left(-\frac{\delta\psi_{KL}}{g_{KL}}\right)\mathcal{F}(\eta_K)\right]. \tag{10}$$

We stress that, in case of a denominator in (9) near zero, i.e. $\eta_K \approx \eta_L$, regularization strategies need to be developed to handle the removable singularity.

3.3 "Sedan" scheme

The earliest reference we could find for the excess chemical potential scheme is the source code of the SEDAN III simulator (Yu and Dutton 1988), therefore in the following, we will likewise refer to this scheme as the *Sedan scheme*. There are benchmarks computed by the device simulator SEDAN III itself available in literature, but to the best of our knowledge there are barely any comparisons of this flux discretization scheme with other schemes known. A numerical analysis focused comparison of this flux approximation is given by Cancès et al. (2021). The scheme is motivated by rearranging the drift part in (5) to include the *excess chemical potential*, $\mu^{ex} = \log \mathcal{F}(\eta) - \eta$, yielding

$$j_s = B(Q_{KL})\mathcal{F}(\eta_L) - B(-Q_{KL})\mathcal{F}(\eta_K) \tag{11}$$

with

$$Q_{KL} = \delta\psi_{KL} + \mu_L^{ex} - \mu_K^{ex} = \delta\psi_{KL} - (\eta_L - \eta_K) + \log\frac{\mathcal{F}(\eta_L)}{\mathcal{F}(\eta_K)}. \tag{12}$$

4 Comparison of flux discretizations

This paper aims to extend a previous discussion (Farrell et al. 2017b) by examining similar aspects for the excess chemical potential flux approximation introduced in Sect. 3.3.

4.1 Taylor expansions

Taylor expansions of the following form dependent on $\delta\psi_{KL}$ and $\delta\eta_{KL}$

$$\begin{aligned} j_k = &-\mathcal{F}(\bar{\eta}_{KL})\delta\psi_{KL} + \mathcal{F}(\bar{\eta}_{KL})\delta\eta_{KL} \\ &+ \alpha_1\delta\psi_{KL}^2\delta\eta_{KL} + \alpha_2\delta\psi_{KL}\delta\eta_{KL}^2 + \alpha_3\delta\eta_{KL}^3, \quad k \in \{g, s, d\} \end{aligned} \tag{13}$$

can be derived for the flux approximations introduced in Sect. 3 for a sufficiently smooth statistics $\mathcal{F}$, when expanding in $\bar{\eta}_{KL} = (\eta_L + \eta_K)/2$, see Abdel (2020) and Farrell et al. (2017b). Here, the fluxes j_g,j_s and j_d correspond to one of the flux discretization schemes introduced in Sect. 3. For the prefactors α_j, $j \in \{1, 2, 3\}$, we have

$$\alpha_j = \alpha_j\Big(\mathcal{F}(\bar{\eta}_{KL}), \mathcal{F}'(\bar{\eta}_{KL}), \mathcal{F}''(\bar{\eta}_{KL}), \mathcal{F}'''(\bar{\eta}_{KL})\Big).$$

The absolute error in these prefactors α_j between the Taylor expansions of the generalized Scharfetter–Gummel scheme and the two modified ones is depicted in Fig. 2. For the depicted figures we choose the statistics function $\mathcal{F}$ as the Blakemore statistics.

For large negative arguments of the function $\mathcal{F}$ the Boltzmann and the Blakemore statistics nearly coincide, corresponding to the non-degenerate case. Hence, the modified Scharfetter–Gummel schemes converge towards the classical scheme (7) and we observe nearly vanishing errors in Fig. 2. For large positive arguments we observe that the errors in the prefactors corresponding to the diffusion enhanced scheme increase with the exponents of $\delta\eta_{KL}$, whereas the error corresponding to the excess chemical potential scheme nearly vanishes. Due to this observation it gives rise to think that in case of no electrical field the excess chemical potential flux performs better than the diffusion enhanced scheme. However, neither the diffusion enhanced nor the excess chemical potential scheme is third-order accurate. To measure the quality of the fluxes in a different manner, second-order error estimates for the local flux errors are considered next.

When neglecting third-order terms, the following error bounds between the modified and the generalized flux dependent on the diffusion enhancement can be derived (Abdel 2020; Farrell et al. 2017b)

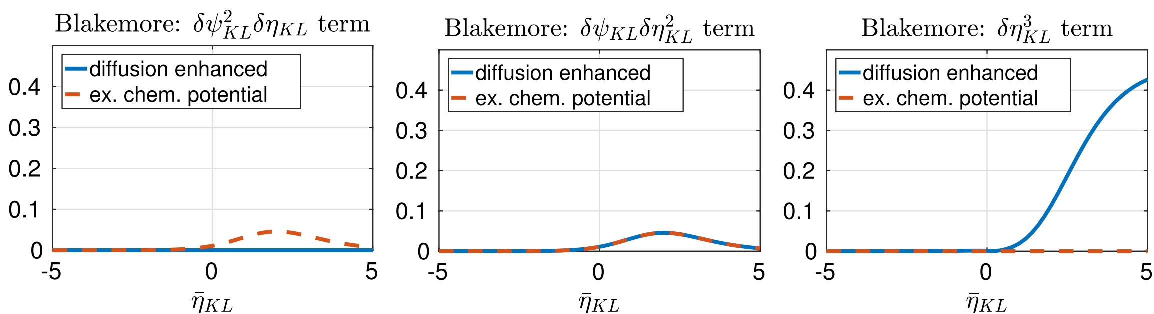

Fig. 2 Errors between the third-order prefactors of Taylor series expansion of the exact Scharfetter–Gummel scheme (6) and the two modified schemes for $\bar{\eta}_{KL} \in [-5, 5]$

$$|j_s - j| \leq \frac{1}{2}\frac{\mathcal{F}(\bar{\eta}_{KL})}{g(\bar{\eta}_{KL})}\Big(|\delta\psi_{KL}\delta\eta_{KL}| + \delta\eta_{KL}^2\Big), \tag{14}$$

$$|j_d - j| \leq \frac{1}{2}\frac{\mathcal{F}(\bar{\eta}_{KL})}{g(\bar{\eta}_{KL})}|\delta\psi_{KL}\delta\eta_{KL}|. \tag{15}$$

The error bounds indicate a better performance of the diffusion enhanced scheme for large values of the diffusion enhancement g, i.e. for statistics strongly deviating from the Boltzmann regime.

4.2 Error between local flux approximations

We study the logarithmic error between the modified flux schemes and the generalized scheme for two fixed averages $\bar{\eta}_{KL}$. The errors for the simulation of a degenerate semiconductor can be seen in Fig. 3. The black dashed lines correspond to thermodynamic consistency, as well as pure drift currents, i.e. $\eta_K = \eta_L$. In both cases, the modified schemes agree exactly with the generalized scheme.

Since $\mathcal{F}(\bar{\eta}_{KL})/g(\bar{\eta}_{KL}) = \mathcal{F}'(\bar{\eta}_{KL})$, the derivative of the statistics function appears in the error estimates (14) and (15). The derivative of the Blakemore statistics decreases for large positive arguments. Hence, we observe in Fig. 3 that increasing the average $\bar{\eta}_{KL}$ results in a comparatively smaller error. Both, the error estimates (14), (15) and Fig. 3 indicate a larger area, where the diffusion enhanced and the generalized scheme agree

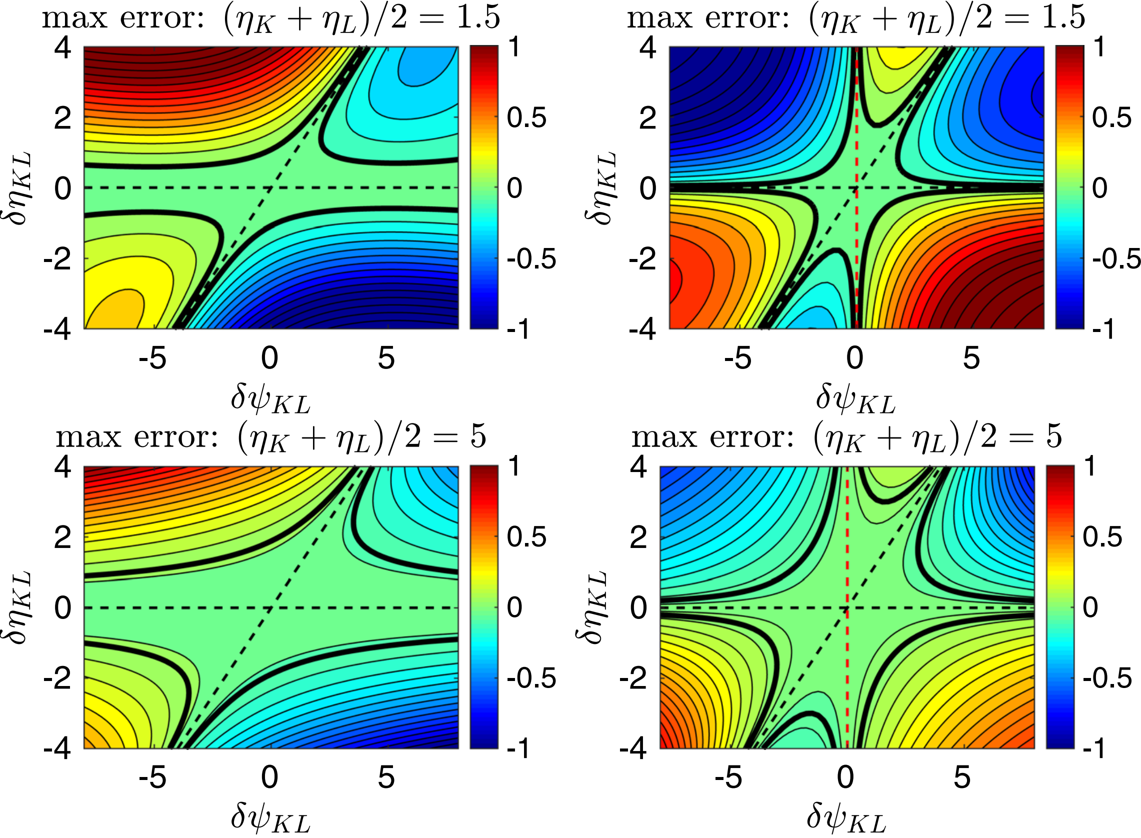

Fig. 3 Logarithmic absolute errors between the Taylor expansions of the generalized Scharfetter–Gummel and the diffusion enhanced scheme (left) and the excess chemical potential scheme (right) for two fixed averages $\bar{\eta}_{KL} = 1.5$ and $\bar{\eta}_{KL} = 5$

well for small values of $\delta\eta_{KL}$ and large values of the potential difference $\delta\psi_{KL}$. Further, the red dashed line in Fig. 3 indicates agreement of the excess chemical potential scheme and the exact solution of (6) for a purely diffusive flux $\mathbf{j}$, i.e. a vanishing electrical field $\delta\psi_{KL} = 0$. This can be proven analytically, see Abdel (2020). In this specific case, the excess chemical potential scheme is the best possible flux approximation.

5 Numerical example

Finally, we study the impact of the different flux approximations on the simulation of degenerate semiconductor devices for a 6μm long GaAs p-i-n diode with a width of 0.5μm and a depth of $1.0 \cdot 10^{-4}$cm. A motivation for this example is given in Farrell et al. (2017b). Since the 3D device only varies along one axis, it suffices to simulate the device along one spatial dimension. On each 2μm long layer (p/n–doped or intrinsic) we choose $N = 3 \cdot 2^{n_{ref}-1}$ uniform nodes. The donor and acceptor doping densities are given by $N_D = 4.35 \times 10^{17}\text{cm}^{-3}$ and $N_A = 4.20 \times 10^{18}\text{cm}^{-3}$. An open source solver, based on `VoronoiFVM` (Fuhrmann 2019–2020), was used which allows to use automatic differentiation. The stationary van Roosbroeck system (1) with zero recombination supplemented with Dirichlet-Neumann boundary conditions is considered. The resulting current voltage curves for a refinement level $n_{ref} = 3$ and the L^∞ errors in the computed total currents based on the different flux approximations for the first nine refinement level are depicted in Fig. 4. It can be observed that eventually the errors in the computed total currents based on the flux schemes converge with order $\mathcal{O}(h^2)$. Furthermore, it suggests that on coarse meshes, which are hard to avoid for expensive 3D simulations, the excess chemical potential flux performs better than the diffusion enhanced scheme, yet multidimensional device set-ups were not simulated.

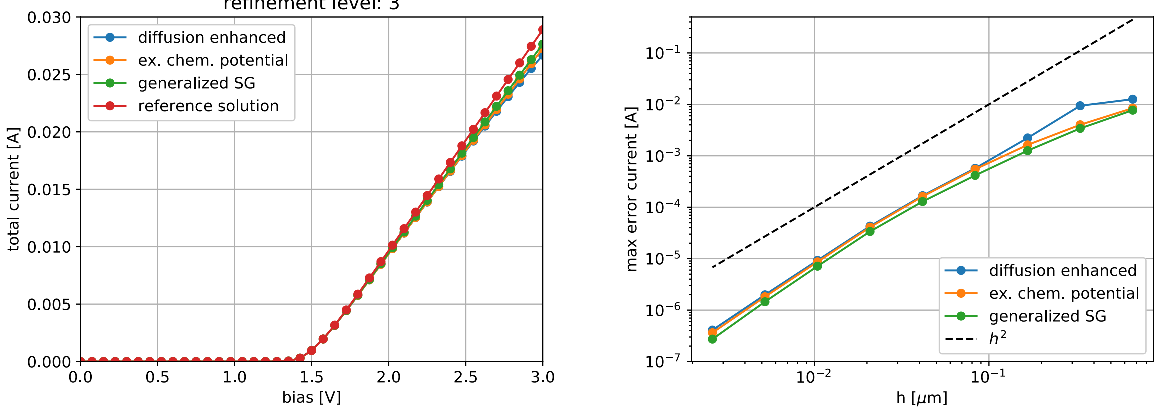

Fig. 4 Left: The I–V curves computed with the different schemes for fixed mesh refinement. The reference solution was computed using the generalized Scharfetter–Gummel scheme on refinement level 10. Right: Convergence studies for the absolute errors of the total currents. The absolute errors correspond to the nine refinement level, where the rightmost point depicts the error on the coarsest mesh

6 Conclusion

Our goal was to assess the quality of the excess chemical potential flux (11) which has received surprisingly little attention in the literature. To this end, we compared it to another modified Scharfetter–Gummel scheme (10) by studying its error with respect to the more accurate but expensive integral flux (6). For this, we analyzed Taylor expansions of the flux discretization schemes, the errors in the local flux approximations and simulated a p-i-n benchmark. Further applications and the impact of this scheme on realistic multidimensional device settings will be part of future research.

Acknowledgements This work was partially supported by the Leibniz competition.

Funding Open Access funding enabled and organized by Projekt DEAL..

Availability of data and material Not applicable.

Compliance with ethical standards

Conflict of interest The authors declare that they have no conflict of interest.

Funding This work was partially supported by the Leibniz competition.

Code availability The solver we used will be available soon on `GitHub`.

Open Access This article is licensed under a Creative Commons Attribution 4.0 International License, which permits use, sharing, adaptation, distribution and reproduction in any medium or format, as long as you give appropriate credit to the original author(s) and the source, provide a link to the Creative Commons licence, and indicate if changes were made. The images or other third party material in this article are included in the article's Creative Commons licence, unless indicated otherwise in a credit line to the material. If material is not included in the article's Creative Commons licence and your intended use is not permitted by statutory regulation or exceeds the permitted use, you will need to obtain permission directly from the copyright holder. To view a copy of this licence, visit http://creativecommons.org/licenses/by/4.0/.

References

Abdel, D.: Comparison of flux discretizations for generalized drift-diffusion systems. Master's thesis, Technical University Berlin (2020)

Bessemoulin-Chatard, M.: A finite volume scheme for convection-diffusion equations with nonlinear diffusion derived from the Scharfetter–Gummel scheme. Numer. Math. **121**, 637–670 (2012)

Blakemore, J.S.: The parameters of partially degenerate semiconductors. Proc. Phys. Soc. A **65**, 460–461 (1952)

Blakemore, J.S.: Approximations for Fermi-Dirac integrals, especially the function $F_{1/2}(\eta)$ used to describe electron density in a semiconductor. Solid State Elect. **25**(11), 1067–1076 (1982)

Cancès, C., Chainais-Hillairet, C., Fuhrmann, J., Gaudeul, B.: A numerical-analysis-focused comparison of several finite volume schemes for a unipolar degenerate drift-diffusion model. IMA J. Numer. Anal. **41**(1), 271–314 (2021)

Eymard, R., Fuhrmann, J., Gärtner, K.: A finite volume scheme for nonlinear parabolic equations derived from one-dimensional local Dirichlet problems. Numer. Math. **102**, 463–495 (2006)

Farrell, P., Doan, DH., Kantner, M., Fuhrmann, J., Koprucki, T., Rotundo, N.: Drift-Diffusion Models. In: Optoelectronic Device Modeling and Simulation: Fundamentals, Materials, Nanostructures, LEDs, and Amplifiers, CRC Press Taylor & Francis Group, pp 733–771 (2017a)

Farrell, P., Koprucki, T., Fuhrmann, J.: Computational and analytical comparison of flux discretizations for the semiconductor device equations beyond Boltzmann statistics. J. Comput. Phys. **346**, 497–513 (2017b)

Farrell, P., Patriarca, M., Fuhrmann, J., Koprucki, T.: Comparison of thermodynamically consistent charge carrier flux discretizations for Fermi-Dirac and Gauss-Fermi statistics. Opt. Quant. Electron. **50**, 101 (2018)

Fuhrmann, J.: VoronoiFVM.jl - Solver for coupled nonlinear partial differential equations based on the Voronoi finite volume method. https://github.com/j-fu/VoronoiFVM.jl, https://doi.org/10.5281/zenodo.3529808(2019–2020)

Gärtner, K.: Existence of bounded discrete steady-state solutions of the van Roosbroeck system with monotone Fermi-Dirac statistic functions. J. Comput. Elect. **14**(3), 773–787 (2015)

Kantner, M.: Generalized Scharfetter–Gummel schemes for electro-thermal transport in degenerate semiconductors using the Kelvin formula for the Seebeck coefficient. J. Comput. Phys. **402**, 109091 (2020)

Koprucki, T., Gärtner, K.: Discretization scheme for drift-diffusion equations with strong diffusion enhancement. Opt. Quant. Elect. **45**, 791–796 (2013)

Patriarca, M., Farrell, P., Koprucki, T., Auf der, Maur M.: Highly accurate discretizations for non-Boltzmann charge transport in semiconductors. pp 53–54, (2018) https://doi.org/10.1109/NUSOD.2018.8570265

Scharfetter, D.L., Gummel, H.K.: Large-signal analysis of a silicon Read diode oscillator. IEEE Trans. Elect. Dev. **16**(1), 64–77 (1969)

Silvaco International: Atlas user's manual. Santa Clara, CA (2016)

Synopsys, Inc: Sentaurus device userguide. Mountain View, CA (2010)

Sze, S.M., Ng, K.K.: Physics of Semiconductor Devices. Wiley, Hoboken (2006)

Yu, Z., Dutton, R.: SEDAN III—A one-dimensional device simulator. www-tcad.stanford.edu/tcad/programs/sedan3.html (1988)

Publisher's Note Springer Nature remains neutral with regard to jurisdictional claims in published maps and institutional affiliations.

7

Modelling charge transport in perovskite solar cells: Potential-based and limiting ion vacancy depletion

D. Abdel et al. Modelling charge transport in perovskite solar cells: Potential-based and limiting ion vacancy depletion. *Electrochimica Acta* 390 (2021), p. 138696. DOI: 10.1016/j.electacta.2021.138696

Abstract From Maxwell-Stefan diffusion and general electrostatics (see Section 2.2), we derive a drift-diffusion model for charge transport in perovskite solar cells (PSCs) where any ion in the perovskite layer may flexibly be chosen to be mobile or immobile. Unlike other models in the literature, our model is based on quasi Fermi potentials instead of densities. This allows to easily include nonlinear diffusion (based on Fermi-Dirac, Gauss-Fermi or Blakemore statistics for example) as well as limit the ion depletion (via the Fermi-Dirac integral of order -1). The latter will be motivated by a grand-canonical formalism of ideal lattice gas. Furthermore, our model allows to use different statistics for different species. We discuss the thermodynamic equilibrium, electroneutrality as well as generation/recombination. Finally, we present numerical finite volume simulations to underline the importance of limiting ion depletion.

Conception: Perovskites are one of the research topics in my research group, for which I developed the research idea and led the team.

Execution: The code implementation has been carried out by Dilara Abdel, the modelling by Petr Vágner and feedback/proofreading/corrections were provided by myself.

Reporting: The text was written jointly.

Due to copyright reasons, this article cannot be included online.

8

Modeling and simulation of the lateral photovoltage scanning method

P. Farrell, S. Kayser, and N. Rotundo. Modeling and simulation of the lateral photovoltage scanning method. *Computer and Mathematics with Applications* 102 (2021), pp. 248–260. DOI: 10.1016/j.camwa.2021.10.017

Abstract The fast, cheap and nondestructive lateral photovoltage scanning (LPS) method detects inhomogeneities in semiconductors crystals, see Section 2.4. The goal of this paper is to model and simulate this technique for a given doping profile. Our model is based on the semiconductor device equations combined with a nonlinear boundary condition, modeling a volt meter. To validate our 2D and 3D finite volume simulations, we use theory developed by Tauc [94] to derive three analytical predictions which our simulation results corroborate, even for anisotropic 2D and 3D meshes. Our code runs about two orders of magnitudes faster than earlier implementations based on commercial software [5]. It also performs well for small doping concentrations which previously could not be simulated at all due to numerical instabilities. We present a convergence study which shows that the LPS voltage converges quadratically. Finally, our simulations provide experimentalists with reference laser powers for which meaningful voltages can still be measured. For higher laser power the screening effect does not allow this anymore.

Conception: Together with Nella Rotundo I designed this paper project. Whereas I focussed on all numerical aspects, Nella Rotundo focussed on the analytical aspect. The modeling was done jointly.

Execution: Stefan Kayser, our postdoc, carried out the implementation which I closely supervised.

Reporting: The paper was written by all three authors.

Due to copyright reasons, this article cannot be included online.

9

Assessing doping inhomogeneities in GaAs crystal via simulations of lateral photovoltage scanning method

S. Kayser et al. Assessing doping inhomogeneities in GaAs crystal via simulations of lateral photovoltage scanning method. *Journal of Crystal Growth* 571 (2021), p. 126248. DOI: 10.1016/j.jcrysgro.2021.126248

Abstract We performed a numerical feasibility study of the application of the lateral photovoltage scanning (LPS) method to detect doping inhomogeneities (striations) in GaAs. Those striations follow the shape of the crystallization front, enabling its visualization. The obtained results allow direct validation of simulated temperature distributions in GaAs crystals. Our simulations revealed that realistic laser powers lead to LPS signals on the order of nanovolts. The actually used LPS measurement setup detects voltages at microvolt scale. So in order to build practical setups, one needs to either use better voltage detection devices or improve the method itself.

Conception: This paper is a practical implication of [PF3] which we jointly developed.

Execution: Stefan Kayser, our postdoc, and myself carried out the implementation. In particular, at the reviewers' request I reran the simulations behind Figure 3 and developed the code for Figure 4.

Reporting: The paper was written by all four authors.

Due to copyright reasons, this article cannot be included online.

10

From atomistic tight binding theory to macroscale drift diffusion: multiscale modeling and numerical simulation of uni-polar charge transport in (In,Ga)N devices with random fluctuations

M. O'Donovan et al. From atomistic tight binding theory to macroscale drift diffusion: multiscale modeling and numerical simulation of uni-polar charge transport in (In,Ga)N devices with random fluctuations. *Journal of Applied Physics* 130.6 (2021), p. 065702. DOI: 10.1063/5.0059014

Abstract Random alloy fluctuations significantly affect the electronic, optical and transport properties of (In,Ga)N-based optoelectronic devices. Transport calculations accounting for alloy fluctuations in the band-edge energies currently use a combination of modified continuum-based models, which neglect to a large extent atomistic effects. In this work, we present a model that bridges the gap between atomistic theory and macroscopic transport models. To do so, we combine atomistic tight-binding theory and continuum-based drift-diffusion solvers, where quantum corrections are included via the localization landscape method. We outline the ingredients of this framework in detail and present first results for uni-polar electron transport in single and multi (In,Ga)N quantum well systems. Overall, our results reveal that both random alloy fluctuations and quantum corrections significantly affect the current voltage characteristics of uni-polar electron transport in such devices. However, our investigations indicate that the importance of quantum corrections and random alloy fluctuations can be different for single and multi quantum well systems.

Conception: The original idea of this project is due to Stefan Schulz and Thomas Koprucki.

Execution: Michael O'Donovan and myself are first authors for having done the most work. Whereas I mostly worked on setting up the transport calculations in `ddfermi`, Michael O'Donovan mostly focussed on the tight-binding calculations and running the final code for various setups.

Reporting: Most of the report has been written by Michael O'Donovan. I wrote the part concerning the drift-diffusion model and the appendix as well as improved other parts of the documents.

Journal of Applied Physics ARTICLE scitation.org/journal/jap

From atomistic tight-binding theory to macroscale drift–diffusion: Multiscale modeling and numerical simulation of uni-polar charge transport in (In,Ga)N devices with random fluctuations

Cite as: J. Appl. Phys. **130**, 065702 (2021); doi: 10.1063/5.0059014
Submitted: 4 June 2021 · Accepted: 23 July 2021 ·
Published Online: 10 August 2021

View Online

Export Citation

CrossMark

Michael O'Donovan,[1,2,a)] Debapriya Chaudhuri,[1] Timo Streckenbach,[3] Patricio Farrell,[3,b)] Stefan Schulz,[1] and Thomas Koprucki[3]

AFFILIATIONS

[1]Tyndall National Institute, University College Cork, Cork T12 R5CP, Ireland
[2]Department of Physics, University College Cork, Cork T12 YN60, Ireland
[3]Weierstrass Institute (WIAS), Mohrenstr. 39, 10117 Berlin, Germany

Note: This paper is part of the Special Topic on Wide Bandgap Semiconductor Materials and Devices.
[a)]**Author to whom correspondence should be addressed:** michael.odonovan@tyndall.ie
[b)]patricio.farrell@wias-berlin.de

ABSTRACT

Random alloy fluctuations significantly affect the electronic, optical, and transport properties of (In,Ga)N-based optoelectronic devices. Transport calculations accounting for alloy fluctuations currently use a combination of modified continuum-based models, which neglect to a large extent atomistic effects. In this work, we present a model that bridges the gap between atomistic theory and macroscopic transport models. To do so, we combine atomistic tight-binding theory and continuum-based drift–diffusion solvers, where quantum corrections are included via the localization landscape method. We outline the ingredients of this framework in detail and present first results for uni-polar electron transport in single and multi- (In,Ga)N quantum well systems. Overall, our results reveal that both random alloy fluctuations and quantum corrections significantly affect the current–voltage characteristics of uni-polar electron transport in such devices. However, our investigations indicate that the importance of quantum corrections and random alloy fluctuations can be different for single and multi-quantum well systems.

© 2021 Author(s). All article content, except where otherwise noted, is licensed under a Creative Commons Attribution (CC BY) license (http://creativecommons.org/licenses/by/4.0/). https://doi.org/10.1063/5.0059014

I. INTRODUCTION

III-nitride (III-N)-based quantum well (QW) structures are at the heart of modern short wavelength light emitting diodes (LEDs).[1,2] Here, (In,Ga)N/GaN multi-QWs (MQWs) are used to realize devices operating in the visible part of the spectrum. While in the blue wavelength range such III-N LEDs offer very high efficiencies, achieving the same at longer wavelengths is very challenging. Therefore, to tailor and guide the design of future energy efficient III-N LED structures operating over a wide spectral range, accurately modeling their fundamental properties is essential.

It is important to note that nitride-based heterostructures have in general very different properties to other III–V material systems, such as GaAs or AlGaAs. This starts with the underlying crystal structure: the thermodynamically stable phase for GaAs is zinc blende, while III-N systems preferentially crystallize in the wurtzite phase.[3–5] This difference in the crystal structure has far reaching consequences, resulting, for instance, in a spontaneous electric polarization vector field in wurtzite III-N systems; such a field is absent in a zinc blende structure.[6] Therefore, in a nitride-based heterostructure, any discontinuity in the polarization vector field leads to a very strong electrostatic built-in field, which then can give rise

© Author(s) 2021

to a quantum confined Stark effect (QCSE).[7,8] The QCSE is further increased by strain dependent piezoelectric polarization contributions.[9,10] As a consequence, the radiative recombination rates in III-N heterostructures are strongly reduced by the QCSE.[7,11,12]

When it comes to modeling charge carrier transport in LED structures utilizing III-N QWs, the effects of the built-in polarization field are taken into account in "standard" one-dimensional (1D) drift–diffusion (DD) simulations. However, in general, the turn-on voltages predicted by such an approach are considerably higher compared to experiments.[13–15] It has recently been shown that this shortcoming in the simulation of (In,Ga)N-based LEDs[16] or uni-polar devices[15] is related to (i) treating these systems as 1D as well as (ii) the semi-classical nature of DD models. Regarding (i), theoretical and experimental studies have revealed that the electronic and optical properties of III-N-based heterostructures are strongly affected by alloy fluctuations and accompanying carrier localization,[17,18] all of which is not fully reflected within a 1D DD transport model.[15,16,19] Furthermore, (ii) the semi-classical nature of DD models neglects quantum mechanical effects, such as tunneling. Fortunately, such quantum effects can be included, to some extent, in DD simulations via the so-called localization landscape theory (LLT)[20–22] or the (nonlocal) effective potential method to smooth band edges.[23–25]

Thus, to accurately guide the design of future III-N-based LEDs, a fully three-dimensional (3D), ideally atomistic, transport model that includes quantum mechanical effects for the *entire* device is required. While atomistic calculations have been performed to target these questions,[26,27] such a treatment is numerically extremely expensive.[16] This becomes even more challenging when device performance studies are required, where, for instance, the well width or the composition in the well and barrier regions of the device is systematically modified. Given the numerical burden of the fully atomistic and quantum mechanical solvers, the workhorse for transport calculations still remains largely DD. The challenge here is now to transfer atomistic effects accurately into a modified, quantum-corrected DD transport model. Previous work, targeting, for instance, (In,Ga)N LED or uni-polar devices, tackled such a multiscale problem in the following way:[16,28] First, a random distribution of In and Ga atoms on either a cubic or wurtzite grid is generated. Second, based on such a distribution, the local In content is determined by using averaging procedures on the underlying grid. Equipped with this information, continuum-based strain and built-in field calculations are performed, which can then be used to generate an "energy landscape" (conduction and valence band edges/confining potential), mainly in the framework of a single-band effective mass approximation (EMA). This information can either be directly used for 3D DD-based transport calculations or even coupled with LLT to account for quantum corrections. It is important to note that such an approach relies on (i) identifying an interpolation procedure for the local alloy content, (ii) the knowledge of how related material parameters change with composition locally, and (iii) assuming that bulk parameters can be used locally to obtain strain and built-in field effects. Finally, it assumes that even when including random alloy fluctuations, the modified continuum-based single-band EMA describes the electronic structure of this complicated system accurately. Thus, overall "atomistic" aspects enter mainly at the In atom distribution level. However, it is difficult to judge how well local fluctuations in strain or built-in fields are captured in comparison with a fully atomistic approach (valence force field plus local polarization theory). Furthermore, consequences of alloy fluctuations for the electronic structure of the well and again how this compares to a fully atomistic description, e.g., tight-binding, are not widely discussed or analyzed.

We have recently established a theoretical framework that allows one to target these questions,[29] which works as follows: First, we generate an energy landscape that is directly obtained from an atomistic tight-binding (TB) model, which accounts for random alloy fluctuations and connected fluctuations in strain and built-in fields on a microscopic level. Second, the electronic structure of, e.g., an (In,Ga)N QW, can be calculated within TB and a single-band EMA (using this landscape) so that the data can be directly compared since both operate on the same alloy microstructure. Here, in principle, the only free parameter in the modified EMA is the effective mass; the confining potential (band edges) is directly obtained from the TB model. Our results showed that when operating on the same alloy microstructure (alloy configuration) and the same confining energy landscape, the modified EMA significantly overestimates the bandgap/transition energy of (In,Ga)N/GaN QWs, at least for In contents larger than 5%. However, as the calculations were performed on the same alloy microstructure, it allows one to adjust the EMA. We have found that using a rigid energy shift within the QW region results in a good agreement between TB and EMA, at least in terms of transition energies and the distribution of (localized) energy states.[29]

In this work, we extend the theoretical framework above to study charge carrier transport in III-N-based devices. We give the details of the method and apply it to uni-polar transport in single QW (SQW) and MQW (In,Ga)N systems. In general, we use the energy landscape calculated from our atomistic TB model in conjunction with LLT to generate a quantum-corrected energy landscape. This landscape presents the backbone of our DD simulation. For the active (In,Ga)N QW region, we use a finite-element mesh with as many nodes as atomic lattice sites, which we later enlarge to work in combination with a specialized finite volume method. In doing so, (n-doped) contact regions can be added to the system on a much coarser grid to model a full device. We highlight that the developed approach can be extended to investigate complete (In,Ga)N-based LED structures (p–i–n systems) as well as AlGaN-based UV LEDs in future studies.

Our obtained results for uni-polar (In,Ga)N SQW and MQW structures show that when including LLT and alloy fluctuations, smaller turn-on voltages are observed in comparison with a standard virtual crystal approximation (VCA) calculation; this agrees with previous studies.[15,16] Furthermore, and as discussed already above, "standard" 1D uni-polar electron transport calculations, which effectively correspond to our VCA results, give too large turn-on voltages when compared to experiment. The fact that our full 3D model gives smaller turn-on voltages compared to VCA suggests already an improved description of experimental findings and highlights again the importance of quantum corrections and alloy fluctuations for an accurate description carrier transport in (In,Ga)N-based devices. We stress that our results are achieved without any re-fitting/adjusting of, e.g., piezoelectric coefficients,

© Author(s) 2021

which is often applied in "conventional" 1D DD calculations found in the literature.[30,31]

The remainder of the paper is organized as follows: We present the theoretical ingredients of our multiscale model, namely, TB, LLT, and DD, as well as the mesh generation (additional information is supplied in an Appendix) in Sec. II. Our results for uni-polar transport in (In,Ga)N-based SQW and MQW systems are detailed in Sec. III. Finally, we summarize our framework and the results in Sec. IV.

II. THEORETICAL FRAMEWORK: FROM AN ATOMISTIC ENERGY LANDSCAPE TO DRIFT–DIFFUSION SIMULATIONS

We present and discuss the different ingredients of our multi-scale framework in this section. We start in Sec. II A with the TB model and briefly describe the procedure to generate an energy landscape that contains the contributions from random alloy fluctuations and thus associated strain and built-in field fluctuations. Section II B details how the obtained landscape is transferred to a finite-element method (FEM) mesh, which presents the starting point for our charge carrier transport calculations. Utilizing this mesh, Sec. II B gives details on (i) how the random alloy fluctuations are treated for later transport calculations and (ii) how the LLT equation is solved on the underlying FEM mesh. The uni-polar transport model based on the derived energy landscape, which we employ for our numerical studies, is introduced in Sec. II D; here, we also describe how the spatially varying band edges are handled numerically.

A. Tight-binding model and local band-edge calculations

In order to capture the effects of (random) alloy fluctuations on the conduction (CBE) and valence band edges (VBE) and ultimately on the electronic structure of the QW active region of a III-N device, we employ atomistic TB theory. In the following, we give a brief overview of the underlying model and how to extract local band edges from a TB model; more details can be found in Refs. 17, 29, and 32. While this approach is general, we discuss in the following an (In,Ga)N/GaN QW system as an example.

The backbone of our theoretical framework is an empirical nearest neighbor sp^3 TB model.[32] The TB parameters were determined by fitting GaN and InN bulk TB band structures to the corresponding hybrid functional density functional theory (DFT) band structures.[32] Given the (large) lattice mismatch between InN and GaN (≈10%), strain effects have to be taken into account in (In,Ga)N/GaN QWs. To obtain an atomistic resolution of the strain in such a structure, the equilibrium positions of all the atoms in the simulation supercell are obtained using a valence force field (VFF) model,[17,32] which has been implemented in the software package LAMMPS.[33] As already discussed above, III-N heterostructures in general exhibit built-in (spontaneous and piezoelectric) polarization vector fields. To account for (local) polarization effects in (In,Ga)N/GaN QWs, a local polarization theory[32] is employed. The TB model summarized in this paragraph has been extensively benchmarked against DFT as well as experimental data.[32,34]

As highlighted above, a key ingredient for DD transport calculations is the (local) CBE and VBE. This information can now be extracted from our TB model by diagonalizing the Hamiltonian at each lattice site.[29] Our previous work[29] already revealed that when using this atomistically generated landscape directly in conjunction with an effective mass model, electron as well as hole ground state energies, and thus the connected transition energies, are significantly underestimated, at least for systems with In contents larger than 5%. However, the broadening of the energy spectrum due to alloy fluctuations was in good agreement between the models, even though carrier localization effects may not be treated accurately in the EMA. The overall agreement between TB and EMA can be improved in terms of transition energies, energy spectrum broadening, and to some extent carrier localization characteristics by applying a (composition dependent) rigid shift to the band edges in the QW region. We apply this approach here too. In doing so, we find indeed good agreement between TB and results obtained within LLT when operating on the confining potential landscape extracted from TB.

B. Device mesh generation for transport calculations

The obtained local band edges on the atomistic wurtzite lattice sites need to be transferred to a mesh that allows us to perform the transport calculations. Two aspects are important here. First, the mesh needs to be fine enough to capture alloy fluctuations in the active region. Second, in regions where no alloy fluctuations are present, the band-edge energies can be obtained from the literature (e.g., n-doped GaN contacts). In this contact region, the mesh can also be chosen much coarser when compared to the atomistic region; this helps to keep the computational cost low. The latter part is very important to make self-consistent 3D DD simulations feasible. A schematic illustration of our approach to address this challenge is shown in Fig. 1. We start from an atomistic TB energy landscape as discussed above and ultimately construct a larger mesh for the DD simulations.

Next, we discuss the post-processing within the atomistic region before we explain the embedding into the larger mesh. Using the atom lattice sites as nodes, we construct a FEM mesh via TetGen.[35,36] The TB energy landscape determines the energy values at the nodes. We stress again that the underlying TB mesh with In, Ga, and N atoms is not used to generate a composition profile/map on which local averages for continuum-based calculations are determined; we use TB directly to define the energy landscape. Figure 2(a) depicts the TB model data for a 3.1 nm thick $In_{0.1}Ga_{0.9}N$ SQW in the x–z-plane, where the z-axis is parallel to the wurtzite c-axis. The depicted test structure has 38 150 atoms and the corresponding FEM mesh has 38 150 nodes, and 280 816 tetrahedra [see Fig. 2(b)]; this mesh represents the atomistic region discussed above. We have employed this transfer of TB data to an atomistic FEM mesh previously[29] to compare the electronic structure of (In,Ga)N/GaN QWs when using atomistic and continuum methods.

In order to perform full-device calculations, contact regions (e.g., n-doped GaN contacts) have to be attached to the atomistic region of the simulation. In the context of DD simulations for semiconductor devices, the finite-volume method (FVM) has been exceptionally successful. Our specific approach described in detail in the Appendix requires a mesh that ensures that the numerical

© Author(s) 2021

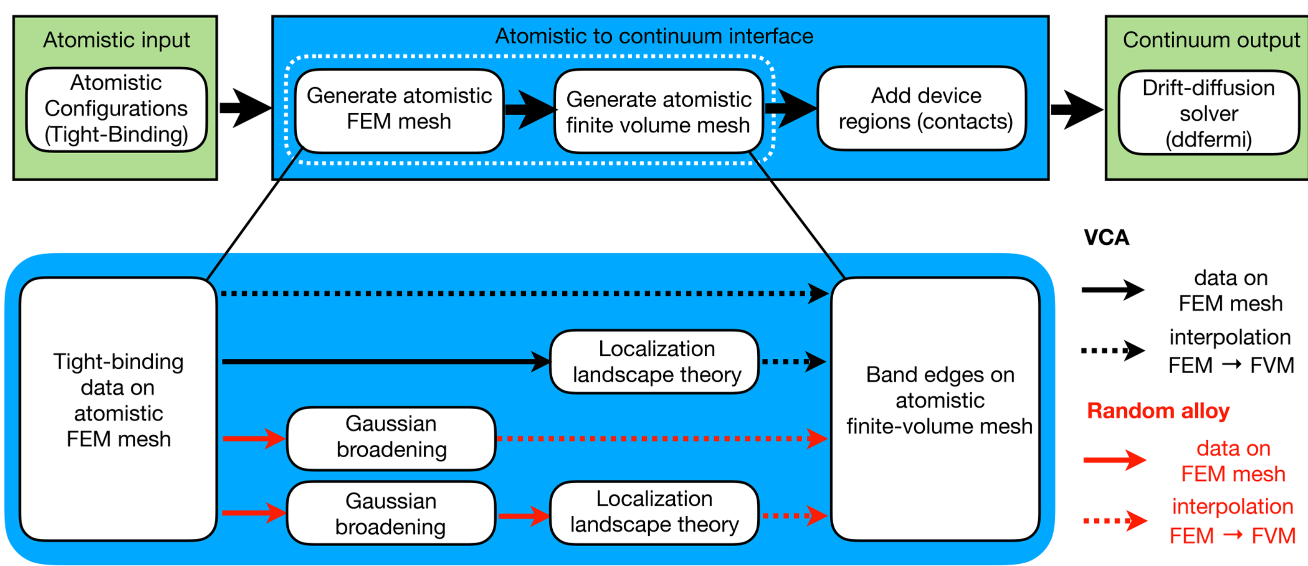

FIG. 1. Schematic workflow to connect an atomistic tight-binding model to a continuum-based drift–diffusion solver (here ddfermi). The connection between the atomistic and continuum-based grid is achieved in three steps. First, we generate an atomistic finite-element method (FEM) mesh with as many nodes as atomic sites. The data on the FEM mesh are then interpolated on a Voronoi finite-volume method (FVM) mesh needed for stable drift–diffusion simulations. Finally, the FVM mesh is enlarged by adding coarser contact and intrinsic regions. The inset details four different ways atomistic band-edge data are transferred to the FVM mesh. Whereas the data paths indicated in black refer to the VCA type of data, the data paths in red refer to random alloy data. Solid arrows indicate an operation (stated in the box) on the FEM mesh, and dashed arrows indicate interpolation to the FVM mesh. The meshes are shown visually in Fig. 2.

fluxes are perpendicular to the cell interfaces. Such a mesh is dual to a boundary conforming a Delaunay tetrahedral mesh. Therefore, the next step is the generation of such a finite-volume mesh from the atomistic FEM mesh, which satisfies this additional requirement. Again via TetGen, we produce a so-called boundary-conforming Delaunay tetrahedral mesh (for details, see the Appendix), which includes the original FEM lattice sites and interpolate the atomistic data onto it; see Figs. 2(b) and 2(c). The FVM mesh has 47 248 nodes and 305 272 tetrahedra. Finally, we attach coarser intrinsic meshes as well as *n*-doped GaN contact regions to both sides of the atomistic region, again using TetGen. Thus, a complete *n*–*i*–*n* diode has been created, see Fig. 2(d), which contains the atomistic region (box with yellow-dashed lines), the coarse grained intrinsic GaN (light blue and green), and *n*-doped GaN (red and purple) regions. While as a test system we have used here an *n*–*i*–*n* structure, the approach can now be easily adapted for a *p*–*i*–*n* setup or other material systems. The resulting boundary-conforming finite-volume mesh of the complete *n*–*i*–*n* structure has in total 61 202 nodes and 369 430 tetrahedra and can be used for DD simulations with ddfermi.[37] The tool chain for creating the combined meshes and transferring TB data has been implemented with WIAS-pdelib[38] and TetGen.[35,36]

C. Localization landscape theory and random alloy fluctuations on a FEM mesh

Having transferred the TB band-edge data to a larger mesh with contact regions as described above, care must be taken when performing DD simulations on this mesh. It has already been discussed in the literature that for transport properties, the spatial length scale of the potential fluctuations is effectively determined by the de Broglie wavelength.[16] Consequently, charge carrier wave functions sample a wider "area" of the confining energy landscape rather than just a single lattice site. While in VCA this may be of secondary importance, in a strongly fluctuating energy landscape, it is important to account for this. The question has been discussed in detail in Ref. 16, and the authors applied a Gaussian averaging procedure to determine the local alloy content. The same *ad hoc* procedure has been employed by DiVito *et al.*[28] While we follow a similar approach here and employ Gaussian averaging, we employ this to the original *band-edge profile* E_c^{TB} from TB

$$E_c^{\sigma}(\mathbf{x}_i) = \frac{\sum_j E_c^{\mathrm{TB}}(\mathbf{x}_j)\exp\left(-\frac{(|\mathbf{x}_i-\mathbf{x}_j|)^2}{2\sigma^2}\right)}{\sum_j \exp\left(-\frac{(|\mathbf{x}_i-\mathbf{x}_j|)^2}{2\sigma^2}\right)} \quad (1)$$

but *not* to the alloy content. Here, $E_c^{\sigma}(\mathbf{x}_i)$ is the CBE energy at the (lattice) site $\mathbf{x}_i$; σ denotes the Gaussian width and acts as a smoothing parameter. This averaging procedure is of course only relevant within the QW(s) and near the well–barrier interface. This scheme has been implemented for the FEM mesh. Nodal values will be interpolated to a finer boundary conforming the FVM mesh, following the approach described in Sec. II B. Given that we will focus our attention on uni-polar transport, this procedure will be applied to the CBE but can in future studies also be applied to the VBE.

© Author(s) 2021

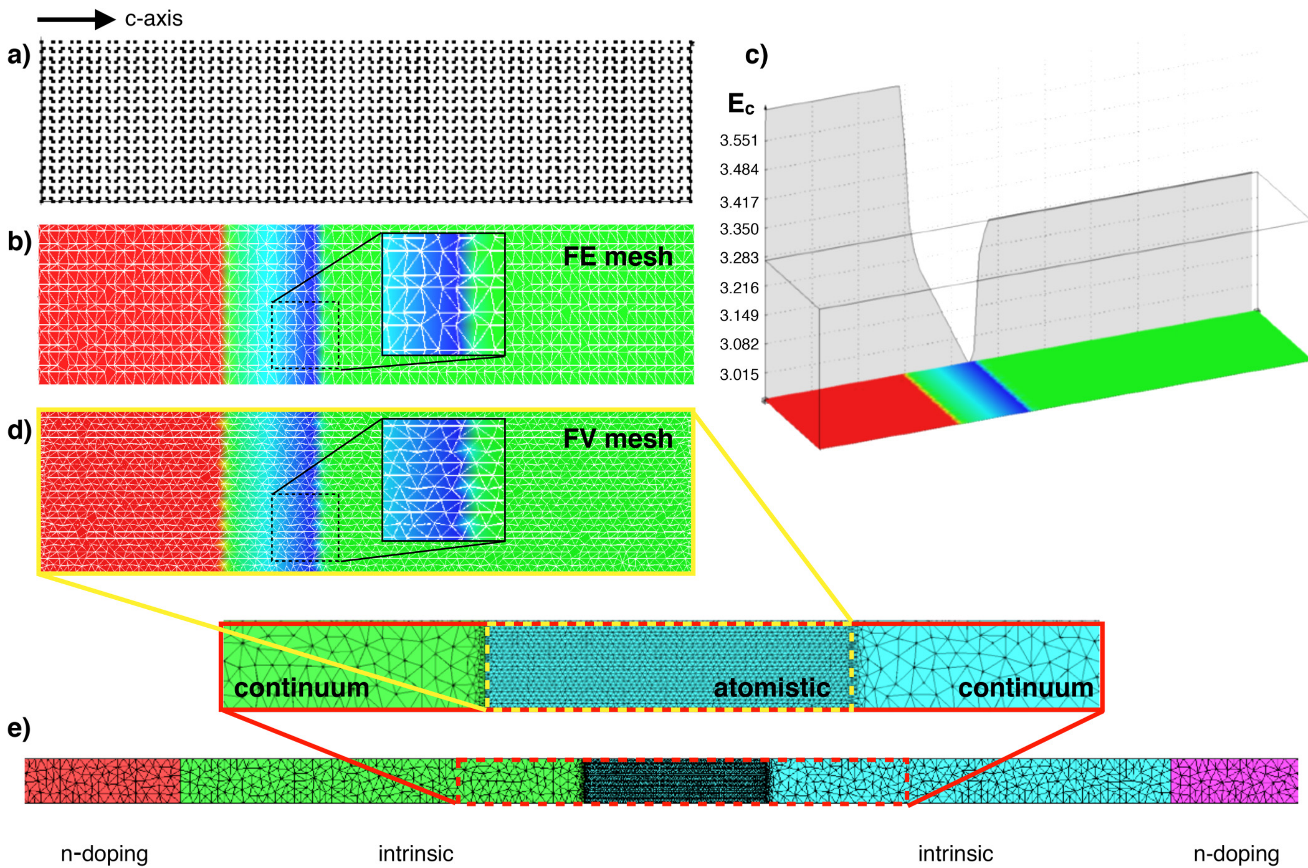

FIG. 2. Transfer of atomistic data to a larger finite-volume mesh for continuum-based drift–diffusion simulations. We start with a point set (a) defined by the atomistic lattice sites as provided by tight-binding. Using TetGen, a tetrahedral finite-element mesh (b) is generated, which has exactly the same number of nodes as there are atoms in (a). In doing so, the tight-binding input is exactly represented on the nodes of the atomistic finite-element method mesh. The colors in (b) represent the values of the conduction band edge E_c, and (c) depicts the E_c profile of an $In_{0.1}Ga_{0.9}N$ single quantum well in virtual crystal approximation. The data from the atomistic finite-element method mesh are then interpolated to a finite-volume mesh (d), namely, a boundary-conforming Delaunay triangulation generated by TetGen.[35,36] After attaching intrinsic device regions and doped contact regions to the atomistic region, the full 3D device mesh (e) for drift–diffusion simulations is established.

We stress again that in Refs. 16 and 28 the In content at each point is computed from a Gaussian average, and then the strain, built-in field, and ultimately the CBE are evaluated in a pure continuum framework. We go beyond this by calculating the CBE (the confining potential) at each (lattice) site from the atomistic TB approach, with no need to calculate local strain or built-in potentials in a continuum-based framework before applying a Gaussian function to the confining potential. Thus, in comparison with Refs. 16 and 28, we have here *a posteriori* broadening and transfer the atomistic effects on the band offset, strain, and built-in field due to alloy fluctuations directly into the confining energy landscape before averaging.

In general, employing such a Gaussian averaging procedure comes at the cost of having to correctly determine the width, σ, *a priori*. To analyze the impact of the σ on the CBE profile, which ultimately will also impact the transport, Fig. 3 shows the profile of $E_c^{\sigma} - q\psi$ in a 3.1 nm wide $In_{0.1}GaN_{0.9}/GaN$ SQW, comparing random alloy fluctuations with different Gaussian widths σ to a VCA. Here, ψ denotes the electrostatic potential in the n–i–n device, including also piezoelectric and spontaneous polarization effects; q denotes the elementary charge. At each plane along the c-direction, the full range of CBE values over the x–y plane is shown, which allows clear visualization of the impact of the alloy fluctuations on the CBE. Several features are important. The most striking difference between the VCA and the smoothed random alloy (RA) CBE is that the potential barrier between the GaN and (In,Ga)N QW material is significantly reduced. This feature is expected to reduce the turn-on voltage of the device and will be discussed in detail further below. Moreover, the barrier–well interface reduces further with increasing σ. However, the reduction between $\sigma = 0.6$ nm and $\sigma = 0.9$ nm is smaller than the reduction from $\sigma = 0.3$ nm to $\sigma = 0.6$ nm, even though the difference in σ values is

© Author(s) 2021

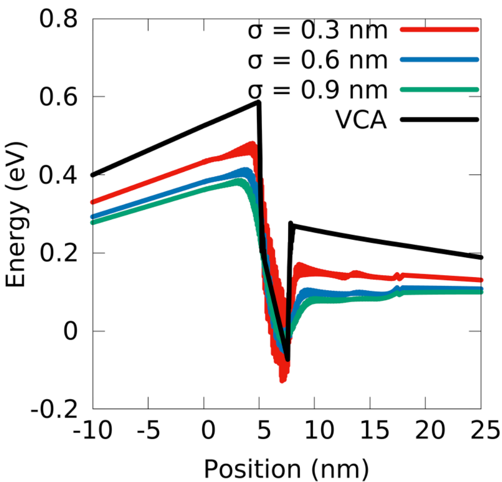

FIG. 3. Randomly fluctuating, smoothed conduction band-edge profile along the *z*- (*c*)-axis of an *n*–*i*–*n* $In_{0.1}Ga_{0.9}N$/GaN single quantum system at zero bias (more details given in the main text). The results are displayed in the *absence* of quantum corrections via LLT but for three different Gaussian widths σ, namely, $\sigma = 0.3$ nm (red), $\sigma = 0.6$ nm (blue), and $\sigma = 0.9$ nm (green), as well as for a "standard" virtual crystal approximation (VCA, black).

the same ($\Delta\sigma = 0.3$ nm). We also note that while the average band-edge energy in the well is basically unaffected by different σ values, the CBE fluctuations in the well noticeably reduce. Consequences of these effects on the current–voltage characteristics are discussed below.

Having determined the local band edges from atomistic TB theory, we can now also include quantum corrections using LLT.[21] These corrections are not limited to a calculation that accounts for random alloy fluctuations; LLT can also be used in conjunction with a VCA description. We note that many commercial software packages targeting carrier transport properties of III-N devices also have the option to include quantum mechanical effects by solving Schrödinger's equation in the active region (QW region) of a device. However, such an approach is numerically very demanding even for a 1D simulation, not to mention a full 3D calculation, which is necessary in the presence of random fluctuations. When using LLT, one avoids having to solve the Schrödinger equation and thus a large eigenvalue problem. In LLT, one is left with a linear partial differential equation, given by[21]

$$\hat{H}^{\mathrm{EMA}}u := -\frac{\hbar^2}{2m^*}\Delta u + Vu = 1. \tag{2}$$

Here, $\hat{H}^{\mathrm{EMA}}$ denotes a single-band effective mass Hamiltonian, m^* the effective (electron or hole) mass, and V the confining potential energy. For the confining potential, V, we use our TB band-edge data. Here, VCA data, $V = E_c^{\mathrm{VCA}}$, or random alloy data, $V = E_c^{\sigma}$, for different σ values can be used. As described in detail in Refs. 16 and 21, once u is determined by solving Eq. (2) with appropriate boundary conditions, one can also extract an effective confining potential W via

$$W(\mathbf{x}_i) = 1/u(\mathbf{x}_i). \tag{3}$$

This effective potential for the energy landscape can be used in DD simulations to include both random alloy fluctuations and quantum corrections at the macroscopic DD scale.[16] More details on LLT are found in Refs. 16, 21, and 22.

Regarding the computational aspects, we numerically solve the LLT equation, Eq. (2), supplied with appropriate Dirichlet and Neumann boundary conditions on the atomistic FEM mesh via a standard FEM.[39] The Dirichlet conditions are applied on the left and right boundaries of the atomistic FEM mesh shown in Fig. 2(b) and are implemented via a penalty technique.[40] The FEM discretization is implemented in WIAS-pdelib,[38] using PARDISO as a linear solver.[41]

Since LLT basically replaces the Schrödinger equation, LLT provides also information about the energy spectrum and the wave functions.[42] Thus, the outcome of the LLT calculations can be directly compared to our TB data. For the SQW structures analyzed in Sec. III, we find very good agreement between TB and LLT when applying a rigid band-edge shift of 129 meV and in line with Ref. 29. All of these provides a feedback loop between our atomistic model, the obtained landscape, and the resulting electronic structure. This benchmarking gives further confidence that the here established simulation framework for performing transport calculations captures alloy fluctuations accurately in SQWs.

Examples for the resulting effective energy landscapes/confining potential energies $W - q\psi$ are given in Fig. 4. We observe that similar to the random alloy case *without* quantum corrections, cf.

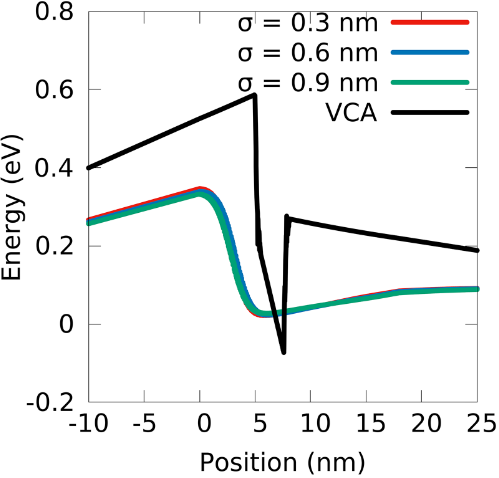

FIG. 4. Randomly fluctuating, smoothed conduction band-edge profile along the *z*- (*c*)-axis of an *n*–*i*–*n* $In_{0.1}Ga_{0.9}N$/GaN single quantum well system at zero bias (more details given in the main text). The results are displayed in the *presence* of quantum corrections via LLT but for three different Gaussian widths σ, namely, $\sigma = 0.3$ nm (red), $\sigma = 0.6$ nm (blue), and $\sigma = 0.9$ nm (green), as well as a "standard" virtual crystal approximation (VCA, black).

© Author(s) 2021

Fig. 3, the LLT treatment leads also to a reduction in the potential barrier between the GaN material and (In,Ga)N QW. Therefore, the strongly fluctuating TB landscape is "softened," given that the carrier wave functions sample a wider "area" on this landscape, as one may expect from a quantum mechanical wave function analysis. However, two additional aspects are important to note. As already highlighted above, LLT can not only be combined with the random alloy system, but can also be employed in a VCA type calculation. Thus, from a VCA plus LLT description, it is also expected that the potential barrier between the GaN and the (In,Ga)N QW material is reduced. Therefore, including quantum corrections in VCA should also affect the turn-on voltage of a device when compared to a "standard" VCA calculation without quantum corrections. Second, as one can infer from Fig. 4, once LLT has been applied, increasing the Gaussian width σ for the CBE softening in the random alloy case has very little impact on the resulting band-edge profile. Below, we will analyze this aspect in greater detail when looking at the I–V curves of (In,Ga)N/GaN-based uni-polar devices.

D. Uni-polar drift–diffusion model with spatially varying band edges

In Secs. II A–II C, we have discussed the mesh generation and also how random alloy fluctuations and quantum corrections in the confining potential are treated. In this section, we focus our attention on the semi-classical van Roosbroeck system, which models DD charge transport in semiconductors.[43] As discussed above, we simulate here uni-polar DD transport in (In,Ga)N-based systems. However, the framework is general and can be directly transferred to the bipolar case.

For a bounded spatial domain $\Omega \subset \mathbb{R}^d$ where $d \in \{1, 2, 3\}$, the stationary van Roosbroeck system[44] consists of two coupled nonlinear partial differential equations of the form

$$-\nabla \cdot (\varepsilon_s(\mathbf{x})\nabla\psi(\mathbf{x})) = q(C(x) - n(x)), \tag{4a}$$

$$\nabla \cdot \mathbf{j}_n = 0 \tag{4b}$$

for $\mathbf{x} \in \Omega$. The Poisson equation, Eq. (4a), describes the electric field $\mathbf{E} = -\nabla\psi$ that is generated by a scalar electric potential $\psi(\mathbf{x})$ in the presence of a free charge carrier density. Here, $\varepsilon_s(\mathbf{x}) = \varepsilon_0\varepsilon_r(\mathbf{x})$ describes the position dependent dielectric constant and q is the elementary charge. In a (doped) uni-polar semiconductor device, the charge density is given by the density of free (negatively charged) conduction band electrons, $n(\mathbf{x})$, and the density of ionized built-in dopants, $C(\mathbf{x}) = N_D^+(\mathbf{x})$, where N_D^+ denotes the density of singly ionized donor atoms. The current density $\mathbf{j}_n(\mathbf{x})$ is given by the usual expression[43]

$$\mathbf{j}_n(\mathbf{x}) = -q\mu_n n(\mathbf{x})\nabla\varphi_n(\mathbf{x}). \tag{5}$$

That is, the negative gradient of the quasi Fermi potential, $\varphi_n(\mathbf{x})$, is the driving force of the current; $\mu_n(\mathbf{x})$ denotes the free carrier mobility.

Using the Boltzmann approximation, the densities of free carriers, $n(\mathbf{x})$, in a solid are given by

$$n(\mathbf{x}) = N_c \exp\left(\frac{q(\psi(\mathbf{x}) - \varphi_n(\mathbf{x})) - E_c^{dd}(\mathbf{x})}{k_B T}\right), \tag{6}$$

where k_B is the Boltzmann constant, T denotes the temperature, $E_c^{dd}(\mathbf{x})$ is the (position dependent) band-edge energy used in the transport calculations, and N_c is the effective density of states,

$$N_c = 2\left(\frac{2\pi m_e^* k_B T}{\hbar^2}\right)^{3/2}.$$

We note that we have different options for setting the band-edge energy E_c^{dd} in the DD simulations. One may choose (smoothed) TB data $E_c^{dd} = E_c^{\sigma}$, VCA results $E_c^{dd} = E_c^{\mathrm{VCA}}$, or the outcome of LLT calculations $E_c^{dd} = W$. A schematic illustration of the different options is given in the inset of Fig. 1. Equation (6) indicates that the electric potential, ψ, leads to a bending of the energy landscape, $E_c - q\psi$, and thus results in a nonlinear, self-consistent coupling to the carrier densities. In the following, we assume a globally constant temperature for carriers and the crystal lattice of $T = 300$ K.

We note that, for instance, due to random alloy fluctuations, the CBE E_c varies spatially. Thus, the electron flux, Eq. (5), needs to be correctly discretized. To this end, we extend the well-known local Scharfetter–Gummel flux approximation[47] to variable band edges, here shown for the CBE E_c. Since by construction of the FVM mesh (more details in the Appendix), the cell edges are orthogonal to the fluxes, and we may consider only 1D fluxes,

$$j_n = -z_n q\mu_n U_T N_c \frac{1}{h}\left\{B\left(-z\frac{\delta\psi - \delta E_c/q}{U_T}\right)\exp(\eta_{n,L}) - B\left(z\frac{\delta\psi - \delta E_c/q}{U_T}\right)\exp(\eta_{n,K})\right\}. \tag{7}$$

The parameter $z_n = -1$ is the charge number for electrons, $B(x) = x/(\exp(x) - 1)$ denotes the Bernoulli function, $U_T = \frac{k_B T}{q}$ the thermal voltage, $\delta\psi = \psi_L - \psi_K$, $\delta E_c = E_{c,L} - E_{c,K}$, and

$$\eta_{n,P} = z_n \frac{E_{c,P} - q(\psi_P - \varphi_{n,P})}{k_B T}, \quad P \in \{K, L\}.$$

The subindices K and L refer to the nodes $\mathbf{x}_K$ and $\mathbf{x}_L$ associated with the corresponding cells. Further details of the numerical implementation of the above expressions, especially how to embed all this into a finite-volume framework, are given in the Appendix. The physical parameters used in the DD simulations are listed in Table I.

III. RESULTS

In this section, we apply the developed framework to uni-polar, n-doped/intrinsic/n-doped (n-i-n), (In,Ga)N/GaN-based devices: We analyze the impact of random alloy fluctuations and quantum corrections introduced by LLT on the I–V curves of such

© Author(s) 2021

TABLE I. Material parameters used in drift–diffusion simulations. Unless otherwise stated, all parameters are taken from Ref. 16.

Physical quantity	Value	Units
m_e^* GaN	0.2	m_0
m_e^* InN	0.07	m_0
μ_n *n*-GaN	200	$cm^2/(V\ s)$
μ_n *i*-GaN	440[45]	$cm^2/(V\ s)$
μ_n *i*-(In,Ga)N	300	$cm^2/(V\ s)$
ε_r^{GaN}	9.7[46]	ε_0
ε_r^{InN}	15.3[46]	ε_0

structures. The results are compared with the data obtained from a VCA description of the same structures. Special attention is paid to the impact of the Gaussian broadening width, σ, on the results. This analysis is carried out for both SQW systems, Sec. III A, as well as for MQW structures consisting of three wells, Sec III B. For all these calculations, the well width is 3.1 nm, the In content in the well is 10%, and the barrier material is GaN. In the MQW system, the width of the barrier between the wells is 8.0 nm. Figure 5 gives a schematic illustration of the system. Except for the VCA systems, all calculations make a random alloy assumption for the InGaN alloy forming the QW; any additional penetration of In atoms into the GaN barrier is not considered. The assumption of such an abrupt interface between InGaN and GaN is consistent with the experimental data in Ref. 18, at least for growth of InGaN on GaN. When capping an InGaN QW with GaN, penetration of In atoms into the GaN barrier may occur. However, recent experimental studies show that by a careful choice of the growth conditions, this effect can be reduced.[48] Given that we are interested in establishing a general simulation framework, these In atom "bleeding" effects are of secondary importance for the present study but can be incorporated in future investigations.

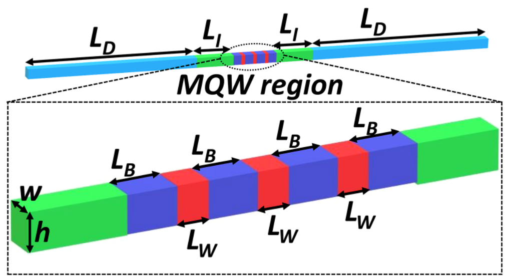

FIG. 5. Schematic illustration of the simulation cell with three quantum wells (QWs) in the active region. The *n*-doped regions (light blue) have a doping density of $n = 5 \times 10^{18}\ cm^{-3}$ and a length of $L_D = 160$ nm. The intrinsic regions on the coarse mesh (green) have a length of $L_I = 40$ nm. The atomistic region, also assumed as intrinsic, contains regions of a GaN barrier material (dark blue) with a length of $L_B = 8.0$ nm and $In_{0.1}Ga_{0.9}N$ QWs (red) with a length of $L_W = 3.1$ nm. The simulation cell has an in-plane dimension of $w \times h = 5.1 \times 4.4\ nm^2$ along the entire system.

A. (In,Ga)N SQW system

In the first step and before looking at a full current–voltage (I–V) curve of the $In_{0.1}Ga_{0.9}N$ SQW system, we focus our attention on the impact of random alloy fluctuations on the results. More specifically, we will study the impact of the Gaussian width σ and thus the related smoothing of the energy landscape on the current. Figure 6 displays the current in the system at a fixed bias of 3V for different σ values. The data are shown when including and when neglecting quantum corrections arising from LLT. The calculations have been performed for five different random alloy configurations in the QW, allowing us to also study the influence of the alloy microstructure on the current; the error bars indicate the standard deviation. One can infer from Fig. 6 that when neglecting LLT effects, the resulting current (strongly) depends on the width of the Gaussian function, at least for $\sigma < 0.6$ nm ($\approx 2a$, where a is the in-plane lattice constant of GaN). Above this threshold, the dependence of the current I on σ is less pronounced. We will discuss the impact of σ on the full I–V curve further below, but noting here that σ may impact the results. In the literature, the value of σ has, for instance, been estimated using atom probe tomography data, and a value of $\sigma_{APT} = 0.6$ nm has been assumed.[16] Turning now to the calculations including quantum corrections via LLT, Fig. 6 reveals that once these effects are taken into account, σ is of secondary importance for the obtained current I at the fixed bias of 3V; this is at least the case for a SQW. We note, however, that this aspect may depend on the in-plane dimensions of the simulation cell and thus needs to be carefully investigated when performing calculations that include random alloy fluctuations in general. This observation agrees with our earlier conclusion that Gaussian smoothing does not affect the band-edge profile, see Fig. 4, when including LLT effects in the calculations.

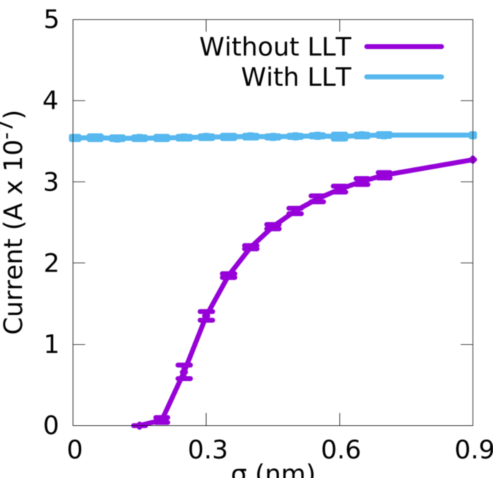

FIG. 6. Current I at a bias of 3V as a function of the Gaussian width, σ, without LLT (purple) and with LLT (blue) corrections for an *n*–*i*–*n* system with a 3.1 nm wide $In_{0.1}Ga_{0.9}N$ single quantum well. The results are averaged over five different microscopic alloy configurations, and errors bars are given by standard deviation.

© Author(s) 2021

Having gained initial insight into the impact of the Gaussian width σ on the current I at a fixed voltage V, in the second step, we focus our attention now on the full I–V curve of the SQW system. Figure 7 depicts the obtained results within the different approaches. Our reference point is again a “standard” VCA (black solid line) model, which neglects both alloy fluctuations and LLT effects. In addition, we present also the data of a combined VCA and LLT treatment. Finally, Fig. 7 displays results for the random alloy case for different σ values (red lines: $\sigma = 0.3$ nm; blue lines: $\sigma = 0.6$ nm) with and without LLT effects included in the calculations. Turning to the result in the absence of LLT first, it becomes clear that when accounting for random alloy fluctuations in the model, the turn on voltage is shifted to lower values in comparison with a standard VCA description. This is also consistent with previous literature results on uni-polar transport calculations of (In,Ga)N/GaN-based QW systems.[15] However, our calculations also reveal, and in line with Fig. 6, that the obtained current at a given voltage V depends on the Gaussian width σ. As already indicated above, when neglecting quantum corrections via LLT, a further analysis is required to determine σ: if σ is too small, the resulting very strong fluctuations in the energy landscape within the well are beyond the applicability of a continuum-based DD model; if σ is too large, the fluctuations in the energy landscape are completely removed as discussed in Sec. II C. Therefore, when neglecting LLT effects, care must be taken when choosing σ.

In the second step, we turn and discuss the I–V curves when *including* effects arising from LLT (dashed lines in Fig. 7, both in the random alloy case but also in the VCA simulations). Looking at the calculations including random alloy fluctuations and LLT first, we observe that the Gaussian width σ is of secondary importance; this is again consistent with our findings in Figs. 4 and 6. We note also that when choosing a relatively large value of σ (e.g., 0.6 nm), the random alloy I–V curves with and without LLT (blue) do not differ significantly. We attribute this to the effect that both LLT and a relatively large Gaussian broadening soften the well–barrier interface and thus reduce the resistivity of the system. Furthermore, the fluctuations in the energy landscape within the QW are reduced, leading to a further decrease in the resistance of the QW region. We note that in the presented test system, the in-plane dimensions of the simulation cell are relatively small, and further test on the impact of σ on the I–V curve may be required in future studies. However, this is beyond the scope of the present work, which introduces the general framework. Nevertheless, our results show that the calculations including random alloy fluctuations and LLT effects give the lowest turn-on voltage and highest current compared to all other models discussed here. However, and interestingly, we find also that the VCA plus LLT calculations give almost the same I–V curve as the quantum-corrected random alloy simulations. This indicates that for a SQW, once LLT is included in the model, the VCA can provide a very good approximation of the I–V characteristics of the uni-polar *n–i–n* system in comparison with a full 3D random alloy model. Furthermore, since the (3D) VCA neglects any in-plane variation in the system, already, a 1D VCA simulation seems to lead to reliable results—as long as LLT is included. Having only to rely on a 1D simulation would obviously reduce the computational cost immensely compared to a full 3D calculation including alloy fluctuations. However, and as we will show in Sec. III B, for a MQW system, a 1D VCA plus LLT calculation is no longer sufficient.

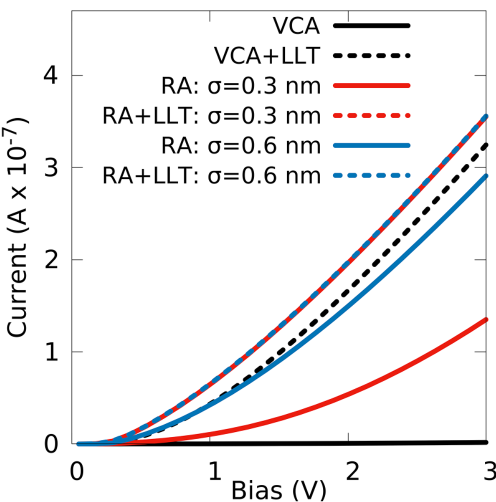

FIG. 7. Current–voltage curves for an *n–i–n* $In_{0.1}Ga_{0.9}N$ single quantum well system, within virtual crystal approximation (VCA, black) and a random alloy (RA) with Gaussian widths of $\sigma = 0.3$ nm (red) and $\sigma = 0.6$ nm (blue). Solid lines show results without quantum corrections, and dashed lines denote results with quantum corrections included via localization landscape theory.

B. (In,Ga)N MQW system

Having discussed a SQW system in Sec. III A, we focus our attention now on a MQW system. Figure 8 shows the I–V curves for a MQW system consisting of three $In_{0.1}Ga_{0.9}N/GaN$ QWs with a barrier width of $L_B = 8.0$ nm. Here, we followed the approach of the SQW, and calculations have been performed using either a VCA treatment or account for random alloy fluctuations in the system. Again, the simulations are carried out both with and without quantum corrections via LLT.

As in the SQW case, VCA calculations neglecting LLT effects show the highest turn-on voltage and lowest current when compared with all other data. When combining VCA and LLT, we find similar to the SQW case that the turn-on voltage is reduced and the current density is increased. However, and this is in *strong contrast* to the SQW data, cf. Fig. 7, in the MQW system, the results from VCA plus LLT deviate noticeably from the outcome of calculations that accounted for both random alloy fluctuations and LLT; cf. Fig. 8. We also note that VCA plus LLT simulations show significant deviations (lower currents, higher turn-on voltages) from random alloy calculations that neglect LLT effects. Overall, we attribute the aspect that random alloy fluctuations seem to become more important in the MQW system to inherent features of LLT. As discussed, for instance, in detail in Refs. 21 and 22, to predict the ground state energy of a QW uainf LLT, the so-called reference energy, E_{ref}, has to be chosen appropriately. However, the choice of E_{ref} not only affects the prediction of the ground state energy of the

© Author(s) 2021

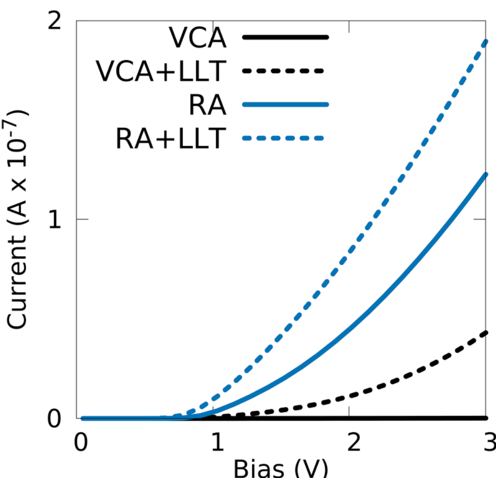

FIG. 8. Current–voltage curves for a three $In_{0.1}Ga_{0.9}N$ quantum well system, within virtual crystal approximation (VCA, black) and when random alloy (RA) fluctuations (Gaussian width of $\sigma = 0.6$ nm) are included in the model (blue). Solid lines indicate results without quantum corrections, and dashed lines show results with quantum corrections included via localization landscape theory.

system, but also affects the effective potential W, Eq. (2), which is used in the DD transport calculations. If the QWs in a MQW system in a DD simulation are energetically aligned, e.g., CBEs of all wells forming the MQW have approximately the same energy for an applied bias, and E_{ref} can be chosen as the bottom of the CBE. However, if there is a large difference in the CBEs of the different wells in the system, LLT may give a poorer approximation of W for the well where the CBE is energetically furthest away from the reference energy E_{ref}. When applying a bias V in an n–i–n system, this situation is often found. As a result, the softening of the well–barrier interface along with an effective decrease of the QW depth (confinement energy) may be different for the different QWs in the MQW system. Obviously, for a SQW system, this issue never arises. However, two important general aspects are to note. First, the LLT treatment of MQWs may be further improved by partitioning the MQW system into different sub-regions in which LLT is then solved separately. This means that one could calculate LLT in each region with its own reference energy and "stitch" the resulting effective potentials together. Such an advanced treatment is beyond the scope of the present work, where we are establishing a general first framework; further refinements can be made in future studies. Second, we note that in a p–i–n system, near the turn-on voltage, the QW band edges are expected to be energetically not too different. In that case, even without partitioning the system, LLT should provide a good approximation for biases near the turn-on voltage.

In principle, the same difficulties with respect to E_{ref} apply here in the random alloy systems when including LLT in the calculations. However, and compared to the outcome of VCA plus LLT studies, our results show that for simulations including alloy fluctuations but neglecting LLT, larger currents are observed. As discussed above, the calculations taking random alloy fluctuations into account automatically include some softening of the well barrier interface. Combining LLT with random alloy fluctuations results in a further increase of the current and reduction of the turn-on voltage. We stress that standard 1D VCA DD calculations presented in the literature on n–i–n (In,Ga)N QW systems always predicted much higher turn-on voltages when compared to the experimental studies.[15] Thus, the here obtained results reveal and support again the origin of this discrepancy: standard 1D VCA calculations neglect alloy fluctuations. Thus, even though E_{ref} still has to be treated carefully, the resulting energy landscape should present an improvement over VCA in terms of the predicted I–V characteristics.

While the above calculations have been performed at a fixed Gaussian width σ of $\sigma = 0.6$ nm, we still need to evaluate the impact of σ on the I–V characteristics. In the SQW case, cf. Fig. 6, the predicted current at a fixed voltage was virtually independent of σ once LLT was applied. Due to the difficulty of choosing E_{ref} in a MQW system, the current may now depend more strongly on the Gaussian width σ. However, our analysis reveals that after LLT has been applied, at a fixed voltage of 3V, the obtained currents differ only by less than 8% from the mean over a σ range from 0 to 0.9 nm (not shown). The change due to different Gaussian widths σ is only a small correction compared to the change between, e.g., VCA and random alloy fluctuation calculations, indicating again that calculations including both random alloy fluctuations and LLT are robust against changes in σ. Random alloy calculations without including LLT follow a similar trend to that of the SQW shown in Fig. 6 (purple) where the result can strongly depend on the choice of σ, particularly for σ less than 0.6 nm.

IV. CONCLUSIONS

In this work, we presented a general framework that allows us to bridge the gap between atomistic tight-binding theory and continuum-based drift–diffusion calculations. The model also includes quantum corrections via the localization landscape method to address charge carrier transport in III-N-based devices. Our approach furthermore enables a feedback loop between atomistic theory and continuum models since both operate on the same confining energy landscape. Current models in the literature mainly use modified continuum-based approaches that generate confining energy landscapes from locally averaged alloy contents and do not offer the option to compare the outcome of this with an atomistic model.

In addition to establishing and providing insight into the workflow of the overall framework, we have also targeted as a test system uni-polar electron transport in (In,Ga)N-based single and multi-quantum well structures. Overall, we find that random alloy fluctuations and quantum corrections significantly impact the current–voltage characteristics of uni-polar (In,Ga)N devices when compared to standard virtual crystal approximation studies, which are at the heart of most literature carrier transport solvers. In general and independent of single and multi-quantum well systems, the combination of quantum corrections and random alloy fluctuations leads to lower turn-on voltages and higher currents when compared to a virtual crystal approximation. Overall, this effect is very important since literature studies on uni-polar carrier transport have revealed that "standard" 1D continuum-

© Author(s) 2021

based transport solvers, effectively corresponding to our virtual crystal results, give turn-voltages considerably larger than the experiment. Thus, our here predicted shift to lower turn-voltages due to quantum corrections and alloy fluctuations indicates an improved description of experimental data. However, we note that the relative importance of quantum corrections and random alloy fluctuations varies between single and multi quantum well systems. We find that in the single quantum well system, quantum corrections are extremely important. As a consequence, in the single quantum well, a combined virtual crystal approximation plus LLT treatment leads to almost the same current–voltage curve as in a calculation that also includes alloy fluctuations. This indicates that for a single quantum well system, 1D calculations including LLT may be sufficient; this reduces the computational demand significantly. However, our analysis also indicates that in a MQW system this finding may not hold. In such cases alloy fluctuations are required and so a full 3D transport calculation must be carried out. Therefore, our investigations highlight that for MQW systems, both atomistic as well as quantum mechanical effects should be taken into account to achieve an accurate description of the I–V characteristics of uni-polar (In,Ga)N-based devices.

We note that while we have applied this model to uni-polar electron transport here, the toolchain is general and can thus be applied to bi-polar devices. Furthermore, it may also be employed to investigate other material systems, e.g., AlGaN, once an atomistic energy landscape is extracted. All these questions can now be targeted in future studies.

ACKNOWLEDGMENTS

The authors thank J. Fuhrmann (WIAS) for fruitful discussions. This work received funding from the Sustainable Energy Authority of Ireland and the Science Foundation Ireland (Nos. 17/CDA/4789 and 12/RC/2276 P2) and the Deutsche Forschungsgemeinschaft (DFG) under Germany's Excellence Strategy EXC2046: MATH+, project AA2-15, as well as the Leibniz competition 2020.

APPENDIX: FINITE-VOLUME DISCRETIZATION

Unlike other previous studies,[16] we discretize Eq. (4) via the finite-volume method (FVM) on Voronoi cells.[43] The 3D mesh is shown in Fig. 2(c). The construction of such a mesh from a boundary-conforming Delaunay triangulation is illustrated in Fig. 9. Here, we briefly outline our approach.

We integrate the system given by Eq. (4) over a test volume ω_k and apply Gauss's divergence theorem, resulting in the integral equations

$$-\int_{\partial\omega_k} \varepsilon_s \nabla\psi \cdot \boldsymbol{\nu}\, ds = q\int_{\omega_k} (C - n(\psi, \varphi_n))d\mathbf{x},$$

$$\int_{\partial\omega_k} \mathbf{j}_n \cdot \boldsymbol{\nu}\, ds = 0$$

for $k = 1, \ldots, N$, where N corresponds to the number of cells. Here, $\boldsymbol{\nu}$ is the outward-pointing unit normal to the control volume ω_k. These equations represent an integral form of the van Roosbroeck system discussed in the main text on every control volume. In particular, the first equation is Gauss's law of electrodynamics. The second equation constitutes a balance law for the electrons. The densities in each control volume change only due to in- and outflow through the boundary.

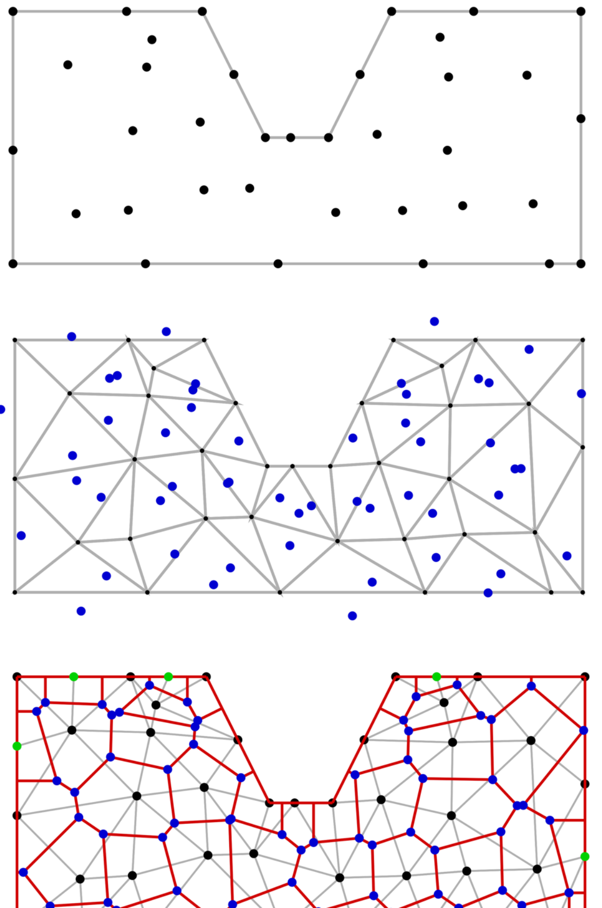

FIG. 9. First row: Piecewise linear description of computational domain with a given point cloud (black dots). Middle row: Delaunay triangulation of domain (gray edges) and triangle circumcenters (blue dots). As some boundary triangles have angles larger than 90° opposite to the boundary, their circumcenters lie outside of the domain. Last row: Boundary-conforming Delaunay triangulation with automatically inserted additional points at the boundary (green dots) by projecting the circumcenters outside onto the boundary of the computational domain. The boundary-conforming Delaunay triangulation is created from the original point cloud (black dots) plus the projected circumcenters (green dots). Now, all circumcenters (blue dots) lie within the computational domain. The boundaries of the (restricted) Voronoi cells are shown as well (red edges). Since the Voronoi cells are constructed from a boundary-conforming Delaunay triangulation, the edge between any two neighboring boundary cells is perpendicular to both boundary nodes. This is by construction also true for interior nodes and the edge separating them. The images were created with triangle.[49]

Next, the surface integrals are split into the sum of integrals over the planar interfaces between the control volume ω_k and its neighbors. Employing one point quadrature rules for the surface

© Author(s) 2021

and volume integrals, we deduce the finite-volume scheme,

$$\sum_{\omega_\ell \in \mathcal{N}(\omega_k)} |\partial\omega_k \cap \partial\omega_\ell| D_{k,\ell} = q|\omega_k|\big(C_k - n(\psi_k, \varphi_{n;k})\big),$$
$$\sum_{\omega_\ell \in \mathcal{N}(\omega_k)} |\partial\omega_k \cap \partial\omega_\ell| j_{n;k,\ell} = 0. \quad \text{(A1)}$$

In the above formulas, $\mathcal{N}(\omega_k)$ denotes the set of all control volumes neighboring ω_k. In 2D, the measure $|\partial\omega_k \cap \partial\omega_\ell|$ corresponds to the length of the boundary line segment and in 3D to the area of the intersection of the boundary surfaces. The measure $|\omega_k|$ is in 2D given by the area and in 3D by the volume of the control volume ω_k. The unknowns ψ_k and $\varphi_{n;k}$ are approximations of the electric potential as well as the quasi Fermi potentials for electrons evaluated at node $\mathbf{x}_k$. The doping is defined by the integral average

$$C_k = \frac{1}{\omega_k}\int_{\omega_k} C(\mathbf{x})\, d\mathbf{x},$$

which can be approximated by its nodal value $C(\mathbf{x}_k)$. The numerical fluxes $D_{k,\ell}$ and $j_{n;k,\ell}$ in Eq. (A1) approximate the fluxes $-\varepsilon\nabla\psi \cdot \boldsymbol{\nu}_{k\ell}$ and $\mathbf{j}_n \cdot \boldsymbol{\nu}_{k\ell}$ in Eq. (4), respectively, on the interfaces between two adjacent control volumes ω_k and ω_ℓ. ψ_k, $\varphi_{n;k}$ and ψ_ℓ, $\varphi_{n;\ell}$.

While the electron flux is numerically approximated via an extension of the Scharfetter–Gummel scheme, Eq. (7), which can handle a spatially varying band-edge profile E_c^{dd}, the electric displacement flux is approximated by

$$D_{k,\ell} = -\varepsilon_s \frac{\psi_\ell - \psi_k}{h_{k,\ell}},$$

where

$$h_{k,\ell} = \|\mathbf{x}_\ell - \mathbf{x}_k\|$$

is the edge length. We point out that the flux approximation in Eq. (A1) is crucial to obtain a stable and physics preserving numerical solution.

DATA AVAILABILITY

The data that support the findings of this study are available from the corresponding author upon reasonable request.

REFERENCES

[1] C. J. Humphreys, MRS Bull. **33**, 459 (2008).
[2] M. Kneissl, T.-Y. Seong, J. Han, and H. Amano, Nat. Photonics **13**, 233 (2019).
[3] C.-Y. Yeh, Z. W. Lu, S. Froyen, and A. Zunger, Phys. Rev. B **46**, 10086 (1992).
[4] S. Strite and H. Morkoc, J. Vac. Sci. Technol. B **10**, 1237 (1992).
[5] H. Morkoc, S. Strite, G. B. Gao, M. E. Lin, B. Sverdlov, and M. Burns, J. Appl. Phys. **76**, 1363 (1994).
[6] F. Bernardini, V. Fiorentini, and D. Vanderbilt, Phys. Rev. B **56**, R10024 (1997).
[7] J. S. Im, H. Kollmer, J. Off, A. Sohmer, F. Scholz, and A. Hangleiter, Phys. Rev. B **57**, R9435 (1998).
[8] D. P. Williams, S. Schulz, A. D. Andreev, and E. P. O'Reilly, J. Sel. Top. Quantum Electron. **15**, 1092 (2009).
[9] O. Ambacher, J. Majewski, C. Miskys, A. Link, M. Hermann, M. Eickhoff, M. Stutzmann, F. Bernardini, V. Fiorentini, V. Tilak *et al.*, J. Phys.: Condens. Matter **14**, 3399 (2002).
[10] D. P. Williams, A. D. Andreev, E. P. O'Reilly, and D. A. Faux, Phys. Rev. B **72**, 235318 (2005).
[11] M. A. Caro, S. Schulz, S. B. Healy, and E. P. O'Reilly, J. Appl. Phys. **109**, 084110 (2011).
[12] C. X. Ren, Mater. Sci. Technol. **32**, 418 (2016).
[13] K. Bulashevich, O. Khokhlev, I. Evstratov, and S. Karpov, in *Light-Emitting Diodes: Materials, Devices, and Applications for Solid State Lighting XVI*, edited by K. P. Streubel, H. Jeon, L.-W. Tu, and N. Linder (International Society for Optics and Photonics (SPIE), 2012), p. 152.
[14] P. McBride, Q. Yan, and C. Van de Walle, Appl. Phys. Lett. **105**, 083507 (2014).
[15] D. Browne, B. Mazumder, Y.-R. Wu, and J. Speck, J. Appl. Phys. **117**, 185703 (2015).
[16] C.-K. Li, M. Piccardo, L.-S. Lu, S. Mayboroda, L. Martinelli, J. Peretti, J. S. Speck, C. Weisbuch, M. Filoche, and Y.-R. Wu, Phys. Rev. B **95**, 144206 (2017).
[17] S. Schulz, M. A. Caro, C. Coughlan, and E. P. O'Reilly, Phys. Rev. B **91**, 035439 (2015).
[18] D. Watson-Parris, M. J. Godfrey, P. Dawson, R. A. Oliver, M. J. Galtrey, M. J. Kappers, and C. J. Humphreys, Phys. Rev. B **83**, 115321 (2011).
[19] T.-J. Yang, R. Shivaraman, J. S. Speck, and Y.-R. Wu, J. Appl. Phys. **116**, 113104 (2014).
[20] D. N. Arnold, G. David, D. Jerison, S. Mayboroda, and M. Filoche, Phys. Rev. Lett. **116**, 056602 (2016).
[21] M. Filoche, M. Piccardo, Y.-R. Wu, C.-K. Li, C. Weisbuch, and S. Mayboroda, Phys. Rev. B **95**, 144204 (2017).
[22] D. Chaudhuri, J. C. Kelleher, M. R. O'Brien, E. P. O'Reilly, and S. Schulz, Phys. Rev. B **101**, 035430 (2020).
[23] D. Ferry, S. Ramey, L. Shifren, and R. Akis, J. Comput. Electron. **1**, 59 (2002).
[24] D. A. Zakheim, A. S. Pavluchenko, D. A. Bauman, K. A. Bulashevich, O. V. Khokhlev, and S. Y. Karpov, Phys. Status Solidi A **209**, 456 (2012).
[25] F. Roemer and B. Witzigmann, Opt. Quantum Electron. **50**, 1 (2018).
[26] J. Geng, P. Sarangapani, K.-C. Wang, E. Nelson, B. Browne, C. Wordelman, J. Charles, Y. Chu, T. Kubis, and G. Klimeck, Phys. Status Solidi A **215**, 1700662 (2018).
[27] M. O'Donovan, M. Luisier, E. P. O'Reilly, and S. Schulz, J. Phys.: Condens. Matter **33**, 045302 (2021).
[28] A. Di Vito, A. Pecchia, A. Di Carlo, and M. Auf Der Maur, J. Appl. Phys. **128**, 041102 (2020).
[29] D. Chaudhuri, M. O'Donovan, T. Streckenbach, S. K. P. O. Marquardt, P. Farrell, T. Koprucki, and S. Schulz, J. Appl. Phys. **129**, 073104 (2021).
[30] J.-R. Chen, S.-C. Ling, H.-M. Huang, P.-Y. Su, T. Ko, T.-C. Lu, H.-C. Kuo, Y.-K. Kuo, and S.-C. Wang, Appl. Phys. B **95**, 145 (2009).
[31] C.-S. Xia, Z. M. S. Li, W. Lu, Z. H. Zhang, Y. Sheng, and L. W. Cheng, Appl. Phys. Lett. **99**, 233501 (2011).
[32] M. A. Caro, S. Schulz, and E. P. O'Reilly, Phys. Rev. B **88**, 214103 (2013).
[33] S. J. Plimpton, J. Comput. Phys. **117**, 1 (1995).
[34] D. S. P. Tanner, P. Dawson, M. J. Kappers, R. A. Oliver, and S. Schulz, Phys. Rev. Appl. **13**, 044068 (2020).
[35] H. Si, ACM Trans. Math. Software **41**, 1 (2015).
[36] H. Si, TetGen version 1.5; see http://tetgen.org/ (accessed December 1, 2015).
[37] D. H. Doan, P. Farrell, J. Fuhrmann, M. Kantner, T. Koprucki, and N. Rotundo, see http://doi.org/10.20347/WIAS.SOFTWARE.DDFERMI for "ddfermi—A Drift-Diffusion Simulation Tool," Weierstrass Institute (WIAS), 2020.
[38] J. Fuhrmann, T. Streckenbach *et al.*, "pdelib: A finite volume and finite element toolbox for PDEs," pdelib version 2.4.20190405, Weierstrass Institute (WIAS), 2019; see http://pdelib.org.
[39] D. Braess, *Finite Elemente* (Springer, Berlin, 1997); see https://doi.org/10.1007/978-3-662-07233-2.

© Author(s) 2021

[40]J. W. Barrett and C. M. Elliott, Numer. Math. **49**, 343 (1986).
[41]O. Schenk, PARDISO version 5.0.0; see http://www.pardiso-project.org (accessed February 22, 2016).
[42]D. N. Arnold, G. David, M. Filoche, D. Jerison, and A. Mayboroda, SIAM J. Sci. Comput. **41**, B69 (2019).
[43]P. Farrell, N. Rotundo, D. H. Doan, M. Kantner, J. Fuhrmann, and T. Koprucki, in *Handbook of Optoelectronic Device Modeling and Simulation*, edited by J. Piprek (CRC Press, 2017), Vol. 2, Chap. 50, pp. 733–771.
[44]W. Van Roosbroeck, Bell Syst. Tech. J. **29**, 560 (1950).
[45]M. Ilegems and H. Montgomery, J. Phys. Chem. Solids **34**, 885 (1973).
[46]M. E. Levinshtein, S. L. Rumyantsev, and S. Shur Michael, *Properties of Advanced Semiconductor Materials* (Wiley & Sons, 2001).
[47]D. L. Scharfetter and H. K. Gummel, IEEE Trans. Electron Devices **16**, 64 (1969).
[48]F. Massabuau, N. Piot, M. Frentrup, X. Wang, Q. Avenas, M. Kappers, C. Humphreys, and R. Oliver, Phys. Status Solidi B **254**, 1600664 (2017).
[49]J. Shewchuk, "Triangle: A two-dimensional quality mesh generator and Delaunay triangulator"; see http://www.cs.cmu.edu/~quake/triangle.html (accessed December 1, 2015).

© Author(s) 2021

11

Nonlinear diffusion, boundary layers and nonsmoothness: Analysis of challenges in drift-diffusion semiconductor simulations

P. Farrell and D. Peschka. Nonlinear diffusion, boundary layers and nonsmoothness: Analysis of challenges in drift-diffusion semiconductor simulations. *Computers and Mathematics with Applications* (2019), pp. 3731–3747. DOI: d2zg

Abstract We study different discretizations of the van Roosbroeck system for charge transport in bulk semiconductor devices that can handle nonlinear diffusion. Three common challenges corrupting the precision of numerical solutions will be discussed: boundary layers, discontinuities in the doping profile, and corner singularities in L-shaped domains. We analyze and benchmark the error and the convergence order of finite difference, finite-element as well as advanced Scharfetter-Gummel type finite-volume discretization schemes. The most problematic of these challenges are boundary layers in the quasi-Fermi potentials near ohmic contacts, which can have a drastic impact on the convergence order. Using a novel formal asymptotic expansion, our theoretical analysis reveals that these boundary layers are logarithmic and significantly shorter than the Debye length.

Conception: In this publication, Dirk Peschka was in charge of the FEM part and I was in charge of the FVM/Scharfetter-Gummel part.

Execution: In this publication, Dirk Peschka was in charge of the FEM part and I was in charge of the FVM/Scharfetter-Gummel part.

Reporting: In this publication, Dirk Peschka was in charge of the FEM part and I was in charge of the FVM/Scharfetter-Gummel part.

ARTICLE IN PRESS
Computers and Mathematics with Applications xxx (xxxx) xxx

Contents lists available at ScienceDirect

Computers and Mathematics with Applications

journal homepage: www.elsevier.com/locate/camwa

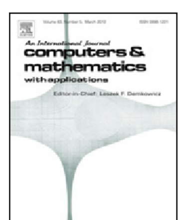

Nonlinear diffusion, boundary layers and nonsmoothness: Analysis of challenges in drift–diffusion semiconductor simulations

Patricio Farrell [a,*], Dirk Peschka [b]

[a] Hamburg University of Technology, Institute for Mathematics, Am Schwarzenberg-Campus 3, 21073 Hamburg, Germany
[b] Weierstrass Institute (WIAS), Mohrenstr. 39, 10117 Berlin, Germany

ARTICLE INFO

Article history:
Received 7 December 2018
Received in revised form 15 May 2019
Accepted 8 June 2019
Available online xxxx

Keywords:
Finite volume method
Finite element method
Nonlinear diffusion and diffusion enhancement
Scharfetter–Gummel scheme
Van Roosbroeck system for semiconductors
Convergence order

ABSTRACT

We study different discretizations of the van Roosbroeck system for charge transport in bulk semiconductor devices that can handle nonlinear diffusion. Three common challenges corrupting the precision of numerical solutions will be discussed: boundary layers, discontinuities in the doping profile, and corner singularities in L-shaped domains. We analyze and benchmark the error and the convergence order of finite difference, finite-element as well as advanced Scharfetter–Gummel type finite-volume discretization schemes. The most problematic of these challenges are boundary layers in the quasi-Fermi potentials near ohmic contacts, which can have a drastic impact on the convergence order. Using a novel formal asymptotic expansion, our theoretical analysis reveals that these boundary layers are logarithmic and significantly shorter than the Debye length.

© 2019 Elsevier Ltd. All rights reserved.

1. Introduction

Understanding charge transport in semiconductors is of vital importance to develop novel electronic devices. The van Roosbroeck system, a drift–diffusion model, is commonly used to describe and numerically solve charge-transport in bulk semiconductors. The assumption that thermodynamic processes in crystalline semiconductors are governed by Boltzmann statistics becomes inaccurate for large densities, *e.g.*, due to high doping or low temperatures [1]. For organic semiconductors this inaccuracy becomes already problematic for low or moderate densities [2,3]. Only recently thermodynamically consistent numerical schemes have been proposed to handle non-Boltzmann statistics [4–8]. A key indicator to measure how well the semiconductor can be described by Boltzmann statistics is the diffusion enhancement [2,9]. In the van Roosbroeck system charge transport is modeled in terms of carrier densities for electrons and holes as well as the electrostatic potential [10]. This approach is fairly common in the mathematical literature regarding semiconductor device modeling [10–13]. However, using quasi-Fermi potentials instead of carrier densities as unknowns can be advantageous for various reasons: thermodynamic descriptions of semiconductors are naturally based on quasi-Fermi potentials and electrostatic potential. The quasi-Fermi potentials also allow a more formalized description of heterojunctions and boundaries using gradient flows [14,15]. Moreover, at heterojunctions and in thermodynamic equilibrium, densities are discontinuous and change over orders of magnitude while the quasi-Fermi potentials are constant. Numerical schemes need to ensure that the densities are positive, which quasi-Fermi potentials guarantee automatically via the equation of

* Corresponding author.
E-mail address: patricio.farrell@tuhh.de (P. Farrell).

https://doi.org/10.1016/j.camwa.2019.06.007
0898-1221/© 2019 Elsevier Ltd. All rights reserved.

Please cite this article as: P. Farrell and D. Peschka, Nonlinear diffusion, boundary layers and nonsmoothness: Analysis of challenges in drift–diffusion semiconductor simulations, Computers and Mathematics with Applications (2019), https://doi.org/10.1016/j.camwa.2019.06.007.

ARTICLE IN PRESS

state. For this reason, we focus in the present work on numerical discretization schemes which are not only expressed in terms of quasi-Fermi potentials but can also handle nonlinear diffusion for non-Boltzmann equations of state.

Ideal metallic contacts, *i.e.*, ohmic contacts, are usually modeled by assuming pointwise electroneutrality and Dirichlet boundary conditions [1,10]. However, as the asymptotic analysis in this study will reveal, this creates severe logarithmic boundary layers in the quasi-Fermi potentials. The physical meaning of the resulting length scale is questionable once the current density exceeds a certain threshold and the boundary layer becomes much shorter than the Debye length, which often is addressed using boundary adapted meshes [16,17]. If the boundary layer is not treated appropriately, standard numerical schemes might fail to provide meaningful solutions. Nevertheless, Markowich [11] showed that the van Roosbroeck model with these Dirichlet conditions is mathematically well-posed. However, since Dirichlet conditions at ohmic contacts have received some physical criticism [10], we point out that also other types of boundary conditions at metallic contacts are discussed in the literature [18], *i.e.*, natural boundary conditions with contact resistance. Additional problems that corrupt the regularity of solutions emerge due to the lack of smoothness of the doping and due to corner singularities, which are present in virtually every realistic semiconductor design. Despite their usefulness for semiconductor simulations, we are not aware of systematic convergence studies for finite element and finite volume discretizations that take into account the effect of nonlinear diffusion, boundary layers, nonsmooth doping profiles and corner singularities.

The present paper aims at bridging this gap and provides a thorough comparison of different discretization philosophies. We study three major challenges for recent finite difference/finite element and finite volume schemes which are designed to deal with nonlinear diffusion in a thermodynamic consistent way and are based on quasi-Fermi potentials as primary variables. In particular, we study the error and convergence rate of the numerical solutions in the presence of: boundary layers, discontinuous doping profile and corner singularities. We provide a theoretical derivation and analysis of the boundary layer near ohmic contacts, using an inner leading-order expansion of a matched asymptotic expansion for the quasi-Fermi potentials. The discontinuity in the doping profile leads to slower convergence, which we examine as well. Finally, we study how an L-shaped domain impacts the convergence order of the solutions due to corner singularities.

In the following section, we introduce the basic semiconductor device equations, the van Roosbroeck system, nondimensionalize it as well as state and solve the leading order inner problem for boundary layers of the quasi-Fermi potentials near ohmic contacts. In Section 3 we provide specific details for the spatial discretization of the van Roosbroeck system, *i.e.*, using finite differences, finite elements, and Scharfetter–Gummel type finite volume methods. The influence of the boundary layers at ohmic contacts as well as the impact of the smoothness of the doping is examined with the help of a 1D problem in Section 4. In Section 5 we then compare how the different discretization schemes handle a 2D L-shaped domain and study the influence of boundary layers and corner singularities on the convergence order in more detail. The simulation data presented in this work is also published in data repository [19] and can be used for comparative benchmark studies.

2. Modeling semiconductors with ohmic contacts

2.1. Stationary van Roosbroeck system

The van Roosbroeck system is a drift–diffusion model, which describes the recombination and transport of charge carriers driven by diffusion and by electric fields within a semiconductor device. It consists of three nonlinear, coupled partial differential equations for the electrostatic potential $\psi : \Omega \to \mathbb{R}$ as well as the non-negative electron and hole densities $n : \Omega \to \mathbb{R}^+$ and $p : \Omega \to \mathbb{R}^+$, namely a Poisson equation and two continuity equations. We consider a homogeneous material and some domain $\Omega \subseteq \mathbb{R}^d$ for $d \in \{1, 2, 3\}$ in an isothermal setting. Then the stationary van Roosbroeck system is given by the system of elliptic partial differential equations

$$-\nabla \cdot (\varepsilon_0 \varepsilon_r \nabla \psi) = q\,(C + p - n)\,, \tag{1a}$$

$$\nabla \cdot \mathbf{j}_n = +qR, \tag{1b}$$

$$\nabla \cdot \mathbf{j}_p = -qR, \tag{1c}$$

where q denotes the elementary charge, ε_0 is the vacuum permittivity and ε_r is the relative permittivity of the material, see Table 2. The recombination rate R and the charge-carrier currents $\mathbf{j}_n, \mathbf{j}_p$ depend on the solution n, p, ψ and vanish in thermal equilibrium. The doping concentration $C\colon \Omega \to \mathbb{R}$ varies spatially and can have discontinuities. The equations of state are given by

$$n(\eta_n) = N_c \mathcal{F}\big(\eta_n\big), \qquad \eta_n(\psi, \varphi_n) = \frac{q(\psi - \varphi_n) - E_c}{k_B T}, \tag{2a}$$

$$p(\eta_p) = N_v \mathcal{F}\big(\eta_p\big), \qquad \eta_p(\psi, \varphi_p) = \frac{q(\varphi_p - \psi) + E_v}{k_B T}, \tag{2b}$$

where the statistical distribution function $\mathcal{F}$ relates the electron and hole densities n, p to the corresponding electrochemical potentials φ_n, φ_p, which are also known as quasi-Fermi potentials. Working with quasi-Fermi potentials has all the

Please cite this article as: P. Farrell and D. Peschka, Nonlinear diffusion, boundary layers and nonsmoothness: Analysis of challenges in drift–diffusion semiconductor simulations, Computers and Mathematics with Applications (2019), https://doi.org/10.1016/j.camwa.2019.06.007.

ARTICLE IN PRESS

advantages mentioned in the introduction, in particular from a modeling and computational point of view. Furthermore, we set the recombination rate to zero as it plays a minor role for most of our considerations.

The effective density of states for electrons in the conduction band N_c and holes in the valence band N_v as well as the corresponding band-edge energies E_c, E_v and the band gap $E_g = E_c - E_v$ are material parameters and assumed to be spatially constant in this paper. Temperature and the Boltzmann constant are denoted with T and k_B. The three most important reference cases for the statistical distribution functions are the Boltzmann, Blakemore and Fermi–Dirac function, denoted by

$$\mathcal{F}(\eta) = \exp(\eta), \tag{3a}$$

$$\mathcal{F}(\eta) = (\exp(-\eta) + \gamma)^{-1}, \tag{3b}$$

$$\mathcal{F}(\eta) = F_\alpha(\eta) = \frac{1}{\Gamma(\alpha+1)} \int_0^\infty \frac{t^\alpha}{\exp(t-\eta)+1}\,\mathrm{d}t, \tag{3c}$$

respectively. For example, the behavior of three-dimensional bulk semiconductors is described most accurately using the Fermi–Dirac–Integral F_α with index $\alpha = 1/2$. For large negative arguments the $F_{1/2}$ can be approximated by either of the other two functions since they all share an exponential tail. By choosing the parameter $\gamma = 0.27$, the Blakemore function (3b) approximates $F_{1/2}$ fairly accurately as long as $\eta \le 1.5$, see [20]. For each distribution function, the corresponding current densities in (1b) and (1c) are

$$\mathbf{j}_n = -q\mu_n n \nabla\varphi_n = -q\mu_n n \nabla\psi + qD_n \nabla n, \tag{4a}$$

$$\mathbf{j}_p = -q\mu_p p \nabla\varphi_p = -q\mu_p p \nabla\psi - qD_p \nabla p. \tag{4b}$$

Using the thermal voltage $U_T = \frac{k_B T}{q}$, the diffusion coefficients D_n, D_p are linked to the carrier mobilities μ_n, μ_p via generalized Einstein relations

$$\frac{D_n}{\mu_n} = U_T\, g(\eta_n), \qquad \frac{D_p}{\mu_p} = U_T\, g(\eta_p), \qquad g(\eta) = \frac{\mathcal{F}(\eta)}{\mathcal{F}'(\eta)}, \tag{5}$$

where g is the diffusion enhancement as motivated in [21]. For the Boltzmann function (3a), we immediately see that $g \equiv 1$, which gives the classical Einstein relation $D_n = \mu_n U_T$. For the Blakemore function (3b), we have $g(\eta) = 1 + \gamma \exp(\eta)$.

The system (1) is supplied with mixed Dirichlet–Neumann boundary conditions. We will briefly discuss the case where the boundary of the domain Ω can be decomposed into ohmic contacts (Γ_α) and an insulating interface (Γ), *i.e.*,

$$\partial\Omega = \Gamma \cup \bigcup_{\alpha=1}^{N_0} \Gamma_\alpha.$$

Ideal semiconductor–metal interfaces, such as ohmic contacts, are modeled by Dirichlet boundary conditions, where we require a local charge neutrality $C + p - n = 0$ and a local equilibrium $\varphi_n = \varphi_p$, where outside thermodynamic equilibrium the value of the quasi-Fermi potential might be different on each Γ_α. On any ohmic contact $\mathbf{x} \in \Gamma_\alpha$ with $\alpha = 1, \ldots, N_0$, we set

$$\psi(\mathbf{x}) = \psi_{\mathrm{bi}}(\mathbf{x}) + U_\alpha, \qquad \varphi_n(\mathbf{x}) = U_\alpha, \qquad \varphi_p(\mathbf{x}) = U_\alpha, \tag{6}$$

where U_α denotes the corresponding externally applied contact voltage and $U_\alpha \equiv 0$ in equilibrium. Here we consider two contacts $N_o = 2$ and set $U_1 = 0$ and $U_2 = V_{\mathrm{ext}}$. These Dirichlet conditions for the potentials correspond to Dirichlet conditions for the densities, which we denote by $n(\mathbf{x}) = n_\alpha$ and $p(\mathbf{x}) = p_\alpha$ for all $\mathbf{x} \in \Gamma_\alpha$. The built-in potential ψ_{bi} at the boundary is defined by the pointwise charge neutrality

$$0 = N_v \mathcal{F}\left(\tfrac{E_v - q\psi_{\mathrm{bi}}(\mathbf{x})}{k_B T}\right) - N_c \mathcal{F}\left(\tfrac{q\psi_{\mathrm{bi}}(\mathbf{x}) - E_c}{k_B T}\right) + C(\mathbf{x}).$$

While for the Boltzmann function monotonicity ensures that such a ψ_{bi} always exists, for the Blakemore function charge neutrality can only be attained at points $\mathbf{x} \in \Omega$ where the doping satisfies $-N_v < \gamma C(\mathbf{x}) < N_c$. We just remark, that in general, this equation yields no closed-form solution, and therefore needs to be computed numerically. The boundary conditions for the more advanced nonlinear semiconductor–metal interfaces such as Schottky contacts or gate contacts can be found in [1,10]. On the remaining non-charged, insulating interfaces we impose (natural) homogeneous Neumann boundary conditions

$$\nabla\psi(\mathbf{x}) \cdot \boldsymbol{\nu} = \mathbf{j}_n(\mathbf{x}) \cdot \boldsymbol{\nu} = \mathbf{j}_p(\mathbf{x}) \cdot \boldsymbol{\nu} = 0 \qquad \text{for all } \mathbf{x} \in \Gamma, \tag{7}$$

where $\boldsymbol{\nu}$ denotes the outward-pointing normal vector to the interface. Finally, we present an argument why the Boltzmann distribution function for the minority charge carriers is accurate near ohmic contacts even if in the interior a non-Boltzmann distribution function is used. First note that most distribution functions, and in particular those in (3), satisfy $\mathcal{F}(\eta) \le \exp(\eta)$. Then, for a doping concentration $C < 0$, we use charge neutrality and the shift $\psi_{\mathrm{bi}} = q^{-1}E_c - U_T w$ to estimate

$$0 = N_v \mathcal{F}(-\tfrac{E_g}{k_B T} + w) - N_c \mathcal{F}(-w) + C \le N_v \exp(-\tfrac{E_g}{k_B T} + w) + C, \tag{8}$$

Please cite this article as: P. Farrell and D. Peschka, Nonlinear diffusion, boundary layers and nonsmoothness: Analysis of challenges in drift–diffusion semiconductor simulations, Computers and Mathematics with Applications (2019), https://doi.org/10.1016/j.camwa.2019.06.007.

ARTICLE IN PRESS

which implies $w \geq \log(-C/N_v) + E_g/(k_BT)$. Assuming $E_g \gg k_BT$ and $|C| \sim N_v$ we finally get $w \gg 1$. A similar argument for $C > 0$ shows that the Boltzmann distribution is a good approximation $\mathcal{F}(w) \sim \exp(w)$ for the equation of state of the minority charge density near ohmic contacts when $|C| \sim N_c$ and $E_g \gg k_BT$.

2.2. Non-dimensionalization

Now we present the non-dimensionalization of the van Roosbroeck system (1), which will also motivate the following boundary layer analysis. First we introduce the scalings,

$$\mathbf{x} \to \ell\,\widetilde{\mathbf{x}}, \quad \psi \to U_T\widetilde{\psi}, \quad \varphi_{n,p} \to U_T\widetilde{\varphi}_{n,p}, \quad (n, p, C) \to (\rho\,\widetilde{n}, \rho\,\widetilde{p}, \rho\,\widetilde{C}),$$

so that we obtain the scaled stationary van Roosbroeck system

$$-\tilde{\nabla}^2\widetilde{\psi} = \frac{\ell^2}{\lambda^2}(\widetilde{C} + \widetilde{p} - \widetilde{n}), \qquad \tilde{\nabla}\cdot\widetilde{\mathbf{j}}_n = +\frac{q\ell}{J}R, \qquad \tilde{\nabla}\cdot\widetilde{\mathbf{j}}_p = -\frac{q\ell}{J}R, \tag{9}$$

with the non-dimensional currents $\widetilde{\mathbf{j}}_n = -\bar{\mu}_n\tilde{n}\tilde{\nabla}\tilde{\varphi}_n$ and $\widetilde{\mathbf{j}}_p = -\bar{\mu}_p\tilde{p}\tilde{\nabla}\tilde{\varphi}_p$, where we introduced the reduced mobilities $\bar{\mu}_n = \mu_n/\mu$ and $\bar{\mu}_p = \mu_p/\mu$. Additionally, we also introduce the length scale λ and the current density scale J

$$\lambda^2 = \frac{\varepsilon_0\varepsilon_r U_T}{q\rho}, \qquad J = \frac{q\mu\rho U_T}{\ell}. \tag{10}$$

We will make specific choices for the characteristic density ρ and current J in the next section. Note that, λ is interpreted as a screening length, whereas in the context of electrolytes J is related to the classical diffusion-limited current density of Nernst, *e.g.*, [22].

When J is set to a typical current value for a given bias V_{ext}, then (10) defines two length scales λ and ℓ, which compete with the *device length scale* in the van Roosbroeck system (9). We denote the device length scale with L. We have $0 < \lambda \ll L$ for large densities ρ, whereas $0 < \ell \ll L$ holds for small densities ρ or for large currents J.

Before we can bring forward an argument about the ordering of the length scales, we need to determine the characteristic density scale ρ. First, the Debye length λ_D is the characteristic length scale, on which deviations from electroneutrality are observed, and typical values for λ_D are in the range of 1 nm to 100 nm. As the screening of charges is dictated by the doping, it makes sense to define $C_{\text{m}} = \max_{\mathbf{x}\in\Omega}|C(\mathbf{x})|$ and then specify $\rho = C_{\text{m}}$ for λ in (10), so that the Debye screening length is

$$\lambda_D^2 = \frac{\varepsilon_0\varepsilon_r U_T}{qC_{\text{m}}}. \tag{11}$$

Second, at ohmic contacts Γ_α where (8) holds for the minority charge density, the corresponding boundary condition is determined from the ohmic contacts for Boltzmann statistics, which are

$$n_\alpha = \frac{1}{2}\left(+C + \left(C^2 + 4N_i^2\right)^{\frac{1}{2}}\right) \quad \text{or} \quad p_\alpha = \frac{1}{2}\left(-C + \left(C^2 + 4N_i^2\right)^{\frac{1}{2}}\right), \tag{12}$$

where $N_i^2 = N_cN_v\exp(-E_g/(k_BT))$. For simplicity we will assume $C = \pm C_{\text{m}}$ at the boundary. The previous assumptions leading to (8) also imply $N_i \ll C_{\text{m}}$, so that to leading order we can expand

$$n_\alpha \approx \begin{cases} N_i^2/C_{\text{m}} & C < 0 \\ C_{\text{m}} & C > 0, \end{cases} \qquad p_\alpha \approx \begin{cases} C_{\text{m}} & C < 0 \\ N_i^2/C_{\text{m}} & C > 0. \end{cases} \tag{13}$$

We are going to discuss the case $C < 0$, where $\delta = N_i/C_{\text{m}} \ll 1$ and $n_\alpha = N_i^2/C_{\text{m}} = C_{\text{m}}\delta^2$, *i.e.*, electrons are the minority carriers.

If we use alternatively $\rho = n_\alpha$ in the scaling for J in (10) then we can define the boundary layer thickness ℓ_J via

$$\ell_J = \frac{q\mu n_\alpha U_T}{J} = \frac{q\mu C_{\text{m}} U_T}{J}\delta^2. \tag{14}$$

If we are interested in situations with $\ell_J \ll \lambda_D$, this requires $J \gg J_{\text{lim}}$, with the intrinsic limiting current J_{lim} defined as

$$J_{\text{lim}} = \frac{q\mu n_\alpha U_T}{\lambda_D} = \frac{q^2\mu N_i^2}{\varepsilon_0\varepsilon_r}\lambda_D. \tag{15}$$

We get surprisingly low intrinsic limiting currents for typical semiconductors and typical Debye lengths, see Table 1. This makes the physical interpretation and local mesh refinement of length scales ℓ_J problematic.

2.3. Boundary layer expansion

We are going to present a concise argument for the existence of boundary layers for the quasi-Fermi potential corresponding to the minority carrier density at ohmic contacts Γ_α. Here we discuss only electrons as minority charge carriers, similar ideas for holes as minority charge carriers follow analogously. We have already discussed that near ohmic contacts the Boltzmann approximation is valid for the minority charge carriers. In order to show and solve the leading

Please cite this article as: P. Farrell and D. Peschka, Nonlinear diffusion, boundary layers and nonsmoothness: Analysis of challenges in drift–diffusion semiconductor simulations, Computers and Mathematics with Applications (2019), https://doi.org/10.1016/j.camwa.2019.06.007.

ARTICLE IN PRESS

Table 1
Typical values of $J_{\lim}$ for semiconductors at $T = 300$ K.

Material	N_i	μ_n	ε_r	Limiting current density $J_{\lim}$
Si	10^{10}cm^{-3}	1400 cm^2/Vs	11.7	$3.5 \cdot 10^{-10}$ A/cm$^2 \cdot \lambda_D$ [nm]
Ge	10^{13}cm^{-3}	3900 cm^2/Vs	16.2	$7.0 \cdot 10^{-4}$ A/cm$^2 \cdot \lambda_D$ [nm]
GaAs	10^{6}cm^{-3}	8500 cm^2/Vs	12.9	$1.9 \cdot 10^{-17}$ A/cm$^2 \cdot \lambda_D$ [nm]

Table 2
Material parameters used for simulations.

Parameter	Value	Parameter	Value
k_{B}	$1.3806503 \cdot 10^{23}$ J/K	ε_{r}	12.9
q	$1.602176565 \cdot 10^{-19}$ C	μ_n	0.85 m^2/Vs
μ_p	0.047 m^2/Vs	ε_0	$8.854187817 \cdot 10^{-12}$ As/Vm
T	300 K	N_c	$4.351959895 \cdot 10^{23}$ m^{-3}
N_v	$9.139615903 \cdot 10^{24}$ m^{-3}	L	10^{-7} m
C_{m}	10^{23} m^{-3}	E_c	1.424 eV
E_v	0 eV		

order inner expansion for the matched asymptotic expansion of the van Roosbroeck system, assume that the length scales are ordered as follows

$$0 < \ell_J \ll \lambda_D \ll L, \tag{16}$$

showing that an asymptotic expansion would require multiple layers to succeed. We will show that, once the current density at an ohmic contact becomes larger than the intrinsic limiting current, logarithmic boundary layers will appear in the quasi-Fermi potential of the corresponding minority carriers. To show this, we examine the leading order asymptotic problem as $\delta = N_i/C_m \to 0$. We fix the scales in the non-dimensionalization by setting $\mu = \mu_n$, $\rho = n_\alpha$ and $J = j_n$. After dropping the tilde symbols in the rescaled van Roosbroeck equations (9) and using (14), the problem reads

$$-\nabla^2\psi = \delta^4 \left(\frac{q\mu_n C_{\mathrm{m}} U_T}{j_n \lambda_D}\right)^2 (C + p - n), \tag{17a}$$

$$-\nabla \cdot n\nabla\varphi_n = \delta^2 \left(\frac{q^2\mu_n C_{\mathrm{m}} U_T}{j_n^2}\right) R. \tag{17b}$$

The scaling $\rho = n_\alpha$ implies that at the ohmic contact the boundary value for the minority charge carrier becomes $n|_{\Gamma_\alpha} = 1$. The reader needs to keep in mind that this is the rescaled version of (12). We expand the solutions using

$$\psi = \psi^0 + \delta\psi^1 + \cdots, \qquad \varphi_n = \varphi_n^0 + \delta\varphi_n^1 + \cdots,$$

and obtain the leading order problem

$$-\nabla^2\psi^0 = 0, \tag{18a}$$

$$-\nabla \cdot n^0\nabla\varphi_n^0 = 0, \tag{18b}$$

where $n^0 = \bar{N}_c \exp(\eta_n^0)$, $\eta_n^0 = \psi^0 - \varphi_n^0 - E_c/(k_B T)$, and $\bar{N}_c = N_c/n_\alpha$. Assuming the ohmic contact Γ_α is located at $x = 0$, the explicit solution is given by

$$\psi^0(x) = \psi_\alpha + \xi x. \tag{19}$$

where the constant $\xi \ll 1$ remains to be determined by matching to an outer solution at the length scale λ_D. For the quasi-Fermi potential we solve an equivalent problem in densities, which can be reduced to the 1D problem

$$\partial_x\left(\partial_x n^0 - n^0\partial_x\psi^0\right) = 0 \tag{20}$$

and has the exact solution

$$n^0(x) = \exp(\xi x) + \frac{1}{\xi}\left(\exp(\xi x) - 1\right). \tag{21}$$

with integration constant $(\partial_x n^0 - n^0\partial_x\psi^0) = 1$ since we chose the scale $J = j_n$. Using the equation of state $n^0 = \bar{N}_c \exp(\psi^0 - \varphi_n^0 - \frac{E_c}{k_B T})$, the quasi-Fermi potential is

$$\varphi_n^0(x) = \psi^0(x) - \log\left(\frac{n^0(x)}{\bar{N}_c}\right) - \frac{E_c}{k_B T} \approx \psi^0(x) - \log\left(\frac{1}{\bar{N}_c}(1 + \xi x) + \frac{x}{\bar{N}_c}\right) - \frac{E_c}{k_B T}$$
$$\approx \psi^0(x) - \log\left(\frac{\varepsilon + x}{\varepsilon}\right) - \log\left(\frac{1}{\bar{N}_c}\right) - \frac{E_c}{k_B T},$$

Please cite this article as: P. Farrell and D. Peschka, Nonlinear diffusion, boundary layers and nonsmoothness: Analysis of challenges in drift–diffusion semiconductor simulations, Computers and Mathematics with Applications (2019), https://doi.org/10.1016/j.camwa.2019.06.007.

ARTICLE IN PRESS

where we approximated using $\xi \ll 1$ several times. Due to the non-dimensionalization the boundary layer width is $\varepsilon = 1$. In the original dimensional outer coordinates, when all quantities are represented in their original scales, we obtain the following leading order the expansion

$$\begin{aligned}\varphi_n^0(x) &= U_T \widetilde{\varphi}_n^0(\ell_J^{-1} x) \\ &= \psi^0(x) - U_T \log\left(\frac{\ell_J + x}{\ell_J}\right) - U_T \log\left(\frac{n_\alpha}{N_c}\right) - \frac{E_c}{q},\end{aligned} \tag{22}$$

where the boundary layer width is ℓ_J. This shows that once the current density at an ohmic contact J exceeds the intrinsic limiting current $J_{\lim}$, then the quasi-Fermi potential of the minority carriers develops a logarithmic boundary layer of size ℓ_J, where

$$0 < \ell_J = \frac{J_{\lim}}{J} \lambda_D \ll \lambda_D, \tag{23}$$

and the electrostatic potential ψ can be approximated by an affine function in this region. The boundary layer analysis of φ_p is entirely analogous.

3. Discretization of the van Roosbroeck system using potentials

Over the past decades many different methods have been proposed to solve the semiconductor device equations numerically. Today, most commonly variants of the finite volume method (FV) are used. However, also discretization schemes based on finite element methods (FE) or finite difference methods (FD) have been developed in the past or are presently used. The finite volume method became very popular after Scharfetter and Gummel published their seminal paper [23] in 1969. For Boltzmann statistics, their scheme can easily deal with the convection-dominated nature of these equations. Even though Scharfetter and Gummel solved the van Roosbroeck system only in one spatial dimension and interpreted their method as a finite difference scheme, others quickly realized that for several space dimensions it is beneficial to translate their scheme into a finite volume setting [10,24–26].

The finite element method is probably the most prominent approach to compute solutions of partial differential equations that arise in the natural sciences [27–30]. It works on general domains, allows a mathematical error analysis and a systematic control over the approximation using the polynomial degree of elements. It is also popular for convection-dominated problems [31,32]. For this reason variants of the finite element method have been applied to the van Roosbroeck system as well [24,33–37]. Most of the authors use the electron and hole densities in the weak formulation. Auf der Maur proposed to use quasi-Fermi potentials as primary variables instead [38]. We follow this approach here.

In the following we are going to explain standard discretization methods to solve the van Roosbroeck system. In one spatial dimension we use a second-order finite difference (FD) method, whereas in two spatial dimensions we use a P_1 finite element (FE) method. We will compare these discretizations with a Voronoï finite volume (FV) method. All three methods are formulated in terms of the quasi-Fermi potentials as primary variables, which transforms the convection-dominated drift–diffusion problem into a nonlinear elliptic system. The advantage of this approach is that quasi-Fermi potentials are the natural variables from a thermodynamic point of view. Additionally, it is easier to control the behavior of solutions at heterointerfaces using these variables. The final nonlinear discrete equations are solved using Newton's method.

In the following we collect the three different components of the solution in the vector-valued function $\mathbf{u} = (\psi, \varphi_n, \varphi_p)\colon \Omega \to \mathbb{R}^3$. Evaluating this function at a specific point $\mathbf{x} \in \Omega$ gives the vector $\mathbf{u}(\mathbf{x}) = \big(\psi(\mathbf{x}), \varphi_n(\mathbf{x}), \varphi_p(\mathbf{x})\big) \in \mathbb{R}^3$. Analogously, we denote the discrete solution with $\mathbf{u}^h = (\psi^h, \varphi_n^h, \varphi_p^h) \in \mathbb{R}^{N\times 3}$, where N is the number of degrees of freedom for each component. The three columns of the matrix $\mathbf{u}^h$ correspond to the three components of the solution, while the kth row of $\mathbf{u}^h$ approximates the solution at a point $\mathbf{x}_k \in \Omega$ and is denoted by $\mathbf{u}_k^h = \mathbf{u}^h(\mathbf{x}_k) = (\psi_k^h, \varphi_{n;k}^h, \varphi_{p;k}^h) \in \mathbb{R}^3$. If we want to distinguish the different numerical solutions from each other, we drop the superscript h and replace it with the acronym of the corresponding discretization method (FD, FE or FV) to make it clear which one is meant.

3.1. Finite difference method

In one spatial dimension we consider the interval $\Omega = [0, 3L]$ for some $L > 0$ and want to approximate the solution $\mathbf{u}$ at discrete points $0 = x_1 < \ldots < x_N = 3L$. In particular we seek to approximate $\psi(x_k) \approx \psi_k^h$, $\varphi_n(x_k) \approx \varphi_{n;k}^h$, and $\varphi_p(x_k) \approx \varphi_{p;k}^h$. The standard 3-point finite difference stencil for the elliptic operator $[Au](x) = -\big(a(x)u'(x)\big)'$ is

$$(Au^h)_k = -\frac{1}{h_k}\left[a_{k+1/2}\frac{u_{k+1}^h - u_k^h}{h_{k+1/2}} - a_{k-1/2}\frac{u_k^h - u_{k-1}^h}{h_{k-1/2}}\right], \tag{24}$$

where $h_{k\pm 1/2} = |x_{k\pm 1} - x_k|$ and $h_k = \frac{1}{2}|x_{k+1} - x_{k-1}|$. The discretization of the Poisson equation (1a) uses a spatially constant $a = \varepsilon_0\varepsilon_r$, whereas in the discretization of the nonlinear transport equation for the electron current we use $a_{k+1/2} = \frac{1}{2}q\mu_n(n_k^h + n_{k+1}^h)$, where $n_k^h = n\big(\eta_n(\mathbf{u}_k^h)\big)$ is the electron density computed from the discrete potentials $\mathbf{u}_k^h$ using

Please cite this article as: P. Farrell and D. Peschka, Nonlinear diffusion, boundary layers and nonsmoothness: Analysis of challenges in drift–diffusion semiconductor simulations, Computers and Mathematics with Applications (2019), https://doi.org/10.1016/j.camwa.2019.06.007.

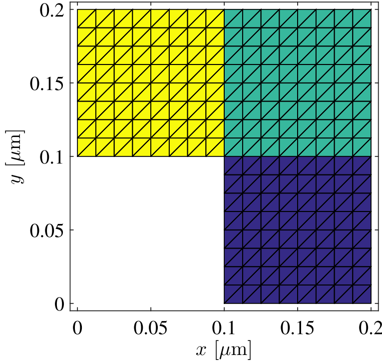

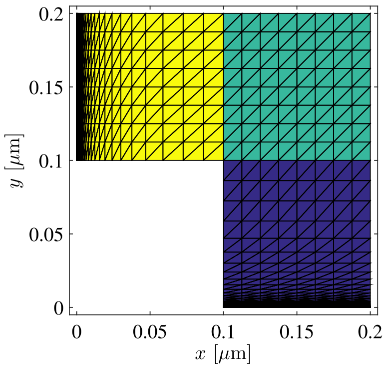

Fig. 1. Domain and mesh with $h \sim 2^{-3}$ (left) uniform and (right) boundary adapted.

the equation of state (2). With vanishing recombination the total current $I = L^2(I_n + I_p)$ is computed from averages of the constant local current density via $I_n = -\frac{1}{3L}\int_0^{3L} q\mu_n n\varphi_n' \mathrm{d}x$ and $I_p = -\frac{1}{3L}\int_0^{3L} q\mu_p p\varphi_p' \mathrm{d}x$. The purpose of the factor L^2 is that we end up with actual currents in Ampere and current densities in Ampere per area, so that one can compare 1D and 2D simulations appropriately. Using trapezoidal rule, I_n is approximated by (analogously for I_p)

$$I_n^h = -\frac{1}{3L}\sum_{k=1}^{N-1} q\mu_n(x_{k+1}-x_k)\frac{(n_k^h + n_{k+1}^h)}{2}\frac{\varphi_{n;k+1}^h - \varphi_{n;k}^h}{x_{k+1}-x_k}, \tag{25}$$

which can be beneficial for its convergence order. A similar strategy will be used to evaluate the currents for the finite element method.

3.2. Finite element method

Assume $\Omega \subset \mathbb{R}^2$ is a polygonal domain and let $\mathcal{T}_h$ be an admissible decomposition of Ω into N_{tria} triangles and N_{vert} vertices, such that $\Omega = \bigcup_{t=1}^{N_{\text{tria}}} \tau_t$ for $\tau_t \in \mathcal{T}_h$ as for example is shown in Fig. 1. Similar as in [33], we solve the stationary van Roosbroeck system (1) using a standard P_1 finite element method. We seek the electrostatic potential and the quasi-Fermi potentials $\mathbf{u}^h = (\psi^h, \varphi_n^h, \varphi_p^h) \in V^h$, such that the van Roosbroeck system can be written in the weak form as

$$0 = \int_\Omega \Big(\varepsilon_0\varepsilon_r \nabla\psi^h \cdot \nabla v_i - q\big(C + p^h - n^h\big)v_i\Big)\,\mathrm{d}x, \tag{26a}$$

$$0 = \int_\Omega \Big(q\mu_n n^h \nabla\varphi_n^h \cdot \nabla v_j - qR(n^h, p^h)v_j\Big)\,\mathrm{d}x, \tag{26b}$$

$$0 = \int_\Omega \Big(q\mu_p p^h \nabla\varphi_p^h \cdot \nabla v_k + qR(n^h, p^h)v_k\Big)\,\mathrm{d}x, \tag{26c}$$

for all suitable test functions $\mathbf{v}^h = (v_i, v_j, v_k) \in V^h$, where $V^h \cong \mathbb{R}^{N_{\text{vert}}\times 3}$ is the $3N_{\text{vert}}$ dimensional space of vectorial continuous functions which are piecewise linear on each triangle τ_t. The carrier densities $n^h = n\big(\eta_n(\psi^h, \varphi_n^h)\big)$, $p^h = p\big(\eta_p(\psi^h, \varphi_p^h)\big)$ depend explicitly on $\mathbf{u}^h$ via the equation of state (2). The basis functions for the function space V^h are uniquely defined by $v_j(\mathbf{x}_k) = \delta_{jk}$, where j, k run over all N_{vert} indices corresponding to vertices $\mathbf{x}_j, \mathbf{x}_k$ of the triangulation. This allows us to represent a solution of (26) as

$$\psi^h(\mathbf{x}) = \sum_{k=1}^{N_{\text{vert}}} \psi_k^h v_k(\mathbf{x}), \quad \varphi_n^h(\mathbf{x}) = \sum_{k=1}^{N_{\text{vert}}} \varphi_{n;k}^h v_k(\mathbf{x}), \quad \varphi_p^h(\mathbf{x}) = \sum_{k=1}^{N_{\text{vert}}} \varphi_{p;k}^h v_k(\mathbf{x}), \tag{27}$$

which explains the equivalence of functions $\psi^h(\mathbf{x}) \in V^h$ and vectors $\psi^h \in \mathbb{R}^{N_{\text{vert}}}$. Some integrals in (26) can be evaluated exactly, the remaining integrals are computed using a standard 7-point Gauss quadrature for triangles [39].

At ohmic contacts Γ_D we impose inhomogeneous Dirichlet boundary conditions $\mathbf{u}_D$ as defined in (6). We realize them by setting $\mathbf{u} = \tilde{\mathbf{u}} + \mathbf{u}_D$ with $\tilde{\mathbf{u}} = 0$ on Γ_D so that all essential boundary conditions are automatically satisfied. This reduces the dimension of the discrete problem to N_{vert} only representing vertices not lying on any Γ_α. For a given ohmic contact α, in order to compute currents, we use an auxiliary function w with $w(\mathbf{x}) = \delta_{\alpha\beta}$ for $\mathbf{x} \in \Gamma_\beta$ and rewrite the currents to

$$I_n^\alpha = \int_{\Gamma_\alpha} \mathbf{j}_n \cdot \boldsymbol{\nu}\,\mathrm{d}a = \int_{\partial\Omega} w\,\mathbf{j}_n \cdot \boldsymbol{\nu}\,\mathrm{d}a = -\int_\Omega \big(q\mu_n n\nabla w \cdot \nabla\varphi_n - qwR\big)\,\mathrm{d}\mathbf{x}, \tag{28a}$$

$$I_p^\alpha = -\int_\Omega \big(q\mu_p p\nabla w \cdot \nabla\varphi_p + qwR\big)\,\mathrm{d}\mathbf{x}. \tag{28b}$$

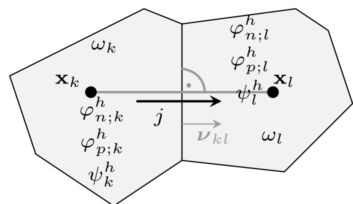

Fig. 2. Two adjacent control volumes ω_k and ω_l with corresponding notation.

Then the total current $I = L(I_n^\alpha + I_p^\alpha)$ can be evaluated using the operators from the existing weak form of the van Roosbroeck system (26). Again, the prefactor L ensures that we obtain a current I in Ampere. The auxiliary function w is chosen by solving $\Delta w = 0$ with Dirichlet data for w mentioned before and with homogeneous Neumann boundary conditions on Γ, *e.g.*, see [40].

3.3. Finite volume method

In this section, we present a Voronoï finite volume technique [1,10,40,41]. Similar as for finite elements, we start by partitioning the domain Ω into non-intersecting, convex polyhedral control volumes ω_k such that $\Omega = \bigcup_{k=1}^{N_{\text{vert}}} \omega_k$. Unlike for finite elements, these control volumes need not to be triangular but fulfill the following orthogonality condition: we associate with each control volume ω_k a node $\mathbf{x}_k \in \omega_k$. For every boundary intersecting control volume, we demand that this node lies on the boundary $\mathbf{x}_k \in \partial\Omega \cap \omega_k$. Assuming that the partition is admissible in the sense of [42], that is for two adjacent control volumes ω_k and ω_l, the edge $\overline{\mathbf{x}_k\mathbf{x}_l}$ of length h_{kl} is orthogonal to $\partial\omega_k \cap \partial\omega_l$, the normal vectors to $\partial\omega_k$ can be calculated by $\boldsymbol{\nu}_{kl} = (\mathbf{x}_l - \mathbf{x}_k)/\|\mathbf{x}_l - \mathbf{x}_k\|$. For each control volume ω_k, the finite volume discretization is given by the three equations:

$$\sum_{\omega_l \in \mathcal{N}(\omega_k)} |\partial\omega_k \cap \partial\omega_l| j_{\psi;k,l} = q|\omega_k| \left(C_k + p_k^h - n_k^h\right), \tag{29a}$$

$$\sum_{\omega_l \in \mathcal{N}(\omega_k)} |\partial\omega_k \cap \partial\omega_l| j_{n;k,l} = +q|\omega_k| R_k, \tag{29b}$$

$$\sum_{\omega_l \in \mathcal{N}(\omega_k)} |\partial\omega_k \cap \partial\omega_l| j_{p;k,l} = -q|\omega_k| R_k. \tag{29c}$$

We denote with $\mathcal{N}(\omega_k)$ the set of all control volumes neighboring ω_k. In 2D, the measure $|\partial\omega_k \cap \partial\omega_l|$ corresponds to the length of the boundary line segment and in 3D to the area of the intersection of the boundary surfaces. Furthermore, in 2D the measure $|\omega_k|$ is given by the area and in 3D by the volume of the control volume ω_k. The unknowns ψ_k^h, $\varphi_{n;k}^h$, $\varphi_{p;k}^h$ correspond to the electrostatic potential as well as the quasi-Fermi potentials for electrons and holes evaluated at node $\mathbf{x}_k$. Accordingly, n_k^h, p_k^h, R_k and C_k are defined as

$$n_k^h = N_c \mathcal{F}\big(\eta_n(\psi_k^h, \varphi_{n;k}^h)\big), \qquad C_k = C(\mathbf{x}_k), \tag{30a}$$

$$p_k^h = N_v \mathcal{F}\big(\eta_p(\psi_k^h, \varphi_{p;k}^h)\big), \qquad R_k = R\big(n_k^h, p_k^h\big). \tag{30b}$$

The notation is explained visually in Fig. 2. The nodes $\mathbf{x}_k$ in the constrained Voronoï tesselation coincide with the vertices of the FE triangulation.

Note that the doping profile C and the recombination rate R are given. The numerical fluxes $j_{\psi;k,l}$, $j_{n;k,l}$ and $j_{p;k,l}$ approximate respectively $-\varepsilon_0\varepsilon_r\nabla\psi \cdot \boldsymbol{\nu}_{kl}$, $\mathbf{j}_n \cdot \boldsymbol{\nu}_{kl}$ and $\mathbf{j}_p \cdot \boldsymbol{\nu}_{kl}$ on the interfaces between two adjacent control volumes ω_k and ω_l. These fluxes can be expressed as functions depending nonlinearly on the values $\psi_k^h, \varphi_{n;k}^h, \varphi_{p;k}^h$ and $\psi_l^h, \varphi_{n;l}^h, \varphi_{p;l}^h$. The flux corresponding to the electrostatic displacement is approximated by

$$j_{\psi;k,l} = -\varepsilon_0\varepsilon_r \frac{\psi_l^h - \psi_k^h}{\|\mathbf{x}_l - \mathbf{x}_k\|}.$$

Next, we discuss numerical flux approximations which appear in the discretizations of the continuity equations.

3.3.1. Flux discretizations for Boltzmann statistics

Choosing the numerical fluxes $j_{n;k,l}$ and $j_{p;k,l}$ correctly is a rather delicate issue as the wrong choice may lead to either instabilities or the violation of thermodynamic principles. Scharfetter and Gummel presented in [23] a suitable choice for Boltzmann statistics. It is possible to derive it from the local one-dimensional homogeneous boundary value problem

$$\partial_x \left(D_n \partial_x n - v n\right) = 0 \quad \text{with } n(x_k) = n_k \text{ and } n(x_l) = n_l$$

Please cite this article as: P. Farrell and D. Peschka, Nonlinear diffusion, boundary layers and nonsmoothness: Analysis of challenges in drift–diffusion semiconductor simulations, Computers and Mathematics with Applications (2019), https://doi.org/10.1016/j.camwa.2019.06.007.

ARTICLE IN PRESS

with the linear diffusion constant $D_n = \mu_n U_T$ and the velocity $v = \mu_n \frac{\psi_l^h - \psi_k^h}{x_l - x_k}$, assuming that the electrostatic potential can be approximated locally with a linear function. We point out once more that the choice for the diffusion constant implies that we are in the Boltzmann regime. The above differential equation is structurally the same as the leading-order equation (20). Since it is homogeneous, it can be interpreted as demanding that the electron flux is constant. The solution to this boundary value problem is readily verified to be

$$n(x) = n_l \frac{1 - e^{\frac{v}{D_n}(x - x_k)}}{1 - e^{\frac{v}{D_n}(x_l - x_k)}} + n_k \frac{e^{\frac{v}{D_n}(x - x_k)} - e^{\frac{v}{D_n}(x_l - x_k)}}{1 - e^{\frac{v}{D_n}(x_l - x_k)}}.$$

Thus the constant Scharfetter–Gummel flux is given by

$$j_{n;k,l} = -\frac{q\mu_n N_c U_T}{x_l - x_k} \left(\exp\left(\eta_{n;k}^h\right) B\left(-\frac{\psi_l^h - \psi_k^h}{U_T} \right) - \exp\left(\eta_{n;l}^h\right) B\left(\frac{\psi_l^h - \psi_k^h}{U_T} \right) \right) \tag{31}$$

with $\eta_{n;k}^h = \eta_n(\psi_k^h, \varphi_{n;k}^h)$ and $\eta_{n;l}^h = \eta_n(\psi_l^h, \varphi_{n;l}^h)$. The Bernoulli function is given by $B(\eta) = \eta/(e^\eta - 1)$. A similar expression can be derived for the hole flux. We point out that only in the Boltzmann regime this flux is thermodynamically consistent in the sense that constant quasi-Fermi potentials imply that the flux vanishes.

Finally, we wish to reinterpret the width of the boundary layer from Section 2 in terms of numerical quantities. Making use of the Boltzmann assumption, we invert (2) for the quasi-Fermi potential to obtain

$$\varphi_n(x) = \psi(x) - U_T \log\left(\frac{n(x)}{N_c} \right) - \frac{E_c}{q}. \tag{32}$$

Now we use the expansion $n(x) \approx \frac{n_l^h - n_k^h}{x_l - x_k}(x - x_k) + n_k^h$, where n_l^h, n_k^h and ψ_l^h, ψ_k^h denote the numerical solution of the electron density and the electrostatic potential at nodes x_l and x_k. Assuming that the ohmic contact is located at x_k, we can derive a considerably simpler approximation for the quasi-Fermi potential by expanding (32) around $x \approx x_k$

$$\varphi_n(x) \approx \psi(x) - U_T \log\left(\frac{x - x_k + \ell_J^h}{\ell_J^h} \right) - U_T \log\left(\frac{n_k^h}{N_c} \right) - \frac{E_c}{q}, \tag{33}$$

very similar to (22) and where

$$\ell_J^h = n_k^h \left(\frac{x_l - x_k}{n_l^h - n_k^h} \right) \approx \left. \frac{n}{n'} \right|_{x = x_k} \approx \ell_J$$

denotes the approximate boundary layer width, an approximation of the previously derived boundary layer width (14). In particular, $\ell_J^h \to \ell_J$ for $h = |x_l - x_k| \to 0$. The approximations follow from the observation that in our setting

$$n' = \frac{q}{k_B T} n(\psi' - \varphi_n') \overset{(22)}{\approx} \frac{q}{k_B T} n \frac{U_T}{\ell_J} = \frac{n}{\ell_J}.$$

3.3.2. *Flux discretization for general statistics*

In the past, techniques for other statistics functions have been suggested [43,44]. For general statistics functions $\mathcal{F}$, ideas from Bessemoulin–Chatard [4] are useful to derive a finite volume scheme for convection–diffusion problems in a *thermodynamically consistent* way by averaging the nonlinear diffusion term appropriately. In [5], the nonlinear diffusion was expressed via the logarithmic average of the nonlinear diffusion enhancement

$$g_{kl} = \frac{\eta_{n;l}^h - \eta_{n;k}^h}{\log \mathcal{F}\left(\eta_{n;l}^h\right) - \log \mathcal{F}\left(\eta_{n;k}^h\right)} \tag{34}$$

along the discretization edge. Using the generalized Einstein relation (5), one immediately observes that the diffusion enhancement g can be seen as a modification factor for the thermal voltage U_T. Replacing U_T in the original expression (31) by $U_T^* = U_T g_{kl}$, we deduce the following modified Scharfetter–Gummel scheme

$$j_{n;k,l} = -\frac{q\mu_n N_c U_T}{x_l - x_k} g_{kl} \left(\mathcal{F}\left(\eta_{n;k}^h\right) B\left(-\frac{\psi_l^h - \psi_k^h}{U_T g_{kl}} \right) - \mathcal{F}\left(\eta_{n;l}^h\right) B\left(\frac{\psi_l^h - \psi_k^h}{U_T g_{kl}} \right) \right), \tag{35}$$

approximating the (electron) current along the edge $\overline{\mathbf{x}_k, \mathbf{x}_l}$. Again, a similar expression can be derived for the hole flux. A problematic aspect of this scheme is that, even though the diffusion enhancement factor g_{kl} is bounded from below by one, it is not straightforward to compute it on a computer when $\eta_{n;k}^h$ approaches $\eta_{n;l}^h$ as the fraction contains a removable singularity. In this case one needs to use a suitable regularization strategy such as a Taylor expansion.

Please cite this article as: P. Farrell and D. Peschka, Nonlinear diffusion, boundary layers and nonsmoothness: Analysis of challenges in drift–diffusion semiconductor simulations, Computers and Mathematics with Applications (2019), https://doi.org/10.1016/j.camwa.2019.06.007.

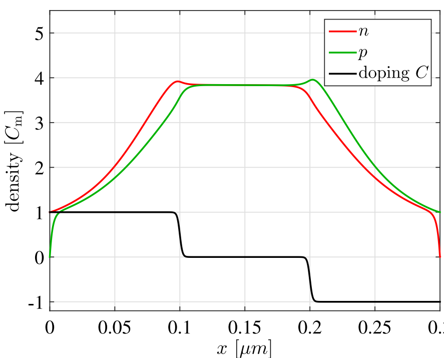

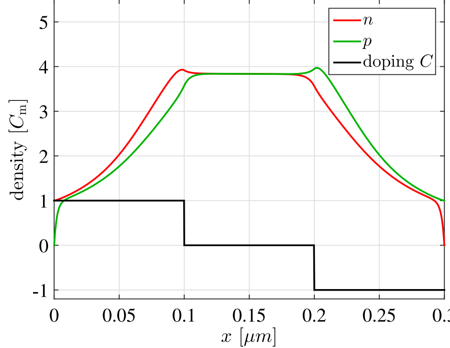

Fig. 3. Electron and hole densities n, p and doping C at bias $V_{\text{ext}} = 3V$ shown (left) with $\kappa = 500$ and (right) with $\kappa = 5 \cdot 10^5$, the former yielding a smooth doping profile and the latter practically a discontinuous one.

4. Numerical comparisons in 1D

In this section, we are going to present numerical solutions of the van Roosbroeck system via FE/FD and the Scharfetter–Gummel FV discretization. In one dimension we focus on two challenges, which have an impact on the convergence rate of solutions: the size of a boundary layer and the regularity of the doping. Since in this section we are mostly concerned with numerical solutions, we will drop the superindex h. If necessary, we replace it with the acronym of the corresponding discretization method. Also we remind the reader that we solve the van Roosbroeck system without recombination, *i.e.*, $R \equiv 0$. Throughout this section, we use the Blakemore distribution function Eq. (3b) with $\gamma = 0.27$.

As discussed before the solutions develop a boundary layer of thickness ℓ_J, which already for small currents is minuscule compared to the size of the computational domain $\mathcal{O}(L)$ – it is even several orders of magnitude smaller than the Debye length λ_D. The physical parameter used here (see Table 2) suggests we have

$$\lambda_D = 13.6\,\text{nm}, \qquad J_{\text{lim}} = 1.2 \cdot 10^{-15}\,\text{A/cm}^2,$$

so that $\ell_J = (J_{\text{lim}}/J)\,\lambda_D$ is much smaller than the Debye length for typical currents J. Thus, it is both physically questionable and numerically hopeless to resolve this length scale explicitly when $J \gg J_{\text{lim}}$. As we have seen in Table 1 for typical semiconductor materials the limiting currents are surprisingly low. Hence, it is likely that boundary layers appear.

Moreover, we are going to highlight the impact of the regularity of the doping on the convergence order of the solutions by comparing smooth and quasi-discontinuous doping profiles. For this purpose, we consider the doping $C\colon \Omega \to \mathbb{R}$ on the domain $\Omega = [0, 3L]$ with $L = 10^{-7}$m given by

$$C(x) = \frac{C_0}{2}\Big[1 + \tanh\big(\kappa(0.1 - x[\mu\text{m}])\big) - \big\{1 + \tanh\big(\kappa(x[\mu\text{m}] - 0.2)\big)\big\}\Big] \tag{36}$$

with ohmic contacts at $x = 0$ and $x = 3L$. Two cases $\kappa = 500$ and $\kappa = 5 \cdot 10^5$ will be studied. Only the first case leads to a doping in which the jumps are resolved by our sequence of meshes

$$h = 3L \cdot 2^{-M} \qquad \text{for} \qquad M = 1, \ldots, 14. \tag{37}$$

The prefactor is set to $C_0 = 10^{23}\text{m}^{-3}$ and constitutes also the largest doping value $C_m = C_0$. The bias is in the range $V_{\text{ext}} \in [0, 3V]$. Hence, as long as $h > L/\kappa$ one will observe an apparent jump discontinuity in the doping C with a direct impact on the convergence rates.

4.1. Resolution of boundary layer

In Fig. 3 the densities n, p and the doping C are shown for the two cases $\kappa = 5 \cdot 10^2$ and $\kappa = 5 \cdot 10^5$ at $V_{\text{ext}} = 3V$. Note that in both cases, the hole density p has a boundary layer at $x = 0$ and the electron density n has a boundary layer at $x = 0.3\ \mu$m. This boundary layer, however, is on the length scale of λ_D and therefore nicely resolved by the mesh. On the level of the plot, the difference in solutions corresponding to the two alternative doping profiles is not visible. In the left panel of Fig. 4 we show the potentials $(\psi, \varphi_n, \varphi_p)$ for $V_{\text{ext}} = 3V$. While the electrostatic potential in both cases is a rather smooth function (blue line), the quasi-Fermi potentials have a boundary layer of size ℓ_J (green and red line) that cannot be resolved on any of the uniform meshes in (37). This logarithmic boundary layer is predicted by our analysis in Section 2. As one can see in Fig. 4 (middle and right panel), the solution effectively jumps within the last interval before the ohmic contact.

An important first observation is that already for moderate mesh sizes the FV quasi-Fermi potentials agree on coarse meshes relatively well with the quasi-Fermi potentials on the finest mesh. This implies that, already on meshes which massively undersample the boundary layer width ℓ_J, the FV solution quite accurately agrees with the asymptotic

ARTICLE IN PRESS

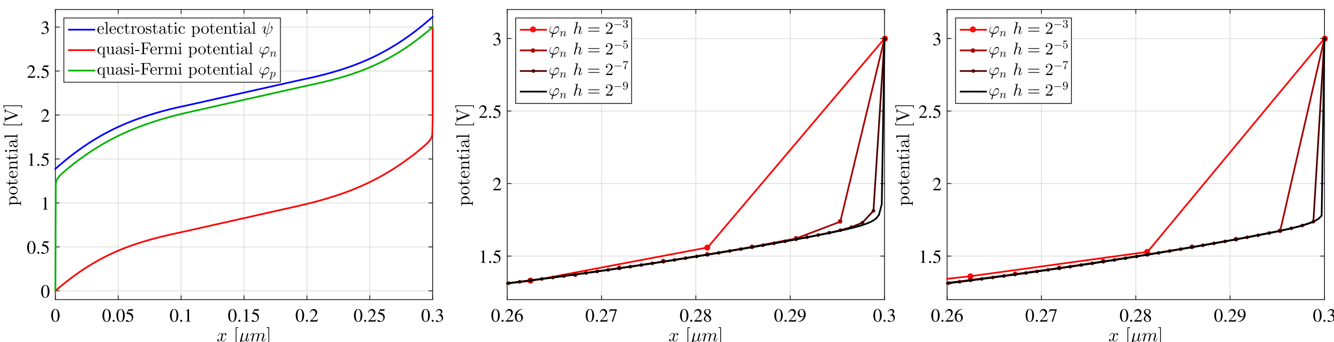

Fig. 4. Quasi-Fermi potentials of electrons and holes φ_n, φ_p and electrostatic potential ψ (left) with bias $V_{\text{ext}} = 3V$ as well as boundary layers in the electron quasi-Fermi potential φ_n near $x = 0.3$ μm for different mesh resolutions h (middle) for finite difference and (right) Scharfetter–Gummel type finite volume discretization for $\kappa = 500$. (For interpretation of the references to color in this figure legend, the reader is referred to the web version of this article.)

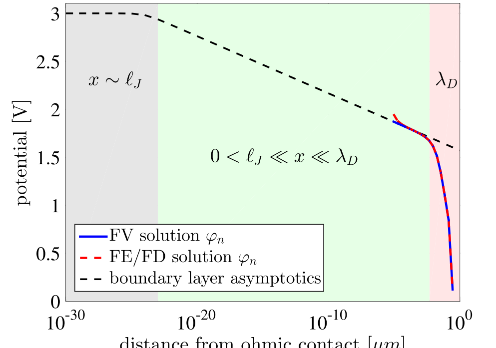

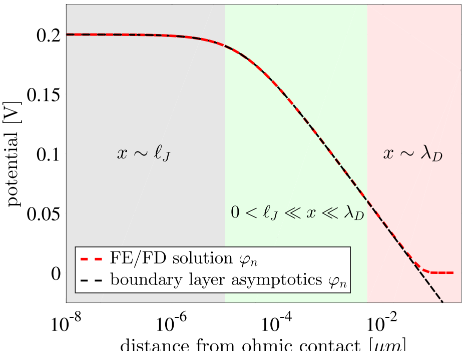

Fig. 5. (left) Electron quasi-Fermi potential φ_n from FD and FV solution compared to the boundary layer asymptotics for $V_{\text{ext}} = 3V$ with boundary layer width $\ell_J \sim 10^{-24}$ μm and a (right) moderate boundary layer $\ell_J \sim 10^{-5}$ μm for an applied voltage $V_{\text{ext}} = 0.2V$ with (left) a linear and (right) logarithmic scaling for the x axis. The FD method using a boundary-adapted mesh is able to resolve the layer.

logarithmic solution, see (22). The FD convergence is considerably slower near the ohmic contact. In particular, on the last few intervals the FD approximation considerably deviates from the asymptotic solution. In order to analyze the behavior near ohmic contacts in more detail, we compare in the left panel of Fig. 5 the electron quasi-Fermi potential φ_n from the FV and FD solutions on the finest mesh with the asymptotic solution from (22) on a semi-logarithmic scale. The figure depicts three different regions shown by the shaded areas. The rightmost shaded area (red) is the outer region where $x \sim \lambda_D$. Then there is a wide transient zone $0 < \ell_J \ll x \ll \lambda_D \ll L$ (green), where the quasi-Fermi potential has a logarithmic singularity. We can see that the FD scheme deviates from the predicted boundary layer asymptotic on the last few grid points, as already observed in Fig. 4.

This singularity is only resolved when $x \sim \ell_J$, where φ_n attains the value set by the Dirichlet boundary condition of the ohmic contact. For example, for $V_{\text{ext}} = 0.2$V we have a moderately small layer width $\ell_J \sim 10^{-3}\lambda_D = 10^{-5}$ μm. The right panel of Fig. 5 shows that in this case the boundary layer is well-resolved. However, for $V_{\text{ext}} = 3V$ the width of the boundary layer is $\ell_J \sim 10^{-24}$ μm, which is beyond any meaningful physical scale for this problem. Note that the FV and the FD solutions agree and follow the intermediate logarithmic singularity set by the asymptotic analysis.

4.2. Regularity of the doping

Next, we discuss the influence of the smoothness of the doping on the convergence order for the different discretization methods. Whenever we compare a coarse discrete solution (of size $2h$) to a finer one (of size h), we restrict the finer solution to the coarser mesh. Then we can subtract $\mathbf{u}^h$ from $\mathbf{u}^{2h}$ and slightly abusing the notation write $\|\mathbf{u}^h - \mathbf{u}^{2h}\|$ for the corresponding norm.

In the left panel of Fig. 6 we show the current as a function of the bias V_{ext} for the FV and FD methods on different meshes for the levels $M = 2, 5, 8$. This already indicates the tendency of the FV method to deliver more accurate solutions on coarser meshes, which is due to the more advanced flux discretization. This becomes even more obvious when comparing the convergence orders for $|I^h - I^{2h}|$ in the right panel of Fig. 6. For the smooth doping with $\kappa = 5 \cdot 10^2$ the FV method has a quadratic convergence $|I^h - I^{2h}| \sim h^2$. This order is influenced by the convergence order of the electrostatic potential and the flux. If the Boltzmann approximation is valid and the electrostatic potential linear, then the flux would be nodally exact. Provided that the doping is sufficiently smooth and the carrier densities converge sufficiently fast, then

Please cite this article as: P. Farrell and D. Peschka, Nonlinear diffusion, boundary layers and nonsmoothness: Analysis of challenges in drift–diffusion semiconductor simulations, Computers and Mathematics with Applications (2019), https://doi.org/10.1016/j.camwa.2019.06.007.

ARTICLE IN PRESS

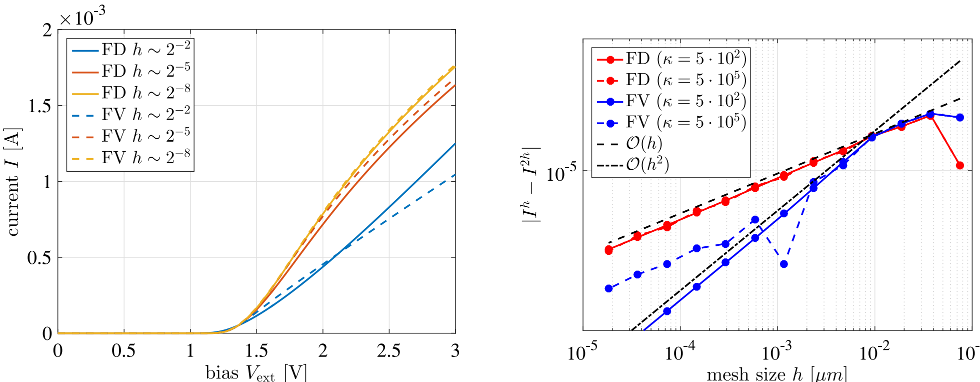

Fig. 6. For different mesh sizes h (left) total current I for the FD and FV discretization (right) and corresponding convergence rates for $\kappa = 5 \cdot 10^2$ and $\kappa = 5 \cdot 10^5$ and $V_{\text{ext}} = 3V$.

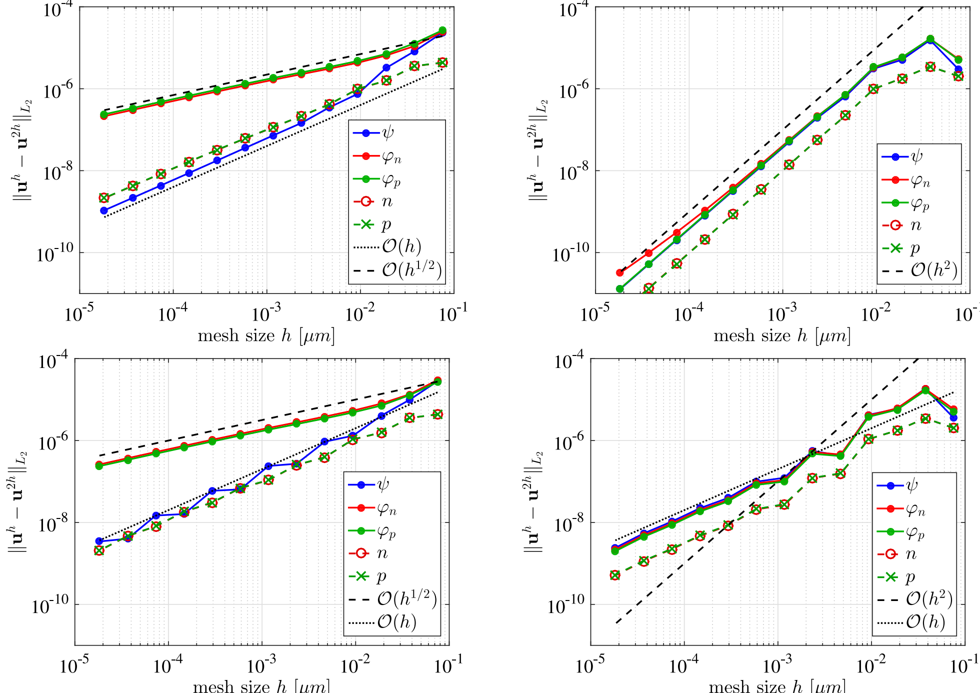

Fig. 7. L_2 convergence rates for solution (left) of the FD discretization and (right) of the FV discretization with $\kappa = 500$ in the top row and for $\kappa = 5 \cdot 10^5$ in the bottom row at $V_{\text{ext}} = 3V$.

both FD and FV discretization of the Poisson equation are second order schemes, see the convergence for n, p, ψ in the right panel of Fig. 7 and the left panel of Fig. 8. For the FD method this argument fails, since the quasi-Fermi potentials only converge with order 1/2 but the densities converge linearly. However, due to the averaging involved in the computation of the current in (28), the convergence order of the FD method in the right panel of Fig. 6 is at least linear.

When the doping is discontinuous ($\kappa = 5 \cdot 10^5$), the bottom row in Fig. 7 shows that also the convergence order of the FV electrostatic potential becomes linear, which is expected by standard FE error estimates. From Figs. 6 and 7 it appears that while the error in the FD method is dominated by the error in the quasi-Fermi potentials, the error in the FV method is dominated by the lack of regularity in the doping.

Interestingly, Fig. 8 (middle panel) shows the FV method also allows to evaluate the convergence in the L_∞ norm for $\kappa = 500$. Even though the L_2 error of the solution converges quadratically, one can observe that first the L_∞ error of φ_n and later of φ_p converge linearly. This is due to the flux approximation scheme being first order consistent in the quasi-Fermi potentials near an ohmic contact with logarithmic singularity. Note, if we had chosen to compute the L_∞ error interpolating the coarser solution to the finer one, we would see no convergence with respect to the grid size defined as in (37).

Even though it appears that the FD scheme cannot compete with the FV method, it is easy to improve it by using boundary-adapted grids as demonstrated in Fig. 8 (right panel). This leads us naturally to our next section, where we study the impact of boundary layers and corner singularities in two spatial dimensions. As boundary layers degrade the

Please cite this article as: P. Farrell and D. Peschka, Nonlinear diffusion, boundary layers and nonsmoothness: Analysis of challenges in drift–diffusion semiconductor simulations, Computers and Mathematics with Applications (2019), https://doi.org/10.1016/j.camwa.2019.06.007.

ARTICLE IN PRESS

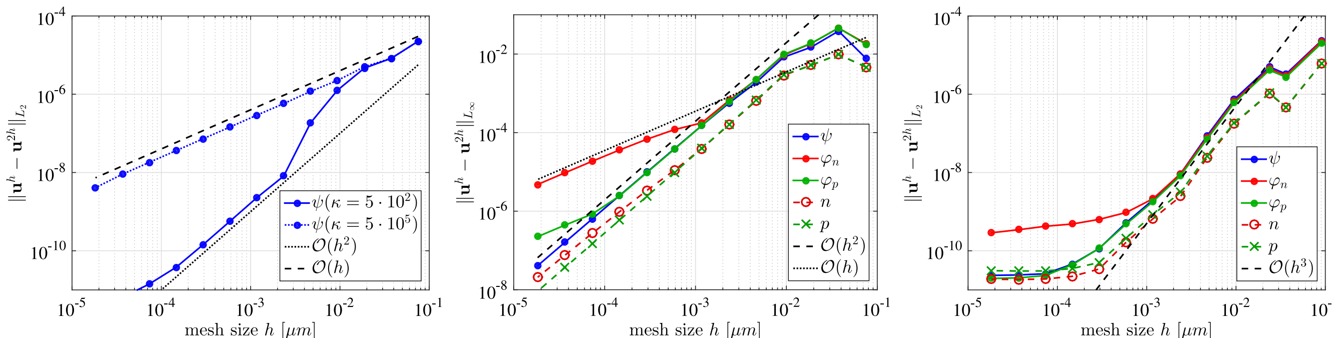

Fig. 8. (left) L_2 convergence of ψ in thermal equilibrium (similar for FV and FD), (middle) L_∞ convergence of FV solution for $\kappa = 500$ and $V_{\text{ext}} = 3V$ as well as (right) L_2 convergence rates for FD discretization on a non-uniform grid for $\kappa = 500$ and $V_{\text{ext}} = 3V$.

convergence order of the FD/FE schemes already in one dimension, we are going to compare solutions computed on uniform meshes with those from boundary adapted meshes. However, we will not employ any local refinement strategy near the corner singularity.

5. Numerical comparisons in 2D

5.1. Corner singularities and boundary adapted meshes

Semiconductor devices may often be angular-shaped. However, in particular L-shaped domains pose numerical difficulties which we would like to study for the FE and FV methods. We consider a two-dimensional L-shaped domain

$$\Omega = [0, 2L]^2 \setminus [0, L]^2 \subset \mathbb{R}^2, \tag{38}$$

as shown in Fig. 1, and impose ohmic contacts at the boundaries $(x, 0)$ and $(0, y)$ for $L \le x, y \le 2L$. All other boundaries are supplied with homogeneous Neumann boundary conditions. The p-i-n doping concentration $C\colon \Omega \to \mathbb{R}$ is given by

$$C(\mathbf{x}) = \begin{cases} +C_0 & 0 \le x \le L/2, \\ -C_0 & 0 \le y \le L/2, \\ +2C_0(L-x)/L & L/2 < x \le L, \\ -2C_0(L-y)/L & L/2 < y \le L, \\ 0 & \text{otherwise} \end{cases} \tag{39}$$

with $\mathbf{x} = (x, y)$ and as before $L = 10^{-7} m = 0.1\ \mu\text{m}$ and $C_0 = C_{\text{m}} = 10^{23}\ \text{m}^{-3}$, see left panel of Fig. 9. With this choice we ensure that the convergence order does not suffer from the regularity of the doping. However, constructing a non-convex domain with a corner angle $\vartheta = \theta\pi$ and $\theta = 3/2$ imposes a corner singularity of the form $\psi(\mathbf{x}) \sim r^{1/\theta}$ as $r \to 0$ for $r = \sqrt{(x-x_0)^2 + (y-y_0)^2}$ at $x_0 = y_0 = 0.1\ \mu\text{m}$. Standard finite element error analysis for the Poisson equation gives $u \in H^\sigma$ with $\sigma = 1 + 1/\theta - \epsilon < 2$ for arbitrary small $\epsilon > 0$, so that

$$\|u - u^h\|_{L_2} \le C \left(h^{l+\sigma-1} + h^{2k}\right) \|u\|_{H^{l+1}}, \qquad l = \min\{k, \sigma - 1\}, \tag{40}$$

where k is the polynomial degree of the FE basis functions [30] used to expand u^h. For linear finite elements we obtain the estimate $\|u - u^h\|_{L_2} \le Ch^{4/3-2\epsilon}\|u\|_{H^{5/3-\epsilon}}$, so that the potentials should converge asymptotically not better than $h^{4/3}$ in the L_2 norm. It remains to be seen how the boundary layer behaves for the FE and FV discretization schemes in two spatial dimensions. In addition to the series of uniformly refined structured meshes, we are also going to investigate the convergence on meshes adapted to the boundary layers. For a general overview of different strategies for singularly perturbed problems, in particular for boundary adapted meshes, we refer to [16]. The boundary layer is constructed using an exponentially graded mesh, where one direction is kept uniform and towards the ohmic contact we refine until the shortest triangle edge is approximately $\sim 10^{-5}L$, see right panel in Fig. 1.

The electron density is shown in the right panel of Fig. 10. Similar to 1D, one can observe a boundary layer in n, which is well resolved by the mesh and of the order of the Debye length λ_D. However, the middle panel of Fig. 10 shows the electron quasi-Fermi potential, which is not resolved and appears to jump on the last few triangles before the ohmic contacts.

Additionally, in Fig. 9 (right panel) the total current density $\mathbf{j} = \mathbf{j}_n + \mathbf{j}_p$ is shown. A careful inspection already indicates the presence of the corner singularity. Note, the corner singularity in the total current density $|\mathbf{j}|$ is slightly obscured by the logarithmic scale.

For simplicity we will focus here on the discussion of the convergence order for the electrostatic potential ψ and the electron quasi-Fermi potential φ_n. The previous analysis in one dimension should then indicate how the other potential

Please cite this article as: P. Farrell and D. Peschka, Nonlinear diffusion, boundary layers and nonsmoothness: Analysis of challenges in drift–diffusion semiconductor simulations, Computers and Mathematics with Applications (2019), https://doi.org/10.1016/j.camwa.2019.06.007.

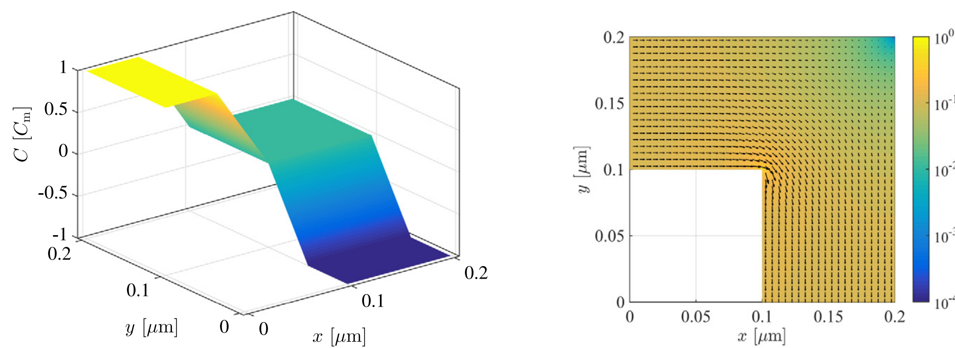

Fig. 9. (left) Continuous doping concentration of *L*-shaped p-i-n diode and (right) total current density $\mathbf{j} = \mathbf{j}_n + \mathbf{j}_p$ in arbitrary units.

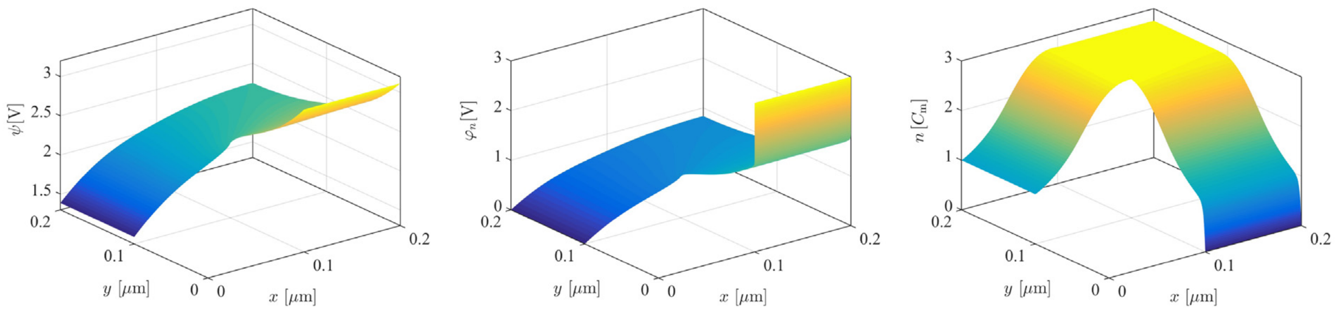

Fig. 10. (left) Electrostatic potential ψ, (middle) quasi-Fermi potential φ_n and (right) electron density n for *L*-shaped p-i-n diode at $V_\mathrm{ext} = 3V$.

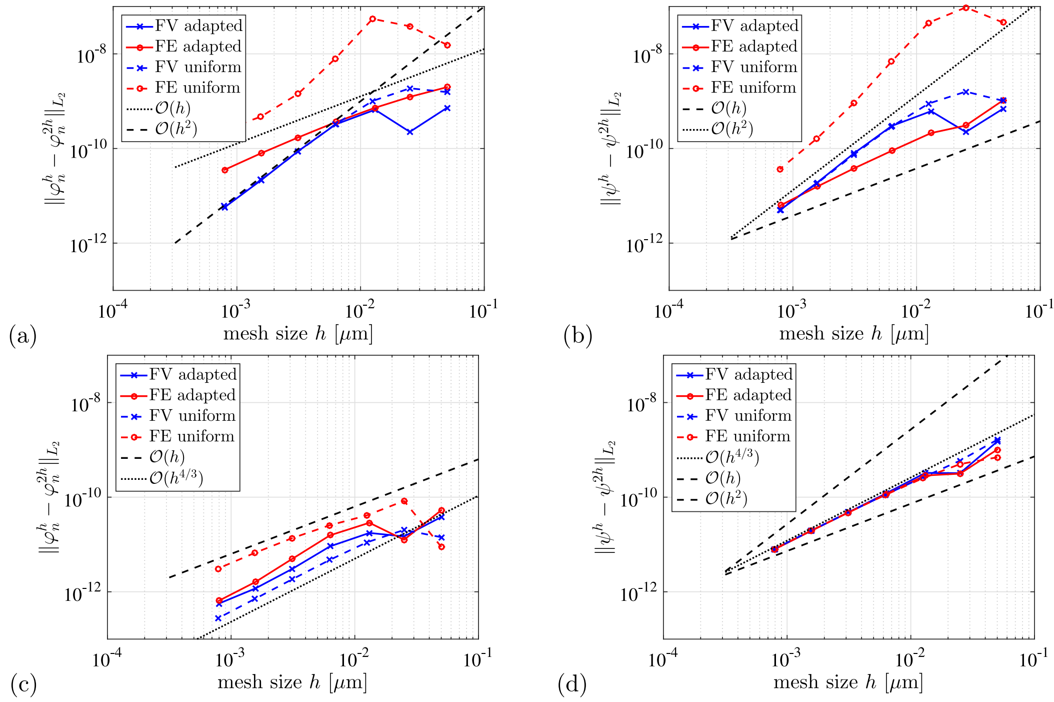

Fig. 11. Convergence of solutions on different meshes as a function of relative triangle size $h = 2^{-\ell}$ for (a) electron quasi-Fermi potential φ_n at $V_\mathrm{ext} = 3V$, (b) electrostatic potential ψ at $V_\mathrm{ext} = 3V$, (c) electron quasi-Fermi potential φ_n at $V_\mathrm{ext} = 0.2V$, (d) electrostatic potential ψ at $V_\mathrm{ext} = 0.2V$.

and densities should converge. We systematically study the experimental order of convergence and compare uniform and boundary adapted meshes.

The upper left panel of Fig. 11 shows the convergence of the electron quasi-Fermi potentials at $V_\mathrm{ext} = 3V$, where the FE and FV are compared on a sequence of uniform and a sequence of boundary adapted meshes. As in 1D, the FV method converges quadratically. Furthermore, for the FV discretization the error seems not to be influenced very much by the boundary adapted meshes. In contrast, the FE method again has a lower convergence order and local adaptivity improves

Please cite this article as: P. Farrell and D. Peschka, Nonlinear diffusion, boundary layers and nonsmoothness: Analysis of challenges in drift–diffusion semiconductor simulations, Computers and Mathematics with Applications (2019), https://doi.org/10.1016/j.camwa.2019.06.007.

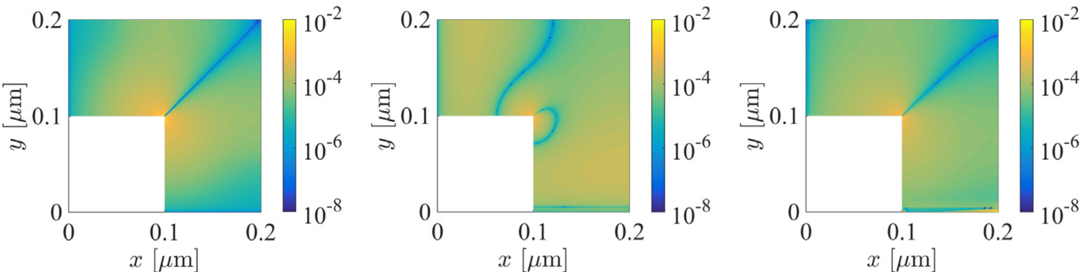

Fig. 12. Local errors for (left) electrostatic potential ψ in thermal equilibrium and at $V_{\text{ext}} = 3\text{V}$ for (middle) FV and for (right) FE electron quasi-Fermi potential.

the L_2 error of the solution by about one order of magnitude. The upper right panel of Fig. 11 shows the convergence of the electrostatic potential at $V_{\text{ext}} = 3V$, for which the convergence rates of both FV methods and the FE method on uniformly refined meshes are of order $\mathcal{O}(h^2)$. Only the FE method with adapted refinement converges slower, between $\mathcal{O}(h)$ and $\mathcal{O}(h^2)$. However, the error lies below the error for the FE with uniform mesh refinement.

The lower panels of Fig. 11 show the solutions at $V_{\text{ext}} = 0.2V$, where the boundary layer is moderate and solutions are closer to thermal equilibrium. Hence, the lower left panel shows the general tendency to have lower errors. However, the convergence is slower with an order between $\mathcal{O}(h)$ and $\mathcal{O}(h^{4/3})$, indicating a stronger influence of the corner singularity. This effect is even more pronounced in the lower right panel, in which for all the used methods the convergence of the electrostatic potential nicely follows the $\mathcal{O}(h^{4/3})$ order predicted by the error analysis of the corner singularity. The existence of the corner singularity for both bias values becomes obvious by a closer examination of the local error $\text{err}(\mathbf{x}) = |\mathbf{u}^h(\mathbf{x}) - \mathbf{u}^{2h}(\mathbf{x})|$ shown in Fig. 12 on a logarithmic scale. At the ohmic contacts the error vanishes since the boundary conditions are solved exactly. A clearly symmetric and dominant corner singularity is visible in the left panel of Fig. 12 for the electrostatic potential at thermal equilibrium. This matches also our previous observation, that the $\mathcal{O}(h^{4/3})$ convergence order is most prominent in the electrostatic potential for low voltages in Fig. 11. In a similar manner, we can see that the local error in the middle and right panel of Fig. 12 has corner singularities. However, while the local error of the electron quasi-Fermi potential of the FV in the middle panel shows no specific problem near the ohmic contact, the FE solution also has additional difficulties at the ohmic contact $y = 0$, where the boundary layer is located, compare with Fig. 10.

Summarizing, in 2D both FE and FV discretizations deliver reasonable results. While the finite volume scheme often shows better convergence rates, the finite element method can be drastically improved by using meshes which are finer near ohmic contacts. We clearly observe that depending on the potential and the selected bias, the error is dominated by the boundary layer or the corner singularity. While the FV method generally handles the boundary layer well, the FE method in 2D introduces extra oscillations in the boundary layer, see Fig. 12.

6. Conclusion

We performed an extensive analysis and comparison of numerical methods for the van Roosbroeck system in one and two spatial dimensions. We compared Scharfetter–Gummel type finite volume discretizations for non-Boltzmann statistics with standard finite element and finite difference methods, where the electrostatic and quasi-Fermi potentials are used as primary variables. This choice of variables transforms the convection-dominated problem with nonlinear diffusion into a nonlinear elliptic system, making it susceptible for these alternative numerical discretization philosophies. A careful asymptotic analysis showed that the quasi-Fermi potentials corresponding to minority carriers have logarithmic boundary layers at ohmic contacts. The typical size ℓ_J of these layers depends on the applied voltage via the current density J, *i.e.*, $\ell_J = \lambda_D (J_{\text{lim}}/J)$, which due to the smallness of J_{lim} generates layers much thinner than the Debye length for a bias V_{ext} slightly above the thermal voltage U_T. We showed that for $\ell_J \ll x \ll \lambda_D$ the quasi-Fermi potential has a logarithmic singularity.

Nevertheless, all studied methods are able to give reliable predictions for the total electrical current and show the expected convergence behavior in the L_2 norm under mesh refinement. The finite volume approach even converges with respect to the L_∞ norm and generally has the best convergence order among all compared methods. For the finite difference and finite element discretizations with quasi-Fermi potentials, the logarithmic boundary layer has the strongest influence on the degradation of the convergence order.

Already in one dimension, the advantageous convergence order of the finite volume convergence order is distorted when discontinuous doping profiles are used. However, when used on uniform meshes, the finite volume method usually outperforms the finite element and finite difference approaches by one order of convergence. But also the finite element method can be significantly improved by refining the computational mesh near ohmic contacts.

In higher dimensions corner singularities can be the ultimate restriction for the convergence order. In practice, their impact is most noticeable at low applied biases. In particular in two dimensions, we have multiple error sources, so

Please cite this article as: P. Farrell and D. Peschka, Nonlinear diffusion, boundary layers and nonsmoothness: Analysis of challenges in drift–diffusion semiconductor simulations, Computers and Mathematics with Applications (2019), https://doi.org/10.1016/j.camwa.2019.06.007.

ARTICLE IN PRESS

that the observed convergence order in the studied range of mesh sizes is not yet in the predicted asymptotic regime dominated by the corner-singularity.

While Dirichlet boundary conditions at ohmic contacts are not always considered to be physically correct in the literature, a similar behavior is relevant for depletion zones, *e.g.*, at p–n junctions with strong reverse bias. This means that the theory for contacts and interfaces should be extended [14,18], making FE more competitive.

Acknowledgments

We thank J. Fuhrmann, L. Heltai, N. Rotundo, D.H. Doan, M. Kantner, A. Glitzky, M. Liero, T. Koprucki, and M. Thomas. This research is supported by MATHEON project OT8 within the Einstein Foundation Berlin.

References

[1] P. Farrell, N. Rotundo, D.H. Doan, M. Kantner, J. Fuhrmann, T. Koprucki, Mathematical methods: drift-diffusion models, in: J. Piprek (Ed.), Handbook of Optoelectronic Device Modeling and Simulation, Taylor & Francis, 2017, pp. 733–772.
[2] G. Paasch, S. Scheinert, Charge carrier density of organics with Gaussian density of states: analytical approximation for the Gauss-Fermi integral, J. Appl. Phys. 107 (10) (2010) 104501, http://dx.doi.org/10.1063/1.3374475.
[3] D.-H. Doan, A. Glitzky, M. Liero, Analysis of a drift–diffusion model for organic semiconductor devices, Z. Angew. Math. Phys. 70 (2) (2019) 55, http://dx.doi.org/10.1007/s00033-019-1089-z.
[4] M. Bessemoulin-Chatard, A finite volume scheme for convection–diffusion equations with nonlinear diffusion derived from the Scharfetter–Gummel scheme, Numer. Math. 121 (4) (2012) 637–670, http://dx.doi.org/10.1007/s00211-012-0448-x.
[5] T. Koprucki, N. Rotundo, P. Farrell, D.H. Doan, J. Fuhrmann, On thermodynamic consistency of a Scharfetter-Gummel scheme based on a modified thermal voltage for drift-diffusion equations with diffusion enhancement, Opt. Quantum Electron. 47 (6) (2015) 1327–1332, http://dx.doi.org/10.1007/s11082-014-0050-9.
[6] P. Farrell, T. Koprucki, J. Fuhrmann, Computational and analytical comparison of flux discretizations for the semiconductor device equations beyond Boltzmann statistics, J. Comput. Phys. 346 (2017) 497–513, http://dx.doi.org/10.1016/j.jcp.2017.06.023.
[7] P. Farrell, M. Patriarca, J. Fuhrmann, T. Koprucki, Comparison of thermodynamically consistent charge carrier flux discretizations for Fermi-Dirac and Gauss-Fermi Statistics, Opt. Quantum Electron. 50 (101) (2018) http://dx.doi.org/10.1007/s11082-018-1349-8.
[8] M. Patriarca, P. Farrell, J. Fuhrmann, T. Koprucki, Highly accurate quadrature-based Scharfetter-Gummel schemes for charge transport in degenerate semiconductors, Comput. Phys. Comm. 235 (2018) 40–49, http://dx.doi.org/10.1016/j.cpc.2018.10.004.
[9] Y. Roichman, N. Tessler, Generalized Einstein relation for disordered semiconductors–implications for device performance, Appl. Phys. Lett. 80 (11) (2002) 1948–1950, http://dx.doi.org/10.1063/1.1461419.
[10] S. Selberherr, Analysis and Simulation of Semiconductor Devices, Springer, Wien, New York, 1984.
[11] P. Markowich, The stationary semiconductor device equations, in: Computational Microelectronics, Springer Wien, 1986.
[12] M. Mock, Analysis of mathematical models of semiconductor devices, in: Advances in Numerical Computation Series, Boole Press, 1983.
[13] F. Brezzi, L. Marini, S. Micheletti, P. Pietra, R. Sacco, S. Wang, Discretization of semiconductor device problems (I), in: Numerical Methods in Electromagnetics, in: Handbook of Numerical Analysis, vol. 13, Elsevier, 2005, pp. 317–441, http://dx.doi.org/10.1016/S1570-8659(04)13004-4.
[14] A. Glitzky, A. Mielke, A gradient structure for systems coupling reaction–diffusion effects in bulk and interfaces, Z. Angew. Math. Phys. 64 (1) (2013) 29–52.
[15] A. Mielke, D. Peschka, N. Rotundo, M. Thomas, On Some Extension of Energy-Drift-Diffusion Models: Gradient Structure for Optoelectronic Models of Semiconductors, in: P. Quintela, et al. (Eds.), Progress in Industrial Mathematics at ECMI 2016, Springer International Publishing, 2017, pp. 291–298.
[16] H.-G. Roos, M. Stynes, L. Tobiska, Numerical methods for singularly perturbed differential equations: convection-diffusion and flow problems, in: Springer Series in Computational Mathematics, Springer, Berlin, Heidelberg, New York, 1996.
[17] M. Stynes, Steady-state convection-diffusion problems, Acta Numer. 14 (2005) 445–508, http://dx.doi.org/10.1017/S0962492904000261.
[18] D. Schroeder, Modelling of interface carrier transport for device simulation, in: Computational Microelectronics, Springer, 1994.
[19] P. Farrell, D. Peschka, Comparison of different discretization methods for semiconductor drift-diffusion problems - data, 2018, http://doi.org/10.20347/WIAS.DATA.3.
[20] J. Blakemore, The parameters of partially degenerate semiconductors, Proc. Phys. Soc. Lond. A 65 (1952) 460–461.
[21] S.L.M. van Mensfoort, R. Coehoorn, Effect of Gaussian disorder on the voltage dependence of the current density in sandwich-type devices based on organic semiconductors, Phys. Rev. B 78 (8) (2008) http://dx.doi.org/10.1103/physrevb.78.085207.
[22] A.J. Bard, L.R. Faulkner, J. Leddy, C.G. Zoski, Electrochemical Methods: Fundamentals and Applications, vol. 2, Wiley New York, 1980.
[23] D. Scharfetter, H. Gummel, Large-signal analysis of a silicon read diode oscillator, IEEE Trans. Electron Devices 16 (1) (1969) 64–77, http://dx.doi.org/10.1109/T-ED.1969.16566.
[24] R.E. Bank, D.J. Rose, W. Fichtner, Numerical methods for semiconductor device simulation, SIAM J. Sci. Stat. Comput. 4 (3) (1983) 416–435, http://dx.doi.org/10.1137/0904032.
[25] R.E. Bank, D.J. Rose, Some error estimates for the box method, SIAM J. Numer. Anal. 24 (1987) 777–787.
[26] P. Farrell, A. Linke, Uniform second order convergence of a complete flux scheme on nonuniform 1d grids, in: C. Cancès, P. Omnes (Eds.), Finite Volumes for Complex Applications VIII - Methods and Theoretical Aspects, 2017, pp. 303–311.
[27] P. Ciarlet, The Finite Element Method for Elliptic Problems, SIAM, 2002, http://dx.doi.org/10.1137/1.9780898719208.
[28] H.C. Elman, D.J. Silvester, A.J. Wathen, Finite Elements and Fast Iterative Solvers: with Applications in Incompressible Fluid Dynamics, in: Numerical Mathematics and Scientific Computation, Oxford University Press, Oxford, 2005, p. xiv+400.
[29] S.C. Brenner, L.R. Scott, The mathematical theory of finite element methods, third ed., in: Texts in Applied Mathematics, vol. 15, Springer, New York, 2008, p. xviii+397, http://dx.doi.org/10.1007/978-0-387-75934-0.
[30] G. Strang, G. Fix, An Analysis of the Finite Element Method, Wellesley-Cambridge Press, 2008.
[31] V. John, P. Knobloch, On spurious oscillations at layers diminishing (SOLD) methods for convection–diffusion equations: Part I–A review, Comput. Methods Appl. Mech. Engrg. 196 (17) (2007) 2197–2215.
[32] G. Pitton, L. Heltai, Accelerating the iterative solution of convection–diffusion problems using singular value decomposition, Numer. Linear Algebra Appl. 26 (1) (2019) e2211, http://dx.doi.org/10.1002/nla.2211.
[33] M. Auf der Maur, M. Povolotskyi, F. Sacconi, A. Pecchia, G. Romano, G. Penazzi, A. Di Carlo, TiberCAD: towards multiscale simulation of optoelectronic devices, Opt. Quantum Electron. 40 (14–15) (2008) 1077–1083.

Please cite this article as: P. Farrell and D. Peschka, Nonlinear diffusion, boundary layers and nonsmoothness: Analysis of challenges in drift–diffusion semiconductor simulations, Computers and Mathematics with Applications (2019), https://doi.org/10.1016/j.camwa.2019.06.007.

ARTICLE IN PRESS

[34] J.J. Barnes, R.J. Lomax, Finite-element methods in semiconductor device simulation, IEEE Trans. Electron Devices 24 (8) (1977) 1082–1089, http://dx.doi.org/10.1109/T-ED.1977.18880.

[35] E.M. Buturla, P.E. Cottrell, B.M. Grossman, K.A. Salsburg, Finite-element analysis of semiconductor devices: the fielday program, IBM J. Res. Dev. 25 (4) (1981) 218–231, http://dx.doi.org/10.1147/rd.254.0218.

[36] M. Zlámal, Finite element solution of the fundamental equations of semiconductor devices. I, Math. Comp. 46 (173) (1986) 27, http://dx.doi.org/10.1090/s0025-5718-1986-0815829-6.

[37] D. Peschka, N. Rotundo, M. Thomas, Towards doping optimization of semiconductor lasers, J. Comput. Theor. Trans. 45 (5) (2016) 410–423, http://dx.doi.org/10.1080/23324309.2016.1189940.

[38] M. Auf der Maur, A multiscale simulation environment for electronic and optoelectronic devices (Ph.D. thesis), University of Rom "Tor Vergata", 2008.

[39] G. Cowper, Gaussian quadrature formulas for triangles, Internat. J. Numer. Methods Engrg. 7 (3) (1973) 405–408.

[40] H. Gajewski, Analysis und Numerik von Ladungstransport in Halbleitern, WIAS Rep. (6) (1993).

[41] K. Gärtner, Existence of bounded discrete steady-state solutions of the Van Roosbroeck system on boundary conforming delaunay grids, SIAM J. Sci. Comput. 31 (2) (2009) 1347–1362, http://dx.doi.org/10.1137/070710950.

[42] R. Eymard, T. Gallouët, R. Herbin, Finite volume methods, in: Solution of Equation in $\mathbb{R}^N$ (Part 3), Techniques of Scientific Computing (Part 3), in: Handbook of Numerical Analysis, vol. 7, Elsevier, 2000, pp. 713–1018.

[43] R. Eymard, J. Fuhrmann, K. Gärtner, A finite volume scheme for nonlinear parabolic equations derived from one-dimensional local Dirichlet problems, Numer. Math. 102 (3) (2006) 463–495.

[44] A. Jüngel, P. Pietra, A discretization scheme for a quasi-hydrodynamic semiconductor model, Math. Models Methods Appl. Sci. 07 (07) (1997) 935–955, http://dx.doi.org/10.1142/S0218202597000475.

Please cite this article as: P. Farrell and D. Peschka, Nonlinear diffusion, boundary layers and nonsmoothness: Analysis of challenges in drift–diffusion semiconductor simulations, Computers and Mathematics with Applications (2019), https://doi.org/10.1016/j.camwa.2019.06.007.

12

Highly Accurate Quadrature-based Scharfetter-Gummel Schemes for Charge Transport in Degenerate Semiconductors

M. Patriarca et al. Highly Accurate Quadrature-based Scharfetter-Gummel Schemes for Charge Transport in Degenerate Semiconductors. *Computer Physics Communications* 235 (2018), pp. 40–49. DOI: 10.1016/j.cpc.2018.10.004

Abstract We introduce a family of two point flux expressions for charge carrier transport described by drift-diffusion problems in degenerate semiconductors with non-Boltzmann statistics which can be used in Voronoi finite volume discretizations. In the case of Boltzmann statistics, Scharfetter and Gummel derived such fluxes by solving a linear two point boundary value problem yielding a closed form expression for the flux. Instead, a generalization of this approach to the nonlinear case yields a flux value given implicitly as the solution of a nonlinear integral equation. We examine the solution of this integral equation numerically via quadrature rules to approximate the integral as well as Newton's method to solve the resulting approximate integral equation. This approach results into a family of quadrature-based Scharfetter-Gummel flux approximations. We focus on four quadrature rules and compare the resulting schemes with respect to execution time and accuracy. A convergence study reveals that the solution of the approximate integral equation converges exponentially in terms of the number of quadrature points. With very few integration nodes they are already more accurate than a state-of-the-art reference flux, especially in the challenging physical scenario of high nonlinear diffusion. Finally, we show that thermodynamic consistency is practically guaranteed.

Conception: I developed and guided, the PhD student Matteo Patriarca for this project.

Execution: Matteo Patriarca carried out the implementation in a feedback loop to-

gether with myself.

Reporting: Matteo Patriarca and myself wrote the publication.

Due to copyright reasons, this article cannot be included online.

13

A Novel Surface Remeshing Scheme via Radial Basis Functions and Higher-Dimensional Embedding

F. Dassi, P. Farrell, and H. Si. A Novel Surface Remeshing Scheme via Radial Basis Functions and Higher-Dimensional Embedding. *SIAM Journal on Scientific Computing* 39.3 (2017), B522–B547. DOI: 10.1137/16m1077015

Abstract Many applications heavily rely on piecewise triangular meshes to describe complex surface geometries. The quality of the meshes directly impacts numerical simulations. In practice, however, one often has to deal with several challenges to construct suitable meshes. Some regions in a naively built mesh may be overrefined, others too coarse. Additionally, the triangles may be too thin or not properly oriented. We present a novel surface remeshing procedure which greatly improves a problematic input mesh and overcomes all of these drawbacks. By coupling surface reconstruction via radial basis functions (RBF) with the higher-dimensional embedding (HDE) surface remeshing technique, we can automatically generate a new anisotropic surface mesh with improved mesh quality. Moreover, we are not only able to refine or coarsen certain mesh regions but also align the triangles according to the curvature of the reconstructed surface. This yields an acceptable trade-off between computational complexity and accuracy.

Conception: Franco Dassi and I developed this project jointly.

Execution: I was in charge of the RBF part which I integrated together with Franco Dassi into his HDE code.

Reporting: The report was written by Franco Dassi and myself.

SIAM J. Sci. Comput.
Vol. 39, No. 3, pp. B522–B547
© 2017 Society for Industrial and Applied Mathematics

A NOVEL SURFACE REMESHING SCHEME VIA RADIAL BASIS FUNCTIONS AND HIGHER-DIMENSIONAL EMBEDDING*

FRANCO DASSI†, PATRICIO FARRELL‡, AND HANG SI‡

Abstract. Many applications heavily rely on piecewise triangular meshes to describe complex surface geometries. The quality of the meshes directly impacts numerical simulations. In practice, however, one often has to deal with several challenges to construct suitable meshes. Some regions in a naively built mesh may be overrefined, others too coarse. Additionally, the triangles may be too thin or not properly oriented. We present a novel surface remeshing procedure which greatly improves a problematic input mesh and overcomes all of these drawbacks. By coupling surface reconstruction via radial basis functions with the higher-dimensional embedding surface remeshing technique, we can automatically generate a new anisotropic surface mesh with improved mesh quality. Moreover, we are not only able to refine or coarsen certain mesh regions but also align the triangles according to the curvature of the reconstructed surface. This yields an acceptable trade-off between computational complexity and accuracy.

Key words. anisotropic meshes, radial basis functions, mesh optimization, variational implicit surfaces, geometry processing

AMS subject classifications. 65M50, 65D05

DOI. 10.1137/16M1077015

1. Introduction.

Countless numerical methods need to transfer information from a continuous domain to discrete points on a mesh. Most commonly this problem arises when solving partial differential equations numerically, but it also appears in the context of surface approximation [12, 19, 21, 35] or medical image reconstruction [16].

Hence, finding *optimal* meshes is of utmost importance. Obviously, optimal can mean many things. For a general overview, we refer to [1, 3, 31]. However, two desirable features stand out. On the one hand, our mesh should be built in such way that the data we are interested in (for instance, the solution of a partial differential equation) are approximated fairly accurately. That is, we want to grasp finer details (for example, along boundary layers) as well as large-scale variations. On the other hand, we want to be able to efficiently compute the discrete approximation and only use nodes which enhance its quality.

This leads naturally in two dimensions (2D) and three dimensions (3D) to anisotropic meshes which are able to achieve a reasonable trade-off between accuracy and efficiency. Anisotropic meshes are often used in the context of finite element and finite volume methods and thus appear very frequently in practical applications [17, 18, 20, 32]. However, how to obtain such an anisotropic mesh for a given application is a very open problem. Unfortunately, not many numerical analysts focus on the art of designing precise meshes but rather on discretization techniques for the solution of the continuous problem (e.g., the governing differential equation).

*Submitted to the journal's Computational Methods in Science and Engineering section May 25, 2016; accepted for publication (in revised form) March 24, 2017; published electronically June 20, 2017.
http://www.siam.org/journals/sisc/39-3/M107701.html
Funding: The work of Franco Dassi was partially supported under the "Leibniz—DAAD Research Fellowship 2014".

†Department Mathematics and Applications, University Milano—Bicocca, Via Roberto Cozzi, 55, 20125 Milan, Italy (franco.dassi@unimib.it).
‡Weierstrass Institute (WIAS), Mohrenstr. 39, 10117 Berlin, Germany (patricio.farrell@wias-berlin.de, si@wias-berlin.de).

In this paper, we study how to automatically obtain curvature-adapted surface meshes from low-quality ones. The initial mesh may be too coarse in certain regions or too dense in others. Also, in practice one also has to deal with improperly oriented triangles. While a stretched triangle is not per se unacceptable, it should not be elongated in the direction where the curvature varies a lot. Figure 1 shows what our method achieves. The original mesh on the left is extremely coarse and uniform. The adapted mesh, on the other hand, is denser and refined where necessary. The stretched triangles reflect the curvature nicely. For example, the curvature along the dashed arrows varies more than along the corresponding solid ones. Hence, we need to refine more in the direction of the dashed arrows, which means that the triangles will be stretched along the solid arrows.

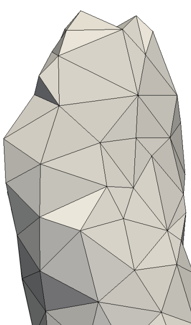
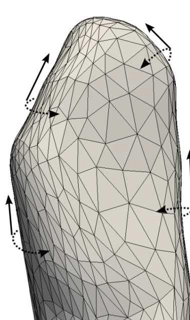

Fig. 1. *A coarse input mesh on the left and the adapted mesh using the novel adaptation procedure on the right. Both figures show a bone from the vertebrae mesh in subsection* 5.4.

The key idea of our method is to combine surface approximation by radial basis functions with the higher-dimensional embedding technique. Radial basis functions (RBFs) have been used for decades in the context of multivariate data approximation [14, 15, 25, 37]. Ironically, their main selling point is that they can be used to interpolate unstructured data without relying on a mesh. Even though they are most commonly used in the context of *meshfree* data approximation, they sometimes have been employed in the context of mesh repair. Carr et al. [6] used polyharmonic radial basis functions to fill in incomplete meshes. Similarly, Marchandise, Piret, and Remacle [30] developed a method to repair meshes obtained from a CAD model or a STereoLithography (STL) triangulation [8].

The higher-dimensional embedding (HDE) was introduced by Cañas and Gortler in [5]. Since then several authors have expanded their ideas [7, 9, 28]. HDE produces an anisotropic triangular curvature-adapted surface mesh that fits an input surface. The anisotropy is obtained by finding a higher-dimensional space in which the mesh is assumed to be uniform and isotropic. Previously, other approaches based on metric tensor fields [19, 21] or minimizing objective functionals [12, 35] have been studied. However, in order to be able to apply either of these strategies one needs to have a priori or a posteriori knowledge of the error, which depends on the problem itself. The HDE, on the other hand, does not require any information on the error. It is solely based on information provided by the embedding map.

The remainder of this paper is organized as follows. After introducing RBFs and the HDE technique in sections 2 and 3, we present our novel surface remeshing approach in section 4 and supplement it in section 5 with extensive numerical studies and successfully apply it to real-life problems.

TABLE 1

Common examples of globally and compactly supported RBFs. All functions are positive definite except the polyharmonic spline which is conditionally positive definite for $d = 3$ with (minimal) order 2. For positive r the truncation operator $(\cdot)_+$ leaves its argument unaltered. For negative arguments it is set to zero. The last column indicates the regularity of the Wendland RBFs.

Global support		Compact support ($d = 3$)	
e^{-r^2}	Gaussian	$\phi_{3,1}(r) = (1-r)_+^4(4r+1)$	C_2
$\sqrt{1+r^2}$	Multiquadric	$\phi_{3,2}(r) = (1-r)_+^6(35r^2+18r+3)$	C_4
$1/\sqrt{1+r^2}$	Inv. multiquadric	$\phi_{3,3}(r) = (1-r)_+^8(32r^3+25r^2+8r+1)$	C_6
r^3	Polyharm. spline	due to Wendland [36]	

For the rest of the paper, we will assume that the surface Γ is given implicitly by the zero level set of some function $F\colon \Omega \subseteq \mathbb{R}^3 \to \mathbb{R}$, i.e.,

$$\Gamma = \left\{(x,y,z)^T \in \Omega \mid F(x,y,z) = 0\right\}, \tag{1}$$

for some bounded domain Ω.

2. Geometry reconstruction with RBFs. RBFs are commonly divided into two categories: positive definite and conditionally positive definite functions. We state both definitions here.

DEFINITION 1 (positive definite function). *Let $\Phi\colon \mathbb{R}^d \to \mathbb{R}$ be a continuous function. We define the matrix $A_{\Phi,X}$ via its ijth entry,*

$$a_{ij} = \Phi(\mathbf{x}_i - \mathbf{x}_j),$$

for any data set $X = \{\mathbf{x}_1, \dots, \mathbf{x}_N\} \subseteq \mathbb{R}^d$ of arbitrary length $N \geq 1$. The function Φ is called positive definite *if the quadratic form*

$$\mathbf{c}^T A_{\Phi,X}\mathbf{c} \tag{2}$$

is positive for all vectors $\mathbf{c} \in \mathbb{R}^N \setminus \{\mathbf{0}\}$.

DEFINITION 2 (conditionally positive definite function). *Let $\mathcal{P}_m(\mathbb{R}^d)$ denote the space of d variate polynomials with absolute degree at most m and dimension $q := \dim \mathcal{P}_m(\mathbb{R}^d) = \binom{m-1+d}{d}$. For a basis $p_1, \dots, p_q$ of this space, define the $N \times q$ polynomial matrix P_X through its ijth entry,*

$$p_{ij} = p_i(\mathbf{x}_j),$$

where $\mathbf{x}_j \in X$. The function Φ is called conditionally positive definite of order m *if the quadratic form* (2) *is positive for all X and for all $\mathbf{c} \in \mathbb{R}^N \setminus \{\mathbf{0}\}$ which additionally satisfy the constraint $P_X^T\mathbf{c} = \mathbf{0}$.*

One typically speaks of RBFs if one additionally assumes that Φ is a radial function, i.e., there exists a function $\phi\colon \mathbb{R}_{\geq 0} \to \mathbb{R}$ such that $\Phi(\mathbf{x}) = \phi(\|\mathbf{x}\|)$. Common examples of RBFs are shown in Table 1. Trivially, a positive definite function is also a conditionally positive definite function of order $m = 0$ and conditionally positive functions of order m are also conditionally positive definite for any order higher than m. Hence, the order usually shall denote the smallest positive integer m.

Suppose we want to recover a function $f\colon \mathbb{R}^d \to \mathbb{R}$ known on some data set $X = \{\mathbf{x}_i\}_{i=1}^N$. We can solve the interpolation problem

$$f(\mathbf{x}_i) = s(\mathbf{x}_i), \qquad 1 \leq i \leq N, \tag{3}$$

for the interpolant $s\colon \mathbb{R}^d \to \mathbb{R}$ using RBFs by making the ansatz

$$s(\mathbf{x}) = \sum_{j=1}^{N} \alpha_j \Phi(\mathbf{x} - \mathbf{x}_j) \tag{4}$$

in the case of a positive definite Φ and

$$s(\mathbf{x}) = \sum_{j=1}^{N} \alpha_j \Phi(\mathbf{x} - \mathbf{x}_j) + \sum_{k=1}^{q} \beta_k p_k(\mathbf{x}) \tag{5}$$

in the case of conditionally positive definite functions. The coefficients $\boldsymbol{\alpha} = (\alpha_j) \in \mathbb{R}^N, \boldsymbol{\beta} = (\beta_k) \in \mathbb{R}^q$ need to be determined by applying the interpolation condition (3) to either (4) or (5). Hence, one needs to solve either

$$A_{\Phi,X}\boldsymbol{\alpha} = \mathbf{f} \qquad \text{or} \qquad \begin{pmatrix} A_{\Phi,X} & P_X \\ P_X^T & 0 \end{pmatrix} \begin{pmatrix} \boldsymbol{\alpha} \\ \boldsymbol{\beta} \end{pmatrix} = \begin{pmatrix} \mathbf{f} \\ \mathbf{0} \end{pmatrix}, \tag{6}$$

where $\mathbf{f} = (f(\mathbf{x}_j))$.

For positive definite functions, the linear system is positive definite by construction. Hence, the coefficients can be determined uniquely. It is also not difficult to verify that the second choice for the interpolant leads to unique coefficients in the case of conditionally positive definite functions; see [37, Theorem 8.21] for details. In the case of conditionally positive definite functions, it is known that at least $N - q$ eigenvalues of the matrix $A_{\Phi,X}$ are positive [37, section 8.1].

Another criterion for classifying RBFs is whether they have compact support or not. This is an advantageous feature for very large data sets since the matrix $A_{\Phi,X}$ becomes sparse if the support radius is small enough. It is well known that for compactly supported RBFs the polynomial part in (5) has to vanish. There are no nontrivial conditionally positive definite functions with compact support [37, Theorem 9.1]. Wendland [36] presented a class of compactly supported RBFs which consist of polynomials within their support. The degree of the polynomials for a given space dimension and smoothness parameter is minimal.

2.1. Surface reconstruction with RBFs. We cannot simply replace the target function f in (3) with the function F whose zero level set describes the implicit surface (1) since the right-hand sides of the linear systems (6) vanish, which implies that the coefficients vanish as well. Carr et al. [6] therefore made the additional assumption that the normal vectors are known. One then can also prescribe on-surface and off-surface points. Assume that the points on the surface are denoted with $X = \{\mathbf{x}_1, \ldots, \mathbf{x}_N\}$ and the corresponding normal vectors with $M = \{\mathbf{n}_1, \ldots, \mathbf{n}_N\}$. Then one can define the surface interpolation problem

$$\begin{aligned} s(\mathbf{x}_i) &= F(\mathbf{x}_i) = 0, & 1 \le i \le N & \quad \text{(on-surface points)}, \\ s(\mathbf{x}_i + \varepsilon\mathbf{n}_i) &= F(\mathbf{x}_i + \varepsilon\mathbf{n}_i) = \varepsilon, & N+1 \le i \le 2N & \quad \text{(off-surface points)}, \end{aligned} \tag{7}$$

for some parameter $\varepsilon > 0$. Since the right-hand side is no longer zero, we now find nontrivial solutions to the linear systems (6). Actually, it is enough to define just one off-set point to get a nontrivial solution. Moreover, it is even possible to add more constraints. For example, if the quality of the approximation does not meet the expectations, one can add more points (which increases of course the linear system that needs to be solved). One possibility [6] is to consider $s(\mathbf{x}_i - \varepsilon\mathbf{n}_i) = F(\mathbf{x}_i - \varepsilon\mathbf{n}_i) = -\varepsilon$ for $2N + 1 \le i \le 3N$. We denote the zero level set of the RBF approximation with Γ_0^s.

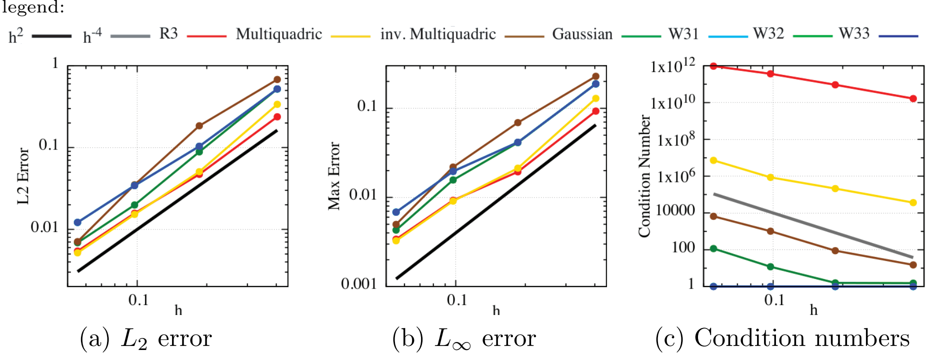

(a) L_2 error (b) L_∞ error (c) Condition numbers

FIG. 2. *Comparison of different RBFs for varying mesh norms for* $\varepsilon = 1/8$ *and the implicit function* F *given by* (10)*. The arguments are scaled by* $1/10$.

2.2. Partitioning the RBF interpolant. To reduce the computational cost when solving the linear system (6) or when projecting points onto the surface (see subsection 4.3) we consider a disjoint partition of the surface

$$\Gamma_h^{ini} = \Gamma_{1,h}^{ini} \cup \Gamma_{2,h}^{ini} \cup \cdots \cup \Gamma_{K,h}^{ini} \tag{8}$$

for $K \in \mathbb{N}$. Let X_i denote the points on the surface patch $\Gamma_{i,h}^{ini}$ and M_i the corresponding normals. Now we can solve the interpolation problem (7) locally defined on each patch $\Gamma_{i,h}^{ini}$ and obtain local interpolants s_i whose zero level sets $\Gamma_0^{s_i}$ approximate $\Gamma_{i,h}^{ini}$. Then the global interpolant is defined as

$$s(x,y,z) := \begin{cases} s_1(x,y,z) & \text{if } (x,y,z)^T \in \Gamma_{1,h}^{ini}, \\ s_2(x,y,z) & \text{if } (x,y,z)^T \in \Gamma_{2,h}^{ini}, \\ \vdots & \vdots \\ s_K(x,y,z) & \text{if } (x,y,z)^T \in \Gamma_{K,h}^{ini}. \end{cases} \tag{9}$$

2.3. Errors and conditioning of the RBF interpolant. In order to study the approximation quality and the conditioning of the RBF interpolant, we choose a simple ellipsoid surface which is given by the zero level set of the function

$$F(x,y,z) = x^2/4 + y^2/4 + z^2/0.2 - 1. \tag{10}$$

The reason for this relatively simple surface is that it allows one to compute the error between our approximation and the exact solution. For nested point sets on the ellipsoid where the mesh norm h (the radius of the largest ball which does not contain any data point) is reduced each time by a factor of two, we see the results in Figure 2. The L_2 and L_∞ errors of all RBF approximations considered seem to converge at least quadratically.

The condition numbers, however, behave quite differently. Whereas all globally supported RBFs behave eventually roughly like h^{-4}, the condition numbers of the compactly supported RBFs grow only very mildly (which is not even visible in the log plot). As mentioned before, this is not a surprise as their compact support leads to a sparse linear system. Even though these results might not yet capture the long term behavior, they are from a computational point of view more interesting as one would like to use as few points as possible.

We report here that other surfaces (sphere and one-sheeted hyperboloid) have been examined with similar results: at least quadratic convergence for both errors and a growth in condition number of at least h^{-4}.

3. Higher-dimensional embedding. The HDE technique fits a triangular surface mesh to a given geometry by enlarging the space we are originally interested in. The key assumption of HDE is that a uniform isotropic mesh in a higher-dimensional space will correspond to an anisotropic mesh in a lower-dimensional space.

This concept is best explained with Figure 3. The left image shows a uniform isotropic triangular mesh in $\mathbb{R}^3$. However, if projected onto $\mathbb{R}^2$ the mesh becomes anisotropic, which is shown in the figure on the right.

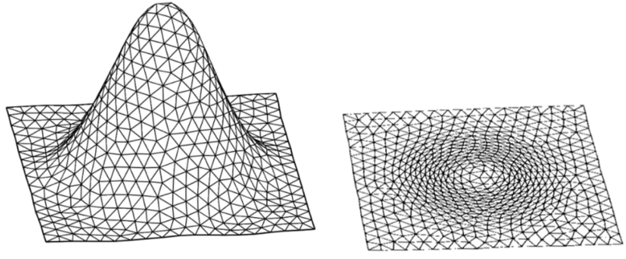

FIG. 3. *An isotropic mesh in the higher-dimensional space* $\mathbb{R}^3$ *(left) and the corresponding anisotropic mesh in* $\mathbb{R}^2$ *(right). This figure encapsulates the key idea behind the HDE technique* [28]. *Courtesy of B. Lévy.*

To obtain an anisotropic curvature-adapted mesh of an input surface $\Gamma \subset \mathbb{R}^3$, we define the embedding map $\Psi : \Gamma \to \mathbb{R}^6$ by

$$\Psi(\mathbf{x}) = (x,\, y,\, z,\, \sigma\, n_x,\, \sigma\, n_y,\, \sigma\, n_z)^T\,, \tag{11}$$

where $\mathbf{n} = (n_x, n_y, n_z)^T$ denotes the unit normal to Γ at $\mathbf{x} = (x,\, y,\, z)^T$ and $\sigma > 0$ is a constant that controls the influence of the normals in the embedding map. For small σ the mapping Ψ is close to the identity in $\mathbb{R}^3$ embedded in $\mathbb{R}^6$, i.e., $\Psi(\mathbf{x}) \approx (x, y, z, 0, 0, 0)^T$. Larger values of σ put more emphasis on the normal components of the surface Γ.

In the higher-dimensional space points on Γ are enriched with surface normal information. Consider for instance two generic points $\mathbf{a}, \mathbf{b} \in \Gamma$ and the edge $\overline{\mathbf{ab}}$. If the surface is a plane, the normals at the endpoints are the same. Consequently, the length of the edge in $\mathbb{R}^3$, denoted with $l_{\mathbf{ab}}$, coincides exactly with the length measured in the higher-dimensional space $l^{6d}_{\mathbf{ab}}$. On the other hand, if the surface is curved, the normals at the endpoints are different and $l^{6d}_{\mathbf{ab}}$ becomes much larger than $l_{\mathbf{ab}}$.

3.1. Mesh generation in higher dimensions. There are two established ways to build a uniform isotropic mesh in the higher-dimensional space. In [28], the authors propose an approach based on the restricted centroidal Voronoi tessellation. Starting from the embedding defined in (11), they compute the Voronoi tessellation of an initial point set $\{\mathbf{p}_i\}_{i=0}^N$. Then, they optimize this tessellation to get a restricted centroidal Voronoi tessellation, i.e., a restricted Voronoi tessellation where $\mathbf{p}_i = \mathbf{g}_i$ for all $i = 1, 2, \ldots, N$. Here, $\mathbf{g}_i$ denotes the centroid of the Voronoi cell associated with the point $\mathbf{p}_i$. The triangular mesh is finally obtained by duality from this Voronoi diagram.

This mesh generation strategy presents a couple of challenges. First, the computation and the optimization of the restricted Voronoi tessellation is made in the higher-dimensional space, incurring a high computational cost. Second, the sharp features of the input geometry are smoothed and overrefined. Moreover, this method can produce invalid meshes with selfintersection.

In [7, 9], a different method was proposed to construct a uniform isotropic mesh in the higher-dimensional space. The idea is to exploit the standard scalar product in the higher-dimensional space. Consider three points $\mathbf{a}$, $\mathbf{b}$, and $\mathbf{c}$ on the surface Γ, then the lengths and the angles in the higher-dimensional space are defined as

$$
\begin{aligned}
l^{6d}_{\mathbf{ab}} &:= \big|\big|\, \Psi(\mathbf{a}) - \Psi(\mathbf{b}) \,\big|\big|_{6\mathrm{d}} := \sqrt{\Big(\Psi(\mathbf{a}) - \Psi(\mathbf{b}), \Psi(\mathbf{a}) - \Psi(\mathbf{b}) \Big)_{6\mathrm{d}}}\,, \\
\cos\left(\theta^{6d}_{\mathbf{acb}}\right) &:= \frac{\Big(\Psi(\mathbf{a}) - \Psi(\mathbf{c}), \Psi(\mathbf{b}) - \Psi(\mathbf{c}) \Big)_{6\mathrm{d}}}{l^{6d}_{\mathbf{ac}}\, l^{6d}_{\mathbf{bc}}}\,.
\end{aligned} \tag{12}
$$

We define a target edge length l^{6d} in the higher-dimensional space. Then the HDE remeshing procedure modifies an initial mesh Γ_h^{ini} in such a way that

$$
l^{6d}_{\mathbf{e}} \approx l^{6d} \qquad \text{and} \qquad \cos\left(\theta^{6d}_{\alpha}\right) \approx \frac{1}{2} \qquad \forall \mathbf{e} \in \mathcal{E} \quad \text{and} \quad \forall \alpha \in \mathcal{A}\,, \tag{13}
$$

where $\mathcal{E}$ and $\mathcal{A}$ are the sets of edges and angles of all mesh triangles.

Remark 3. The method proposed in [7, 9] does not embed the mesh in $\mathbb{R}^6$. Only the lengths and angles are computed in the higher-dimensional space. The mesh is modified in $\mathbb{R}^3$ by standard mesh operations for triangular elements such as edge flipping, edge splitting/contraction, and node smoothing.

This method overcomes all of the previously discussed drawbacks. It is computationally cheaper, the sharp features of the input mesh are preserved, and no triangle of the resulting mesh intersects with itself [9].

4. Surface remeshing by RBF and HDE. In this section, we describe in detail the novel anisotropic curvature adapted remeshing procedure. Starting from a conformal triangular surface mesh Γ_h^{ini}, we proceed as follows:

(1) Build RBF approximation Γ_0^s of the initial surface mesh Γ_h^{ini} (subsection 4.1), and
(2) Construct final adapted mesh Γ_h^{fin} via HDE including:
   - local mesh modifications (subsection 4.2), and
   - projections onto the surface Γ_0^s (subsection 4.3).

4.1. Building RBF approximation. When constructing the continuous approximation of Γ_h^{ini}, the user has to specify the type of RBF Φ, the parameter ε, and the number of partitions K. In order to set up the interpolation problem defined in (7), we use the vertices of Γ_h^{ini} as interpolation nodes X. By averaging the normals of the triangles that share a generic vertex $\mathbf{x}_i$, we define the normals $\mathbf{n}_i$ at this point and obtain the set M. Finally, we construct and solve the linear system (6) to derive the continuous interpolant s.

4.2. Surface remeshing via HDE. Our surface remeshing algorithm is stated in Algorithm 1. It takes five inputs:

- σ, the (anisotropy) parameter of the embedding map Ψ;
- l^{6d}, the target edge length in the higher-dimensional space;
- Γ_h^{ini}, the initial surface mesh;
- `lenFactor`, the relative tolerance in the interval $(0, 1)$ for the target edge length l^{6d}; and
- `maxIter`, the maximal number of iterations.

The last two parameters are the stopping criteria we employ for our algorithm. It is possible to incorporate other stopping criteria such as (anisotropic) mesh quality measures.

Starting from the initial mesh Γ_h^{ini}, this algorithm iteratively modifies the mesh to make it as uniform as possible with respect to the embedding map Ψ. The algorithm terminates either when all edge lengths are within a prescribed tolerance of the target edge length (line 11 in Algorithm 1), or when it reaches the maximal number of iterations `maxIter`. Since there is no guarantee that *all* $6d$ edge lengths will satisfy the condition in line 11, the additional parameter `maxIter` is used to force the algorithm to terminate. In section 5, we always consider `lenFactor`=0.4 and `maxIter`=9.

Algorithm 1. The anisotropic mesh adaptation.

IMPROVE(σ, l^{6d}, Γ_h^{ini}, `lenFactor`, `maxIter`)
1: **for** $i = 1, \ldots,$ `maxIter` **do**
2: **repeat**
3: contract all edges which satisfy $l_{\mathbf{e}}^{6d} < 0.5\, l^{6d}$;
4: smooth 30% of vertices;
5: flip edges if (14) holds;
6: **until** $l_{\mathbf{e}}^{6d} \geq 0.5\, l^{6d}$ for all edges $\mathbf{e}$
7: split all edges which satisfy $l_{\mathbf{e}}^{6d} > 1.5\, l^{6d}$;
8: flip edges if (14) holds;
9: smooth 30% of vertices;
10: flip edges if (14) holds;
11: **if** $|l_{\mathbf{e}}^{6d} - l^{6d}|/l^{6d} <$ `lenFactor` for all edges $\mathbf{e}$ **then**
12: break;
13: **end if**
14: **end for**

This algorithm employs the common local mesh modification procedures such as edge flipping, edge contraction, edge splitting, and vertex smoothing [10, 21, 23, 24], but it computes the edge lengths and angles in the higher-dimensional space. In the following, we first explain these mesh modifications.

The most challenging task is to correctly implement the edge splitting and edge contraction operations. Indeed both of these operations require adding or moving nodes in such a way that they stay on the surface. In section 4.3, we explain a special projection method which achieves this.

Edge-flip. Consider two triangles $\Delta_{\mathbf{abc}}$ and $\Delta_{\mathbf{bad}}$ whose common edge is $\overline{\mathbf{ab}}$. Flipping the edge $\overline{\mathbf{ab}}$ creates two new triangles $\Delta_{\mathbf{cda}}$ and $\Delta_{\mathbf{dcb}}$ and replaces the edge $\overline{\mathbf{ab}}$ with $\overline{\mathbf{cd}}$; see Figure 4.

It is not always possible to flip the edge $\overline{\mathbf{ab}}$ in a triangular surface mesh. The edge $\overline{\mathbf{ab}}$ is flippable if it satisfies the following conditions:

(i) $\overline{\mathbf{ab}}$ does not belong to the boundary of the mesh;
(ii) $\overline{\mathbf{cd}}$ does not already belong to the mesh;

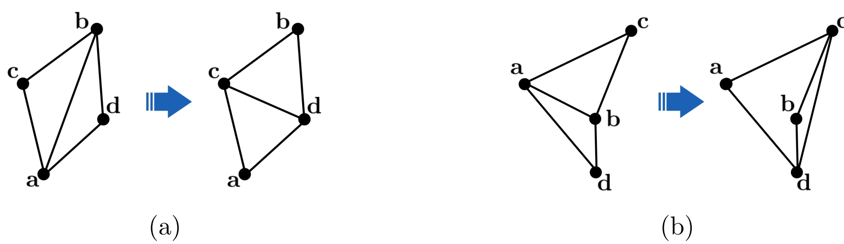

(a) (b)

FIG. 4. *Example for an edge flip* (a) *and two neighboring triangles in* (b) *that do not satisfy criterion* (iii).

(iii) the internal angles of the triangles satisfy

$$\theta_{\mathbf{abc}} + \theta_{\mathbf{abd}} < \pi \qquad \text{and} \qquad \theta_{\mathbf{bac}} + \theta_{\mathbf{bad}} < \pi\,;$$

(iv) the angle between the normals of the triangles $\Delta_{\mathbf{abc}}$ and $\Delta_{\mathbf{bad}}$ is lower than some threshold value. Here we set 80°.

If an edge $\overline{\mathbf{ab}}$ satisfies all these conditions, it is flippable. We decide to actually flip the edge $\overline{\mathbf{ab}}$ if the relation

$$\theta^{6d}_{\mathbf{acb}} + \theta^{6d}_{\mathbf{adb}} > \pi \tag{14}$$

holds, where $\theta^{6d}_{\mathbf{acb}}$ and $\theta^{6d}_{\mathbf{adb}}$ are the angles measured in the higher-dimensional space. This condition is inspired by the well-known Delaunay criterion, reinterpreted in the higher-dimensional space [11].

Edge contraction and edge splitting. We try to approximately match all edge lengths of our mesh to a given target edge length l^{6d} by

- contracting the edge $\mathbf{e}$ if $l^{6d}_{\mathbf{e}} < 0.5\, l^{6d}$,
- splitting the edge $\mathbf{e}$ if $l^{6d}_{\mathbf{e}} > 1.5\, l^{6d}$, and
- otherwise applying neither edge contraction nor edge splitting.

Node smoothing. Unlike the previous mesh modification procedures, this operation does not change the topology of the mesh. It simply moves a point $\mathbf{x}$ to a new location $\mathbf{x}'$. This new location can be computed as follows:

$$\mathbf{x}' = \mathbf{x} + \alpha \sum_{\mathbf{x}_i \in \omega_{\mathbf{x}}} w(d(\mathbf{x}\,, \mathbf{x}_i))\mathbf{u}_i\,. \tag{15}$$

Here α is a scaling parameter, $w : \mathbb{R} \to \mathbb{R}$ is a weight function, $\omega_{\mathbf{x}}$ is the set of vertices that are connected to the old point $\mathbf{x}$, $\mathbf{u}_i$ denotes the unit vectors that point from $\mathbf{x}$ to $\mathbf{x}_i$ and d is the distance between $\mathbf{x}$ and $\mathbf{x}_i$.

Different choices of α and w in (15) lead to different node smoothing methods. Here we use the node smoothing method proposed in [9]. That means the distances d are computed in the higher-dimensional space and the parameter α is set to $1/(\sum_{\mathbf{x}_i \in \omega_{\mathbf{x}}} w(d(\mathbf{x}\,, \mathbf{x}_i)))$ and $w(x) := (1 - x^4)e^{-x^4}$ as introduced in [4].

4.3. Projection of nodes onto $\boldsymbol{\Gamma}^s_{\mathbf{0}}$. In this section, we describe how we apply edge splitting and edge contraction while constraining all new points onto the RBF surface Γ^s_0. Applying these operations naively will fail.

Projection after edge splitting or node smoothing. If we apply edge splitting or node smoothing to a triangular surface mesh, it is not a priori guaranteed that these operations yield a new point that lies on the reconstructed surface Γ_0^s.

Consider, for instance, the edge splitting operation. If we simply halve the edge, the new point lies only under very special circumstances on Γ_0^s. Moreover, since the new point is usually not on the surface, the unit normal is not defined. Node smoothing leads to a similar problem.

To avoid this issue, we exploit a projection algorithm. If we split an edge or move a point using node smoothing, we project the resulting point onto the RBF surface reconstruction Γ_0^s. Hartmann [22] provided a robust algorithm to project a point onto a surface defined via the zero level set of a function. This procedure is a combination of orthogonal projections on tangent planes as well as tangent parabolas. It requires only first-order derivatives and uses a steepest descent method. In our case, the surface is described via Γ_0^s, i.e., the zero level set of the interpolant s. Figure 5 provides a two-dimensional example of node projection after edge splitting.

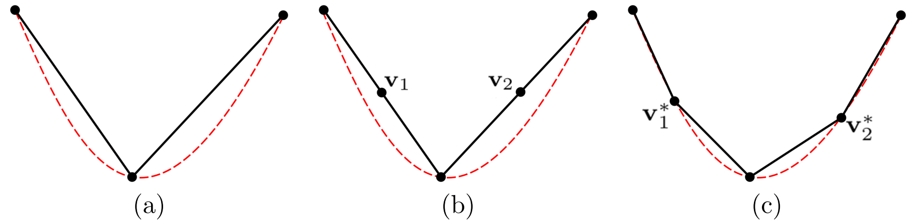

FIG. 5. *Figure* (a) *shows a coarse input mesh (solid line) which approximates the reconstructed curve (dashed line). In figure* (b) *the edges are halved. The midpoints* $\mathbf{v}_1$ *and* $\mathbf{v}_2$ *do not lie on the reconstructed curve. Finally, figure* (c) *shows the new points* $\mathbf{v}_1^*$ *and* $\mathbf{v}_2^*$ *projected onto the dashed curve using a steepest descent method.*

Edge contraction to endpoint. An edge $\mathbf{e}$ can be contracted to different locations. We decide to contract it to one of the endpoints [11] to avoid having to project this point onto Γ_0^s. The endpoints lie on Γ_0^s by construction where the normals are well defined. Figure 6 provides a two-dimensional example.

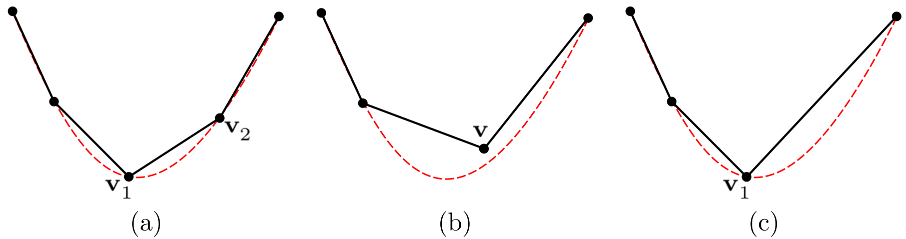

FIG. 6. *Figure* (a) *shows a fine input mesh (solid line) which approximates the reconstructed curve (dashed line). In figure* (b), *the edge* $\overline{\mathbf{v}_1\mathbf{v}_2}$ *is contracted to its midpoint* $\mathbf{v}$, *which does not lie on the reconstructed curve. However, in figure* (c) *the edge* $\overline{\mathbf{v}_1\mathbf{v}_2}$ *in contracted to the endpoint* $\mathbf{v}_1$ *which by construction automatically lies on the dashed curve.*

Defining normals on $\boldsymbol{\Gamma_0^s}$. Consider the interpolant s and the RBF approximation of the discrete input surface Γ_0^s. We use the gradient components of the function s to obtain the unit normal of Γ_0^s for a point $\mathbf{x} = (x, y, z)^T$.

Let $(\nabla s)_x$, $(\nabla s)_y$, and $(\nabla s)_z$ be the x, y, and z the components of s, respectively. Then, the unit normal $\mathbf{n} = (n_x, n_y, n_z)^T$ at point $\mathbf{x}$ is defined as

$$n_x := \frac{(\nabla s)_x}{||\nabla s||}, \quad n_y := \frac{(\nabla s)_y}{||\nabla s||}, \quad n_z := \frac{(\nabla s)_z}{||\nabla s||}, \tag{16}$$

where $||\nabla s||$ denotes the standard Euclidean norm of ∇s. We point out that by construction $||\nabla s||$ does not vanish on Γ_0^s.

Overlapping and projection. To reduce the computational effort, we may choose to partition the domain according to (8). Then the interpolant s whose zero level set defines the surface Γ_0^s is given by (9).

Each time we project some node onto the surface, we have to determine the local function s_i on which we want to project. However, near the boundary between neighboring patches the node can be projected on more than one local interpolant. Also having to determine which local interpolant to project on involves a costly point search algorithm. Unfortunately, we cannot use a standard nearest-neighbor search since it is not a priori guaranteed that the closest reconstructed patch is the one we want to project our point on.

For a given patch $\Gamma_{i,h}^{ini}$ with $1 \leq i \leq K$, we assign to each of its points the flag i. Whenever we halve an edge, we have to project the new point on one of the patches. If both endpoints belong to the same patch, the new point inherits the same flag and we project it on this patch. On the other hand, if the endpoints have different flags, say i and j, we assign to the new point the flag $k := \min\{i, j\}$ and project it on $\Gamma_0^{s_k}$.

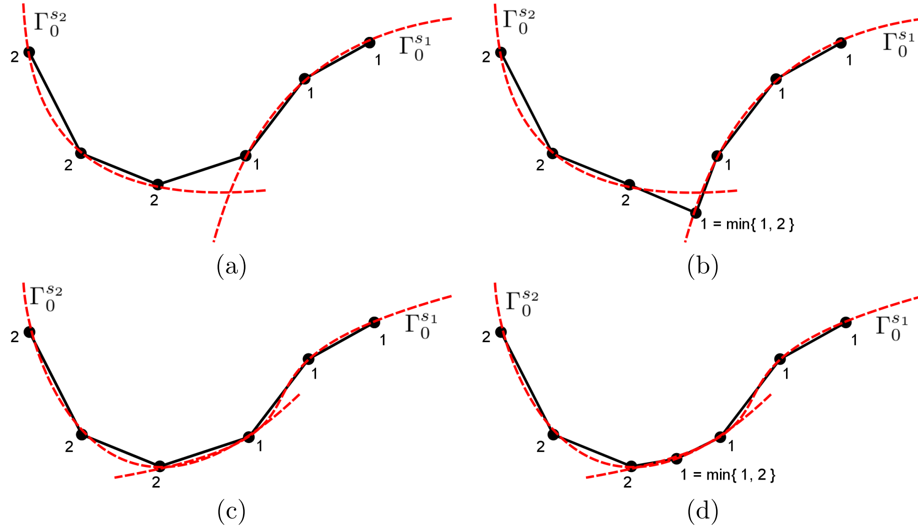

Fig. 7. *A two-dimensional example illustrating the discontinuity arising from projecting on a partitioned surface. The dashed lines are the reconstructed curves. For each point we denote the patch it belongs to by a number* (a). *When we split an edge whose endpoints belong to different patches, we choose the smaller one, leading to a discontinuity (a kink) in the surface* (b). *The third figure shows the new curves constructed from overlapping interpolation point sets* (c). *This considerably reduces the discontinuity along the boundary between both patches* (d).

This strategy will avoid the onerous searching procedure, but it may lead to discontinuities near the boundary of two patches; see Figure 7 (a) and (b). Hence, we introduce overlapping patches. Consider a partition $\Gamma_{i,h}^{ini}$ and the set of vertices

that lie on its boundary. We add to the sets X_i and M_i the vertices of Γ_h^{ini} which share a triangle T that has at least one vertex on the boundary of the patch $\partial\Gamma_{i,h}^{ini}$; see Figure 8. This process is usually also done for the neighboring patch, creating two patches which now overlap. If necessary, we successively increase the overlap, thus enlarging the sets X_i and M_i; see Figure 8 (c) and (d). The parameter Ov will count how many overlap layers have been added. The impact of this parameter on the global approximation is studied in subsection 5.1.1.

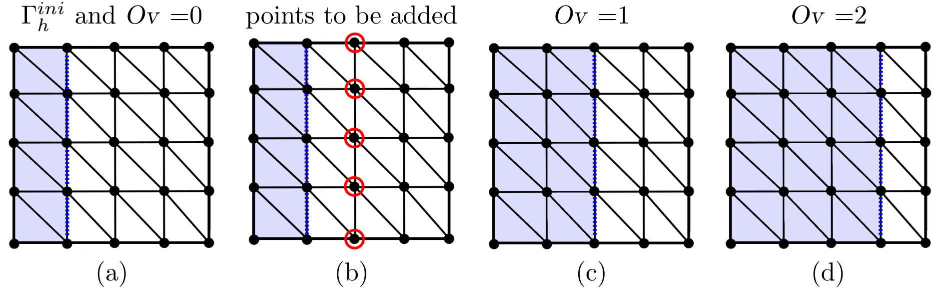

FIG. 8. *A simple example of the overlap for a structured mesh on a square. In* (a) *the original patch* $\Gamma_{1,h}^{ini}$ *is shown. Furthermore,* (b) *shows the patch* $\Gamma_{1,h}^{ini}$, *its boundary* $\partial\Gamma_{1,h}^{ini}$, *and the points which will be added, highlighted with circles. The cases* $Ov = 1$ *and* $Ov = 2$ *are provided in* (c) *and* (d), *respectively.*

5. Numerical examples. In the following, we study different input meshes to assess the quality and robustness of our new anisotropic remeshing method, described in section 4. We start by examining three model geometries to analyze the condition numbers as well as the impact of the different parameters such as the overlap parameter Ov, the edge length l^{6d}, and the embedding parameter σ on the final mesh Γ_h^{fin}. Additionally, we show that our method can not only be used to fill in more detail but also to thin out very complex meshes. In the last subsection, we apply our method to real-life examples from medical applications for which we would like to build anisotropic meshes.

To assess the degree of anisotropy of our mesh, we compute the *global aspect ratio*

$$q_{\Gamma_h} := \max_{T\in\Gamma_h} q_T\,, \tag{17}$$

where $q_T := R_T/(2\,r_T)$ is the so-called *aspect ratio* of the triangle T. Here R_T and r_T are the radii of the circumscribed and inscribed circle of T, respectively [34]. We observe that $q_T \geq 1$ by construction. If $q_T = 1$, then T is an equilateral triangle, while if $q_T \gg 1$, the triangle T is stretched.

The partitioning strategy described in section 2.2 helps to reduce the linear systems to a size where we can use unpreconditioned direct solvers for all examples in this section. For our computations we have used the PARDISO solver [26, 33]. However, if the systems become even larger, it is necessary to employ iterative solvers. If the matrix $A_{\Phi,X}$ is symmetric positive definite, we can use the conjugate gradients method. On the other hand, if the matrix has the saddle-point structure given in (6), the whole system is no longer guaranteed to be positive definite and one could use GMRES. Another way to reduce the computational cost is to employ preconditioners. Finding useful preconditioners for RBF systems is still an open topic [2, 29]. In order to take advantage of the saddle-point structure for conditionally positive RBFs, one might

adapt ideas from [13]. In general, it is well known that the condition numbers grow when two points on the surface become very close [37]. Hence, distributing the points in such a way that the separation distance (the smallest distance between any two points in the data set) is comparable to the mesh norm is useful.

5.1. Sensitivity analysis of the parameters. We analyze the most relevant parameters in the adaptation procedure for a model input mesh (the cat mesh shown in Figure 9 on the left). More precisely, in subsection 5.1.1, we focus on the influence of the Ov parameter when constructing Γ_0^s. In subsection 5.1.2 we compute the condition numbers of the matrices for different partitions. In subsection 5.1.3, we conduct a sensitivity analysis of the target edge length l^{6d} and the embedding parameter σ. Finally, in subsection 5.1.4, we study the input tolerance `lenFactor` which serves as one of our termination criteria. Throughout this subsection, we consider the discrete input surface shown in Figure 9 (left).

5.1.1. Overlap analysis. We study more carefully the influence of the overlap parameter Ov. This is a key parameter when partitioning like in (8) since it reduces the discontinuities of Γ_0^s along the patch boundaries. To understand its effect on the reconstructed geometry, we use thin plate splines, $\varepsilon = 0.1$ and $K = 20$.

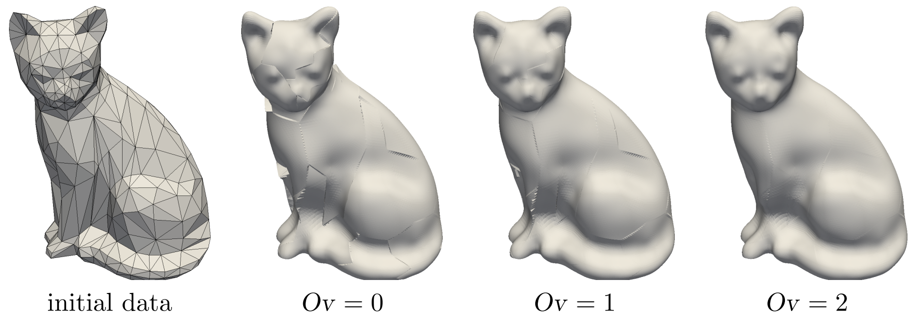

initial data $Ov = 0$ $Ov = 1$ $Ov = 2$

FIG. 9. *The cat geometry used for the sensitivity analysis of the overlap parameter Ov, the edge length l^{6d}, and the embedding parameter σ. The RBF surface reconstruction Γ_0^s for the cat with different values for Ov.*

From Figure 9 we infer that the smoothness of the approximation increases for higher values of the parameter Ov. Heuristically, an overlap parameter of 2 or 3 yields acceptable approximations.

5.1.2. Condition number analysis. In this subsection, we analyze how the stability of the linear systems (6) benefits from the partitioning introduced in section 2.2. We choose thin plate splines, $\epsilon = 0.1$ and $Ov = 2$. We report the largest and the smallest condition numbers among all partition matrices, denoted by $\max_{\text{cond}}$ and $\min_{\text{cond}}$, respectively. Naturally, for $K = 1$ the partition consists only of one patch and both numbers coincide. The results are shown in Table 2. The condition numbers decrease for lager values of K.

5.1.3. Mesh adaptation parameters. Next, we perform experiments to analyze the sensitivity of the target length l^{6d} and the embedding parameter σ. To construct Γ_0^s, we use as before thin plate splines, $\varepsilon = 0.1$ and $K = 20$. Additionally, we set $Ov = 2$ and consider the following sets of values:

$$\sigma \in \{1, 5, 10\} \quad \text{and} \quad l^{6d} \in \{20, 15, 10\}.$$

Table 2
Largest and smallest condition numbers for different numbers of partitions K.

K	$\max_{\text{cond}}$	(matrix size)	$\min_{\text{cond}}$	(matrix size)
1	2.1292e+16	(704)	2.1292e+16	(704)
3	2.8812e+15	(268)	1.6045e+13	(242)
6	9.8719e+14	(148)	3.3762e+12	(130)
9	6.9304e+14	(100)	9.4852e+11	(90)

In Figure 11, we show the resulting meshes and provide a quantitative analysis in Table 3. Our remeshing algorithm behaves as expected. If we fix the parameter σ and decrease l^{6d}, the resulting mesh becomes finer; see the columns in Figure 11 and Table 3.

On the other hand, if we fix the target edge length l^{6d} and increase the parameter σ, we observe a similar behavior; see the rows of Figure 11 and Table 3, respectively. The lengths in the higher-dimensional space (12) grow when increasing the parameter σ, which implies there is a greater amount of sampling to achieve the same target edge length. However, since σ controls the influence of the normals in the embedding map, the sampling is localized only in high curvature regions; see the details in Figure 10.

In Table 3, we also collect the computation times. More specifically, *RBF* refers to the time required to construct the RBF approximation while *remesh* is the average time of one iteration in the adapation procedure of Algorithm 1. As expected the time to construct the RBF approximation is not influenced by the remeshing parameters. However, the time for the remeshing procedure grows for higher values of σ and lower values of l^{6d} since these two parameters increase the sampling of the initial mesh.

Furthermore, to understand how different the mesh Γ_h is from the geometry reconstructed via the RBFs Γ_0^s, we introduce the *Hausdorff distance*

$$\text{dist}(\Gamma_h, \Gamma_0^s) := \max_{T \in \Gamma_h} s(\mathbf{x}_{\text{bar},T}) , \tag{18}$$

where $\mathbf{x}_{\text{bar},T}$ is the barycenter of the triangle T and s is the signed distance function whose zero level set defines the reconstructed surface Γ_0^s. The smaller the Hausdorff distance, the closer is the final mesh Γ_h to the surface Γ_0^s.

Finally, in Table 4, we provide the percentage of each mesh operation during the remeshing process.

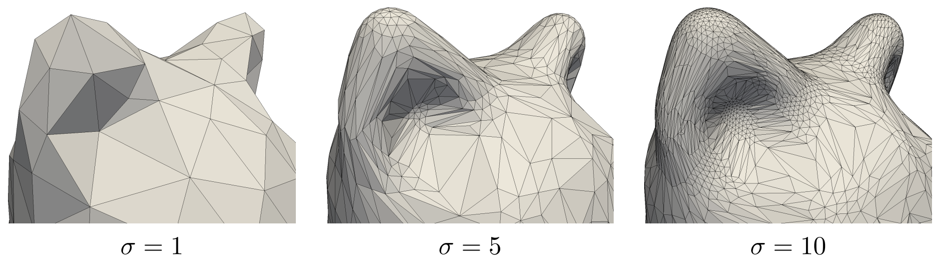

$\sigma = 1$ $\sigma = 5$ $\sigma = 10$

Fig. 10. *A detail of the cat for $l^{6d} = 15$ and different values of σ. In this region the normals vary greatly. Hence, the mesh adaptation procedure refines more and more for increasing values of σ.*

5.1.4. The termination tolerance lenFactor. In this subsection, we analyze the impact of the termination parameter `lenFactor` on the adaptation procedure. To construct Γ_0^s, we use as before thin plate splines, $\varepsilon = 0.1$, $K = 20$, and $Ov = 2$.

Table 3
Global aspect ratios q_{Γ_h}, number of elements (#ele.), Hausdorff distance (HD dist.), time spent on creating the RBF surface reconstruction, as well as the remeshing procedure (average time for one iteration) for different values of σ and l^{6d}.

$l^{6d} \setminus \sigma$	1		5		10	
20	q_{Γ_h}	2.597e+00	q_{Γ_h}	1.449e+01	q_{Γ_h}	3.567e+01
	#ele.	1826	#ele.	3318	#ele.	7743
	HD dist.:	1.3794e-02	HD dist.:	6.5628e-03	HD dist.:	2.8499e-03
	RBF:	0.197 sec.	RBF:	0.201 sec.	RBF:	0.198 sec.
	remesh:	0.544 sec.	remesh:	0.804 sec.	remesh:	1.461 sec.
15	q_{Γ_h}	1.684e+00	q_{Γ_h}	8.441e+00	q_{Γ_h}	2.076e+01
	#ele.	2142	#ele.	4960	#ele.	13 248
	HD dist.:	9.3048e-03	HD dist.:	3.5687e-03	HD dist.:	1.6709e-03
	RBF:	0.207 sec.	RBF:	0.196 sec.	RBF:	0.198 sec.
	remesh:	0.556 sec.	remesh:	0.832 sec.	remesh:	1.786 sec.
10	q_{Γ_h}	2.419e+00	q_{Γ_h}	1.914e+01	q_{Γ_h}	2.935e+01
	#ele.	3264	#ele.	10 029	#ele.	27 943
	HD dist.:	4.5342e-03	HD dist.:	1.1085e-03	HD dist.:	1.0419e-03
	RBF:	0.198 sec.	RBF:	0.198 sec.	RBF:	0.199 sec.
	remesh:	0.577 sec.	remesh:	0.989 sec.	remesh:	2.284 sec.

Table 4
Percentage breakdown of operations in remeshing procedure for each choice of σ and l^{6d}.

$l^{6d} \setminus \sigma$	1		5		10	
20	flips:	18%	flips:	22%	flips:	21%
	smooth:	15%	smooth:	21%	smooth:	41%
	contr:	33%	contr:	27%	contr:	17%
	split:	34%	split:	30%	split:	21%
15	flips:	17%	flips:	19%	flips:	16%
	smooth:	19%	smooth:	33%	smooth:	54%
	contr:	31%	contr:	22%	contr:	12%
	split:	33%	split:	26%	split:	18%
10	flips:	15%	flips:	14%	flips:	10%
	smooth:	28%	smooth:	51%	smooth:	71%
	contr:	27%	contr:	15%	contr:	5%
	split:	30%	split:	20%	split:	14%

We fix the target edge length $l^{6d} = 15$, the embedding parameter $\sigma = 5$, as well as `maxIter` $= 100$, and vary the tolerances `lenFactor`. In particular, we use the following tolerances:

$$\texttt{lenFactor} = \{0.2, 0.3, 0.4, 0.5\}.$$

For each value of `lenFactor` we report in Table 5 the number of iterations, `#iter`, as well as the minimal and maximal $6d$ edge lengths of the mesh, $l^{6d}_{\min}$ and $l^{6d}_{\max}$, respectively. Since our algorithm does not guarantee that all final $6d$ edge lengths are within the `lenFactor` tolerance of the target edge length, the adaptation procedure may require a large number of iterations if the tolerance `lenFactor` is small. Indeed when we set `lenFactor` to 0.1 or 0.2, the maximal number of iterations is reached and Algorithm 1 stopped without satisfying this condition. However, in both these cases $l^{6d}_{\min}$ and $l^{6d}_{\max}$ are close to the target edge length $l^{6d} = 15$, which means that the mesh is approximately uniform and isotropic in the higher-dimensional space.

5.2. Bunny. We examine the well-known Stanford bunny, depicted in Figure 12. To construct Γ^s_0, we use thin plate splines, $\varepsilon = 0.001$, $K = 200$, and $Ov = 3$. The largest condition number for this setup is given by $\max_{\text{cond}} = 1.7997e{+}12$ (matrix size:

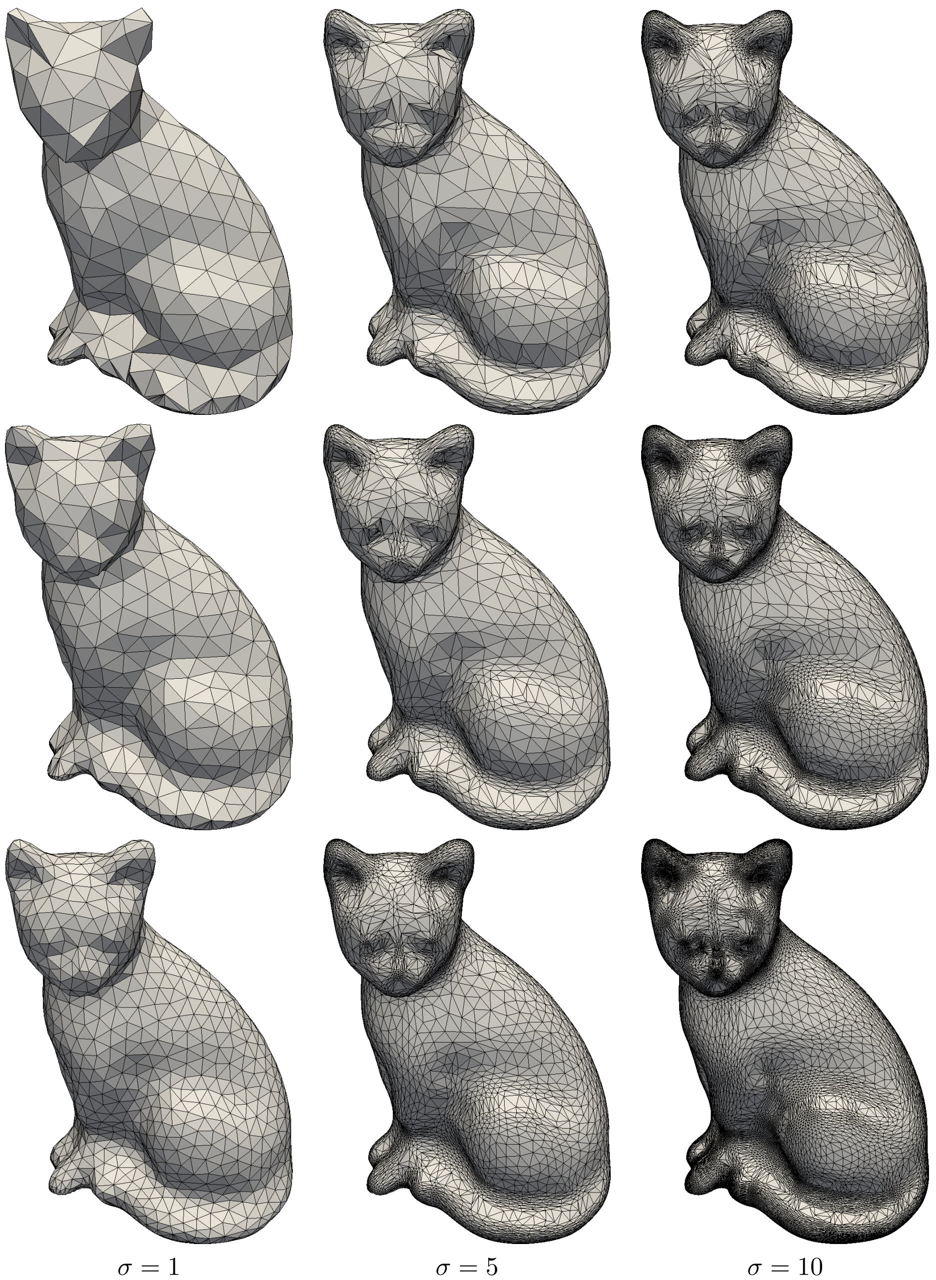

FIG. 11. *Adapted cat meshes for different values of* σ *(columns) and* $l^{6d} = 20, 15, 10$ *(rows, from top to bottom).*

940) and the smallest one by $\min_{\text{cond}} = 1.2369e{+}11$ (matrix size: 664). We run the anisotropic adaptation procedure with $l^{6d} = 0.001$ and $\sigma = 1.0$. In Figure 12, we show both the initial and the resulting mesh. The resulting mesh is strongly anisotropic; in fact. the global aspect ratio q_{Γ_h} is $3.989e{+}02$ and it is more refined than the initial

Table 5

Experiments for different `lenFactor`*: The table shows the number of iterations,* `iter`*, minimal and maximal* 6d *edge lengths of the mesh,* $l^{6d}_{\min}$ *and* $l^{6d}_{\max}$*, for varying termination tolerances* `lenFactor`*. The first two lines show that the algorithm stopped because* `maxIter` $= 100$ *was reached. In the other three cases, the algorithm terminated since all edge lengths are within the prescribed tolerance. In this case, the number of iterations are reported as well.*

`lenFactor`	#`iter`	$l^{6d}_{\min}$	$l^{6d}_{\max}$
0.1	**100**	10.627	16.013
0.2	**100**	10.627	16.013
0.3	85	10.503	15.859
0.4	5	9.1762	16.009
0.5	1	7.9340	17.667

one. While the initial mesh has 69 451 elements, the final one has 110 350 triangles.

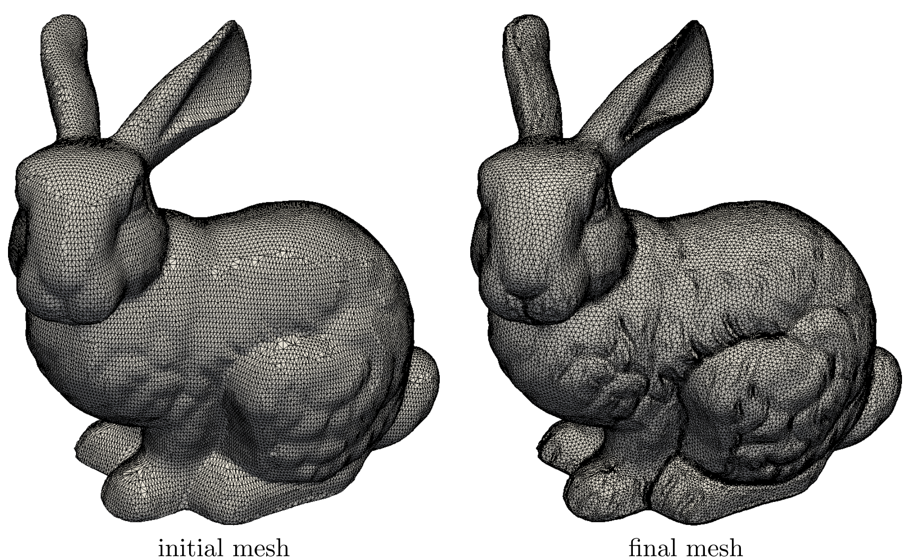

Fig. 12. *The initial bunny mesh (left) and the resulting anisotropic adapted one (right).*

The triangles are aligned and stretched according to the curvature of the surface. This can be clearly seen when zooming in on the ears of the bunny; see Figure 13. In the initial mesh Γ_h^{ini}, the triangles are too big to capture the helix of the bunny's ears and their orientation and shape do not reflect the curvature of the surface. However in the final mesh Γ_h^{fin} all these problems disappear.

Moreover, the final anisotropic adapted mesh exhibits a more detailed structure. For instance, unlike for the initial mesh Figure 12 (left), finer details in the fur of the bunny are clearly visible in the final mesh; see Figure 12 (right).

5.3. Lucy. In both previous examples, we started from a coarse initial mesh that poorly approximates the input geometry. However, our mesh anisotropic mesh adaptation procedure can also be used to simplify a dense initial mesh, coarsening it in regions with little curvature variation.

We consider the geometry shown in Figure 14. This mesh is another well-known benchmark in surface mesh adaptation ("Lucy"). Here the mesh is so fine that one would not be able to see the faces of the triangles because of the density of the edges;

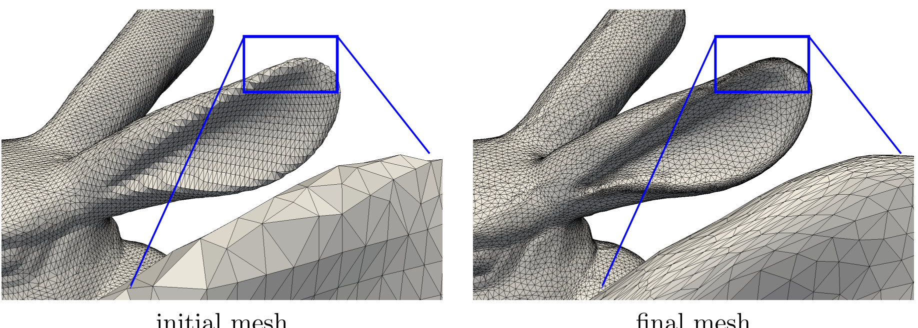

FIG. 13. *A detail of the initial bunny mesh (left) and the same detail for the anisotropic adapted one (right).*

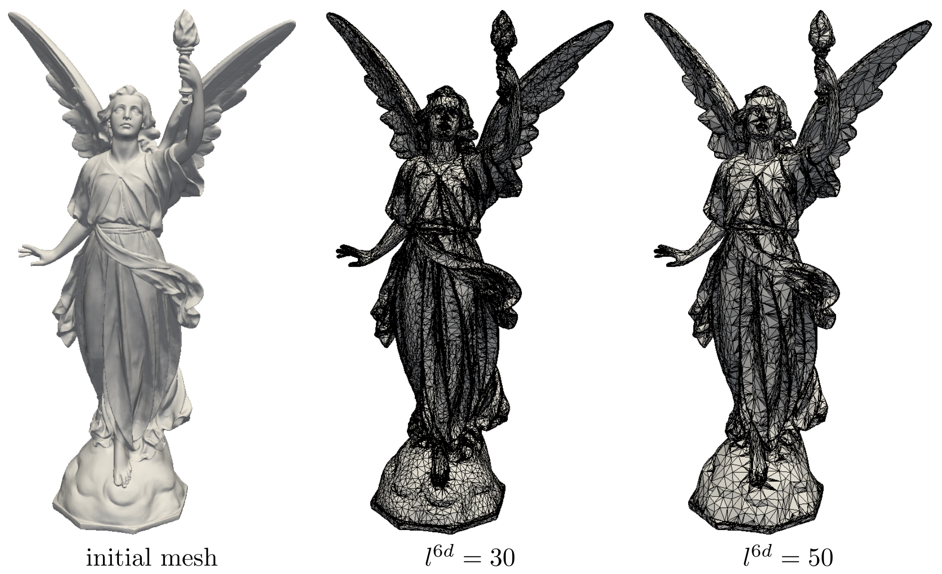

FIG. 14. *The "Lucy" mesh (excluding edges) with* 510 180 *elements as well as the thinned out meshes for* $l^{6d} = 30$ *and* 141 674 *elements as well as for* $l^{6d} = 50$ *and* 67 888 *elements.*

see Figure 14 left. Hence, we only show the faces of the surface without the edges. To construct the surface approximation, we use thin plate splines, $\varepsilon = 0.1$, $K = 3000$, $Ov = 3$, and the $\sigma = 10$. We point out that the number of partitions is rather high. If we want to reduce the number of partitions or avoid dealing with large dense linear systems, we can employ compactly supported RBFs. The largest condition number for this setup is given by $\max_{\text{cond}} = 2.0923e{+}20$ (matrix size: 2960) and the smallest one by $\min_{\text{cond}} = 5.8935e{+}15$ (matrix size: 2158).

The initial mesh offers a very fine approximation of the input geometry, but managing this huge data set requires an unacceptably high computational cost. By choosing a large target length l^{6d} our anisotropic adaptation procedure effectively becomes a mesh simplification method. The mesh detail in Figure 15 shows that the shape of the initial mesh is still preserved, but uses considerably fewer elements. To be more precise, we reduce the number of elements by 73% for $l^{6d} = 30$ and by 87%

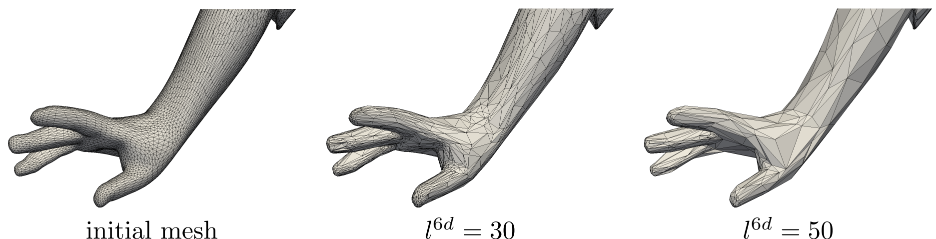

FIG. 15. *A detail of the "Lucy" mesh which is thinned out according to different target edge lengths.*

for $l^{6d} = 50$. The final meshes are more anisotropic compared to the initial one. We increase the global aspect ratio q_{Γ_h} from 1.21 to 95.83 and to 65.04, for $l^{6d} = 30$ and $l^{6d} = 50$, respectively.

5.4. Real-life examples. Finally, we study two real-life applications from magnetic resonance imaging processes.

Bronchus. This mesh represents the trachea and the main branches of the bronchi [16]. The geometry is rather complex. It consists of a sequence of branches that become smaller at each bifurcation. Triangles in the initial mesh are not aligned according to the curvature of the geometry; see Figure 16 and the detail in Figure 17.

The surface Γ_0^s is built using thin plate splines, $\varepsilon = 0.1$, $K = 200$, and $Ov = 3$. The largest condition number for this setup is given by $\max_{\text{cond}} = 2.5151e{+}12$ (matrix size: 462) and the smallest one by $\min_{\text{cond}} = 2.2246e{+}7$ (matrix size: 474). We set σ to 1 and consider three different target edge lengths:

$$l^{6d} \in \{0.25,\, 0.5,\, 1.0\}\,.$$

After applying our remeshing procedure the previously problematic triangles disappear and are replaced by new curvature-aligned ones. This example underlines the flexibility of the proposed adaptation procedure. In fact, it is possible to achieve different tasks by tuning the parameter l^{6d}. On the one hand, if we consider a large value for l^{6d}, the remeshing process becomes a mesh simplification method; see the detail in Figure 17 corresponding to $l^{6d} = 1.0$. On the other hand, if we consider a relatively short target edge length, our algorithm creates a surface mesh that is smoother and finer than the initial one; see the detail in Figure 17 corresponding to $l^{6d} = 0.25$. Moreover, if we tune the target length in such a way that we obtain approximately the same number of elements as in Γ_h^{ini}, the computational effort to deal with this mesh is the same as before but its triangles are curvature-aligned. See Figure 17 with target edge length $l^{6d} = 0.5$.

This observation is numerically verified by the data in Table 6. Here we state the number of elements in the initial and adapted meshes for different target lengths. In this table, we additionally provide the values of the global aspect ratio q_{Γ_h} which quantify the degree of anisotropy.

Vertebrae. Finally, we look at a mesh which represents one vertebra of the dorsal spine. The triangles in the Γ_h^{ini} are highly irregular. Many regions are too coarse and nonsmooth; see the initial mesh in Figure 18 and the detail in Figure 19.

The surface Γ_0^s is built using thin plate splines, $\varepsilon = 0.1$, $K = 19$, and $Ov = 2$. The largest condition number for this setup is given by $\max_{\text{cond}} = 4.5525e{+}11$ (matrix size: 462) and the smallest one by $\min_{\text{cond}} = 4.8159e{+}10$ (matrix size: 378).

Table 6
The number of elements for the bronchus meshes. We provide the percentage of the triangles in the mesh with respect to the number of triangles in the adapted meshes as well as the global aspect ratios and the timings defined in the previous section.

	Initial mesh	$l^{6d} = 0.5$	$l^{6d} = 1.0$	$l^{6d} = 0.25$
#ele.	42 692	34 954	12 026	132 784
	100%	82%	28%	311%
q_{Γ_h}	6.00e+01	1.28e+02	7.53e+02	7.08e+02
RBF	-	27.306 sec.	27.261 sec.	27.651 sec.
Remesh	-	1.821 sec.	2.818 sec.	4.158 sec.

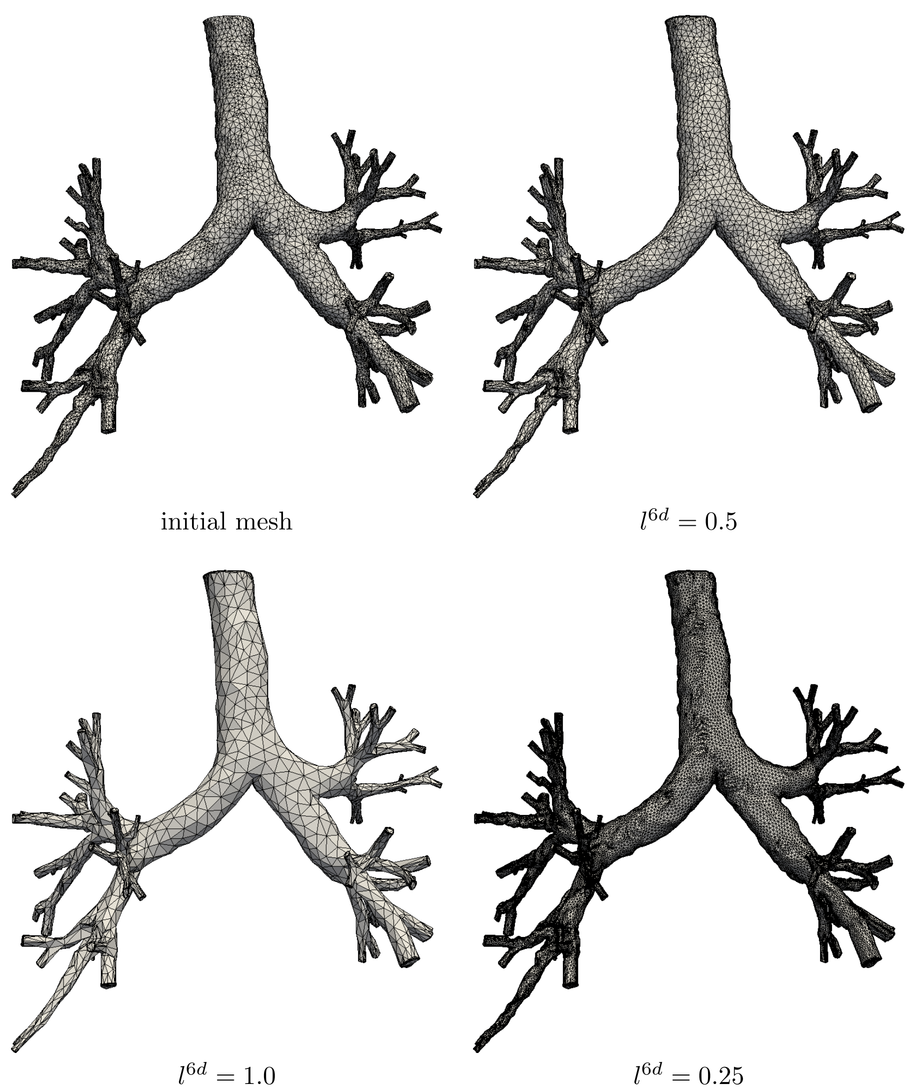

Fig. 16. *The initial bronchus mesh, courtesy of Fetita et al.* [16]*, and the adapted ones for different target edge lengths.*

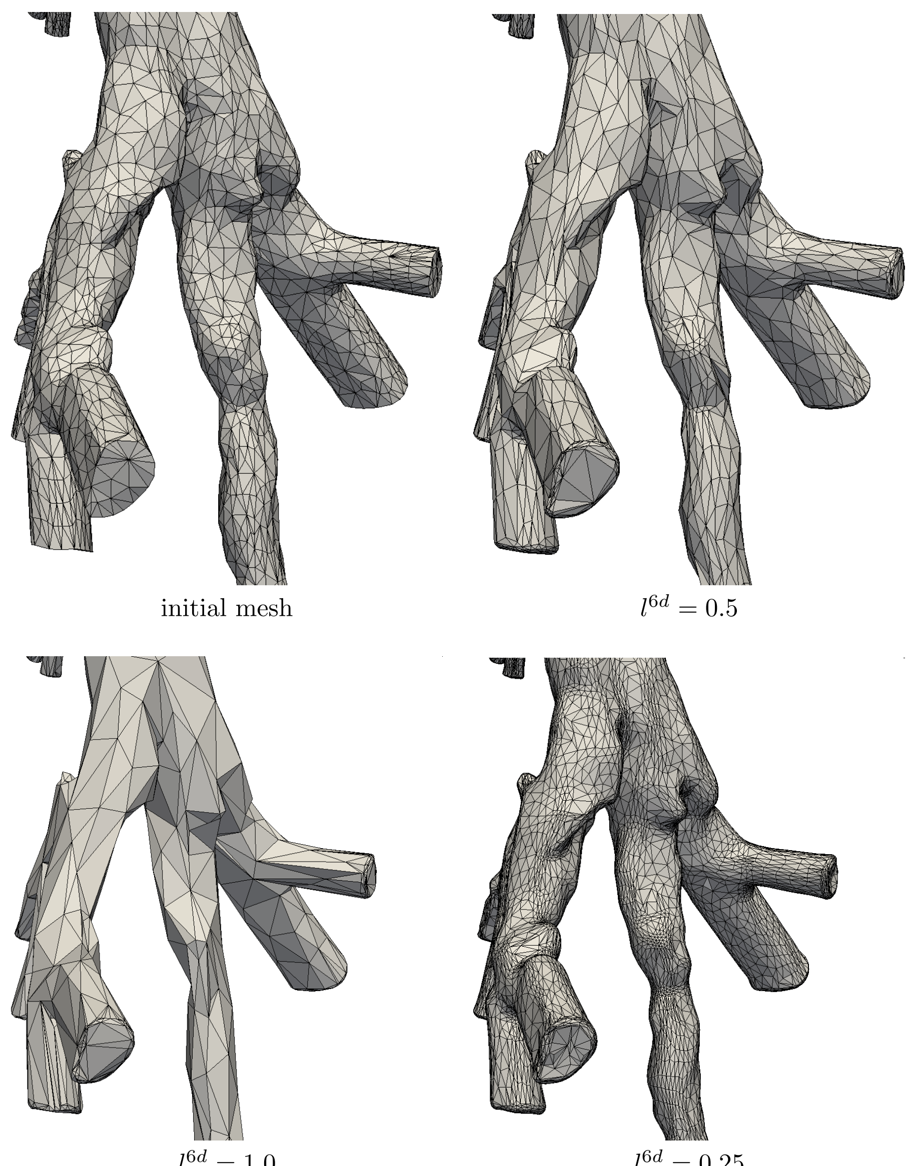

FIG. 17. *A detail of the initial bronchus mesh and the adapted ones for different target edge lengths.*

We set σ to 5 and consider three different edge lengths:

$$l^{6d} \in \{0.5,\, 1.5,\, 3.0\}\,.$$

The triangles in the resulting meshes are perfectly oriented and stretched to fit the input geometry, which can be seen in Figure 19. Even though some regions in the input mesh are too coarse and miss some details, in the final adapted meshes these undesirable features completely disappear; see Figure 19. Moreover, the smaller l^{6d}, the smoother the approximation of the input surface. In Table 7, we show the

computation times for each case.

TABLE 7
The number of elements for the vertebrae meshes. We provide the percentage of the triangles in the mesh with respect to the number of triangles in the adapted meshes as well as the global aspect ratios and the timings defined in the previous section.

	Initial mesh	$l^{6d} = 0.5$	$l^{6d} = 1.5$	$l^{6d} = 3.0$
#ele.	1928 100%	123 572 6409%	15 557 807%	3710 192%
q_{Γ_h}	3.27e+01	2.74e+02	2.84e+02	2.93e+02
RBF	-	0.953 sec.	0.964 sec.	0.940 sec.
Remesh	-	10.387 sec.	1.868 sec.	0.758 sec.

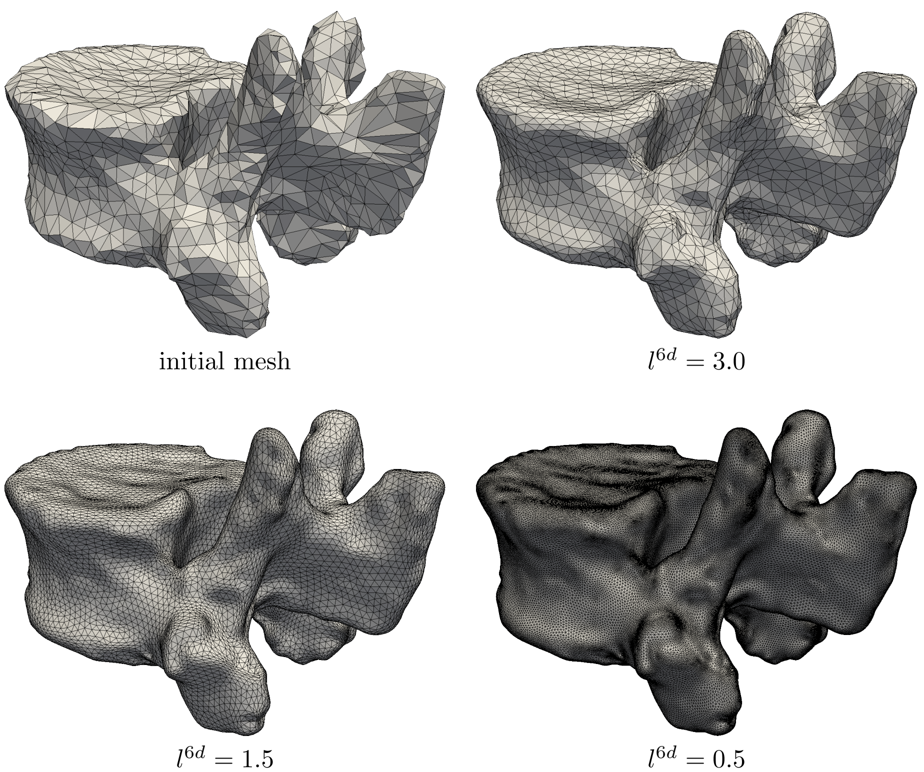

FIG. 18. *The initial vertebrae mesh and the adapted ones with different target edge lengths.*

We conclude this section with a comparison between our algorithm and the state-of-the-art open-source software package *Geogram* [27]. *Geogram* also implements the HDE for surface remeshing, using the algorithm in [28]. The difference in our algorithm is that *Geogram* directly uses the input surface information whereas we reconstruct a new surface. The initial mesh is the same one as in Figure 18. For the comparison, we used the mesh generated with a target edge length of $l^{6d} = 0.5$ (bottom right in Figure 18). *Geogram's* output mesh was obtained using the release version on a MacBook Pro with CPU Intel i7 quad core and 16 GB memory via the command `vorpalite spineNew.1.mesh output.mesh pts=95000 aniso=5`. We specified approximately the same number of mesh points as in the $l^{6d} = 0.5$ mesh as

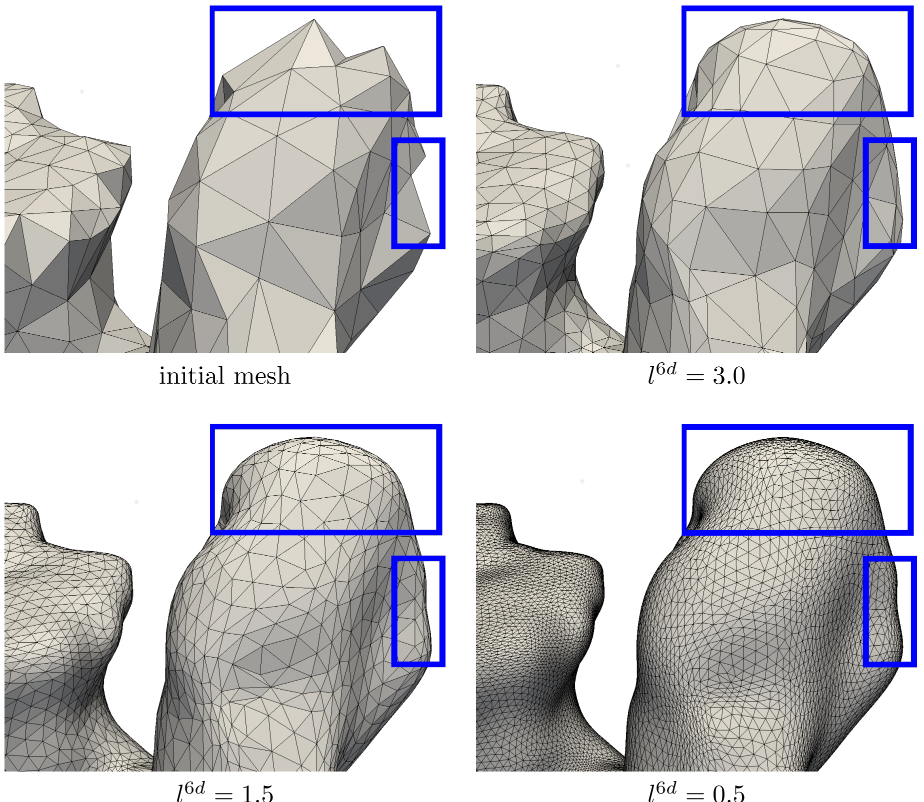

FIG. 19. *A detail of the initial vertebrae mesh and its corresponding adaptations for different target edge lengths.*

well as the same anisotropy parameter $\sigma = 5$. The resulting surfaces and meshes are shown in Figure 20. In terms of the CPU time, *Geogram* runs very fast (4.74 seconds), compared to our preliminary unoptimized time, which is about 90 seconds. However, we do observe the effect of the fundamental difference between both algorithms: the mesh produced by *Geogram* is not as smooth as ours. Furthermore, our algorithm seems to approximate the curvature of the underlying surface better and the anisotropy of the surface is more pronounced as the detail in Figure 20 reveals.

6. Conclusion. We presented a new anisotropic surface remeshing algorithm, which can be used to improve problematic inputs coming from discrete surface data sets. The anisotropy is guided by the curvature of the surface. Depending on the target edge length parameter, our new method becomes either a mesh simplification, a surface remeshing, or a mesh refinement algorithm. In particular, when the initial mesh is extremely coarse, the algorithm increases the resolution of the poor initial data. The influence of the different parameters in the algorithm were studied and tested on several classical and even real-life meshes. To reduce the computational cost a partitioning strategy with an overlap was introduced. A very moderate overlap already led to useful meshes. We discussed how standard meshing procedures such as edge splitting and edge contraction could be adapted in such a way that they can be projected on the continuous surface reconstruction provided by the RBFs. We showed how much

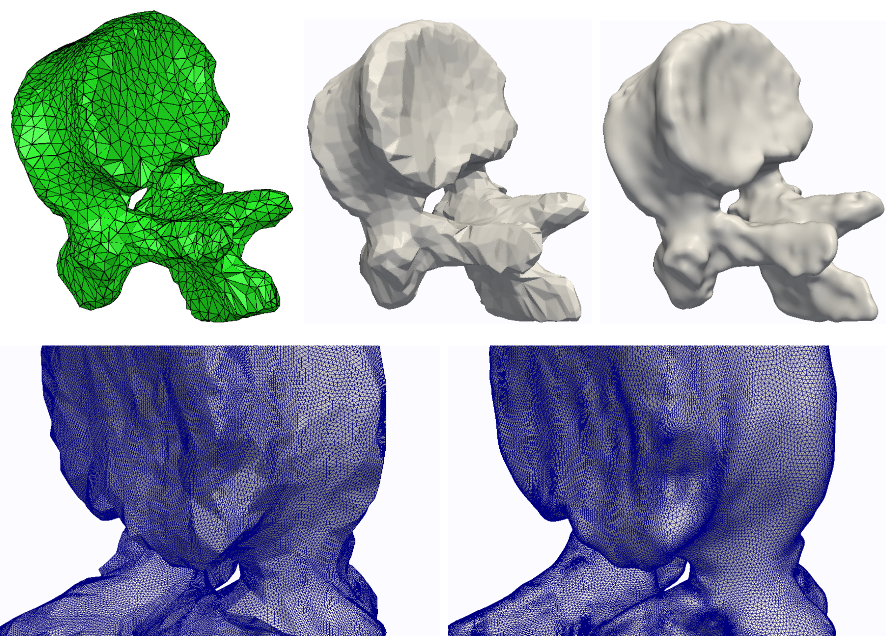

FIG. 20. *First row: the input mesh (left), the reconstructed surfaces by* Geogram *(middle), and our algorithm (right). Second row: a comparison of the resulting meshes using* Geogram *(left) and our algorithm (right).*

each remeshing procedure contributed to the remeshing algorithm and broke down the timings spent on reconstructing the surface and adapting the mesh. Furthermore, we studied the influence of the target edge length and the normal parameter σ. As expected a larger normal parameter σ led to more edges in high-curvature regions. We showed that the degree of anisotropy could be increased considerably while keeping the number of elements relatively low. Finally, we compared our algorithm to the state-of-the-art software package *Geogram* and demonstrated the advantages of our algorithm in terms of smoothness and anisotropic curvature approximation. In this paper, we assume that the discrete data represent a smooth surface. Future research may look at discrete data which contain sharp features.

REFERENCES

[1] P. Alliez, M. Attene, C. Gotsman, and G. Ucelli, *Recent advances in remeshing of surfaces*, in Shape Analysis and Structuring, D. L. and M. Spagnuolo, eds., Springer, Berlin, Heidelberg, 2008, pp. 53–82, https://doi.org/10.1007/978-3-540-33265-7_2.

[2] R. K. Beatson, J. B. Cherrie, and C. T. Mouat, *Fast fitting of radial basis functions: Methods based on preconditioned GMRES iteration*, Advances in Computational Mathematics, 11 (1999), pp. 253–270, https://doi.org/10.1023/A:1018932227617.

[3] M. W. Bern and D. Eppstein, *Mesh generation and optimal triangulation*, in Computing in Euclidean Geometry, Lecture Notes Series on Computing 4, D.-Z. Du and F. K.-M. Hwang, eds., 2nd ed., World Scientific, River Edge, NJ, 1995, pp. 47–123, http://citeseerx.ist.psu.edu/viewdoc/summary?doi=10.1.1.39.7447.

[4] F. J. Bossen and P. S. Heckbert, *A pliant method for anisotropic mesh generation*, in Proceedings of the 5th International Meshing Roundtable, Sandia National Laboratories, Albuquerque, NM, 1996, pp. 63–74, http://citeseerx.ist.psu.edu/viewdoc/summary?doi=10.1.1.40.7910.

[5] G. D. Cañas and S. J. Gortler, *Surface remeshing in arbitrary codimensions*, Vis. Comput., 22 (2006), pp. 885–895, https://doi.org/10.1007/s00371-006-0073-8.

[6] J. C. Carr, R. K. Beatson, J. B. Cherrie, T. J. Mitchell, W. R. Fright, B. C. McCallum, and T. R. Evans, *Reconstruction and representation of 3d objects with radial basis functions*, in Proceedings of the 28th Annual Conference on Computer Graphics and Interactive Techniques, ACM, New York, 2001, pp. 67–76, https://doi.org/10.1145/383259.383266.

[7] F. Dassi, A. Mola, and H. Si, *Curvature-adapted remeshing of CAD surfaces*, Procedia Engineering, 23rd International Meshing Roundtable (IMR23), 82 (2014), pp. 253–265, https://doi.org/10.1016/j.proeng.2014.10.388.

[8] F. Dassi, S. Perotto, L. Formaggia, and P. Ruffo, *Efficient geometric reconstruction of complex geological structures*, Math. Comput. Simulation, 106 (2014), pp. 163–184, https://doi.org/10.1016/j.matcom.2014.01.005.

[9] F. Dassi and H. Si, *A curvature-adapted anisotropic surface re-meshing method*, in New Challenges in Grid Generation and Adaptivity for Scientific Computing, Springer, Cham, 2015, pp. 19–41, https://doi.org/10.1007/978-3-319-06053-8_2.

[10] H. L. de Cougny and M. S. Shephard, *Surface meshing using vertex insertion*, in Proceedings of the 5th International Meshing Roundtable, Citeseer, 1996, pp. 243–256, http://citeseerx.ist.psu.edu/viewdoc/summary?doi=10.1.1.17.4294.

[11] H. Edelsbrunner, *Geometry and Topology for Mesh Generation*, Cambridge Monogr. Appl. Comput. Math. 7, Cambridge University Press, Cambridge, UK, 2001, https://doi.org/10.1017/CBO9780511530067.

[12] J. Escobar, G. Montero, R. Montenegro, and E. Rodríguez, *An algebraic method for smoothing surface triangulations on a local parametric space*, Internat. J. Numer. Methods in Engrg., 66 (2006), pp. 740–760, https://doi.org/10.1002/nme.1584.

[13] P. Farrell and J. Pestana, *Block preconditioners for linear systems arising from multiscale collocation with compactly supported RBFs*, Numer. Linear Algebra Appl., 22 (2015), pp. 731–747, https://doi.org/10.1002/nla.1984.

[14] P. Farrell and H. Wendland, *RBF multiscale collocation for second order elliptic boundary value problems*, SIAM J. Numer. Anal., 51 (2013), pp. 2403–2425, https://doi.org/10.1137/120898383.

[15] G. E. Fasshauer, *Meshfree Approximation Methods with MATLAB*, Interdiscip. Math. Sci. 6, World Scientific, Hackensack, NJ, 2007, https://doi.org/10.1142/6437.

[16] C. Fetita, S. Mancini, D. Perchet, F. Preteux, M. Thirie, and L. Vial, *An image-based computational model of oscillatory flow in the proximal part of tracheobronchial trees*, Comput. Methods Biomech. Biomed. Engin., 8 (2005), pp. 279–293, https://doi.org/10.1080/10255840500289624.

[17] L. Formaggia, S. Micheletti, and S. Perotto, *Anisotropic mesh adaptation in computational fluid dynamics: Application to the advection-diffusion-reaction and the Stokes problems*, Appl. Numer. Math., 51 (2004), pp. 511–533, https://doi.org/10.1016/j.apnum.2004.06.007.

[18] L. Formaggia and S. Perotto, *New anisotropic a priori error estimates*, Numer. Math., 89 (2001), pp. 641–667, https://doi.org/10.1007/s002110100273.

[19] P. J. Frey, *Generation and adaptation of computational surface meshes from discrete anatomical data*, Internat. J. Numer. Methods Engrg., 60 (2004), pp. 1049–1074, https://doi.org/10.1002/nme.992.

[20] P. J. Frey and F. Alauzet, *Anisotropic mesh adaptation for CFD computations*, Comput. Methods Appl. Mech. Engrg., 194 (2005), pp. 5068–5082, https://doi.org/10.1016/j.cma.2004.11.025.

[21] P. J. Frey and H. Borouchaki, *Geometric surface mesh optimization*, Comput. Vis. Sci., 1 (1998), pp. 113–121, https://doi.org/10.1007/s007910050011.

[22] E. Hartmann, *On the curvature of curves and surfaces defined by normal forms*, Comput. Aided Geom. Des., 16 (1999), pp. 355–376, https://doi.org/10.1016/S0167-8396(99)00003-5.

[23] H. Hoppe, *Progressive meshes*, in Proceedings of the 23rd Annual Conference on Computer Graphics and Interactive Techniques, ACM, New York, 1996, pp. 99–108, https://doi.org/10.1145/237170.237216.

[24] H. Hoppe, T. DeRose, T. Duchamp, J. McDonald, and W. Stuetzle, *Mesh optimization*, in Proceedings of the 20th Annual Conference on Computer Graphics and Interactive Techniques, ACM, New York, 1993, pp. 19–26, http://citeseerx.ist.psu.edu/viewdoc/download?doi=10.1.1.6.2515&rep=rep1&type=pdf.

[25] A. Iske, *Multiresolution Methods in Scattered Data Modelling*, Lect. Notes Comput. Sci. Eng. 37, Springer, Berlin, 2004, https://doi.org/10.1007/978-3-642-18754-4.

[26] A. Kuzmin, M. Luisier, and O. Schenk, *Fast methods for computing selected elements of the Greens function in massively parallel nanoelectronic device simulations*, in Euro-Par 2013 Parallel Processing, Lecture Notes in Comput. Sci. 8097, F. Wolf, B. Mohr, and D. Mey, eds., Springer, Berlin, Heidelberg, 2013, pp. 533–544, https://doi.org/10.1007/978-3-642-40047-6_54.

[27] B. Levy, *Geogram version* 1.3.10, http://alice.loria.fr/software/geogram/doc/html/index.html (2016).

[28] B. Lévy and N. Bonneel, *Variational anisotropic surface meshing with Voronoi parallel linear enumeration*, in Proceedings of the 21st International Meshing Roundtable, Springer, Berlin, Heidelberg, 2013, pp. 349–366, https://doi.org/10.1007/978-3-642-33573-0_21.

[29] L. Ling and E. J. Kansa, *Preconditioning for radial basis functions with domain decomposition methods*, Math. Comput. Modelling, 40 (2004), pp. 1413–1427, https://doi.org/10.1016/j.mcm.2005.01.002.

[30] E. Marchandise, C. Piret, and J.-F. Remacle, *CAD and mesh repair with radial basis functions*, J. Comput. Phys., 231 (2012), pp. 2376–2387, https://doi.org/10.1016/j.jcp.2011.11.033.

[31] E. Marchandise, J.-F. Remacle, and C. Geuzaine, *Optimal parametrizations for surface remeshing*, Eng. Comput., 30 (2014), pp. 383–402, https://doi.org/10.1007/s00366-012-0309-3.

[32] V. Nivoliers, B. Lévy, and C. Geuzaine, *Anisotropic and feature sensitive triangular remeshing using normal lifting*, J. Comput. Appl. Math., 289 (2015), pp. 225–240, https://doi.org/10.1016/j.cam.2015.01.041.

[33] O. Schenk, *PARDISO version* 5.0.0, http://www.pardiso-project.org (accessed 2016-02-22).

[34] J. R. Shewchuk, *What is a good linear finite element? Interpolation, conditioning, anisotropy, and quality measures*, in Proceedings of the 11th International Meshing Roundtable, Springer-Verlag, Berlin, 2002, pp. 115–126, http://citeseerx.ist.psu.edu/viewdoc/summary?doi=10.1.1.19.2164.

[35] V. Surazhsky and C. Gotsman, *Explicit surface remeshing*, in Proceedings of the 2003 Eurographics/ACM SIGGRAPH Symposium on Geometry Processing, Eurographics Association, Aire-la-Ville, Switzerland, 2003, pp. 20–30, http://dl.acm.org/citation.cfm?id=882370.882373.

[36] H. Wendland, *Piecewise polynomial, positive definite and compactly supported radial functions of minimal degree*, Adv. Comput. Math., 4 (1995), pp. 389–396, https://doi.org/10.1007/BF02123482.

[37] H. Wendland, *Scattered Data Approximation*, Cambridge Monogr. Appl. Comput. Math. 17, Cambridge University Press, Cambridge, UK, 2005, https://doi.org/10.1017/CBO9780511617539.

14

Tetrahedral Mesh Improvement Using Moving Mesh Smoothing, Lazy Searching Flips, and RBF Surface Reconstruction

F. Dassi et al. Tetrahedral Mesh Improvement Using Moving Mesh Smoothing, Lazy Searching Flips, and RBF Surface Reconstruction. *Computer-Aided Design* (2017). DOI: 10.1016/j.cad.2017.11.010

Abstract Given a tetrahedral mesh for example be used in a FVM simulation as described in Section 3.1 as well as objective functionals measuring the mesh quality which take into account the shape, size, and orientation of the mesh elements, our aim is to improve the mesh quality as much as possible. In this paper, we combine the moving mesh smoothing, based on the integration of an ordinary differential equation coming from a given functional, with the lazy flip technique, a reversible edge removal algorithm to modify the mesh connectivity. Moreover, we utilize radial basis function (RBF) surface reconstruction to improve tetrahedral meshes with curved boundary surfaces. Numerical tests show that the combination of these techniques into a mesh improvement framework achieves results which are comparable and even better than the previously reported ones.

Conception: I was in charge of the RBF part.

Execution: I was in charge of the RBF part.

Reporting: I was in charge of the RBF part.

ARTICLE IN PRESS

Computer-Aided Design ▮ (▮▮▮▮) ▮▮▮–▮▮▮

Contents lists available at ScienceDirect

Computer-Aided Design

journal homepage: www.elsevier.com/locate/cad

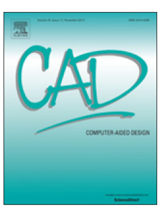

Tetrahedral mesh improvement using moving mesh smoothing, lazy searching flips, and RBF surface reconstruction ☆

Franco Dassi [a], Lennard Kamenski [b,*], Patricio Farrell [b], Hang Si [b]

[a] *Dipartimento di Matematica e Applicazioni, Università degli Studi di Milano-Bicocca, Via Cozzi 53, 20125 Milano, Italy*
[b] *Weierstrass Institute for Applied Analysis and Stochastics, Mohrenstr. 39, 10117 Berlin, Germany*

ARTICLE INFO

Keywords:
Mesh improvement
Mesh quality
Edge flipping
Mesh smoothing
Moving mesh
Radial basis functions

ABSTRACT

Given a tetrahedral mesh and objective functionals measuring the mesh quality which take into account the shape, size, and orientation of the mesh elements, our aim is to improve the mesh quality as much as possible. In this paper, we combine the *moving mesh smoothing*, based on the integration of an ordinary differential equation coming from a given functional, with the *lazy flip* technique, a reversible edge removal algorithm to modify the mesh connectivity. Moreover, we utilize *radial basis function* (RBF) surface reconstruction to improve tetrahedral meshes with curved boundary surfaces. Numerical tests show that the combination of these techniques into a mesh improvement framework achieves results which are comparable and even better than the previously reported ones.

© 2017 Elsevier Ltd. All rights reserved.

1. Introduction

The key mesh improvement operations considered in this work are *smoothing*, which moves the mesh vertices, *flipping*, which changes the mesh topology without moving the mesh vertices, and a *smooth boundary reconstruction*. Previous work shows that the combination of smoothing and flipping achieves better results than if applied individually [1,2]. In this paper, we combine the recently developed flipping and smoothing methods into one mesh improvement scheme and apply them in combination with a smooth boundary reconstruction via radial basis functions.

Mesh smoothing improves the mesh quality by improving vertex locations, typically through Laplacian smoothing or some optimization-based algorithm. Most commonly used mesh smoothing methods are Laplacian smoothing and its variants [3,4], where a vertex is moved to the geometric center of its neighboring vertices. While economic, easy to implement, and often effective, Laplacian smoothing guarantees neither a mesh quality improvement nor mesh validity. Alternatives are optimization-based methods that are effective with respect to certain mesh quality measures such as the ratio of the area to the sum of the squared edge lengths [5], the ratio of the volume to a power of the sum of the squared face areas [6], the condition number of the Jacobian matrix of the affine mapping between the reference element and physical elements [7], or various other measures [1,8–10]. Most of the optimization-based methods are local and sequential, combining Gauss–Seidel-type iterations with location optimization problems over each patch. There is also a parallel algorithm that solves a sequence of independent subproblems [11].

In our scheme, we employ the moving mesh PDE (MMPDE) method, defined as the gradient flow equation of a meshing functional (an objective functional in the context of optimization) to move the mesh continuously in time. Such a functional is typically based on error estimation or physical and geometric considerations. Here, we consider a functional based on the equidistribution and alignment conditions [12] and employ the recently developed direct geometric discretization [13] of the underlying meshing functional on simplicial meshes. Compared to the aforementioned mesh smoothing methods, the considered method has several advantages: it can be easily parallelized, it is based on a continuous functional for which the existence of minimizers is known, the functional controlling the mesh shape and size has a clear geometric meaning, and the nodal mesh velocities are given by a simple analytical matrix form. Moreover, the smoothed mesh will stay valid if it was valid initially [14].

Flipping is the most efficient way to locally improve the mesh quality and it has been extensively addressed in the literature [15,1,16,2]. In the simplest case, the basic flip operations, such as 2-to-3, 3-to-2, and 4-to-4 flips, are applied as long as the mesh quality can be improved. The more effective way is to combine several basic flip operations into one edge removal operation, which extends the 3-to-2 and 4-to-4 flips. This operation removes the common edge of $n \geq 3$ adjacent tetrahedra by replacing them with $m = 2n - 4$ new tetrahedra (the so-called n-to-m flip). There are at most C_{n-2} possible variants to remove an edge by a n-to-m flip,

☆ This special issue was edited by Scott Canann, Steven J. Owen & Hang Si.

* Corresponding author.
E-mail addresses: franco.dassi@unimib.it (F. Dassi), kamenski@wias-berlin.de (L. Kamenski), farrell@wias-berlin.de (P. Farrell), si@wias-berlin.de (H. Si).

https://doi.org/10.1016/j.cad.2017.11.010
0010-4485/© 2017 Elsevier Ltd. All rights reserved.

Please cite this article in press as: Dassi F., et al. Tetrahedral mesh improvement using moving mesh smoothing, lazy searching flips, and RBF surface reconstruction. Computer-Aided Design (2017), https://doi.org/10.1016/j.cad.2017.11.010.

ARTICLE IN PRESS

where $C_n = \frac{(2n)!}{(n+1)!\,n!}$ is the Catalan number. If n is small (e.g., $n < 7$), one can enumerate all possible cases, compute the mesh quality for each case, and then pick the optimal one. Another way is to use dynamic programming to find the optimal configuration. However, the number of cases increases exponentially and finding the optimal solution with brute force is very time-consuming.

In this paper, we propose the so-called *lazy searching flips*. The key idea is to automatically explore sequences of flips to remove a given edge in the mesh. If a flip sequence leads to a configuration which does not improve the mesh quality, the algorithm reverses this sequence and explores another one (see Section 3 and Figs. 2a to 2c). Once an improvement is found, the algorithms stops the search and returns without exploring the remaining possibilities.

When considering more arbitrary meshes (which may not be piecewise planar), we need to make sure that new nodes are added in a consistent way. To achieve this we use *RBF surface reconstruction* as introduced in [17]. Radial basis functions are a very useful tool in the context of higher-dimensional interpolation as they dispense with the expensive generation of a mesh [18–20]. Here, we will employ them to approximate the underlying continuous surface so that we can project nodes onto it as proposed in [21,22]. This problem turns out to be very challenging for meshes with arbitrary boundary. Hence, we begin with a relatively simple mesh. For more complicated examples we first refine the boundary by using the RBF reconstruction and projection method and then keep the boundary nodes fixed while interior nodes may move.

In this paper, we provide a detailed numerical study of a combination of the MMPDE smoothing with the lazy searching flips and RBF surface reconstruction. More specifically, we compare the results of the whole algorithm with `Stellar` [2], `CGAL` [23] and `mmg3d` [24]. We also compare the lazy searching flips and the MMPDE smoothing with the flipping and smoothing procedures provided by `Stellar`.

2. The moving mesh PDE smoothing scheme

The key idea of this smoothing scheme is to move the mesh vertices via a moving mesh equation, which is formulated as the gradient system of an energy functional (the MMPDE approach). Originally, the method was developed in the continuous setting [25,26]. In this paper, we use its discrete form [13,14,27], for which the mesh vertex velocities are expressed in a simple, analytical matrix form, which makes the implementation more straightforward to parallelize.

2.1. Moving mesh smoothing

Consider a polygonal (polyhedral) domain $\Omega \subset \mathbb{R}^d$ with $d \geq 1$. Let $\mathcal{T}_h$ denote the simplicial mesh as well as $\#\mathcal{N}_h$ and $\#\mathcal{T}_h$ the numbers of its vertices and elements, respectively. Let K be a generic mesh element and $\hat{K}$ the reference element taken as a regular simplex with volume $|\hat{K}| = 1/\#\mathcal{T}_h$. Further, let F_K' be the Jacobian matrix of the affine mapping $F_K : \hat{K} \to K$ from the reference element $\hat{K}$ to a mesh element K. For notational simplicity, we denote the inverse of the Jacobian by $\mathbb{J}_K$, i.e., $\mathbb{J}_K := (F_K')^{-1}$ (see Fig. 1).

Then, the mesh $\mathcal{T}_h$ is uniform if and only if

$$|K| = \frac{|\Omega|}{\#\mathcal{T}_h} \quad \text{and} \quad \frac{1}{d}\,\mathrm{tr}\left(\mathbb{J}_K^T \mathbb{J}_K\right) = \det\left(\mathbb{J}_K^T \mathbb{J}_K\right)^{\frac{1}{d}} \quad \forall K \in \mathcal{T}_h. \qquad (1)$$

The first condition requires all elements to have the same size and the second requires all elements to be shaped similarly to $\hat{K}$ (these conditions are the simplified versions of the equidistribution and alignment conditions [28,26]).

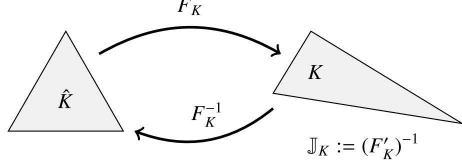

Fig. 1. Reference element $\hat{K}$, mesh element K, and the corresponding mappings F_K and F_K^{-1}.

The corresponding energy functional for which the minimization will result in a mesh satisfying Eq. (1) as closely as possible is

$$I_h = \sum_K |K|\; G\left(\mathbb{J}_K, \det \mathbb{J}_K\right) \qquad (2)$$

with

$$G(\mathbb{J}, \det \mathbb{J}) = \theta\left(\mathrm{tr}\left(\mathbb{J}\mathbb{J}^T\right)\right)^{\frac{dp}{2}} + (1-2\theta)\, d^{\frac{dp}{2}} (\det \mathbb{J})^p, \qquad (3)$$

where $\theta \in (0, 0.5]$ and $p > 1$ are dimensionless parameters (in Section 6, we use $\theta = 1/3$ and $p = 3/2$). This is a specific choice and other meshing functionals are possible. The interested reader is referred to [29] for a numerical comparison of meshing functionals for variational mesh adaptation.

In Eq. (2), I_h is a Riemann sum of a continuous functional for variational mesh adaptation based on equidistribution and alignment [12] and depends on the vertex coordinates $\boldsymbol{x}_i$, $i = 1, \ldots, \#\mathcal{N}_h$. The corresponding vertex velocities $\boldsymbol{v}_i$ for the mesh movement are defined as

$$\boldsymbol{v}_i := \frac{d\boldsymbol{x}_i}{dt} = -\left(\frac{\partial I_h}{\partial \boldsymbol{x}_i}\right)^T, \quad i = 1, \ldots, \#\mathcal{N}_h, \qquad (4)$$

where the derivatives $\frac{d\boldsymbol{x}_i}{dt}$ are considered to be row vectors.

2.2. Vertex velocities and the mesh movement

The vertex velocities $\boldsymbol{v}_i$ can be computed analytically [13, Eqs (39) to (41)] using scalar-by-matrix differentiation [13, Sect. 3.2]. Denote the vertices of K and $\hat{K}$ by $\boldsymbol{x}_j^K$ and $\hat{\boldsymbol{x}}_j$, $j = 0, \ldots, d$, and define the element edge matrices as

$$E_K = [\boldsymbol{x}_1^K - \boldsymbol{x}_0^K, \ldots, \boldsymbol{x}_d^K - \boldsymbol{x}_0^K],$$
$$\hat{E} = [\hat{\boldsymbol{x}}_1 - \hat{\boldsymbol{x}}_0, \ldots, \hat{\boldsymbol{x}}_d - \hat{\boldsymbol{x}}_0].$$

Note, that $\hat{E}E_K^{-1} = \mathbb{J}_K$. Then, the local mesh velocities are given element-wise [13, Eqs (39) and (41)] by

$$\begin{bmatrix} (\boldsymbol{v}_1^K)^T \\ \vdots \\ (\boldsymbol{v}_d^K)^T \end{bmatrix} = -G_K E_K^{-1} + E_K^{-1}\frac{\partial G_K}{\partial \mathbb{J}}\hat{E}E_K^{-1} + \frac{\partial G_K}{\partial \det \mathbb{J}}\frac{\det(\hat{E})}{\det(E_K)}E_K^{-1}, \qquad (5)$$

$$(\boldsymbol{v}_0^K)^T = -\sum_{j=1}^{d} (\boldsymbol{v}_j^K)^T,$$

where $G_K = G(\mathbb{J}_K, \det \mathbb{J}_K)$ and

$$\frac{\partial G_K}{\partial \mathbb{J}} = \frac{\partial G}{\partial \mathbb{J}}(\mathbb{J}_K) = dp\theta\left(\mathrm{tr}(\mathbb{J}_K\mathbb{J}_K^T)\right)^{\frac{dp}{2}-1}\mathbb{J}_K^T,$$
$$\frac{\partial G_K}{\partial \det \mathbb{J}} = \frac{\partial G}{\partial \det \mathbb{J}}(\det \mathbb{J}_K) = p(1-2\theta)d^{\frac{dp}{2}}(\det \mathbb{J}_K)^{p-1}$$

are the derivatives of G with respect to its first and second argument [13, Example 3.2] evaluated at $\mathbb{J} = \mathbb{J}_K$ and $\det(\mathbb{J}) = \det \mathbb{J}_K$.

Please cite this article in press as: Dassi F., et al. Tetrahedral mesh improvement using moving mesh smoothing, lazy searching flips, and RBF surface reconstruction. Computer-Aided Design (2017), https://doi.org/10.1016/j.cad.2017.11.010.

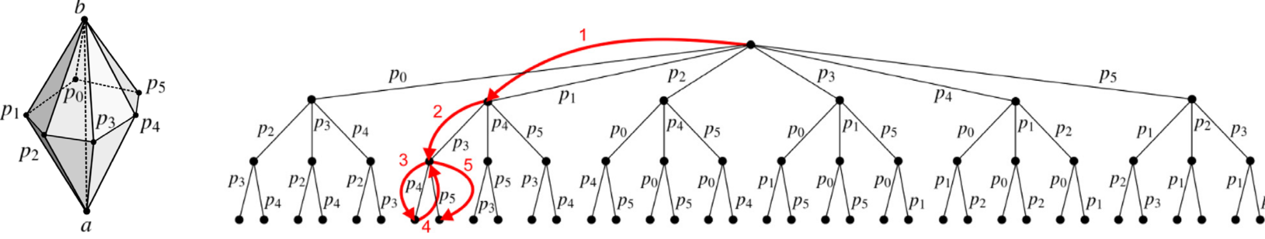

(a) The initial state.

(b) The lazy flip search tree for removing the edge $[a, b]$. p_i identifies the face $[a, b, p_i]$ which is flipped via a 2-to-3 flip. The search path is highlighted with arrows.

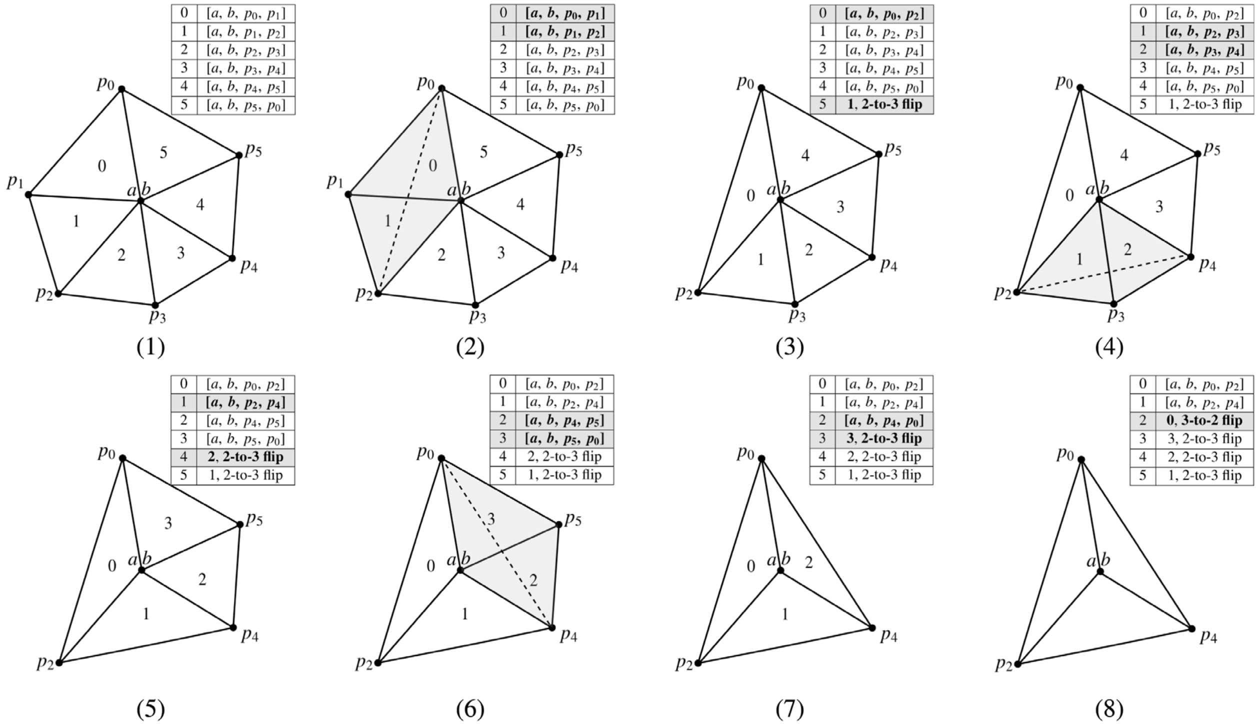

(c) The sequence of flips. The edge $[a, b]$ is represented by one vertex in the center (except (8)). A face $[a, b, p_i]$ is represented by an edge. Arrays attached to each figure show the current content of A. (1) $n = 5$ tetrahedra share the edge $[a, b]$. In (2) and (3), $[a, b, p_1]$ is removed by a 2-to-3 flip. In (4) and (5), a 2-to-3 flip is performed on $[a, b, p_3]$. In (6) and (7), $[a, b, p_5]$ is removed by a 2-to-3 flip. In (8), the edge $[a, b]$ is removed by a 3-to-2 flip.

Fig. 2. An example of an edge removal by a sequence of flips.

The moving mesh equation (4) becomes

$$\frac{d\boldsymbol{x}_i}{dt} = \sum_{K \in \omega_i} |K| \, \boldsymbol{v}_{i_K}^K, \quad i = 1, \ldots, \#\mathcal{N}_h, \tag{6}$$

where ω_i is the patch of the vertex $\boldsymbol{x}_i$ and i_K is the local index of $\boldsymbol{x}_i$ on K.

The moving mesh governed by Eq. (6) will stay nonsingular if it is nonsingular initially: the minimum height and the minimum volume of the mesh elements will stay bounded from below by a positive number depending only on the initial mesh and the number of the elements [14]. This holds for the numerical integration of Eq. (6) as well if the ODE solver has the property of monotonically decreasing energy [14]. For example, algebraically stable Runge–Kutta methods preserve this property under a mild step-size restriction [30].

During smoothing, we use the current vertex locations as the initial position and integrate Eq. (6) for a time period (with the proper modification for the boundary vertices, see Section 2.3). The connectivity is kept fixed during the smoothing step. The time integration can be carried out for a given fixed time period or adaptively until the change of the energy functional (2) is smaller than the prescribed absolute or relative tolerances, that is until

$$|I_h(t_{n+1}) - I_h(t_n)| \le \varepsilon_{abs} \quad \text{or} \quad |I_h(t_{n+1}) - I_h(t_n)| \le \varepsilon_{rel} I_h(t_{n+1}).$$

In our examples in Section 6, we use the explicit Runge–Kutta Dormand–Prince ODE solver [31] and integrate until $t = 10$, which worked well with the provided examples.

2.3. Velocity adjustment for the boundary vertices

The velocities of the boundary vertices need to be modified. If $\boldsymbol{x}_i$ is a fixed boundary vertex, then its velocity is set to zero Otherwise, $\boldsymbol{x}_i$ is allowed to move along a boundary curve or a surface represented by the zero level set of a function ϕ and its velocity is modified so that its normal component along the curve (surface) is zero:

$$\nabla \phi(\boldsymbol{x}_i) \cdot \frac{\partial \boldsymbol{x}_i}{\partial t} = 0.$$

For the special case of a piecewise linear complex (PLC) [32] the velocity adjustment is straightforward:

facet vertices: project the velocity onto the facet plane,

Please cite this article in press as: Dassi F., et al. Tetrahedral mesh improvement using moving mesh smoothing, lazy searching flips, and RBF surface reconstruction. Computer-Aided Design (2017), https://doi.org/10.1016/j.cad.2017.11.010.

ARTICLE IN PRESS

segment vertices: project the velocity onto the segment line,
corner vertices: set the velocity to zero.

For a general non-polygonal or non-polyhedral domain, a simple way to adjust the boundary vertices is to move the vertex and then project it onto the boundary to which it belongs, which proved to work well for simple surface geometries (see Section 6.2). However, for complicated geometries, this simple projection can fail and a more reliable approach is needed.

3. Lazy searching flips

In this section, we explain how to remove an edge and how to reverse the removal using flips. In addition, we present the lazy searching algorithm which can be used to improve the quality of a mesh.

3.1. Edge removal and its inverse

A basic edge removal algorithm performs a sequence of elementary 2-to-3 and 3-to-2 flips [33]. We extend this algorithm by allowing the flip sequence to be reversed. Our algorithm saves the flips online and it uses no additional memory.

Let $[a, b] \in \mathcal{T}_h$ be an edge with endpoints a and b and $A[0, \dots, n-1]$ be the array of $n \geq 3$ tetrahedra in $\mathcal{T}_h$ sharing $[a, b]$. For simplicity, we assume that $[a, b]$ is an interior edge of $\mathcal{T}_h$, so that all tetrahedra in A can be ordered cyclically such that the two tetrahedra $A[i]$ and $A[(i+1) \bmod n]$ share a common face. The index i takes values in $\{0, 1, \dots, n-1\}$. Throughout this section, additions involving indices will be modulo n.

Given such an array A of n tetrahedra, we want to find a sequence of flips that will remove the edge $[a, b]$. Moreover, we also want to be able to reverse this sequence in order to return to the original state.

Our edge removal algorithm includes two subroutines

$$[\texttt{done}, m] := \texttt{flipnm}(A[0, \dots, n-1], \texttt{level}),$$
$$\texttt{flipnm_post}(A[0, \dots, n-1], m)$$

with an array A (of length n) of tetrahedra and an integer `level` defining the maximum recursive level as input.

`flipnm` executes "forward" flips to remove the edge $[a, b]$. It returns a Boolean value indicating whether the edge is removed or not and an integer m ($3 \leq m \leq n$). If the edge is not removed (`done` $=$ `FALSE`), m indicates the current size of A (initially, $m := n$).

`flipnm_post` must be called immediately after `flipnm`. It releases the memory allocated in `flipnm` and can perform "backward" flips to undo the flip sequence performed by `flipnm`.

The basic subroutine `flipnm`($A[0, \dots, n-1]$, `level`) consists of the following three steps:

Step 1. Return `done` $=$ `TRUE` if $n = 3$ and `flip32` is possible for $[a, b]$ and `done` $=$ `FALSE` otherwise.

Step 2. For each $i \in \{0, \dots, n-1\}$ try to remove the face $[a, b, p_i]$ by `flip23`. If it is successfully flipped, reduce the size of A by 1. Update $A[0, \dots, n-2]$ so that it contains the current set of tetrahedra sharing the edge $[a, b]$. Reuse the last entry, $A[n-1]$, to store the information of this `flip23` (see Fig. 2c). It then (recursively) calls `flipnm`($A[0, \dots, n-2]$, level). When no face can be removed, go to Step 3.

Step 3. If `level` > 0, try to remove an edge adjacent to $[a, b]$ using `flipnm`. For each $i \in \{0, \dots, n-1\}$, let $[x, y]$ be given by either edge $[a, p_i]$ or edge $[b, p_i]$. Initialize an array $B[0, \dots, n_1-1]$ of $n_1 \geq 3$ tetrahedra sharing $[x, y]$ and call `flipnm`($B[0, \dots, n_1-1]$, level-1). If $[x, y]$ is successfully removed, reduce $|A|$ by 1. Update $A[0, \dots, n-2]$ to contain the current set of tetrahedra sharing the edge $[a, b]$. Reuse the last entry, $A[n-1]$, to store the information of this `flipnm` and the address of the array B (to be able to release the occupied memory later). Then (recursively) call `flipnm`($A[0, \dots, n-2]$). Otherwise, if $[x, y]$ is not removed, call `flipnm_post`($B[0, \dots, n_1-1], m_1$) to free the memory. Return `done` $=$ `FALSE` if no edge can be removed.

Since `flipnm` is called recursively, not every face and edge should be flipped in Steps 2 and 3. In particular, if B is allocated, i.e., `flipnm` is called recursively, we skip flipping faces and edges belonging to the tetrahedra in $A \cap B$.

In the simplest case, that is, ignoring the option to reverse the flips, `flipnm_post`($A[0, \dots, n-1], m$) simply walks through the array A from $A[m]$ to $A[n-1]$ and checks if a `flipnm` flip has been saved. If so, the saved array address B is extracted and its memory is released.

In Step 2 there are at most $\binom{n}{n-3}/(n-3)!$ different flip sequences, depending on the specific choice of faces in A. Each individual flip sequence is equivalent to a sequence of the n vertices (apexes) in the link of the edge $[a, b]$. We reuse the entries of A to store each flip sequence. After a 2-to-3 flip, the number of the tetrahedra in array A is reduced by one (two tetrahedra out, one tetrahedron in), since only one of the three new tetrahedra contains the edge $[a, b]$. The remaining tetrahedra are shifted by one in the list, so that the last entry, $A[n-1]$, can be used to store this flip (cf. Fig. 2c). In particular, the following information is saved:

- a flag indicating a 2-to-3 flip;
- the original position i, meaning that the face $[a, b, p_i]$ is flipped.

Both is compressed and stored in the entry $A[n-1]$ (note that a flag requires just a few bits of space). This stored data allows us to perform the reversal of a 2-to-3 flip as follows:

- use A and the position i with

  $$A[i-1] = [a, b, p_{i-1}, p_{i+1}]$$

  to locate the three tetrahedra sharing the edge $[p_{i-1}, p_{i+1}]$: $[p_{i-1}, p_{i+1}, a, b]$, $[p_{i-1}, p_{i+1}, b, p_i]$, and $[p_{i-1}, p_{i+1}, p_i, a]$;
- perform a 3-to-2 flip on these three tetrahedra;
- insert two new tetrahedra into the array A:

  $$A[i-1] = [a, b, p_i, p_{i-1}],$$
  $$A[i] = [a, b, p_i, p_{i+1}].$$

In Step 3, if the selected edge $[a, p_i]$ is removed, the sequence of flips to remove $[a, p_i]$ is stored in B. We then use the last entry $A[n-1]$ to store this sequence of flips. In particular, the following information is saved:

- a flag indicating that this entry stores the flip sequence to remove the edge $[a, p_i]$;
- the original position i, i.e., the edge $[a, p_i]$ is flipped;
- the address of the array B which stores the flip sequence.

This information allows us to reverse this sequence of flips exactly.

3.2. Lazy searching flips

During the mesh improvement process we perform flips to improve the mesh quality. Let us consider the case when it becomes necessary to remove an edge. The maximum possible number of

Please cite this article in press as: Dassi F., et al. Tetrahedral mesh improvement using moving mesh smoothing, lazy searching flips, and RBF surface reconstruction. Computer-Aided Design (2017), https://doi.org/10.1016/j.cad.2017.11.010.

flips for an edge removal is the Catalan number C_{n-2} (n is the size of A). Hence, the direct search for the optimal solution is only meaningful if n is very small. In most situations, an edge may not be flipped if we restrict ourselves to adjacent faces of the edge. Our strategy is to search and perform the flips as long as they improve the current mesh quality. Our lazy searching scheme is not restricted by the number n and can be extended to adjacent edges.

The lazy searching flip scheme is like a walk in a k-ary search tree (a rooted tree with at most k children at each node, see Fig. 2b). The root represents the edge $[a, b]$ to be flipped and each of the tree nodes represents either an adjacent face $[a, b, p_i]$ or an adjacent edge $[a, p_i]$ or $[b, p_i]$ of $[a, b]$. The edges of the tree represent our search paths. In particular, the directed edge from `level` l to $l+1$ represents either a `flip23` or a `flipnm`, and the reversed edge represents the inverse operation. The tree depth is given by the parameter `level`.

At `level` > 0, in order to decide if an adjacent face $[a, b, p_i]$ should be flipped, we check if $[a, b, p_i]$ is flippable and make sure that this flip improves the local mesh quality. Note that we need to check only two of the three new tetrahedra: $[a, p_{i-1}, p_i, p_{i+1}]$ and $[b, p_{i-1}, p_i, p_{i+1}]$. The tetrahedron $[a, b, p_{i-1}, p_{i+1}]$ will be involved in the later flips, and will be flipped if the edge $[a, b]$ is flipped.

Once an improvement is found, the algorithm moves on to the next edge without exploring other possibilities.

4. Radial basis functions to handle curved boundaries

We describe in this section how to project the mesh on a smooth surface in order to deal with curved boundaries. We achieve this with the help of radial basis functions (RBFs), see [18–20].

4.1. Basic concepts and examples

Let $\mathcal{P}_m(\mathbb{R}^d)$ denote the space of d variate polynomials with absolute degree at most m and dimension $q := \dim \mathcal{P}_m(\mathbb{R}^d) = \binom{m-1+d}{d}$. For a basis $p_1, \ldots, p_q$ of this space, define the $M \times q$ polynomial matrix P_X through its ijth entry,

$$p_{ij} = p_i(\mathbf{x}_j)\,,$$

where $\mathbf{x}_j \in X$ and $X = \{\mathbf{x}_1, \ldots, \mathbf{x}_M\} \subseteq \mathbb{R}^d$ denotes a data set. The function Φ is called *conditionally positive definite of order m* if the quadratic form

$$\mathbf{c}^T A_{\Phi,X}\mathbf{c}$$

for the distance matrix $A_{\Phi,X}$ with its ijth entry defined by

$$(A_{\Phi,X})_{ij} = \Phi(\mathbf{x}_i - \mathbf{x}_j)\,,$$

is positive for all data sets X and for all $\mathbf{c} \in \mathbb{R}^M \setminus \{\mathbf{0}\}$ which additionally satisfy the constraint $P_X^T\mathbf{c} = \mathbf{0}$.

Conditionally positive functions of order m are also conditionally positive definite for any order higher than m. Hence, the order shall denote the smallest positive integer m. A conditionally positive definite function of order $m = 0$ is called *positive definite*.

One speaks of radial basis functions if one additionally assumes that Φ is a radial function, i.e., there exists a function $\phi : \mathbb{R}_{\geq 0} \to \mathbb{R}$ such that $\Phi(\mathbf{x}) = \phi(\|\mathbf{x}\|)$. Common examples of RBFs include:

$$\begin{aligned}
\text{Gaussian:}\quad & e^{-\|\mathbf{x}\|^2},\\
\text{Multiquadric:}\quad & \sqrt{1+\|\mathbf{x}\|^2},\\
\text{Inverse Multiquadric:}\quad & 1/\sqrt{1+\|\mathbf{x}\|^2},\\
\text{Polyharmonic Spline:}\quad & \|\mathbf{x}\|^3.
\end{aligned}$$

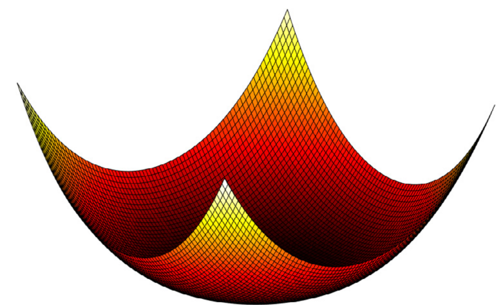

Fig. 3. The polyharmonic spline $\|\mathbf{x}\|^3$.

For the numerical examples in this paper, we exclusively use the polyharmonic spline $\|\mathbf{x}\|^3$ (Fig. 3) which is conditionally positive of order 2.

We assume now that the interpolant $s : \mathbb{R}^d \to \mathbb{R}$ is given by a linear combination of translated radial basis function, augmented by a polynomial part, i.e.

$$s(\mathbf{x}) = \sum_{j=1}^{M} \alpha_j \Phi(\mathbf{x} - \mathbf{x}_j) + \sum_{k=1}^{q} \beta_k p_k(\mathbf{x}). \qquad (7)$$

Thus, we have $M + q$ unknown coefficients, M of which are determined from the interpolation conditions and q conditions from requiring that $P_X^T\mathbf{c} = \mathbf{0}$. For positive definite functions, the linear system is positive definite by construction. Hence the coefficients can be determined uniquely. It is also not difficult to verify that the interpolation and polynomial constraint conditions for conditionally positive definite functions lead to a uniquely solvable system, see [20, Theorem 8.21] for details. In the case of conditionally positive definite functions, it is known that at least $M - q$ eigenvalues of the matrix $A_{\Phi,X}$ are positive [20, Section 8.1].

4.2. Surface reconstruction with RBFs

We will assume that the surface Γ is given implicitly by the zero level set of some function $F : \Omega \subseteq \mathbb{R}^3 \to \mathbb{R}$, i.e.

$$\Gamma = \left\{(x, y, z)^T \in \Omega \mid F(x, y, z) = 0\right\}\,, \qquad (8)$$

for some bounded domain Ω.

We cannot simply assume that the target function (which we wish to interpolate) is the zero level set of the function F since the right-hand side of the linear system one needs to solve would vanish which in turn implies that the coefficients vanish as well. Carr et al. [17] therefore made the additional assumption that the normal vectors are known. Then one can also prescribe on-surface and off-surface points. Assume that the points on the surface are denoted with $X = \{\mathbf{x}_1, \ldots, \mathbf{x}_N\}$ and the corresponding normal vectors with $M = \{\mathbf{n}_1, \ldots, \mathbf{n}_N\}$. We define the surface interpolation problem

$$\begin{aligned}
s(\mathbf{x}_i) = F(\mathbf{x}_i) &= 0, & 1 \leq i \leq N\\
s(\mathbf{x}_i + \varepsilon\mathbf{n}_i) = F(\mathbf{x}_i + \varepsilon\mathbf{n}_i) &= \varepsilon, & N+1 \leq i \leq 2N
\end{aligned} \qquad (9)$$

for some parameter $\varepsilon > 0$. Since the right-hand side of the linear system does not vanish anymore, we find a nontrivial solution. Recently, this surface interpolation technique was combined with the higher dimensional embedding technique [21,22] to construct curvature-aligned anisotropic surface meshes. In this context the data set X corresponds to the vertices of the mesh.

ARTICLE IN PRESS

Algorithm 1 The proposed mesh improvement scheme.

IMPROVE($\mathcal{T}_h^{ini}$, $\theta_{\lim}$)

1: **repeat**
2:   **repeat**
3:     **repeat**
4:       **repeat**
5:         **repeat**
6:           *MMPDE-based smoothing*
7:           *RBF surface reconstruction*
8:           *lazy flips*
9:         **until** no point is moved or no flip is done or $Q(\mathcal{T}_h) \geq \theta_{\lim}$ → smooth and flip
10:         remove the edges $l_{\mathbf{e}} < 0.5\, l_{\text{ave}}$
11:         *lazy flips*
12:       **until** no edge is contracted or $Q(\mathcal{T}_h) \geq \theta_{\lim}$
13:       split the edges $l_{\mathbf{e}} > 1.5\, l_{\text{ave}}$
14:       *RBF surface reconstruction*
15:       *lazy flips*
16:     **until** no edge is split or $Q(\mathcal{T}_h) > \theta_{\lim}$
17:     split the tetrahedra K such that $\theta_{\min,K} < \theta_{\lim}$
18:     *lazy flips*
19:   **until** no tetrahedron is removed or $Q(\mathcal{T}_h) > \theta_{\lim}$ → main loop
20:   change the flip criterion for the *lazy flips*
21: **until** no operation is done in the main loop or $Q(\mathcal{T}_h) > \theta_{\lim}$

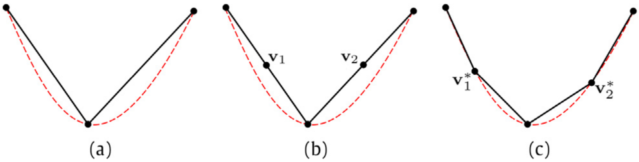

Fig. 4. Edge splitting. In (a), a coarse input mesh (solid line) approximates the reconstructed curve (dashed line). In (b), the edges are halved, the midpoints $\mathbf{v}_1$ and $\mathbf{v}_2$ are not on the curve. In (c), new points $\mathbf{v}_1^*$ and $\mathbf{v}_2^*$ are projected onto the curve using a steepest descent method.

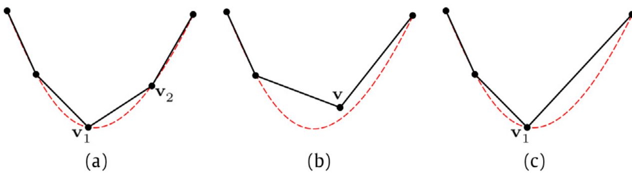

Fig. 5. Edge contraction. In (a), a fine input mesh (solid line) approximates the reconstructed curve (dashed line). In (b), the edge $\overline{\mathbf{v}_1\mathbf{v}_2}$ is contracted into its midpoint $\mathbf{v}$, which is not on the curve. In (c), the edge $\overline{\mathbf{v}_1\mathbf{v}_2}$ is contracted into its end point $\mathbf{v}_1$, which, by construction, is on the curve.

4.3. Projection onto the reconstructed surface

There are two important parts of the projection algorithm: edge splitting and edge contraction. If we split an edge or move a point during smoothing, we project the resulting point onto the RBF surface reconstruction (Fig. 4).

The projection itself is realized with ideas from [34]. This procedure is a combination of orthogonal projections on tangent planes as well as tangent parabolas. It requires only first order derivatives and uses a steepest descent method. The combination of this projection method with RBF surface reconstruction has also been discussed in [21,22].

When it becomes necessary to contract an edge, we contract it into one of its endpoints (Fig. 5).

5. Mesh improvement strategy

The goal of the proposed algorithm is to obtain a new isotropic mesh whose elements come "as close as possible" to the equilateral one. To achieve this goal, we combine the local and global mesh operations described in Sections 2 and 3.

5.1. Mesh quality

To say "as close as possible to an equilateral tetrahedron" is somewhat vague from a mathematical point of view. To have a more precise criterion, the majority of the mesh improvement algorithms define a computable quantity $q(K)$ which quantifies how far a tetrahedron K is from being equilateral [2,24,35–38]. Here, we take into account the following two:

Aspect ratio: This is one of the most classical ways to evaluate the quality of a tetrahedron. It is defined as

$$q_{ar}(K) := \sqrt{\frac{2}{3}}\frac{L}{h}, \tag{10}$$

where L is the longest edge and h is the shortest altitude of the tetrahedron K. By construction, $q_{ar}(K) \geq 1$ and an equilateral tetrahedron is characterized by $q_{ar}(K) = 1$.

Min–max dihedral angle: For each tetrahedron K we consider both the minimal and the maximal dihedral angles $\theta_{\min,K}$ and $\theta_{\max,K}$. An equilateral tetrahedron has $\theta_{\min,K} = \theta_{\max,K} = \arccos(1/3) \approx 70.56°$. Applying an operation that increases $\theta_{\min,K}$ or decreases $\theta_{\max,K}$ of a given tetrahedron K makes K "closer" to the equilateral shape. Note that this is not a classical quality measure since we associate two quantities with each tetrahedron, which is one of the novel aspects of the proposed mesh improvement procedure.

These two quality measures refer to a single tetrahedron K of the mesh. However, the design of our mesh improvement scheme requires a quality measure for the *whole* mesh as a stopping criterion. To estimate the quality of the whole mesh, we define the global parameter

$$Q(\mathcal{T}_h) := \min_{K \in \mathcal{T}_h} \left(\theta_{\min,K}\right). \tag{11}$$

Please cite this article in press as: Dassi F., et al. Tetrahedral mesh improvement using moving mesh smoothing, lazy searching flips, and RBF surface reconstruction. Computer-Aided Design (2017), https://doi.org/10.1016/j.cad.2017.11.010.

ARTICLE IN PRESS

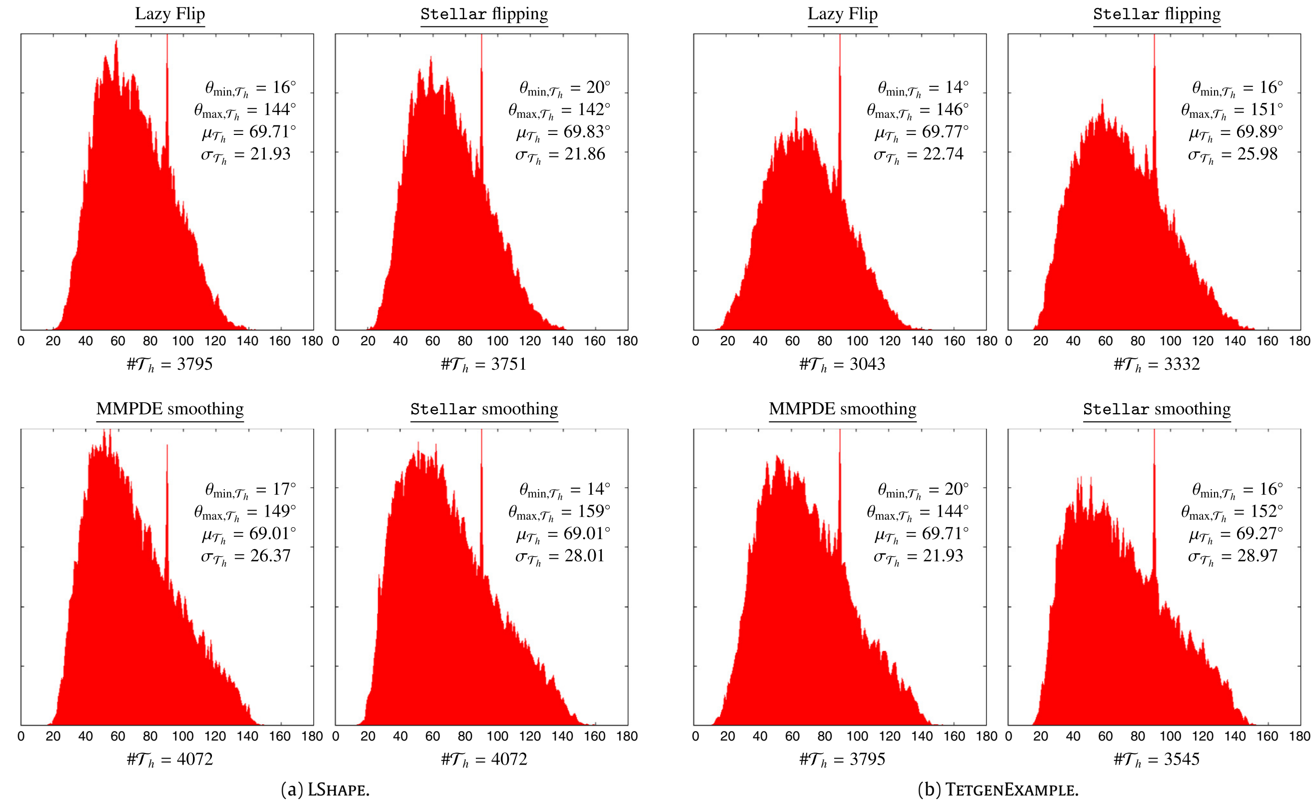

(a) LShape. (b) TetgenExample.

Fig. 6. Comparison of flipping only (first row) and smoothing only (second row) for the initial meshes LShape and TetgenExample.

If we consider a target dihedral angle θ_{lim} and obtain a mesh $\mathcal{T}_h$ with $Q(\mathcal{T}_h) > \theta_{\text{lim}}$, then *all* dihedral angles are guaranteed to be greater than θ_{lim}.

5.2. The scheme

The inputs for the mesh improvement algorithm are a tetrahedral mesh $\mathcal{T}_h^{ini}$ of a PLC and a target minimum angle θ_{lim}. The output is a mesh $\mathcal{T}_h^{fin}$ where each element has a minimum dihedral angle greater than θ_{lim}.

The scheme is presented in Algorithm 1 and consists of five nested "**repeat ...until**" loops, whose stopping criterion depends on the operations done inside the loop and $Q(\mathcal{T}_h)$. We apply the MMPDE smoothing and the *lazy flip* in the most internal loop (lines 5 to 9). The *lazy flip* is also exploited in the outer loops both on the whole mesh (lines 11, 15 and 18) and on the tetrahedra involved in the local operations (lines 10, 13 and 17).

It is possible to consider several flipping criteria for the *lazy flip*, which makes the design of the scheme flexible. We exploit this feature by using two objective functionals and changing the flipping criterion in each iteration of the outer loop (line 20) by

1. maximizing $\theta_{\min,K}$ and minimizing $\theta_{\max,K}$ (simultaneously),
2. minimizing the aspect ratio.

The stopping criterion is always based on the minimal dihedral angle, $Q(\mathcal{T}_h)$, and the number of operations done.

After a number of iterations both the flipping and the smoothing procedure can stagnate, i.e., the mesh $\mathcal{T}_h$ converges to a fixed configuration where neither flips nor smoothing can improve the quality of the mesh. Unfortunately, it is not a priori guaranteed that such a mesh satisfies the constraint on the target minimum dihedral angle θ_{lim}. To overcome this difficulty, we apply edge splitting, edge contraction, and point insertion when this stagnation occurs (lines 10, 13 and 17 in Algorithm 1).

For the edge contraction and splitting, we use the standard edge length criterion: we compute the average edge length l_{ave} of the actual mesh, contract the edges shorter than $0.5\, l_{\text{ave}}$ (line 10), and split (halve) the ones longer than $1.5\, l_{\text{ave}}$ (line 13). In line 17, we split a tetrahedron K with $\theta_{\min,K} < \theta_{\text{lim}}$ via a standard 1-to-4 flip by placing the newly added point at the barycenter of K [39]. In this way, the algorithm constructs via flipping and smoothing a mesh satisfying $Q(\mathcal{T}_h) > \theta_{\text{lim}}$. At the moment, we are not interested in optimizing these operations, we exploit them only to overcome the stagnation of the algorithm.

The MMPDE smoothing can be easily parallelized because the nodal velocities in each smoothing step can be assembled through independent element-wise computation (Eqs. (5) and (6)), similar to the assembly of a finite element stiffness matrix. We parallelize the computation of the nodal velocities with OpenMP [40]. Once the velocities are computed, all mesh nodes are moved simultaneously and independently of each other. On the other hand, the *lazy flip* may propagate to neighbors and neighbors of neighbors, thus, it is complex and difficult to parallelize; in our tests we use a sequential implementation.

6. Numerical examples

We test the proposed mesh improvement algorithm and compare it with the mesh improvement algorithm of `Stellar` [2], the remeshing procedure of `CGAL` [23], and `mmg3d` [24]. We compare the histograms of the dihedral angles of final meshes, the minimal and the maximal dihedral angles $\theta_{\min,\mathcal{T}_h}$ and $\theta_{\max,\mathcal{T}_h}$, the mean dihedral angle $\mu_{\mathcal{T}_h}$, and its standard deviation $\sigma_{\mathcal{T}_h}$.

Please cite this article in press as: Dassi F., et al. Tetrahedral mesh improvement using moving mesh smoothing, lazy searching flips, and RBF surface reconstruction. Computer-Aided Design (2017), https://doi.org/10.1016/j.cad.2017.11.010.

ARTICLE IN PRESS

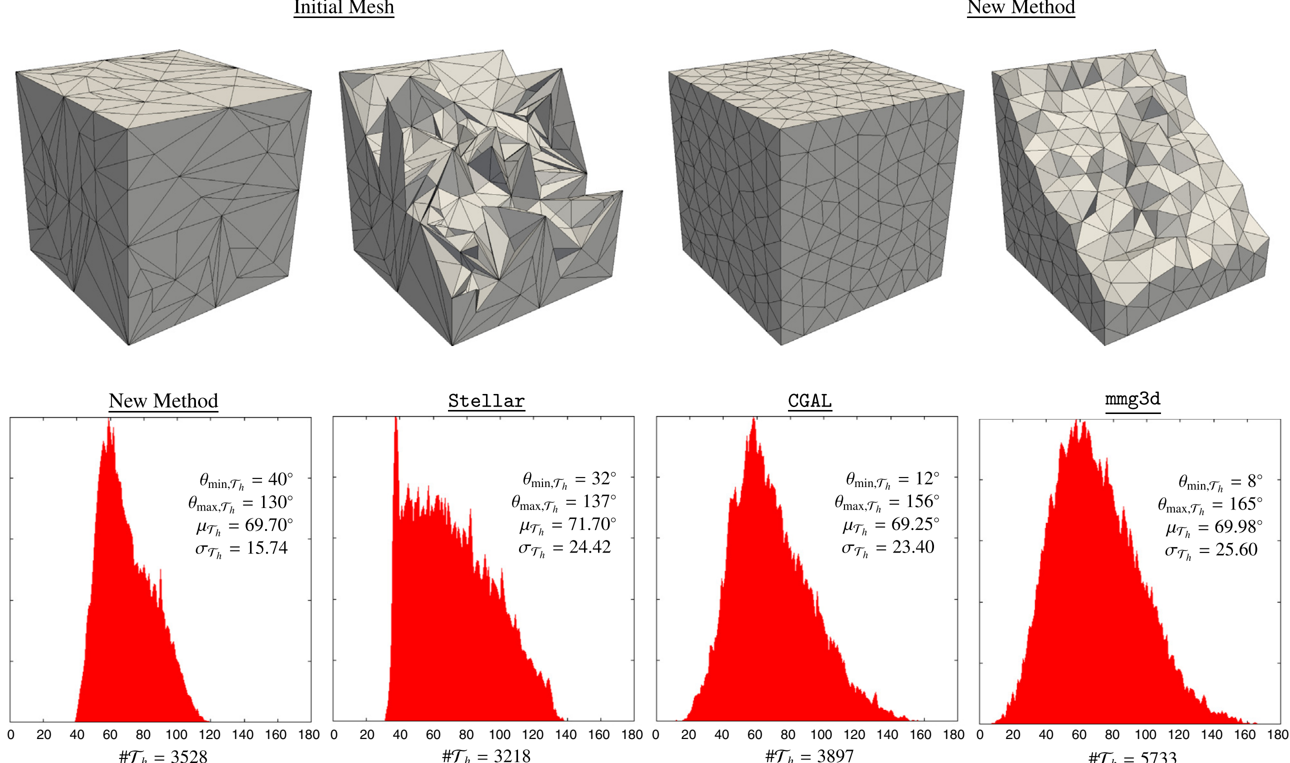

Fig. 7. RAND1. The initial mesh with $\#\mathcal{T}_h = 5104$, the final (optimized) mesh, and statistics of dihedral angles for the final meshes.

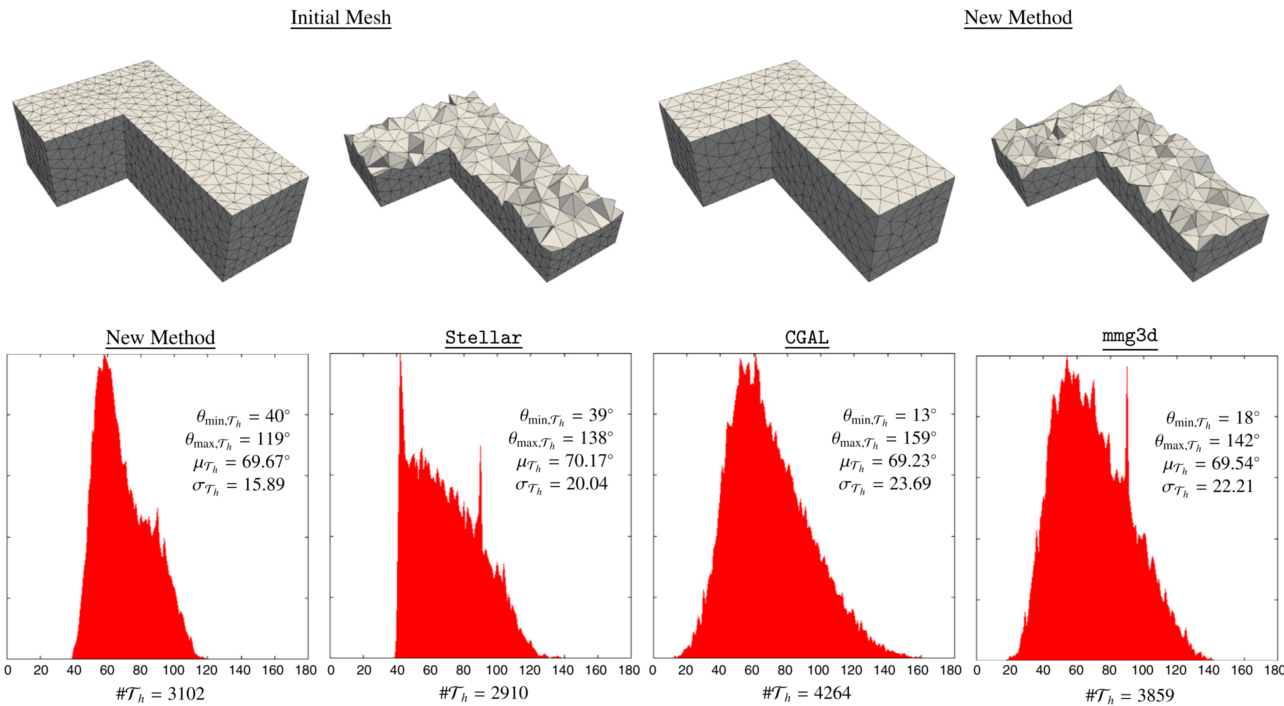

Fig. 8. LSHAPE. The initial mesh with $\#\mathcal{T}_h = 4072$, the final (optimized) mesh, and statistics of dihedral angles for the final meshes.

6.1. Piecewise linear complexes (PLCs)

To analyze the effectiveness of the proposed mesh improvement scheme in case of a piecewise linear complex domain, we consider the following three examples (for more PLC examples, see [41]):

- RAND1 tetrahedral meshes of a cube generated by inserting randomly located vertices inside and on the boundary [2] (Fig. 7),
- LSHAPE is a tetrahedral mesh of an L-shaped PLC generated by `TetGen` [33] without optimizing the minimal dihedral angle (switches `-pa0.019`, Fig. 8),

Please cite this article in press as: Dassi F., et al. Tetrahedral mesh improvement using moving mesh smoothing, lazy searching flips, and RBF surface reconstruction. Computer-Aided Design (2017), https://doi.org/10.1016/j.cad.2017.11.010.

ARTICLE IN PRESS

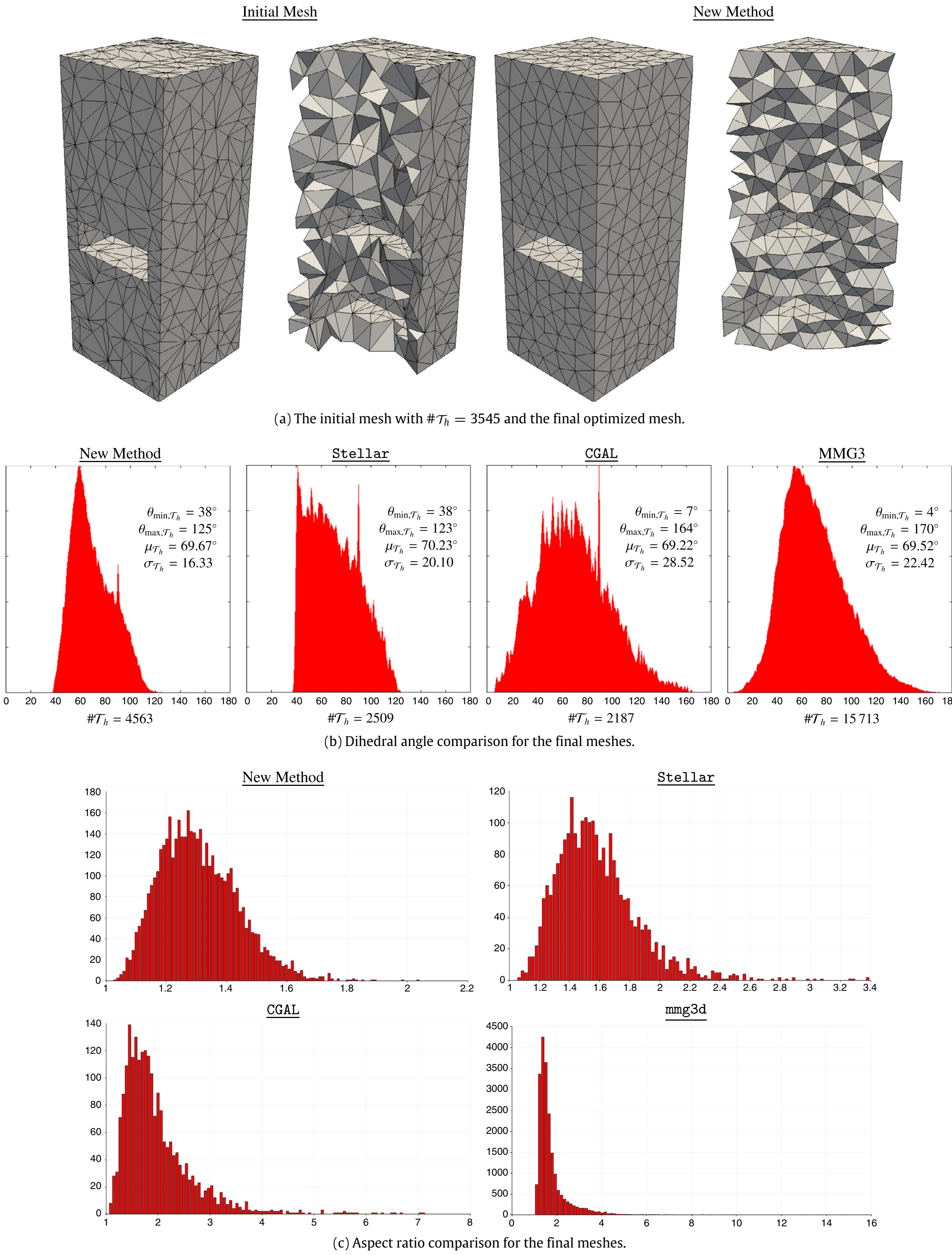

(a) The initial mesh with $\#\mathcal{T}_h = 3545$ and the final optimized mesh.

(b) Dihedral angle comparison for the final meshes.

(c) Aspect ratio comparison for the final meshes.

Fig. 9. TetgenExample. The initial mesh with $\#\mathcal{T}_h = 3545$, the final (optimized) mesh, and statistics of the dihedral angles and the aspect ratio.

Please cite this article in press as: Dassi F., et al. Tetrahedral mesh improvement using moving mesh smoothing, lazy searching flips, and RBF surface reconstruction. Computer-Aided Design (2017), https://doi.org/10.1016/j.cad.2017.11.010.

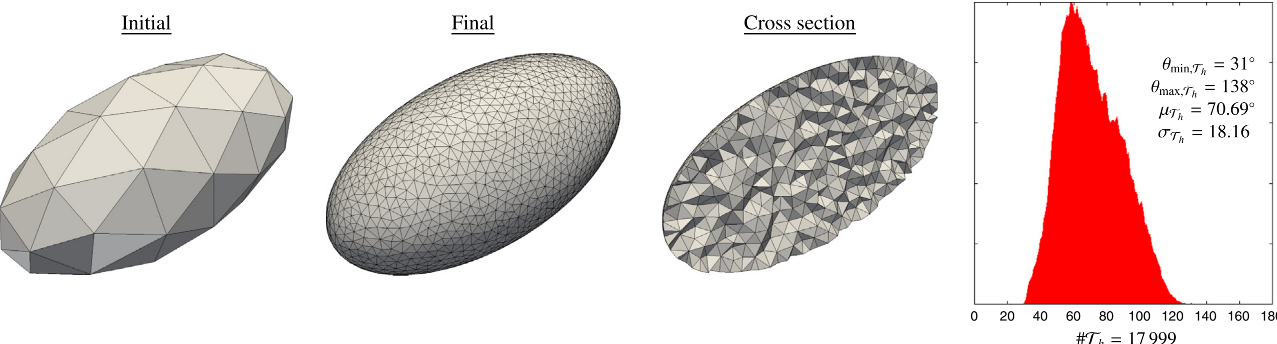

Fig. 10. Example of tetrahedral mesh improvement with a curved (reconstructed) surface.

- TetgenExample is a tetrahedral example mesh of a non-convex PLC with a hole provided by `TetGen` (Fig. 9).

Smoothing and flipping by themselves. Before testing the full mesh improvement scheme, we test the effectiveness of the MMPDE smoothing and the *lazy flip* by themselves and employ smoothing and flipping separately, i.e., we improve a tetrahedral mesh exploiting *only* the flipping operation or the vertex smoothing. We compare our results with the ones provided by `Stellar` for the examples LShape and TetgenExample.

The results of the *lazy flip* are comparable to the `Stellar` flips (Fig. 6, first row). However, the MMPDE smoothing is better than its counterpart in `Stellar` (Fig. 6, second row): in both examples it achieves larger $\theta_{\min,\mathcal{T}_h}$, noticeably smaller $\theta_{\max,\mathcal{T}_h}$, and a smaller standard deviation of the mean dihedral angle.

Full scheme. We compare the whole scheme with the mesh improvement algorithm of `Stellar` [2], the remeshing procedure of `CGAL` [23], and `mmg3d` [24] (Figs. 7 to 9).

Although all methods provide good results, the new scheme is better: $\theta_{\min,\mathcal{T}_h}$ is larger than the value obtained by `CGAL` or `mmg3d` and comparable to the value obtained by `Stellar`. Moreover, $\theta_{\max,\mathcal{T}_h}$ is smaller than the values obtained by `Stellar`, `CGAL`, or `mmg3d` in all examples but one see Fig. 9a.

Our method provides mean dihedral angles $\mu_{\mathcal{T}_h}$ around 69.6°, which is close to the optimal value of $\arccos(1/3) \approx 70.56°$. Moreover, standard deviations $\sigma_{\mathcal{T}_h}$ are always smaller than the ones of other methods. Indeed, we get a distribution of dihedral angles close to the mean value. This quantitative consideration becomes clearer from the shape of the histograms in Figs. 7 to 9.

For the TetgenExample (Fig. 9) we also provide aspect ratio histograms (the results for the other examples are very similar and we omit them). The aspect ratio of an equilateral tetrahedron is equal to 1 and the more a tetrahedron is distorted and stretched the greater its aspect ratio becomes. Our method and `Stellar` clearly provide the best aspect ratio distribution. For our method, the vast majority of tetrahedra have an aspect ratio smaller than 1.8. The `Stellar` mesh is slightly worse with most of its tetrahedra having aspect ratios below 2.6.

6.2. Curved boundary domains

In the last part of this section, we experimentally demonstrate some examples with curved domains. We study two types of examples: one academic example for using the RBF surface reconstruction to project the boundary vertices on the smooth approximation of the discrete surface and two more complex examples with fixed boundary vertices.

First, we consider the discrete ellipsoid mesh (Fig. 10). Though it has a simple geometry, it requires some effort since the boundary is curved and no longer a PLC. The main challenge is to project the boundary vertices back onto the smooth surface if they leave it after a mesh improvement step. For this reason, we reconstruct the surface via RBFs (see Section 4.2) to assist the mesh optimization and project the moved (smoothed) boundary vertices to the reconstructed surface. Fig. 10 shows that RBF reconstruction smoothes the initially rough surface approximation. The obtained tetrahedral mesh has high quality: the mean dihedral angle is close to the optimal value (≈70.69°) and the standard deviation of the dihedral angles is small (≈18.16°).

However, it has to be pointed out that complicated boundaries cannot be handled as easily as an ellipsoid and require more sophisticated methods.

In our next examples, we restrict ourselves to the case of fixed boundary vertices since `Stellar` does not handle curved surfaces described via an implicit function, start with a good isotropic triangular mesh as input, and keep the boundary vertices fixed for each of the algorithms.

Fixed boundary. The next two examples are meshes of a spinal bone and of an elephant (Figs. 11 and 12). The initial surface meshes in both examples are constructed by means of the higher dimensional embedding approach for surface mesh reconstruction [22] and their minimal face angles are approximately 33°. The initial volume meshes are constructed by `TetGen` using the `-Y` flag to preserve the fixed boundary.

Figs. 11 and 12 present the histograms of the dihedral angles of the resulting optimized meshes. In comparison to the PLC examples, where the geometry is simpler and the boundary vertices are allowed to move, the smallest dihedral angles for the spinal bone and the elephant examples are worse (smaller) than for the PLC examples. In comparison to `Stellar`, our algorithm achieves better values for $\theta_{\min,\mathcal{T}_h}$ and $\theta_{\max,\mathcal{T}_h}$, as well as a smaller mean deviation from the mean value.

These examples, too, show the "aggressive" nature of the `Stellar` mesh improvement algorithm, which aggressively removes vertices during the mesh improvement. In contrast, our mesh improvement scheme is able to produce a high-quality mesh while keeping the number of vertices close to the original input.

7. Conclusions

Mesh improvement is a challenging problem and we tackled it by combining several recently developed techniques, namely, moving mesh smoothing, lazy flipping, and RBF surface reconstruction. In comparison to the mesh improvement algorithm `Stellar` and the re-meshing procedures provided by `CGAL` and `mmg3d`, we obtain better results in terms of the distributions of dihedral angles for all considered examples. However, there are several directions in which this work could be extended.

Please cite this article in press as: Dassi F., et al. Tetrahedral mesh improvement using moving mesh smoothing, lazy searching flips, and RBF surface reconstruction. Computer-Aided Design (2017), https://doi.org/10.1016/j.cad.2017.11.010.

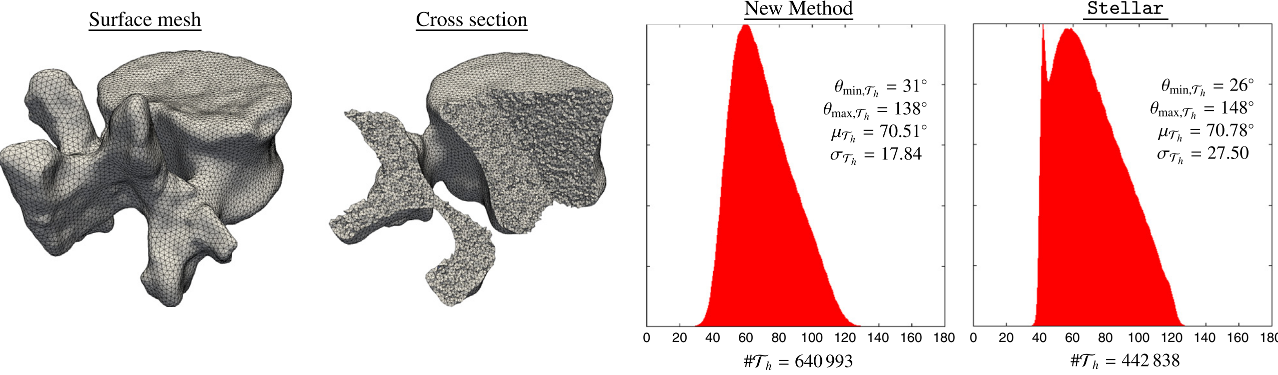

Fig. 11. Spine example: the initial mesh with $\#\mathcal{T}_h = 688\,420$ and the final optimized mesh.

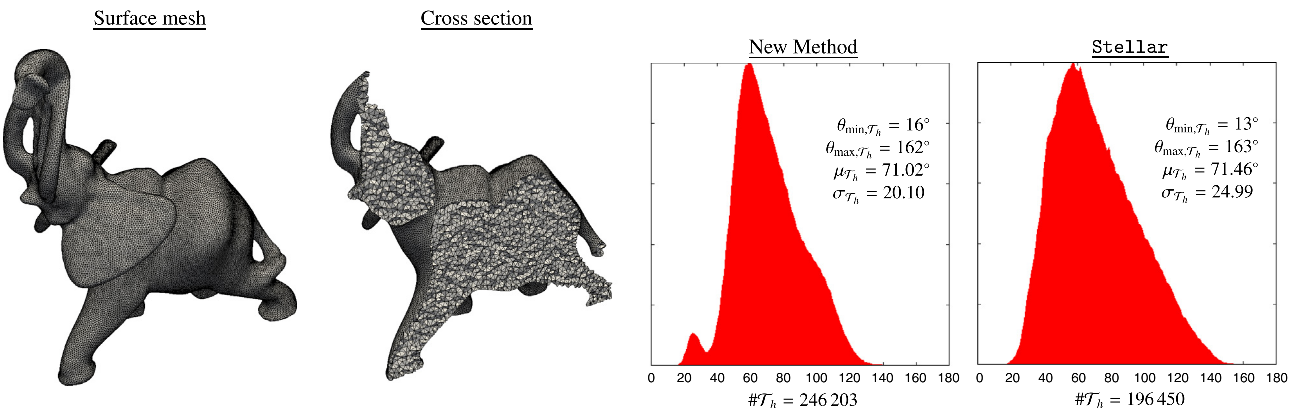

Fig. 12. Elephant example: the initial mesh with $\#\mathcal{T}_h = 260\,401$ and the final optimized mesh.

First, for smooth and relatively simple boundaries, our approach works excellently but complicated curved boundaries pose a challenging problem. One possible solution could be the direct incorporation of the boundary description into the MMPDE smoothing scheme (parametrization) so that the boundary vertices will always stay on the surface. This will avoid the sometimes troublesome projection of vertices and velocities back onto the surface after a smoothing step.

Second, we need to find a more sophisticated method for edge contraction and splitting in order to improve the performance of both the MMPDE smoothing and the lazy flip.

Third, the MMPDE smoothing is based on the moving mesh method [13] which allows the definition of a metric field. Hence, the moving mesh smoothing can be extended to the adaptive and anisotropic setting.

Acknowledgments

The work of Franco Dassi was partially supported by the “Leibniz-DAAD Research Fellowship 2014”. The authors are thankful to Jeanne Pellerin for her support in computing the examples with `mmg3d` [24].

References

[1] Freitag LA, Ollivier-Gooch C. Tetrahedral mesh improvement using swapping and smoothing. Internat J Numer Methods Engrg 1997;40(21):3979–4002.
[2] Klingner BM, Shewchuk JR. Aggressive tetrahedral mesh improvement. In: Proceedings of the 16th International meshing roundtable. 2007. p. 3–23. http://graphics.cs.berkeley.edu/papers/Klingner-ATM-2007-10.
[3] Field DA. Laplacian smoothing and Delaunay triangulations. Commun Appl Numer Methods 1978;4:709–12.
[4] Lo SH. A new mesh generation scheme for arbitaar planar domains. Internat J Numer Methods Engrg 1985;21:1403–26.
[5] Bank RE. PLTMG: A software package for solving elliptic partial differential equations. Frontiers in applied mathematics, vol. 15, Philadelphia, PA: Society for Industrial and Applied Mathematics (SIAM); 1994, users' guide 7.0.
[6] Shephard M, Georges M. Automatic three-dimensional mesh generation by the finite octree technique. Internat J Numer Methods Engrg 1991;32:709–49.
[7] Freitag LA, Knupp PM. Tetrahedral mesh improvement via optimization of the element condition number. Internat J Numer Methods Engrg 2002;53(6): 1377–1391.
[8] Knupp PM. Achieving finite element mesh quality via optimization of the Jacobian matrix norm and associated quantities. Part I–A framework for surface mesh optimization. Internat J Numer Methods Engrg 2000;48:401–20.
[9] Knupp PM. Applications of mesh smoothing: copy, morph, and sweep on unstructured quadrilateral meshes. Internat J Numer Methods Engrg 1999;45(1): 37–45.
[10] Canann SA, Tristano JR, Staten ML. An approach to combined Laplacian and optimization-based smoothing for triangular, quadrilateral, and quad-dominant meshes. In: Proceedings of the 7th International Meshing Rountable. 1998.
[11] Freitag L, Jones M, Plassmann P. A parallel algorithm for mesh smoothing. SIAM J Sci Comput 1999;20(6):2023–40.
[12] Huang W. Variational mesh adaptation: isotropy and equidistribution. J Comput Phys 2001;174(2):903–24.
[13] Huang W, Kamenski L. A geometric discretization and a simple implementation for variational mesh generation and adaptation. J Comput Phys 2015;301:322–37.
[14] Huang W, Kamenski L. On the mesh nonsingularity of the moving mesh PDE method. Math Comput (electronically), 2017. http://dx.doi.org/10.1090/mcom/3271.
[15] Joe B. Construction of three-dimensional improved-quality triangulations using local transformations. SIAM J Sci Comput 1995;16(6):1292–307.
[16] George P, Borouchaki H. Back to edge flips in 3 dimensions. In: Proceedings of the 12th international meshing rountable (September 2003).
[17] Carr JC, Beatson RK, Cherrie JB, Mitchell TJ, Fright WR, McCallum BC, Evans TR. Reconstruction and representation of 3d objects with radial basis functions. In: Proceedings of the 28th annual conference on computer graphics and interactive techniques. ACM; 2001. p. 67–76.

ARTICLE IN PRESS

[18] Fornberg B, Flyer N. A primer on radial basis functions with applications to the geosciences. Philadelphia, PA, USA: Society for Industrial and Applied Mathematics; 2015.

[19] Iske A. Multiresolution methods in scattered data modelling. Lecture notes in computational science and engineering, vol. 37, Berlin: Springer; 2004.

[20] Wendland H. Scattered data approximation. Cambridge monographs on applied and computational mathematics, vol. 17, Cambridge: Cambridge University Press; 2005.

[21] Dassi F, Farrell P, Si H. A novel remeshing scheme via radial basis functions and higher dimensional embedding. WIAS Preprint 2265.

[22] Dassi F, Farrell P, Si H. An anisoptropic surface remeshing strategy combining higher dimensional embedding with radial basis functions. Procedia Eng 2016;163:72–83, 25th International Meshing Roundtable.

[23] The CGAL Project, CGAL User and Reference Manual, 4.8 Edition, 2016. https://doc.cgal.org/4.8.

[24] Dobrzynski C. MMG3D: User Guide, Technical Report RT-0422, INRIA, 2012. https://hal.inria.fr/hal-00681813.

[25] Huang W, Ren Y, Russell RD. Moving mesh partial differential equations (MMPDES) based on the equidistribution principle. SIAM J Numer Anal 1994;31(3):709–30.

[26] Huang W, Russell RD. Adaptive moving mesh methods. Applied mathematical sciences, vol. 174, New York: Springer; 2011.

[27] Huang W, Kamenski L, Si H. Mesh smoothing: an MMPDE approach, Research Notes of the 24th International Meshing Roundtable 2015.

[28] Huang W. Mathematical principles of anisotropic mesh adaptation. Commun Comput Phys 2006;1(2):276–310.

[29] Huang W, Kamenski L, Russell RD. A comparative numerical study of meshing functionals for variational mesh adaptation. J Math Study 2015;48(2):168–86.

[30] Hairer E, Lubich C. Energy-diminishing integration of gradient systems. IMA J Numer Anal 2014;34(2):452–61.

[31] Dormand JR, Prince PJ. A family of embedded Runge-Kutta formulae. J Comput Appl Math 1980;6(1):19–26.

[32] Miller GL. Control volume meshes using sphere packing. In: Solving irregularly structured problems in parallel: 5th international symposium, IRREGULAR'98 Berkeley, California, USA, August 9–11, 1998 proceedings. Berlin, Heidelberg: Springer Berlin Heidelberg; 1998. p. 128–31 (Chapter).

[33] Si H. TetGen, a Delaunay-based quality tetrahedral mesh generator. ACM Trans Math Software 2015;41(2):11:1–36. http://tetgen.org.

[34] Hartmann E. On the curvature of curves and surfaces defined by normal forms. Comput Aided Geom Design 1999;16(5):355–76.

[35] Geuzaine C, Remacle J-F. Gmsh: A 3-D finite element mesh generator with built-in pre- and post-processing facilities. Internat J Numer Methods Engrg 2009;79(11):1309–31. http://gmsh.info.

[36] Hecht F. New development in freefem++. J Numer Math 2012;20(3–4):251–65.

[37] Shewchuk JR. What is a good linear finite element? Interpolation, conditioning, anisotropy, and quality measures 2002.

[38] Field DA. Qualitative measures for initial meshes. Internat J Numer Methods Engrg 2000;47(4):887–906.

[39] Edelsbrunner H, Ablowitz MJ, Davis SH, Hinch EJ, Iserles A, Ockendon J, Olver PJ. Geometry and topology for mesh generation. Cambridge monographs on applied and computational mathematics, New York, NY, USA: Cambridge University Press; 2006.

[40] Dagum L, Menon R. OpenMP: an industry standard api for shared-memory programming. IEEE Comput Sci Eng 1998;5(1):46–55.

[41] Dassi F, Kamenski L, Si H. Tetrahedral mesh improvement using moving mesh smoothing and lazy searching flips. Procedia Eng 2016;163:302–14, 25th International Meshing Roundtable.

Please cite this article in press as: Dassi F., et al. Tetrahedral mesh improvement using moving mesh smoothing, lazy searching flips, and RBF surface reconstruction. Computer-Aided Design (2017), https://doi.org/10.1016/j.cad.2017.11.010.

15

Computational and Analytical Comparison of Flux Discretizations for the Semiconductor Device Equations beyond Boltzmann Statistics

P. Farrell, T. Koprucki, and J. Fuhrmann. Computational and Analytical Comparison of Flux Discretizations for the Semiconductor Device Equations beyond Boltzmann Statistics. *Journal of Computational Physics* 346 (2017), pp. 497–513. DOI: 10.1016/j.jcp.2017.06.023

Abstract We compare three thermodynamically consistent numerical fluxes known in the literature, appearing in a Voronoi finite volume discretization of the van Roosbroeck system with general charge carrier statistics. Our discussion includes an extension of the Scharfetter-Gummel scheme to non-Boltzmann (e. g. Fermi-Dirac) statistics. It is based on the analytical solution of a two-point boundary value problem obtained by projecting the continuous differential equation onto the interval between neighboring collocation points. Hence, it serves as a reference flux. The exact solution of the boundary value problem can be approximated by computationally cheaper fluxes which modify certain physical quantities. One alternative scheme averages the nonlinear diffusion (caused by the non-Boltzmann nature of the problem), another one modifies the effective density of states. To study the differences between these three schemes, we analyze the Taylor expansions, derive an error estimate, visualize the flux error and show how the schemes perform for a carefully designed p-i-n benchmark simulation. We present strong evidence that the flux discretization based on averaging the nonlinear diffusion has an edge over the scheme based on modifying the effective density of states.

Conception: The idea of this project was almost exclusively due to myself and improved

by ideas from the other co-authors.

Execution: The execution was exclusively performed by myself.

Reporting: The reporting was mostly performed by myself.

Due to copyright reasons, this article cannot be included online.

16

Uniform Second Order Convergence of a Complete Flux Scheme on Unstructured 1D Grids for a Singularly Perturbed Advection–Diffusion Equation and Some Multidimensional Extensions

P. Farrell and A. Linke. Uniform Second Order Convergence of a Complete Flux Scheme on Unstructured 1D Grids for a Singularly Perturbed Advection–Diffusion Equation and Some Multidimensional Extensions. *Journal of Scientific Computing* 72.1 (2017), pp. 373–395. DOI: 10.1007/s10915-017-0361-7

Abstract The accurate and efficient discretization of singularly perturbed advection-diffusion equations on arbitrary 2D and 3D domains remains an open problem. An interesting approach to tackle this problem is the complete flux scheme (CFS) proposed by G. D. Thiart and further investigated by J. ten Thije Boonkkamp. For the CFS, uniform second order convergence has been proven on structured grids. We extend a version of the CFS to unstructured grids for a steady singularly perturbed advection-diffusion equation. By construction, the novel finite volume scheme is nodally exact in 1D for piecewise constant source terms. This property allows to use elegant continuous arguments in order to prove uniform second order convergence on unstructured one-dimensional grids. Numerical results verify the predicted bounds and suggest that by aligning the finite volume grid along the velocity field uniform second order convergence can be obtained in higher space dimensions as well.

Conception: The idea of this project was mostly due to Alexander Linke.

Execution: The execution of this project was mostly due to myself.

Reporting: The reporting of this project was performed by myself.

Due to copyright reasons, this article cannot be included online.

17

On Thermodynamic Consistency of a Scharfetter-Gummel Scheme Based on a Modified Thermal Voltage for Drift-Diffusion Equations with Diffusion Enhancement

T. Koprucki et al. On Thermodynamic Consistency of a Scharfetter-Gummel Scheme Based on a Modified Thermal Voltage for Drift-Diffusion Equations with Diffusion Enhancement. *Optical and Quantum Electronics* 47.6 (2015), pp. 1327–1332. DOI: 10.1007/s11082-014-0050-9

Abstract Driven by applications like organic semiconductors there is an increased interest in numerical simulations based on drift-diffusion models with arbitrary statistical distribution functions. This requires numerical schemes that preserve qualitative properties of the solutions, such as positivity of densities, dissipativity and consistency with thermodynamic equilibrium. An extension of the Scharfetter-Gummel scheme guaranteeing consistency with thermodynamic equilibrium is studied. It is derived by replacing the thermal voltage with an averaged diffusion enhancement for which we provide a new explicit formula. This approach avoids solving the costly local nonlinear equations defining the current for generalized Scharfetter-Gummel schemes.

Conception: This project has been devised by Thomas Koprucki.

Execution: I was involved in the implementation of the method.

Reporting: I helped writing the report.

Due to copyright reasons, this article cannot be included online.

Selbstständigkeitserklärung

Die hier präsentierte Habilitationsleistung habe ich selbstständig verfasst. Bei den gemeinschaftlichen Publikationen habe ich die Namen der Ko-Autor:innen angegeben und den eigenen Anteil gekennzeichnet. Hiermit gebe ich mein Einverständnis, dass meinen Ko-Autor:innen Kenntnis von diesem Antrag gegeben wird.

Berlin, den 30. März 2022

Erklärung über abgeschlossene oder schwebende Habilitationsverfahren

Ich habe an keiner anderen Universität ein Habilitationsverfahren weder abgeschlossen noch initiiert.

Berlin, den 30. März 2022